

Development of a Bonding Concept for MOEMS Packaging: Reactive Nanocomposites

Zur Erlangung des akademischen Grades eines
Doktors der Ingenieurwissenschaften (Dr.-Ing.)
bei der KIT-Fakultät für Maschinenbau
des Karlsruher Instituts für Technologie (KIT)
angenommene

Dissertation

von

Dipl.-Ing. Matthias Peter Kremer

Hauptreferent: Prof. Dr. Andreas E. Guber

Korreferenten: Prof. Dr. Jan G. Korvink,
Prof. Dr. Bernhard Wolf

Prüfungsvorsitz: Prof. Dr.-Ing. Xu Cheng

Tag der mündlichen Prüfung: 19.11.2018



This document is licensed under a Creative Commons Attribution-
NoDerivatives 4.0 International License (CC BY-ND 4.0):
<https://creativecommons.org/licenses/by-nd/4.0/deed.en>

Für Julia und Emilie

Die Liebe ist im
Grunde die Kraft und
die Macht, die allein
das Leben lebenswert
machen kann.

(Konrad Adenauer)

Acknowledgements

This thesis is the outcome of my work at *CTR Carinthian Tech Research AG* during the last three years. It was a very nice time and I felt privileged about being able to live in such a wonderful surrounding as Villach, to work with great colleagues and pursuing my academic degree by a very renowned university in Germany. I want to thank a lot of people:

First of all, I have to thank Prof. Dr.-Ing. Andreas E. Guber (Karlsruhe Institute of Technology – Institute of Microstructure Technology) for supervision and supporting this work even from a distance, for helpful discussions and personal advice. I would like to thank Prof. Dr. Jan G. Korvink (Karlsruhe Institute of Technology – Institute of Microstructure Technology) and Prof. Dr. Bernhard Wolf (Technical University of Munich) for taking over the two co-examinations, which is much appreciated. Thanks to Dr. Andreas Tortschanoff and Dr. Ali Roshanghias, who supervised my work locally at *CTR*. I have to emphasize Andi's support: he enabled me to work at *CTR* in the first place and introduced me to the fascination of moonlight ski touring. A big thanks goes to all colleagues at *CTR* (special shout-out to Michael, Marcelo, Markus, Matic and Marijana - guys whose names start with "M" are awesome!), who made working really fun and always a good time and great coffee. Thank you Michael, for introducing me to the amazing sport of mountain biking and always waiting for me along the trails due to my limited riding capabilities. I am happy to be able to call so many of you friends now.

Very special thanks to Julian Szász, who is not just one of the best friends one can have but also provided me with first-class SEM imaging support and very useful technical input. Also for support with SEM measurements, I have to thank Anže Abram from *Institut Jožef Stefan*. Furthermore I need to express my thanks to Dr. Ernst Hinteregger and Franz Wroddnig from *Treibacher Industrie AG* for con-

Acknowledgements

tinuing help with SEM imaging and XRD measurements. For support with TEM imaging and print head cross sectioning I have to thank the colleagues at *USTEM, Technical University of Vienna*.

Many thanks also go out to my new colleagues in Dublin at Trinity College. Welcoming me there so warmly immediately after my arrival made change of location much easier and eventually also finishing the write-up of this thesis. Especially the crazy crew from my new office has to be mentioned, comprising Akshara, Stephen (thanks for the River Rock water...), Jane, Gaurav, Kiril, Robbie, Sonia, Diego, Chuan and last but definitely not least João and Katarzyna! In addition, for supporting me while struggling with the English language, Jane, Stephen, Robbie, Katarzyna and Cormac deserve a special shout-out.

A huge thank you goes to my parents who supported me throughout my studies not just financially, but more importantly morally and made my development and my achievements so far possible.

Finally, I will express my greatest gratitude towards my wonderful wife Julia, who makes living a joy and supports me in countless ways through all my struggles. If it wasn't for you, I might have never finished this thesis. Thank you for being with me. ♡

The \LaTeX code for this document was inspired by Manuel Kühner's thesis template www.bedienhaptik.de/latex-template/.

Funding Acknowledgment

This work was conducted within the EPPL - Enhanced Power Pilot Line project. The project EPPL is co-funded by grants from Austria, Germany, The Netherlands, France, Italy, Portugal and the ENIAC Joint Undertaking and is coordinated by Infineon Technologies Austria AG.

Abstract

Most modern bonding techniques in microsystems technologies make use of high temperatures. While this is necessary to establish strong bonding forces, it can cause significant problems. Especially when dealing with delicate microelectromechanical systems (MEMS) devices, high temperatures can destroy the functional structures. Furthermore, it is often required to bond different materials, which can lead to intrinsic tensions caused by differences in the material's coefficients of thermal expansion.

Reactive bonding using integrated reactive material systems (iRMS) has gained attention throughout the last years. As an internal heat source for bonding, these systems promise a feasible way to join heterogeneous materials without applying too much thermal stress to the whole device [1]. These concepts usually comprise multiple alternating layers of reactive materials such as Al, Ti, Ni, Co, Zr, Pd or Pt which undergo a self-propagating high temperature synthesis (SHS)-reaction [2, 3].

While the bonding results with iRMS are compelling, there are two major drawbacks hindering the usage in high volume industrial scales. First, the fabrication of hundreds of alternating layers via magnetron sputtering is very time consuming and costly. Second, the deposited iRMS layers are highly reactive but still subject to patterning process steps like lithography, etching and lift-off, which can be dangerous in regard of unintended ignition.

The scope of this thesis is to develop a novel concept for reactive bonding based on a single printed layer of a reactive nanocomposite (RNC), containing intermixed metal nanoparticles.

The joining concept proposed is based on four process steps: The nanoparticles are dispersed in a volatile organic solvent to enhance handling properties and prevent unintended ignition. After deposition of the dispersion by printing technologies onto the first substrate, the solvent evaporates, leaving a dry layer of intermixed reactive nanoparticles. A second substrate is aligned on top of the reactive layer and while applying pressure, the reactive nanocomposite layer is ignited by a laser pulse. The resulting self-sustaining exothermic reaction creates a sufficient amount of heat to establish a bond between the substrates, without significantly heating the surrounding areas at the same time.

The concept was developed and evaluated for feasibility in regard of deposition techniques, reaction parameters and materials. A series of experiments was conducted comprising dispersion, mechanical activation and ignition. Ultimately, a brief set of tests for bonding of two fused silica substrates was conducted negative outcome. All intermediate experiments were followed by extensive characterization and analysis measures using scanning electron microscopy (SEM), energy-dispersive x-ray spectroscopy (EDX), scanning white light interferometry, x-ray powder diffractometry (XRD), high resolution transmission electron microscopy (HR-TEM), differential thermal analysis (DTA), differential scanning calorimetry (DSC) and high-speed imaging. Finally, the experimental results were evaluated and an outlook is given on the steps necessary to realizing printed-RNC enabled bonding.

Results confirmed the practicability of the concept based on high reactivity of nanoparticles and suitable deposition methods. In regard of the current state of the art in bonding techniques and the outlined demand for new low temperature bonding processes this thesis makes a good case for further developing the proposed concept into an operational, market-ready technology.

Zusammenfassung

In nahezu allen modernen Füge-technologien, die in der Mikrosystemtechnik Anwendung finden, kommen hohe Temperaturen zum Einsatz. Zwar sind diese notwendig, um die erwünschten Verbindungen herzustellen, können aber zu erheblichen Problemen führen. Insbesondere im Zusammenhang mit sensiblen mikroelektromechanischen Systemen (MEMS) können hohe Temperaturen die funktionellen Strukturen beschädigen. Hinzu kommt, dass häufig das Fügen von unterschiedlichen Materialien gefordert wird. Aufgrund von Differenzen in den Wärmeausdehnungskoeffizienten der Werkstoffe können hohe Temperaturen während des Fügeprozesses zu intrinsischen Spannungen im Bauteil führen. Dies führt zu erhöhter Ausfallquote und reduzierter Lebensdauer der Produkte.

Reaktives fügen mittels integrierter Reaktivsysteme (integrated reactive material systems – iRMS) wurde in jüngerer Vergangenheit vermehrt untersucht, da es eine vielversprechende Methode liefert um heterogene Materialkombinationen ohne großen thermischen Eintrag in das System zu Verbinden [1]. Diese Konzepte setzen auf eine große Zahl abwechselnd aufgetragener Schichten von reaktiven Materialien wie zum Beispiel Al, Ti, Ni, Co, Zr, Pd oder Pt. Im Schichtstapel kann eine selbsterhaltende exotherme Reaktion ablaufen, welche äußerst lokal für einen sehr kurzen Zeitraum hohe Temperaturen erzeugt [2, 3].

Die mit iRMS-Fügen erzielten Ergebnisse sind überzeugend, es gibt allerdings zwei große Nachteile. Erstens ist die Herstellung von hunderten abwechselnden Schichten mittels Magnetron Sputtering sehr zeitaufwändig und kostspielig. Der zweite Nachteil ist die Notwendigkeit der Strukturierung der reaktiven Stapel. Dies wird mittels Lithographie- und Ätzprozessen durchgeführt, und birgt ob der hohen Re-

aktivität der Schichtstapel ein nicht zu vernachlässigendes Risiko zur ungewollten Zündung.

Ziel dieser Arbeit ist es, ein neues reaktives Fügekonzept zu entwickeln, das auf einer einzelnen gedruckten Schicht eines reaktiven Nanokomposits bestehend aus metallischen Nanopartikeln basiert.

Das Fügekonzept basiert auf vier Prozessschritten: Durch dispergieren der Nanopartikel in einem organischen Lösungsmittel wird ungewollter Zündung vorgebeugt und die Handhabung wird vereinfacht. Nach dem Dispensieren der Dispersion mittels Drucktechnologien auf den ersten Fügepartner wird das Lösungsmittel entfernt und die Schicht reaktiver Nanokomposite getrocknet. Der zweite Fügepartner wird anschließend ausgerichtet und unter Anpressdruck wird die reaktive Schicht mittels Laserpuls gezündet. Die daraus folgende selbsterhaltende exotherme Reaktion gibt genügend Wärme frei um die Bauteile zu fügen, während die umliegenden Bereiche nicht signifikant erhitzt werden.

Experimentelle Untersuchungen des Dispergierens, zur mechanischen Aktivierung der Nanokomposite und zur Zündung wurden durchgeführt. Schlussendlich wurde eine kurze Serie von Fügeversuchen mit Silica-Gläsern durchgeführt, jedoch mit negativem Ergebnis. Allen Vorversuchen wurden umfangreiche Charakterisierungen und Analysen der Materialien, Reaktionsprodukte und Reaktionsparameter mittels Elektronenmikroskopie, energiedispersiver Röntgenspektroskopie, Weißlichtinterferometrie, Röntgenstrukturanalyse, Transmissionselektronenmikroskopie, Differenz-Thermoanalyse, dynamischer Differenzkalorimetrie und Hochgeschwindigkeitsbildgebung hintenangestellt. Abschließend wurden die Ergebnisse der Experimente ausgewertet und es wird ein Ausblick gegeben, der die notwendigen Schritte zur Realisierung vom Fügen mit gedruckten, reaktiven Nanokompositen darstellt.

Die Ergebnisse haben die Praktikabilität des Konzepts auf Grund der hohen Reaktivität der Nanopartikel und Eignung zum Drucken bestätigt. In Anbetracht des aktuellen Standes der Technik in Mikrofügetechnologien und dem dargestellten Bedarf an neuen Niedrigtemperaturprozessen stellt diese Arbeit ein überzeugendes Argument für die Weiterentwicklung des Konzepts zur vollen Einsatzfähigkeit und Marktreife dar.

Contents

| | |
|---|-----------|
| Acknowledgements | v |
| Abstract | ix |
| Zusammenfassung | xi |
| 1 Introduction | 1 |
| 1.1 Thesis Outline | 6 |
| 2 MOEMS Packaging | 9 |
| 2.1 Temperature Induced Stress in MOEMS Packages | 10 |
| 2.2 Bonding Techniques for MOEMS Packaging | 12 |
| 2.2.1 Review | 24 |
| 3 Self-propagating High Temperature Synthesis and Reactive Bonding | 27 |
| 3.1 Modeling of Reactions | 30 |
| 3.2 Reactive Bonding | 33 |
| 4 Printing and Fluid Deposition Methods | 37 |
| 4.1 Inkjet Printing | 38 |
| 4.2 Aerosol-Jet Printing | 43 |
| 4.3 Screen Printing | 44 |
| 4.4 Direct writing | 45 |
| 4.5 Review | 46 |
| 5 Printed Reactive Nanocomposite Layers – Concept Development | 49 |
| 5.1 Materials and Processing | 50 |
| 5.1.1 Thermodynamic Properties | 52 |
| 5.2 Theory of Reaction | 53 |
| 5.2.1 Intermetallic Phase Formation | 54 |

Contents

| | | |
|----------|---|------------|
| 6 | Experimental Work | 57 |
| 6.1 | Materials Characterization | 58 |
| 6.1.1 | Particle Size, Size Distribution and Morphology | 59 |
| 6.1.2 | Chemical Composition and Percentage of Pure Metal | 63 |
| 6.1.3 | Nature and Thickness of Passivation Layer and Percentage of Pure Metal | 67 |
| 6.2 | Reactive Nanocomposite Fabrication | 69 |
| 6.2.1 | Inert Environment – Oxygen contamination | 70 |
| 6.2.2 | Grinding | 71 |
| 6.2.3 | Ultrasonication | 71 |
| 6.2.4 | Particle Dispersion | 72 |
| 6.2.5 | Pressing | 74 |
| 6.2.6 | Heat chuck | 76 |
| 6.3 | Reaction Experiments | 78 |
| 6.3.1 | Ignition Mechanisms | 79 |
| 6.3.2 | Reaction Front Propagation Velocity | 87 |
| 6.4 | Reaction Products Analysis | 89 |
| 6.4.1 | XRD | 89 |
| 6.4.2 | TEM | 94 |
| 7 | Discussion | 99 |
| 7.1 | Initial Experiments | 99 |
| 7.2 | Mechanically Activated Samples | 100 |
| 7.3 | Oxygen Contamination | 105 |
| 7.4 | Reactive Nanocomposite Bonding – Initial Trials | 108 |
| 8 | Summary and Outlook | 111 |
| 8.1 | Summary | 111 |
| 8.2 | Outlook | 115 |
| 8.2.1 | Closing Remarks and Recommended Actions | 118 |
| A | Reactants Size Distributions | 121 |
| B | Material Data | 125 |
| B.1 | Material Data Used for Critical Layer Thickness Calculation | 130 |
| C | Sample Database | 131 |
| D | Datasheets | 147 |
| | Bibliography | 155 |
| | List of Figures | 173 |

| | |
|--|------------|
| List of Tables | 177 |
| Abbreviations, Nomenclature and Symbols | 179 |
| Curriculum Vitae | 183 |
| Own Publications | 185 |

1 Introduction

Contents

| | |
|------------------------------|---|
| 1.1 Thesis Outline | 6 |
|------------------------------|---|

The Eniac Joint Undertaking funding consortium defined in their 2012 call among others two key enabling technologies (KET) for Europe’s microelectronic industry to maintain and strengthen its position in the global industrial market, namely *Semiconductor Process and Integration (Enabling)* and *Equipment, Materials & Manufacturing (Enabling)*. Within these KETs, a number of grand challenges were pointed out, which to tackle would be of utmost importance. Heterogeneous integration technologies fall into two grand challenges, one for each mentioned KET: *Opportunities in System in Package* and *Manufacturing* [4], respectively.

The opportunities in *system in package* are the overall footprint reduction of the micro systems by integration of a number of functionalities in one device. Novel manufacturing methods are required to realize these integrated systems. The integration of sensors, actuators and computational capabilities into a common package is called smart systems integration and one of the key requirements for future industry 4.0 applications [5]. These new components and devices are expected to have a broader field of application due to higher input/output density, higher power density, smaller feature size, better performance, better thermo-mechanical characteristics and better cost effectiveness. The trend towards higher integration density of functionalities in one device beyond increasing the number of transistors within one chip is often referred to as *More than Moore*, extending *Moore’s Law* for semiconductors [6]. These trends lead to new challenges in the development of bonding and joining techniques as the boundary conditions for the joints change. One of the tasks in work package 3, *Semiconductor Assembly and 3-D Integration*,

1 Introduction



Figure 1.1: Overview of the workpackages of the Enhanced Power Pilot Line (EPPL) project [7]. This work was executed within workpackage 3, *Semiconductor Assembly and 3-D Integration*.

of the EU funded project Enhanced Power Pilot Line (EPPL) is to cope with these challenges. Figure 1.1 shows an overview of work packages of the EPPL project, in which this work was conducted. Within work package three, the emphasis for this work was on 3-D integration. New material combinations and miniaturization of components create new challenges for the employed bonding techniques, rendering the requirement for novel joining approaches.

One aspect that has to be addressed when integrating different kinds of micro devices such as sensors and actuators into heterogeneous systems is the joining of various materials, i.e. glasses, silicon, metals. To enable such joints of different materials, it is crucial to develop new low temperature bonding methods. Low process temperatures are important for joining of materials with different coefficients of thermal expansion, as these differences lead to intrinsic stress, reducing the life time of the system, when the joining process involves the heating of both parts. A second aspect is, the fact that delicate micro structures which are to be integrated into the system often cannot withstand high temperatures.

When dealing with Micro-Electro-Mechanical Systems (MEMS), hermeticity is often an additional requirement for the package. Especially in the case of Micro-Opto-Electro-Mechanical Systems (MOEMS), hermeticity can quickly become crucial, as it increases the overall system performance by several orders of magnitude [8]. Fig-

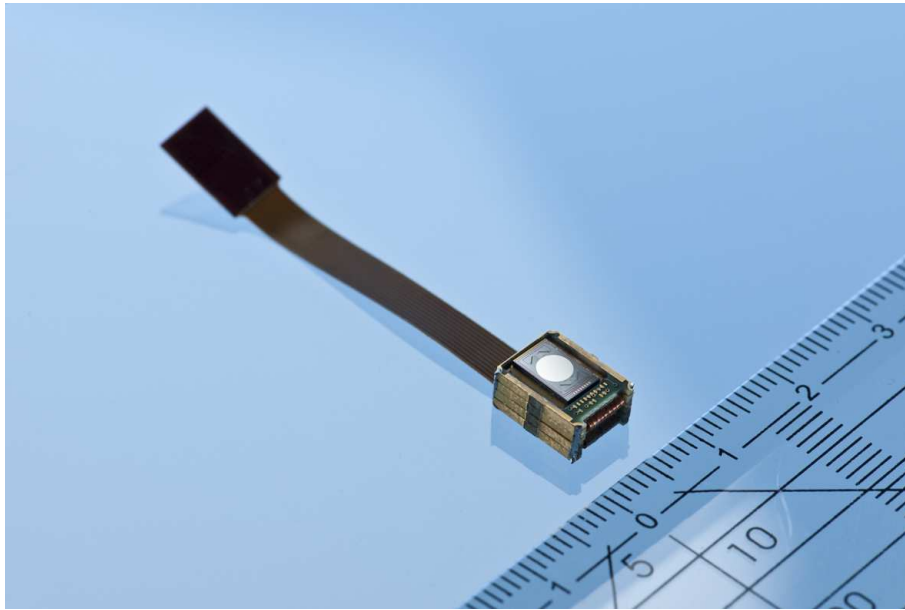


Figure 1.2: Photograph of a MOEMS micro mirror device with system-integrated optical position feedback [9].

Figure 1.2 shows a representative MOEMS device, which is an oscillating micromirror with system-integrated optical position feedback. The performance of such micromirrors is strongly influenced by any atmosphere inside the package because of damping effects, which would constrain the oscillation. As the mirror device needs an optical interface towards the outer environment a transparent material like glass is needed as one of the package materials [10]. Additionally to the mechanical aspects, in microelectronics packaging, the joints are often expected to be electrically conductive.

Using reactive materials as an integrated energy source for soldering with extremely localized heating is a very promising approach to solve this task. Derived from thermite reactive welding which has been used for well over a century by now [12], this technique has been introduced to the field of micro assembly in 2001 [13]. This approach uses a reactive foil comprising multiple alternating layers of reactive components such as Ni-Al, which is applied to the joint. The alternating layers have thicknesses in the regime of tens of nanometers to increase the reactive surface and, thus enhance the reactivity of the system. The bond is realized by initiating a Self-Propagating High Temperature Synthesis (SHS) reaction in this front. The initiation – also called ignition because of the similarity of SHS reactions

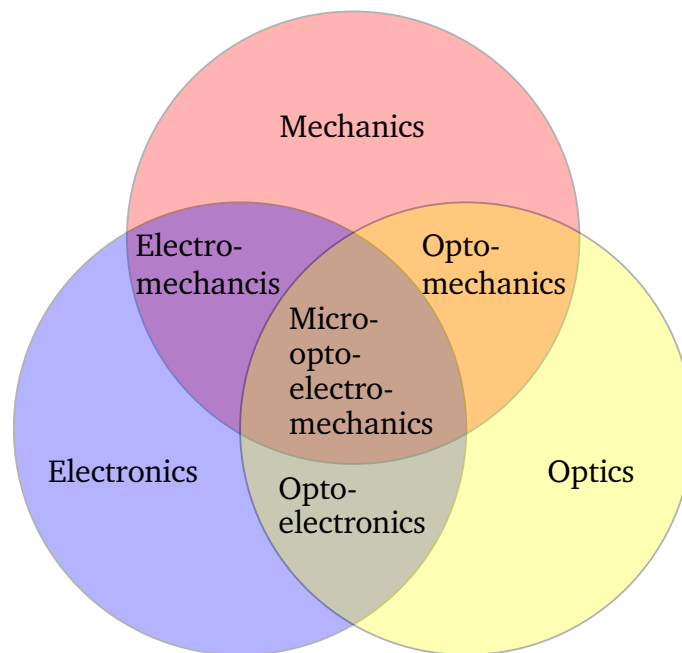


Figure 1.3: Venn diagram showing the concept of MOEMS definition description as introduced by Motamedi [11].

to combustions – can be executed by applying a short heat pulse, using e.g. laser radiation, electric current, mechanical impact or mechanical contact to a hot wire. The intermetallic NiAl phase is formed during the solid-state reaction. The reaction front propagates through the bonding layer with speeds in the range of meters per second and dissipates a high amount of energy in very short time frame. The adiabatic reaction temperature reaches more than 1600 °C. The adjacent solder is melted by the heat and immediately cools down again, as the reaction front passes quickly and no further energy is put into the system. After recrystallization of the solder the joint is established, while the surrounding areas and parts are not heated significantly.

The reactive foils described above are available on the market but have not been used extensively in the industry so far. Possible reasons for this are: First, the free-standing foil has to be cut into the required shapes, producing work time and waste. Second, high brittleness of the foil makes handling and application of cut pieces difficult. Third, undesired ignition can occur during the cutting and application steps leading to low overall yield of the system.

Improving the reactive foil concept, more recently Integrated Reactive Material Systems (iRMS) were introduced [14]. The iRMS approach makes use of the same reaction mechanism but constitutes directly deposited multiple layers of the reactants onto one of the components. Deposition of the reactive layers is done using magnetron sputtering. Bonding with iRMS was successfully demonstrated for more than twenty different material systems [15]. Despite these results, reactive bonding with directly deposited multilayers has not been used widely in industrial applications.

A major drawback of the concept is the need for patterning methods. As by sputter deposition the whole wafer or device is covered with the reactants, the reactive layers have to be patterned afterwards. This is usually done by lithographic means. Although lithographic processes are well established in the microelectronics industry, the structuring and etching of highly reactive layers is quite a challenging task and is considered a safety issue, as the unintended ignition of reactive material represents a fire hazard.

Addressing this issue, in the last three years a novel bonding concept called Reactive Nanocomposite (RNC) bonding was developed and is investigated in this thesis. The goal was to develop a bonding technology feasible for MOEMS packaging tasks with heterogeneous materials combinations. Thus, the novel concept had to rely on a low temperature process like reactive bonding. Additionally, a technique was sought after, which does not require patterning processes like lithography. To enable the deposition of a bonding layer in arbitrary patterns printing technologies were evaluated. Complying with these boundary conditions, the RNC concept was developed:

Using a dispersion of nanoparticles of the reactants, a bonding layer can be deposited in a single dispensing step and in any arbitrary pattern. Combining the advantages of reactive multilayer systems by applying homogeneously intermixed nanometer sized particles of the reactants with the versatility of free-form dispensing of fluids by printing, the novel concept promises suitability for a large number of applications.

Figure 1.4 shows a schematic drawing of the application of the RNC bonding concept with a MOEMS mirror device. The picture depicts the micro-mirror, the reactive bonding layer, the capping substrate and the ignition via laser pulse.

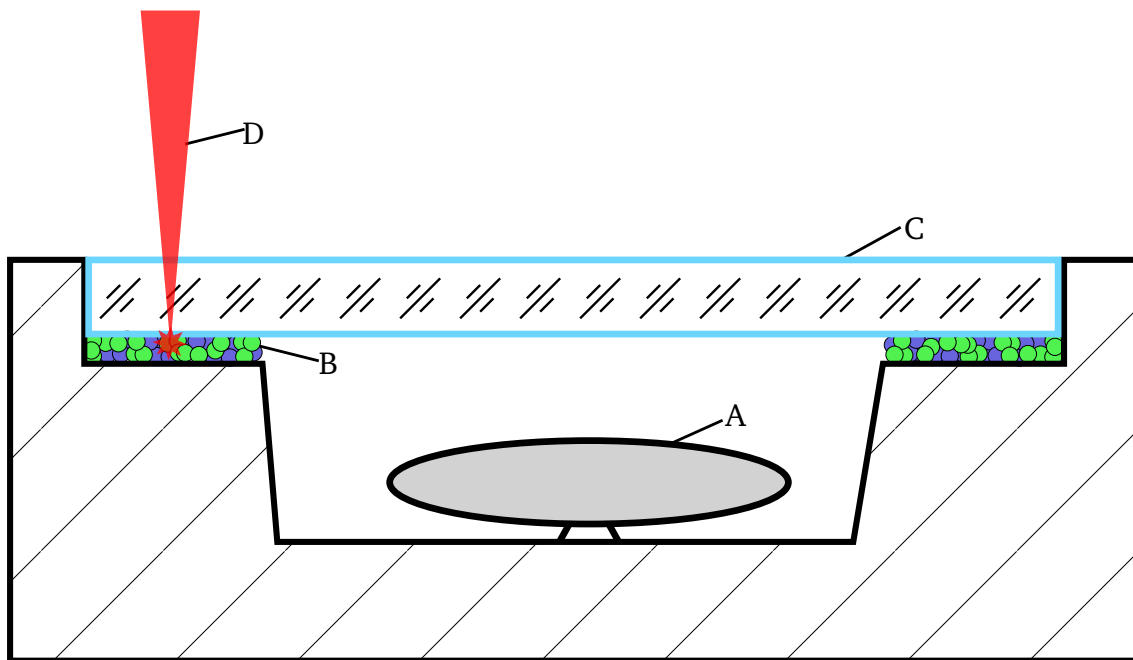


Figure 1.4: Schematic drawing of the RNC bonding concept, showing A) the MOEMS mirror, B) the reactive nanocomposite, C) the glass cap and D) laser ignition.

1.1 Thesis Outline

Following this introduction, in chapter 2, *MOEMS Packaging*, the main requirements for bonding technologies in MEMS packaging are described. Based on a Finite Element Modelling (FEM) simulation approach the occurrence of intrinsic stress in a MOEMS package due to Coefficient of Thermal Expansion (CTE) mismatch will be elucidated. Subsequently, an overview of the current state of the art in conventional bonding technologies for MEMS packaging is given. Twelve different bonding processes are introduced and compared regarding important process parameters such as temperature and compatible materials. Benefits and drawbacks of the different technologies are pointed out and it will be shown that currently no technique excels in all criteria, proving the need for novel bonding techniques for MOEMS packaging.

In chapter 3, *Self-propagating High Temperature Synthesis and Reactive Bonding*, reactive material systems for SHS reactions are introduced, accompanied by a brief overview of the historical developments of the research in this field. Modeling ap-

proaches found in established and more recent literature for SHS reactions are discussed. Finally, two bonding processes based on NanoFoils and iRMS are described in detail.

An introduction to various printing and dispensing technologies for fluid deposition shall be given in chapter 4, *Printing and Fluid Deposition Methods*. The techniques are compared regarding their process parameters, such as resolution, process complexity and speed.

Based on the findings of the preceding chapters, the development of a novel bonding concept based on printed RNC layers is described in chapter 5, *Printed Reactive Nanocomposite Layers – Concept Development*. Starting from the chosen materials systems, the concept is detailed including a description of the thermodynamic properties and phase formation during the reaction. Based on the models introduced in section 3.1, critical parameters for the proposed bonding concept are estimated.

Following the development of the concept, experiments are documented in chapter 6, *Experimental Work*. Characterization of initial materials and reaction products is presented in detail using a number of analysis tools. Experimental set-up, process steps and reaction observations are illustrated.

The findings of the experiments are summed up and discussed in chapter 7, *Discussion*. Particularly, the influence of various process steps on the reactivity of the samples and the number of unsuccessful bonding attempts using the reactive materials are explained.

Finally, a perspective for the concept is given in section 8.2, *Outlook*, defining future steps that should be investigated to eventually realize bonding with printed RNC layers.

Detailed data about the materials analysis, sample composition and data sheets can be found in the appendices Appendix A, *Reactants Size Distributions*, Appendix B, *Material Data*, Appendix C, *Sample Database* and Appendix D, *Datasheets*, respectively.

2 MOEMS Packaging

Contents

| | |
|--|----|
| 2.1 Temperature Induced Stress in MOEMS Packages | 10 |
| 2.2 Bonding Techniques for MOEMS Packaging | 12 |
| 2.2.1 Review | 24 |

With MEMS being a successor of the Integrated Circuits (IC) development, MEMS packages were initially built using electronics packaging technologies [16]. Since more than twenty years, MEMS packaging has been addressed explicitly as different from IC packaging but is still of great interest to current research [10, 17–20]. Packaging of micro-opto electromechanical systems is a challenging task, as there are several crucial yet competing requirements, namely an optical interface, hermeticity, wafer based production compatibility and production costs [5]:

Optical interface As optical devices, MOEMS require an interface to the outside world which is transparent to visible light. Such interfaces or windows can be made of several materials, out of which fused silica is the most common one. Generally, the window material is different from standard MEMS substrates like Si. This leads to a very important property of bonding technologies for MOEMS packaging: The process needs to be compatible with different materials which have a high mismatch in their CTE.

Hermeticity To enable proper function of the device, vacuum conditions (i.e. pressure inside the package not exceeding 0.1 Pa) may be required inside the

MOEMS package [10]. Especially oscillating micro mirrors like shown in Figure 1.2 show increased performance by several orders of magnitude when packaged under vacuum instead of standard atmosphere.

Wafer to Wafer Bonding (W2W) and Chip to Wafer Bonding (C2W) compatibility

W2W packaging is usually preferable over C2W in regard of cost reduction, but sometimes several components have to be integrated into one package leading to the requirement of chip scale packaging. An ideal bonding technology would be compatible with both scenarios, reducing process adaption expenses.

Costs As packaging tasks can be responsible for up to 75 % of MOEMS manufacturing costs, employing a low cost bonding process could significantly reduce overall system prices [5].

2.1 Temperature Induced Stress in MOEMS Packages

As described in the introduction of this chapter, one of the most important properties is the compatibility with materials of high CTE mismatch. In the case of inhomogeneous material combinations, which are commonly found in MOEMS packaging tasks, as introduced in chapter 1, one has to expect differences in the material's CTE. Heating of the package during a bonding process can therefore be problematic: Due to the differences, the components don't expand uniformly during the heating process, thus leading to unequal expansion in the moment of establishment of the bond. Cooling after the process results in intrinsic stress in the bonded parts at operating temperature. This stress reduces the performance and lifetime of the devices significantly [21]. Figure 2.1 shows a schematic drawing of the temperature induced stress and resulting deformation in a package comprising a bottom substrate, the bonding layer and a top substrate with different CTEs.

A FEM simulation approach was employed to verify the effect for a representative

2.1 Temperature Induced Stress in MOEMS Packages

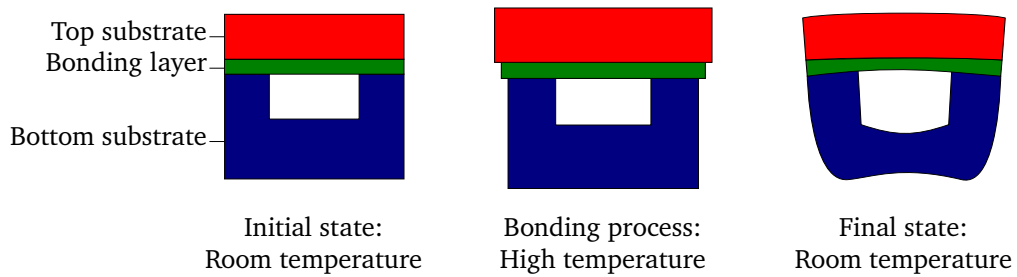


Figure 2.1: Drawing depicting the warpage of a package due to CTE mismatch and thermal loading during the bonding process. From left to right: initial state – top substrate (red), adhesive layer (green) and bottom (blue) substrate well aligned at room temperature. During the bonding process – the CTE mismatch leads to differences in thermal expansion; in this state the bond is established. After the bonding process – tensile and compressive stress lead to warpage of the package.

materials combination, Si and fused silica. Figure 2.3 shows the warpage induced by high temperature bonding of materials with CTE mismatch by the example of silicon for the bottom substrate and fused silica for the capping material, as determined in the simulation. The bottom substrate expands to a greater extent than the top substrate. The boundary conditions for this simulation were defined as follows:

- Bottom substrate: Si, $C_{Si} = 2.6 \times 10^{-6} \text{ K}^{-1}$
- Top substrate: Fused silica, $C_{Glass} = 0.55 \times 10^{-6} \text{ K}^{-1}$
- Bonding layer: Gold thin film, $C_{Au} = 0.9 \text{ K}^{-1}$
- Zero strain temperature $T_0 = 350 \text{ }^\circ\text{C}$
- Simulation temperature $T = 25 \text{ }^\circ\text{C}$

The simulation was conducted using *Solidworks 2016 SP5.0 (Dassault Systems)* and the *Thermal Structural Analysis Package (FFEPlus solver)*. A test structure with a square footprint with a side length of 10 mm and a square cavity in the top substrate of 7 mm side length was designed. The bottom substrate has a thickness of 2.5 mm and the glass cap of 0.75 mm, respectively. The cavity in the silica substrate is 1.5 mm deep. A bond frame with a thickness of 100 μm was chosen. Using a symmetric design the simulation was executed on one half of the system. Figure 2.2 shows a technical drawing of the model employed for the simulation in a cross section view. The initial conditions were set to zero strain at 350 $^\circ\text{C}$, represent-

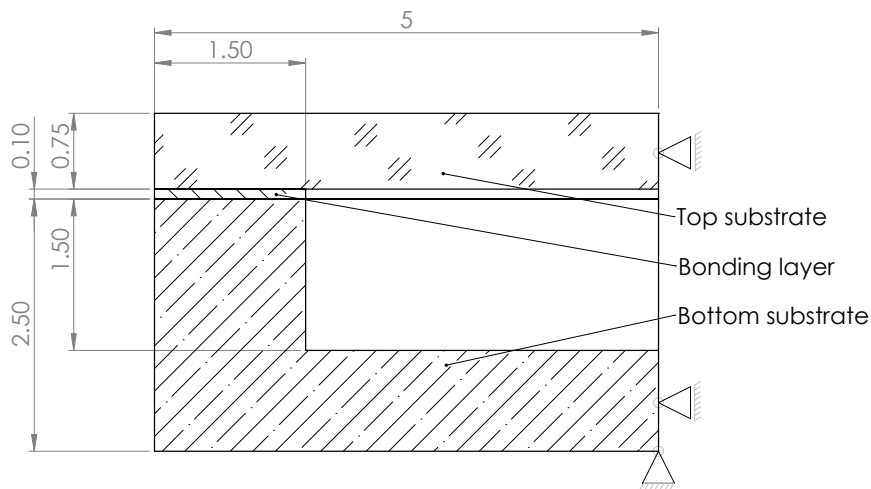


Figure 2.2: Technical drawing of the model employed in the simulation in cross section view.

ing the bonding temperature. Simulation results for stress and displacement were obtained for a subsequent temperature drop to 25 °C, equaling room temperature after the bonding process. It was found that maximum deformation of the sample at the edges would reach values as high as 3.2 μm . Van Mises tensions reached maximum values of around $8 \times 10^8 \text{ N/m}^2$ at the respective locations, exceeding tensile strength of glass ($3.3 \times 10^7 \text{ N/m}^2$) by more than an order of magnitude.

Figures 2.3 (top) and (bottom) show the simulation results for tension and displacement, respectively. Magnitude of effects is depicted by color graph and exaggerated deformation.

2.2 Bonding Techniques for MOEMS Packaging

For comparison of bonding technologies for MOEMS packaging, key process parameters to take into account are temperature, materials compatibility (in respect to common MOEMS materials like fused silica, silicon, gold, etc.), hermeticity, manufacturing complexity (as a result of required cleanroom class, surface flatness and roughness), status of industrialization, necessity of patterning, W2W or C2W com-

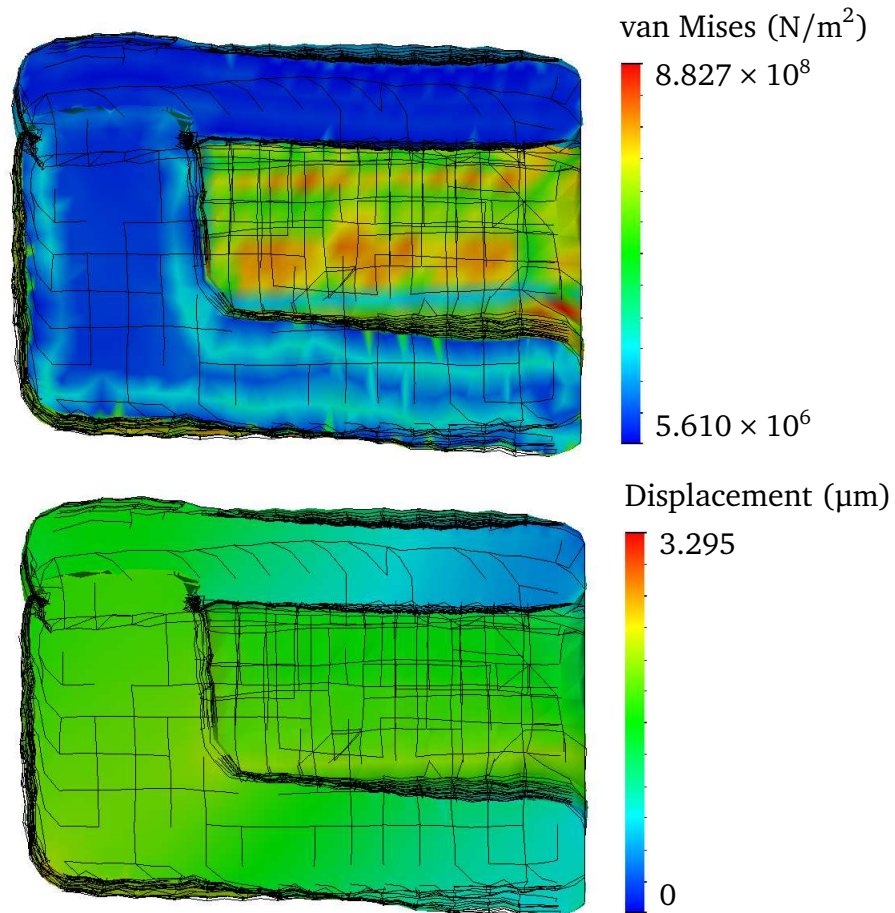


Figure 2.3: Warpage due to heating while bonding of two materials with different CTE. Final state after bonding at 350 °C and subsequent cooling to room temperature is depicted: FEM model shows tension (top) and displacement (bottom) by color graph and exaggerated deformation. Static displacement of more than 3 μ m and van Mises tension of up to 8×10^8 N/m² were found.

patibility and costs [22]. Twelve established bonding technologies are introduced in the following paragraphs and compared regarding their suitability for MOEMS packaging. Figure 2.4 shows an overview of the presented bonding technologies, divided into processes using an intermediate layer and those without.

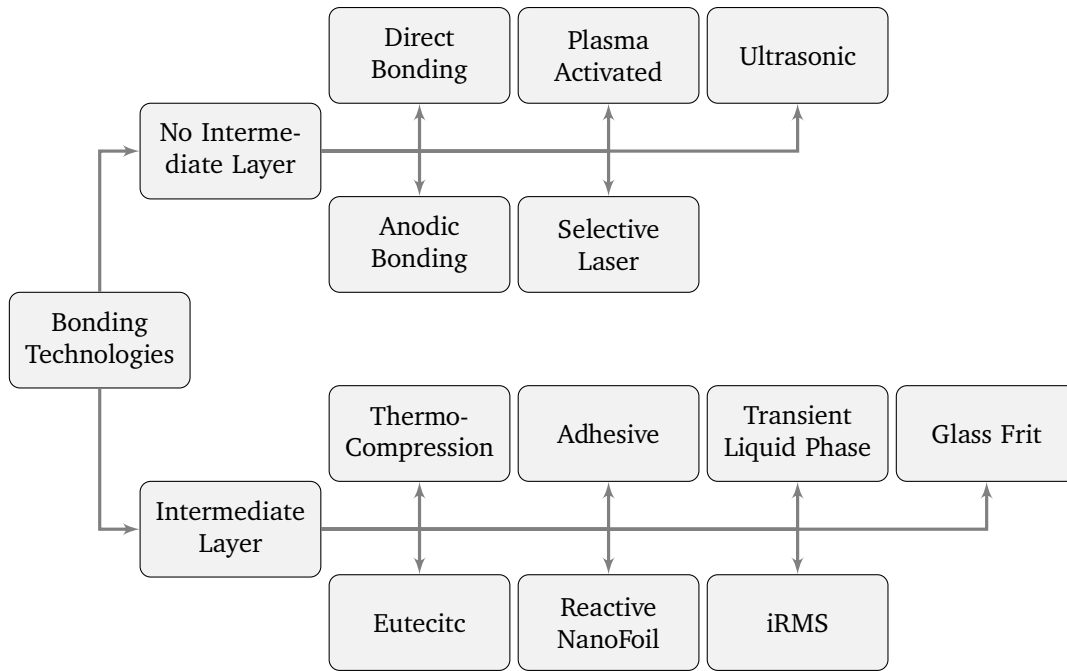


Figure 2.4: Systemization of bonding technologies, inspired by [23].

Anodic Bonding

This technology was specifically developed for the bonding of borosilicate glass to silicon and can be employed for few other materials such as low temperature cofired ceramics (LTCC) and some metals in combination with glass, too [24–26]. The substrates are aligned and exposed to elevated temperatures of 300 °C to 600 °C while applying a high voltage electrostatic field (300 V to 1500 V) [27]. The electrical field is applied in such way that the glass component is the cathode of the system and the second component the anode, respectively [28]. The high potential causes an electrostatic force that closes the gap between the two parts [17]. Na⁺-ion movement within the glass layer towards the negative potential leads to an

high concentration of O^- -ions at the bonding surface and results in the formation of a thin layer of SiO_2 at the interface [29]. Bonding strength and yield both increase with increasing voltage and temperature [30]. This method was employed in combination with glass-frit bonding as an intermediate process step by Langa et al. for an experimental packaging of micromirror devices [31]. Advantages and disadvantages are summarized in table 2.1.

Table 2.1: Anodic bonding: Advantages and disadvantages

| Advantages | Disadvantages |
|-----------------------------|-----------------------------------|
| Glass compatible | High temperatures |
| High hermeticity achievable | High surface quality requirements |
| High bond strength | |
| Vacuum compatible | |

Direct Bonding

Direct bonding is one of the classic wafer-bond techniques used in microelectronics manufacturing. It does not make use of an intermediate bonding layer between the bonding partners [32]. Cohesion of the substrates is based on Van-der-Waals forces which become dominant when two surfaces of very high cleanliness, flatness and low roughness are brought in close contact with each other [33]. The wafers have to be mirror polished and chemically cleaned before alignment and pressure application. Bonds established at room temperature have comparatively low strength, which is why heat treatment is applied to mono-material systems to increase the strength. Temperatures as high as 1100 °C are used for the thermal bond strengthening of Si/Si bonds [34]. Such high temperature annealing can hardly be applied to two material systems, due to CTE mismatch and chemical reactions which might occur at the interface and is therefore a major disadvantage (see table 2.2). Many different applications have been realized with this technique, emerging far from the semiconductor field, as it enables the joint of a large range of materials including heterogeneous materials combinations [35].

Table 2.2: Direct bonding: Advantages and disadvantages

| Advantages | Disadvantages |
|----------------------------|--|
| Hermeticity | Very high surface quality requirements |
| Bond strength | Very high surface cleanliness requirements |
| Broad variety of materials | High temperature Only W2W |

Plasma-Activated Bonding

Plasma-activated bonding is derived from direct bonding with the aim to reduce process temperatures. By plasma cleaning the wafers are prepared for bonding, enabling temperatures of about 400 °C [36]. While this is well below the 1000 °C of direct bonding it is still considered a high temperature process in the scope of this work. Due to the change in surface chemistry caused by the plasma processing a reduced quality of surface roughness is required in comparison to direct bonding [37]. The plasma treatment increases the affinity of the surfaces to each other by producing reactive ions which will catalyze the bonding process. Gases employed for plasma pretreatment are mainly Ar, O₂, N₂ and H₂, depending strongly on the materials to bond [38]. Some approaches have shown the feasibility of the technology for MOEMS packaging in respect to the wide range of compatible materials but still face the need of thermal annealing [39, 40], see table 2.3 for respective advantages and disadvantages.

Table 2.3: Plasma-activated bonding: Advantages and disadvantages

| Advantages | Disadvantages |
|-------------------|------------------------------------|
| Glass as material | High surface quality requirements |
| Hermeticity | Very high cleanliness requirements |
| Bond strength | Thermal annealing |

Ultrasonic Bonding

This process is derived from ultrasonic wire bonding and ultrasonic welding which are mature and commonly used processes in Microsystem Technologies (MST) [41]. However, ultrasonic bonding as a packaging technique is a not fully established technology which shows some promising aspects for MEMS package sealing. The cap is pressed onto the bottom substrate and while applying a normal force an ultrasonic shear movement is induced. Thus, the bonding frame gets cold welded due to high friction [42]. The process takes place at room temperature and does not involve many complicated process steps. However, the limited hermeticity achievable using ultrasonic bonding is a drawback with regard to MOEMS packaging [43], resulting in a surplus of disadvantages, see Table 2.4.

Table 2.4: Ultrasonic bonding: Advantages and disadvantages

| Advantages | Disadvantages |
|-------------------------|-----------------------------------|
| Low process temperature | Limited hermeticity |
| Glass compatible | Narrow material range |
| | High surface quality requirements |

Glass Frit Bonding

A high viscosity paste containing micron-sized glass particles (glass frit) is deposited via screen printing onto the substrates [44]. During a preheating process the binder material is removed by evaporation [45]. While applying pressure and heat, the particles are sintered, forming a uniform intermediate layer which cohesively bonds to the substrates [32].

Glass frit bonding is compatible with silicon, glass and some kinds of ceramics [46]. The bond is very high-temperature stable, but requires high temperatures during bonding itself [47]. High bond strength and good vacuum compatibility have led to wide usage of this process in many different kinds of applications [48]. Utilization for MOEMS packaging has been shown feasible for some specific applications like scanning micromirrors [49]. Accordingly, more advantages than disadvantages for MOEMS packaging can be named in table 2.5.

Table 2.5: Glass frit bonding: Advantages and disadvantages

| Advantages | Disadvantages |
|----------------------------------|--------------------------------|
| Glass compatible | High temperature |
| Broad material range | Mask process (screen printing) |
| Hermeticity | |
| Low surface quality requirements | |

Thermocompression Bonding

Thermocompression bonding is diffusion bonding at the interface of two metallic layer at high pressure and elevated temperature [50]. Both substrates are coated by a metallic layer of the same material, which can be Al, Au or Cu [51]. While applying heating (260 °C to 500 °C) the substrates are pressed to each other at high pressure (4 MPa to 9 MPa), enabling diffusion of the surface atoms into the adjacent layers [52]. Since the aforementioned metals can be deposited on a variety of substrates, joining these using thermocompression bonding is generally possible.

High bond strength and good hermeticity especially for thick bonding layers have been reported [52]. An equal amount of pros and cons is listed in table 2.6.

Table 2.6: Thermocompression bonding: Advantages and disadvantages

| Advantages | Disadvantages |
|--------------------|------------------|
| Hermeticity | High temperature |
| Wide material band | Mask process |

Eutectic Bonding

Eutectic bonding makes use of the effect that some alloys have a eutectic point which is well below the melting point of the raw metal components. These can be Au-Sn, Al-Ge or Au-Si, for example [53]. A thin film of each material is deposited onto the bonding partners. Once they are brought into contact and temperature is increased atomic diffusion takes place and an alloy is formed on the interface. When the heating process reaches the eutectic temperature which is the melting point of the alloy, the material on the interface melts. This leads to the following effects. First, the diffusion on the new interfaces between raw material and liquid alloy is accelerated, leading to an increase in fraction of the alloy. Second, the liquid phase connects well with the adjacent solid interfaces. After the heat cycle and the solidification of the alloy a solid state bond is established [54]. The eutectic points of some alloys are as low as 280 °C (AuSn, [53]), making the technology an attractive option for MEMS packaging [55], as stated in table 2.7.

Table 2.7: Eutectic bonding: Advantages and disadvantages

| Advantages | Disadvantages |
|----------------------------------|-------------------|
| Glass as material | High temperatures |
| Low surface quality requirements | Mask process |
| Hermeticity | |

Adhesive Bonding

Adhesive bonding is more a general term than a name for a specific bonding process, as many different kinds of adhesives are available. Thus, the materials range is very broad [56]. Some adhesives are thermally cured, therefore needing elevated process temperatures, while others harden at room temperature under UV light activation [57]. Deposition of the adhesive layer can be performed by spin coating or spray coating with subsequent patterning, but also by mask-less deposition techniques such as direct writing. In comparison to other bonding processes, adhesive bonding performs inferior in terms of hermeticity and bond strength, while being very tolerant to rough and uneven substrate surfaces [58], see table2.8.

Table 2.8: Adhesive bonding: Advantages and disadvantages

| Advantages | Disadvantages |
|----------------------------------|-----------------------------|
| Wide range of materials | Low hermeticity |
| Low temperatures | Low bond strength |
| Mask-less process | Low temperature resistivity |
| Low surface quality requirements | |

Reactive NanoFoil Bonding

Bonding with reactive foils is a relatively new process based on the usage of energy dissipated by an exothermic reaction to locally melt a solder layer and thus bond two parts without significant heat impact on the system [59]. Currently there is one commercially available product enabling this process called NanoFoils® by Indium Corp., USA [60]. Free-standing reactive foils with thicknesses in the range of 40 μm, 60 μm and 80 μm are used as energy source for this bonding process [61]. The foils are produced by magnetron sputtering of the reactive materials alternatively in a layer-by-layer fashion. The reactants are NiV (with 95 wt% Ni and 5 wt% V) and Al. Each layer of reactive material is around 25 nm thick, thus enabling a high active surface area in the foil [59, 62].

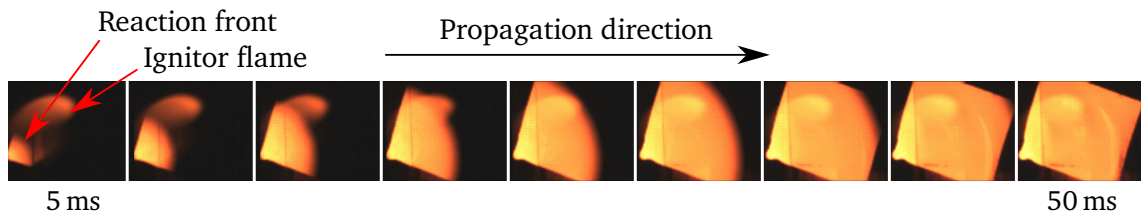


Figure 2.5: Frames grabbed from a high-speed video taken of a NanoFoil combustion. Video was taken at a framerate of 2000 fps, time between showed images is 5 ms.

The foils can be cut to shape by ultrashort laser pulsed cutting, water-jet cutting or manual cutting with a blade. By any means, ignition has to be prevented during cutting and preparation of the samples. The foils are placed in between the bonding partner and while applying a normal pressure, the reaction is ignited. A gasless self-sustaining high-temperature reaction propagates throughout the foil, dissipating enough energy to melt the adjacent solder in a short time frame of only a few ms. Due to the very localized nature of the process, materials with high discrepancies in their CTE can be bonded. A major drawback is the need for placing the freestanding foil onto the substrates either manually or with pick-and-place machines, which makes the process only suitable for Chip to Chip Bonding (C2C) bonding. Table 2.9 lists the respective up- and downsides.

Figure 2.5 shows a series of images taken from a video of a NanoFoil combustion. The video was shot with a framerate of 2000 fps, the time between showed images is 5 ms.

Table 2.9: Reactive NanoFoil bonding: Advantages and disadvantages

| Advantages | Disadvantages |
|------------------|--------------------------------|
| Low temperature | High surface flatness required |
| Fast | Narrow materials range |
| Good hermeticity | Complex to handle and pattern |

Integrated Reactive Materials Systems (iRMS)

Bonding with iRMS was introduced as a further development of the NanoFoil bonding process [1]. It makes use of the same kind of reactions based on self-sustaining high temperature synthesis via gasless combustion. Instead of using freestanding foils, this technology employs reactive layers which were directly sputtered onto one of the bonding partners [63]. This technology is superior to NanoFoil bonding in some regards, such as the enhanced adhesion to the bonding partners and the capability of using the process at wafer level [64]. However, the use of highly reactive layers at wafer level comes with some disadvantages as well. The deposition of a large number of alternating layers takes a considerable amount of time, which unlike with NanoFoil cannot be executed in parallel to other work steps [65]. After the deposition, the reactive material has to be structured to form the required bonding frames for the package. Patterning is performed by lithography and subsequent etching, which comes with enhanced risk of unintended ignition of the reactive layers [66]. Bonding with iRMS was proven to be very feasible for MEMS packaging, however, due to the time consuming manufacturing process and the risks of unintended ignition it has not yet found been employed in commercial high volume production [67], refer to table 2.10.

Table 2.10: iRMS bonding: Advantages and disadvantages

| Advantages | Disadvantages |
|---|--|
| Very broad materials range including MOEMS relevant materials | High risk of ignition during process preparation |
| High hermeticity | Patterning complexity |
| CTE mismatch compatible | Very time consuming |

Transient Liquid Phase Diffusion Bonding

This bonding process appeals because of the bond's capability to withstand much higher temperatures than the process temperature. The bonding partners are

coated with a thin metal layer of either Cu, Ag, Au or Ni on the first substrate and In or Sn on the second, respectively [68]. Deposition of the initial materials can be done by a variety of methods, e.g. magnetron sputtering or electroplating. During the process, the parts are brought into close contact and moderate heating in the range of 175 °C to 300 °C is applied. When the melting points of both bonding materials are reached, the separate phases mix due to atomic diffusion [69]. The resulting alloy has a much higher melting point than the initial components, leading to an immediate recrystallization [70]. The high melting point of the final bonding layer's material leads to high temperature stability of the bond. Due the molten state of the intermediate materials surface roughnesses can be compensated well and high hermeticity can be obtained [71]. Differences between bonding and remelt temperature can be as high as 700 °C for the Ag-In system [68]. Table 2.11 gives an overview of the respective advantages and disadvantages.

Table 2.11: Transient liquid phase diffusion bonding: Advantages and disadvantages

| Advantages | Disadvantages |
|------------------------------|----------------------|
| Hermeticity | High temperature |
| Withstands high temperatures | Narrow material band |
| | Mask process |

Selective Laser Bonding

Using a focused laser to locally heat and melt a solder layer is called selective laser bonding. A scanning laser is used to trace a focal spot with high optical power density along the bond frame of a package. The laser radiation has to pass through one of the substrates to reach the desired location, thus requiring a material which is transparent to the laser wavelength. Silicon features high transparency in the far infrared, making CO₂ lasers with a wavelength of $\lambda = 10.6 \mu\text{m}$ suitable for bonding Si-Si [72]. For systems comprising materials with transparency in the visible regime like Si-Pyrex, solid state lasers can be employed with wavelengths in the near infrared below 1000 nm [73]. The overall thermal impact on the MOEMS system is low due to selectively heating the solder layer. The respective bonding surfaces of

the substrates have to be coated with a contact layer, which usually is a sputter deposited metalization using Al or Au. However, the bond quality is dependent on the laser scribe velocity and best results were only achieved at low process speeds of only 0.5 mm/s. Since the actual bonding is a soldering process good hermeticity is achievable at such low scribe rates [74]. Pros and cons are listed in table 2.12.

Table 2.12: Selective laser bonding: Advantages and disadvantages

| Advantages | Disadvantages |
|------------------------|--|
| Very localized heating | Narrow materials range |
| Good hermeticity | One material has to be optically transparent |
| Mask-less process | Slow process |

2.2.1 Review

To estimate the demand of novel bonding technologies, the currently available ones have to be compared and evaluated regarding their suitability for MOEMS packaging. A concise comparison of all introduced bonding processes by their main properties and parameters is given in Table 2.13. Additionally to the comparison in regard of the technological feasibility, economical aspects have to be taken into account to fully review the described methods.

Deposition and patterning complexity were used as an indicator of process cost and therefore as the economical criterion. Process temperature, the main property influencing the capability of bonding different materials of high CTE mismatch, was chosen as the main criterion for assessing the technological suitability.

Achievable hermeticity was taken into account as the runner up criterion. The review of bonding techniques is visualized by plotting the various processes according to their performance in the aforementioned criteria. Figure 2.6 shows the resulting plot with the deposition and patterning complexity on the x -axis and MOEMS packaging suitability on the y -axis, respectively.

While *iRMS* bonding features the highest feasibility for MOEMS packaging, the process's economical properties are almost the worst in this overview due to the need

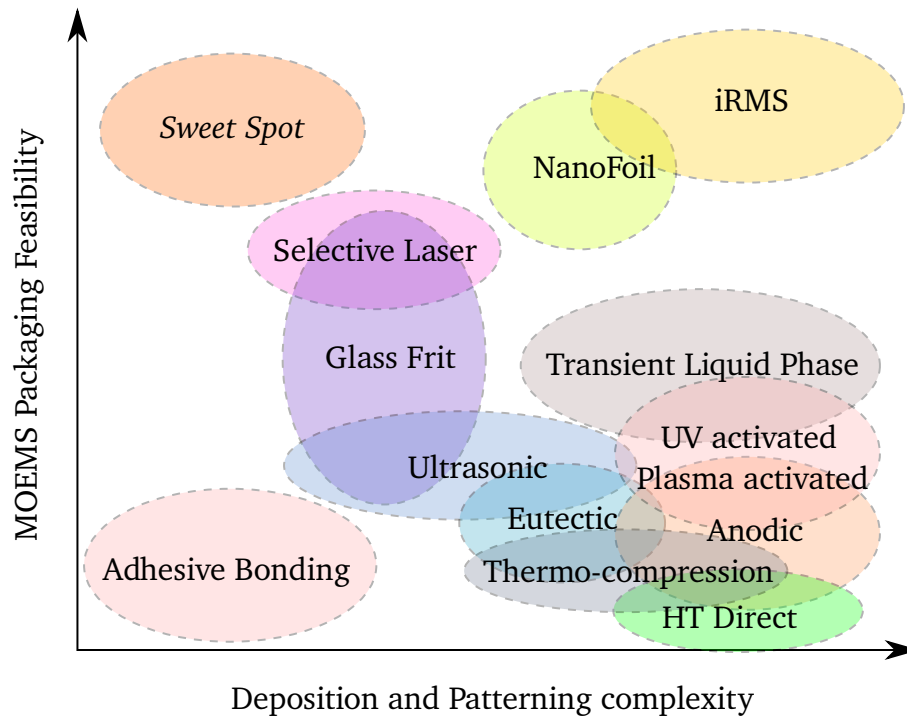


Figure 2.6: Comparative plot of different bonding techniques. MOEMS packaging feasibility is regarded in respect to low process temperatures and hermeticity.

of depositing hundreds of alternating layers of reactants. *Adhesive bonding* excels in the cost aspect, whereas it is hardly suitable for MOEMS packaging due the poor hermeticity achievable and the comparatively low bonding forces. The plot clearly shows that none of the established bonding technologies reach the *sweet spot* of low cost and high feasibility. *Selective laser bonding* is the currently available technique which comes closest towards the aspired region, but a narrow band of compatible materials and a very slow process speed impede its broad application. To satisfy the rising need for MOEMS devices and higher heterogeneous integration density, as described in chapter 1, *Introduction*, the development of new bonding technologies which come closer to this *sweet spot* is of great importance.

Table 2.13: Comparison of bonding techniques employed in microsystems technologies. Table layout adapted from [75].

| Bonding process | | Anodic | HT Direct | Plasma activated | Ultrasonic | Glass frit | Thermo-compression | Eutectic | Adhesive | Reactive NanoFoil | iRMS | Transient Liquid Phase | Selective Laser |
|-------------------------------|------------|-------------|-----------|------------------|------------|-------------|--------------------|----------|----------|-------------------|------------|------------------------|-----------------|
| Broad Material Range | | ● | ● | ● | ○ | ◐ | ● | ● | ● | ● | ● | ● | ● |
| Typical Temperature | 1000 °C | ○ | ● | ● | ○ | ○ | ○ | ● | ○ | ○ | ○ | ◐ | ○ |
| | 400 °C | ● | ○ | ● | ○ | ○ | ● | ● | ● | ○ | ○ | ◐ | ○ |
| | 200 °C | ○ | ○ | ● | ○ | ● | ◐ | ● | ● | ○ | ○ | ○ | ○ |
| | 25 °C | ○ | ○ | ◐ | ● | ○ | ○ | ○ | ● | ● | ● | ○ | ● |
| Vacuum compatibility | <1 mbar | ● | ● | ● | ◐ | ● | ● | ● | ◐ | ● | ● | ● | ● |
| | <0.01 mbar | ● | ● | ◐ | ○ | ○ | ● | ● | ○ | ◐ | ◐ | ● | ● |
| Maximum Surface roughness | <1 μm | ○ | ○ | ○ | ● | ○ | ○ | ● | ● | ● | ● | ● | ○ |
| | <20 nm | ○ | ○ | ○ | ● | ● | ○ | ● | ● | ● | ● | ● | ● |
| | <2 nm | ● | ○ | ● | ● | ● | ● | ● | ● | ● | ● | ● | ● |
| | <0.1 nm | ● | ● | ● | ● | ● | ● | ● | ● | ● | ● | ● | ● |
| Surface Flatness | low | ○ | ○ | ○ | ○ | ● | ● | ● | ● | ○ | ○ | ● | ○ |
| | high | ● | ● | ● | ● | ○ | ○ | ○ | ○ | ● | ● | ○ | ● |
| Cleanroom Class | | 100 | 10 | 10 | none | 1000 | 10 | 100 | 100 | none | none | 1000 | 1000 |
| High Sensitivity to particles | | ◐ | ● | ● | ○ | ○ | ◐ | ◐ | ◐ | ○ | ○ | ● | ● |
| High Volume Industrialization | | ● | ● | ○ | ○ | ● | ● | ● | ● | ○ | ○ | ○ | ○ |
| Direct patterning | | ○ | ○ | ○ | ◐ | ● | ○ | ○ | ● | ○ | ○ | ○ | ● |
| High Costs | | ◐ | ● | ● | ○ | ○ | ● | ◐ | ○ | ○ | ◐ | ● | ◐ |
| References | | [17, 25–31] | [32–34] | [36–40] | [41–43] | [32, 44–49] | [50–52] | [53–55] | [56–58] | [59–62] | [1, 63–67] | [68–71] | [72–74] |

● = yes / applies / feasible, ◐ = partly true / applicable, ○ = no / does not apply / unfeasible

3 Self-propagating High Temperature Synthesis and Reactive Bonding

Contents

| | |
|-------------------------------------|----|
| 3.1 Modeling of Reactions | 30 |
| 3.2 Reactive Bonding | 33 |

Exothermic reactions have been used as a source of energy for welding and soldering applications for well over one hundred years, invented by Goldschmidt and Vautin in 1898 [12]. This method, firstly described as thermite welding, was mainly used in railroad building in the early 19th century [76]. The concept uses a self-sustaining exothermic chemical redox reaction at the joint. The reaction product is elemental iron and due to the high reaction temperatures the iron melts and fills in the joining gap in molten form. Iron(III)-Oxide and elemental aluminium powders are used as reactants. The powders are mixed in a crucible and ignited using a magnesium torch. During the redox-reaction ($\text{Fe}_2\text{O}_3 + 2\text{Al} \rightarrow 2\text{Fe} + \text{Al}_2\text{O}_3$) temperatures may reach up to 2270 K, resulting in molten reaction products [77]. Due to lower density of aluminium oxide, the molten products are separated by gravitation and the desired iron flows through the drainage into the joining gap. Figure 3.1 shows a schematic drawing of the welding process using the thermite reaction: the crucible is filled with the reactive powder mixture, comprising Fe_2O_3 and Al, and placed above the joint gap. After ignition with a Mg torch, the self-propagating exothermic reaction produces elemental Fe and Al_2O_3 , which are present in molten phase due to high reaction temperature. Gravitational phase separation takes place and the molten Fe is extracted from the crucible through a

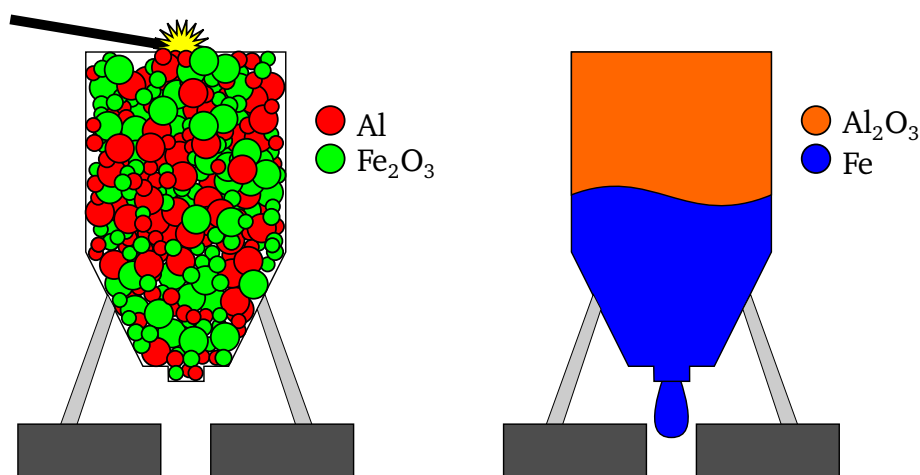


Figure 3.1: Schematic drawing of the concept of thermite railroad welding. The crucible is placed above the weld gap filled with mixed powders of Fe₂O₃ and Al. The mixture is ignited with a magnesium torch, resulting in a self-propagating exothermic reaction. During the reaction, the reactants as well as the reaction products (Fe, Al₂O₃) melt. Gravity induced phase separation of the products enables easy removal of the elemental iron through the drainage and filling of the weld gap.

drainage, filling the joint gap.

In 1967, Merzhanov and colleagues described the phenomenon of Solid Flame (SF) in metal powders for the first time [78]. Most SF reactions are combustion reactions just like the thermite reaction, but with the significant difference, that the reactants and the reaction products remain in the solid phase throughout the reaction. It was noticed, that with some material combinations, although the reaction mechanism was comparable, the reaction temperatures were higher than the materials' melting temperatures, hence leading to molten products. Investigating the reaction products, it was found that novel alloys and intermetallic phases could be obtained using these reactions, leading to the new term Self-Propagating High Temperature Synthesis (SHS). The formation of an intermetallic phase does not necessarily comprise establishment of chemical bonds [79]. Thus, the term *reaction* might not be considered accurate from a chemist's point of view. To facilitate reading of the manuscript and in agreement with the cited literature, the term *reaction* shall be used in this work.

A lot of attention was drawn towards the synthesis of exotic alloys by these reactions, as the method does not rely on high energy input [80–82]. Soon SHS reactions became the topic of interest in many research projects, resulting in a number of investigations on different materials, i.e. various carbides, aluminides, silicides and borides [77, 82–84], thermodynamic modeling [3, 85–95], ignition techniques [96, 97], particle size effects [98] and applications [82, 99–108].

Table 3.1 shows an overview of selected material combinations which can undergo SHS reactions and respective thermodynamic properties: stoichiometry, enthalpy of formation ΔH_f , adiabatic reaction temperature T_{Ad} and the state of the reaction products at the reaction temperature.

A more comprehensive list of materials combinations which can undergo said reactions is presented in the Appendix in Table B.1.

Table 3.1: Thermodynamic properties of selected Aluminide-SHS reactions [109]. A comprehensive list of Boride-, Carbide-, Silicide- and Aluminide-SHS reactions is shown in Appendix B. The two highlighted reactions were subject to further investigation in this work.

| Reaction mechanism | ΔH_f (kJ/mol) | T_{Ad} (K) | State of reaction products at temperature |
|--------------------|-----------------------|--------------|---|
| Pt+Al → PtAl | -100 | 3072 | Liquid |
| Pd+Al → PdAl | -92 | 2652 | Liquid |
| Co+Al → CoAl | -60 | 1911 | Solid and liquid |
| Ni+Al → NiAl | -59 | 1911 | Solid and liquid |
| Zr+Al → ZrAl | -45 | 1752 | Solid and liquid |
| Ti+Al → TiAl | -36 | 1499 | Solid |

3.1 Modeling of Reactions

As mentioned above, a large number of mathematical models of SHS reactions has been developed. Following the calculations by Rybanin and Sobolev [110, 111]¹, one can estimate the heat transfer within the reactive layer as well as into the adjacent inert layers. To maintain a self-propagating reaction, the reactive material has to be continuously re-ignited at the interface of the reaction zone and the unreacted material. Therefore, the heat on said interface of must not fall below a certain threshold to keep the reaction *alive*. The requirements to maintain this threshold can be expressed as a combination of several boundary conditions. These depend to a great extent on material properties such as thermal conductivity, heat capacity and density. For a given combination of reactive media and substrates these physical properties are assumed constant. Directly derived from the chosen material system are furthermore key parameters of the reaction, namely activation energy, adiabatic reaction temperature and combustion rate. These parameters are also considered invariant for our examination, leaving only geometric properties as variables.

For simplification the model is regarded as a two dimensional system, equaling a cross-section through the stack of substrates and reactive layer. The reaction propagates along one dimension in this model, while heat transfer occurs in both dimensions. Rybanin and Sobolev further simplify by distinguishing thermally thick and thermally thin layers. The differences are defined as follows:

- Thermally thin: Temperature is constant along the Y -axis at the propagation front, hence

$$\left(\frac{\partial T}{\partial Y}\right)\Big|_{0 \leq Y \leq 2H} = 0 \quad (3.1)$$

- Thermally thick: Temperature not constant along the Y -axis at the propagation front, hence

$$\left(\frac{\partial T}{\partial Y}\right)\Big|_{0 \leq Y \leq 2H} \neq 0 \quad (3.2)$$

¹Unfortunately, the translated papers by Rybanin and Sobolev as cited above ([110, 111]) contain some typographic errors in the formulas, which presumably occurred during the translation. The calculations in this work are based on the formulas from the original papers [112, 113].

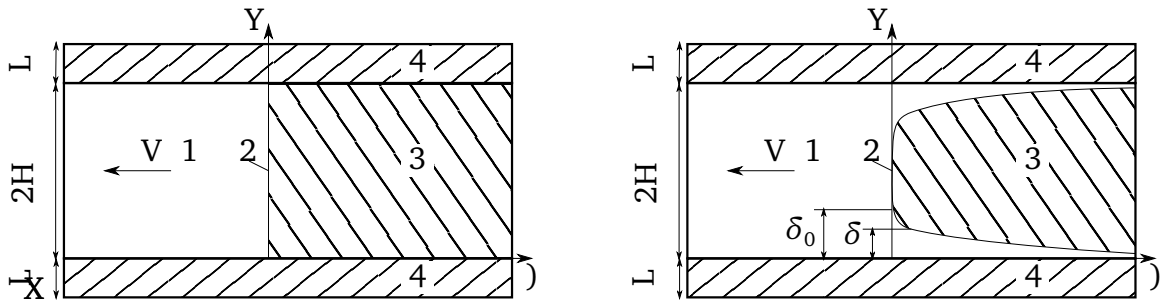


Figure 3.2: Axis description for modeling of the reaction front: thermally thin model with constant reaction front along Y -axis (left) and thermally thick model with inhomogeneous temperature along the reaction front (right). The reaction front propagates in V direction along the X axis. The numbered parts are valid for both systems: 1) unreacted reactive material, 2) reaction front, 3) reacted material and 4) inert surrounding material. Adapted from [112, 113].

In both cases the thermophysical properties of the reaction products and educts are assumed to be constant and homogeneous throughout their respective phases. Finally, in the former case, only two non-constant parameters are left: the amount of reactive material and the ambient temperature. In the two dimensional the model quantity of educts is equivalent to the thickness of the reactive layer.

Figure 3.2 shows the definition of the coordinate systems for the model. It is postulated, that the main requirement which has to be fulfilled to sustain a self-propagating reaction is:

$$C_x - C_y - C_z > C_{ig} \quad (3.3)$$

With C_x the heat of reaction, C_y the amount of energy dissipated by thermal conduction into the surrounding inert material, C_z the amount of energy dissipated into the reaction products and C_{ig} the ignition energy threshold. Additionally the following boundary conditions are presumed:

$$\lambda_x, \rho_x, c_x = const. \quad (3.4)$$

$$T_c, E, a_f, U, \gamma_{cr} = const. \quad (3.5)$$

With material constants (Equation 3.4) thermal conductivity λ , density ρ and heat capacity c with index x being either f for the reactive material or i of inert material, respectively. From the material constants derived invariable reaction parameters

3 Self-propagating High Temperature Synthesis and Reactive Bonding

(Equation 3.5): combustion temperature without heat loss T_c , initial temperature T_0 , activation energy E , effective temperature conductivity $a_f = \frac{\lambda}{\rho c}$, combustion rate without heat losses U and γ_{cr} , a dimensionless parameter characterizing the quantity of heat losses from the reaction zone in the inert material. For the thermally thick model, an additional parameter $\delta(x)$ is introduced, describing the thickness of the unreacted material adjacent to already reacted material. Its maximum value δ_0 is reached at $X = 0$, where the temperature is constant within $\delta_0 < Y < 2H - \delta_0$. All parameters and constants are depending on the actual material system employed.

Based on this assumption and a given heat threshold that has to be reached at the reaction front one can calculate a critical layer thickness Δ_{cr} for a homogeneous reactive material at a given ambient temperature, below which that threshold would not be reached. A self-propagating reaction will therefore not be sustainable with a thinner layer and will extinguish. With the universal gas constant R , the critical layer thickness Δ_{cr} calculates as [110]:

$$\Delta_{cr} = \frac{(T_c - T_0)Ea_f}{RT_c^2 U \gamma_{cr}} \sqrt{\frac{\lambda_i \rho_i c_i}{\lambda_f \rho_f c_f}} \quad (3.6)$$

More recent modeling approaches have used numerical molecular dynamics simulations describing the materials interactions on an atomic level, employing an embedded atom method [89]. Henz *et al.* describe the process of formation of intermetallic NiAl based on nanoparticles with diameters below 10 nm.

The main reaction driving force is diffusion dominated. Figure 3.3 shows a graphical representation of their simulation result of the fusion of Ni and Al particles. In this study the reaction of two single particles forming one intermetallic particle was investigated for three different sizes (3000 Atoms to 36 000 Atoms). The largest number is equivalent to an Al particle with 10 nm diameter. Simulating the fusion process of to such particles for a few ns took more than 48 h using 64 CPUs. Consequently, the simulation was not expanded to the reaction through a mixture of a large number of particles.

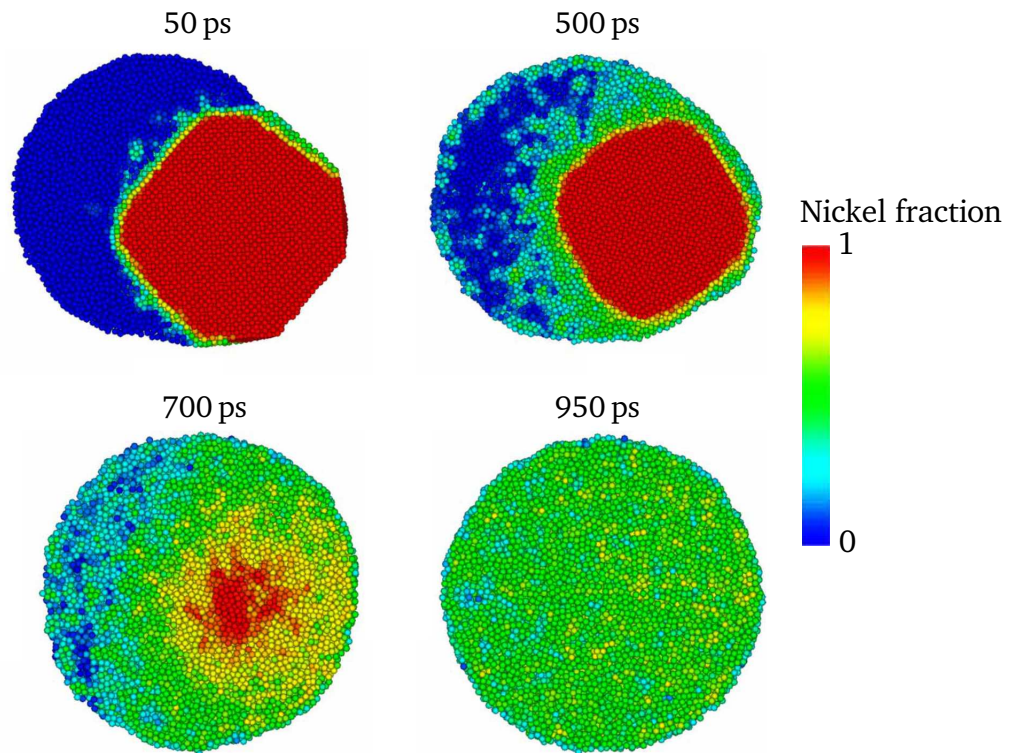


Figure 3.3: Molecular dynamics simulation of Ni and Al nanoparticle fusion. Color graph shows Ni fraction, while Al fraction equals $1 - \text{Ni}$. Process propagation is depicted in four phases as described by Henz *et al.* [89]

3.2 Reactive Bonding

Being a successor of the initial thermite process, reactive welding drew a lot of attention [102, 108, 114–121]. Despite the long history, only in the past fifteen years, research groups started to adapt comparable processes for joining challenges in MEMS packaging, using the term of *reactive bonding*, in compliance with established bonding technologies (see section 2.2) [1, 13, 14, 59, 63, 64, 122]. While the new processes completely differ from Goldschmidt’s thermite welding in means of employed materials, the concept of using the energy emitted by a self-sustaining reaction for bonding is comparable.

The concepts mostly rely on the following process structure: A reactive material is applied to the gap in between the two surfaces which are to be joined. The bonding surfaces are coated with a solder layer, while applying pressure, the intermediate layer is ignited by a short pulse of energy and the following exothermic reaction

3 Self-propagating High Temperature Synthesis and Reactive Bonding

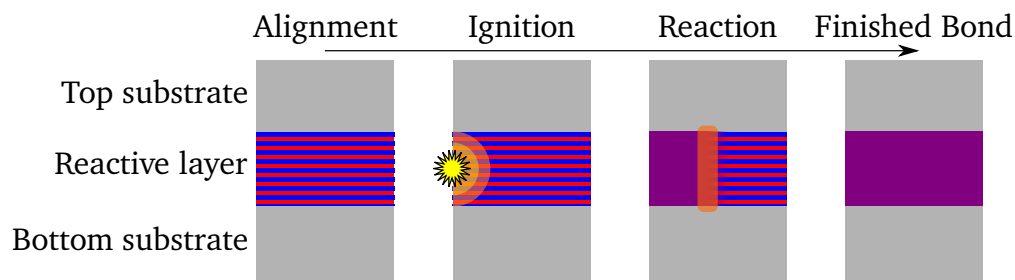


Figure 3.4: Schematic drawing of the iRMS bonding concept. The reactive multilayer system is directly deposited onto the bottom substrate. After patterning by lithographic means, the top substrate is aligned and while applying pressure, the reaction is initiated. Adapted from [59].

leads to melting of the solder. Ignition can be done by various means, i.e. electric current, heat contact, laser pulse or mechanical impact. A comparison of ignition mechanisms is given in subsection 6.3.1. The solder solidifies immediately after the reaction front has passed and forms a bond at the adjacent surfaces of the bonding partner and the reaction products. As process takes place in only a few milliseconds and the emitted energy is mostly used for melting the solder, the surrounding material's temperature does not significantly rise.

Micron-sized powders which have been mainly used for SHS reactions in previously mentioned works suffer in this context from the problem of relatively large distance between the particles interfaces. The path of diffusion for the reactant's atoms is several orders of magnitude smaller. Nano sized particles or multilayers overcome this problem, since the distances between particle interfaces are in the same range as the diffusion path' lengths.

Common among the new processes is the usage of reactive multilayer systems. These comprise layers with a thickness in the nanometer regime and are alternately stacked up to a total thickness of some tens of micrometers [109].

Bonding with reactive multilayers was realized with free standing reactive foils and with directly deposited multilayers as well (iRMS). Reactive foils for bonding are commercially available with the brand name NanoFoil[®] by Indium Corp. The reactive layers are manufactured by alternating magnetron sputtering of the reactants. Figure 3.4 shows a schematic drawing of the multilayer enabled reactive bonding process. The reactive layers are directly sputtered onto the bottom substrate. After

lithographic patterning, comprising resist coating, exposure, lift-off, the top substrate is aligned and pressed on to the bonding layer. While applying pressure the reaction is initiated. After the reaction front has propagated throughout the bonding layer, the desired bond is established. Bonding with iRMS was developed as a wafer-level process, while bonding with NanoFoil is mainly feasible for chip-scale integration. The reactive foils are patterned by laser cutting and applied to the joint with pick-and-place machines.

Main advantages of multilayer systems are the large reactive surface area leading to very high reaction front propagation velocities in the regime of tens of meters per second, low ignition energy thresholds and low porosity of the reaction products. The inherent disadvantage of multilayer systems is the time consuming, complex and expensive manufacturing of hundreds of alternating layers and the need for patterning technologies like lithography or laser cutting [14, 65].

4 Printing and Fluid Deposition Methods

Contents

| | |
|------------------------------------|----|
| 4.1 Inkjet Printing | 38 |
| 4.2 Aerosol-Jet Printing | 43 |
| 4.3 Screen Printing | 44 |
| 4.4 Direct writing | 45 |
| 4.5 Review | 46 |

Many different fundamentally varying fluid deposition methods are available, which can generally be divided into two categories: one – depositing in a patterned manner, i.e. applying the fluid only to certain areas of the substrate, and second – to fully cover the substrate with the fluid. In the scope of this work we will focus on the first category, as methods belonging to the latter one like spray-, dip- or spin-coating intrinsically require patterning techniques to be applied afterwards. As for the patterned category, a further differentiation can be made between contact- and non-contact printing technologies. Common contact printing technologies are roll to roll-printing, screen printing and direct writing. Inkjet- and aerosoljet printing are the predominant non-contact printing technologies. Figure 4.1 shows a systematic differentiation between the different fluid deposition methods introduced in this chapter. Each method was evaluated for the feasibility of application for the proposed bonding technique in aspects of material compatibility, resolution and production scale properties.

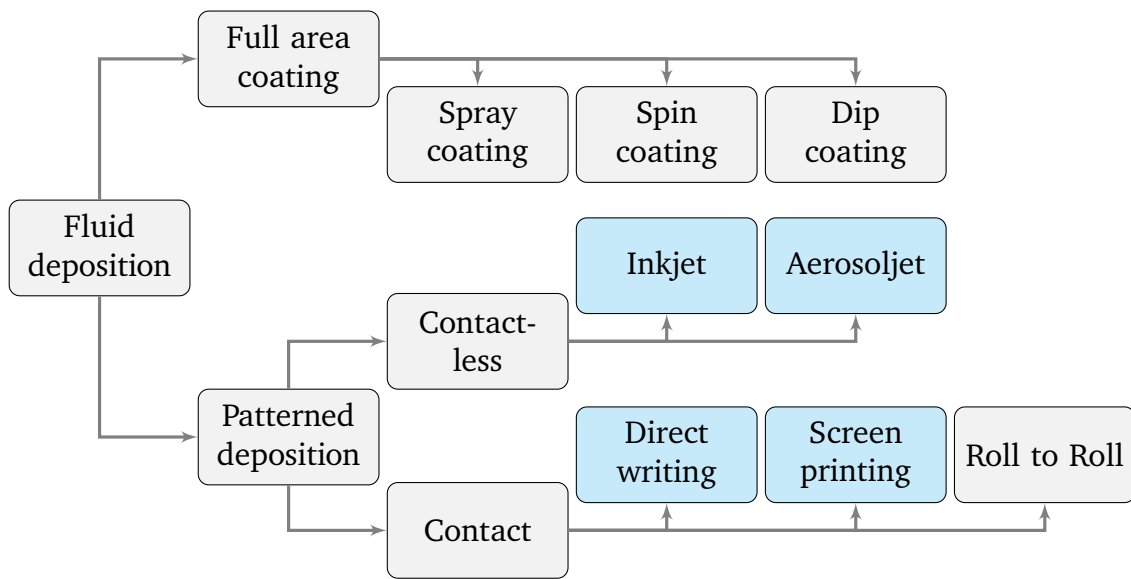


Figure 4.1: Systemization of some relevant fluid deposition technologies. Emphasized printing technologies are discussed in more detail in this work.

4.1 Inkjet Printing

Inkjet Printing (IJP) belongs to the contact-less printing methods, in which droplets of the ink are jetted towards the substrate. Since its invention in 1980 the technique has been mainly used for text and graphical printing. However, during the past ten years, IJP has become more and more of a manufacturing method, being able to precisely deposit a broad range of materials in arbitrary patterns onto almost any substrate [123]. The volumes of the droplets usually range from 5 pL to 200 pL resulting in printing resolutions of up to 1200 DPI, which is equivalent to feature sizes as small as 20 μm . Resolutions of up to 10 μm were reached in experimental setups [124]. The droplets are fired with high frequencies, enabling fast production [123].

Printheads containing up to several hundred nozzles are classified as either Continuous Inkjet (CIJ) or Drop on Demand Inkjet (DOD) printheads. CIJ heads continuously jet droplets towards the substrate. The droplets are electrostatically loaded and can be directed in to a waste reservoir when necessary. DOD printheads are passive in the idle state and only jet droplets when requested. The printhead contains a small ink reservoir behind each nozzle which can be exposed to a sharp

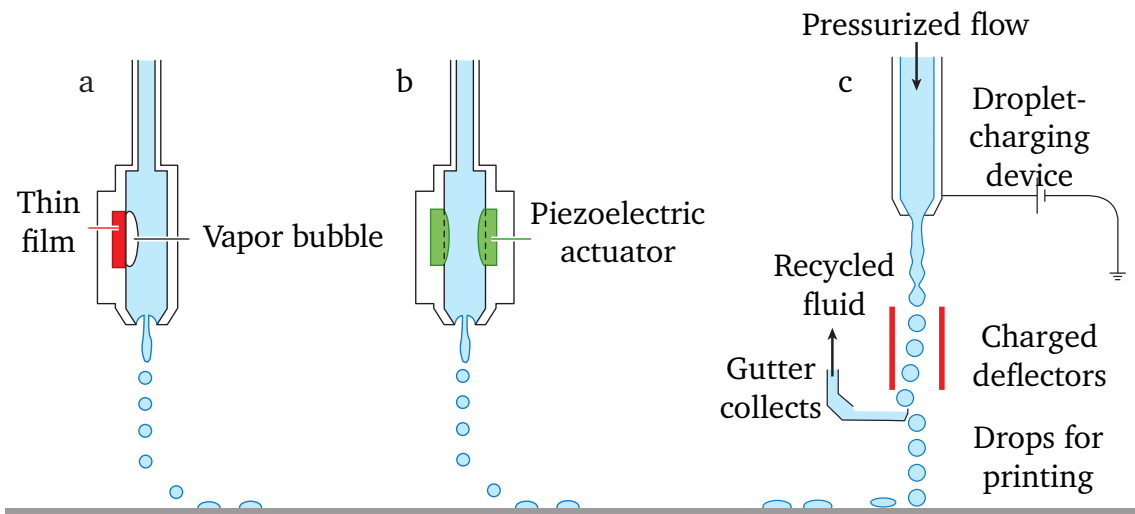


Figure 4.2: Working principles of *a* thermal and *b* piezo DOD and *c* CIJ printheads. Adapted from [125].

pressure increase, leading to the ejection of a droplet. Two subcategories of DOD printheads are distinguished: thermal and piezoelectric printheads. The pressure pulse is generated by ohmic heating of a sidewall of the ink cavity in thermal printheads. The heating leads to rapid evaporation of a small amount of ink, thus generates a bubble. The volume expansion of the ink during bubble generation forces the ejection of a droplet from the nozzle. Piezoelectric printheads make as the name indicates usage of a piezoelectric actuator. By running a pulsed current, expansion and contraction of the actuator are driven, enabling controlled ejection of droplets from the nozzle. Figure 4.2 shows a schematic comparison of DOD and CIJ printheads.

As thermal printheads are cheaper than piezoelectric, they are most commonly found in consumer inkjet devices. In industrial and research environments, where jetting of functional inks is required, piezoelectric printheads are preferred, as the heating of functional inks above the boiling point cannot always be tolerated. Though piezoelectric printheads are not as restrictive regarding the ink's properties as thermal printheads, the rheological characteristics have to meet very specific criteria. These requirements are a result of high shear stress which is imposed on the ink during droplet ejection and the desired jetting behavior, meaning production of uniform droplets without spraying or the development of satellites. Important

empirical numbers which are used for characterizing the rheological properties are Reynolds number Re , Weber number We and Ohnesorge number Oh which are defined as follows:

$$Re = \frac{\rho v d}{\mu} \quad (4.1)$$

$$We = \frac{\rho v^2 d}{\sigma} \quad (4.2)$$

$$Oh = \frac{\sqrt{We}}{Re} = \frac{\mu}{\sqrt{\rho \sigma d}} \quad (4.3)$$

With the ink's properties ρ , μ , σ and v , namely density, dynamic viscosity, surface tension and velocity respectively and the nozzle diameter d [126–128]. Using Re and We one can describe the dynamic jetting properties of an ink according to the listed process parameters. Empirical studies have led a process window as shown in Figure 4.3 framed by ranges of Re and We [125].

Oh , however, is an indicator for the relationship of rheological properties of the ink and the nozzle geometry and is independent from the ink's velocity. It is therefore widely applicable to determine the jettability of an ink for a certain nozzle. For good jetting behavior Oh should be in the range 0.1 to 1 – at higher values the ink does not break free from the nozzle due to high damping forces inside the liquid, while at lower values severe satellite formation and spraying occurs easily [129]. For good printability, viscosity should range from 1 mPas to 25 mPas and surface tension from 25 mN/m to 50 mN/m [130]. Additionally, the valid regions for these parameters are strongly influenced by the hardware used. Respective values of isopropyl alcohol, a solvent which is commonly used in experimental inks, are $\rho = 0.786 \text{ g/cm}^3$, $\mu = 1.96 \text{ mPas}$ and $\sigma = 21.7 \text{ mN/m}$ at room temperature [131, 132]. The materials of the printhead have direct impact on the wetting behavior at the nozzle. Finally, the driving parameters for the printhead like temperature, piezo pulse shape and jetting frequency are crucial to printing performance.

Taking dimensions and materials parameters of the printhead into account as well as rheological properties of the ink enables Continuous Fluid Dynamics (CFD) modeling of the jetting behavior. The printhead nozzle geometry was measured from

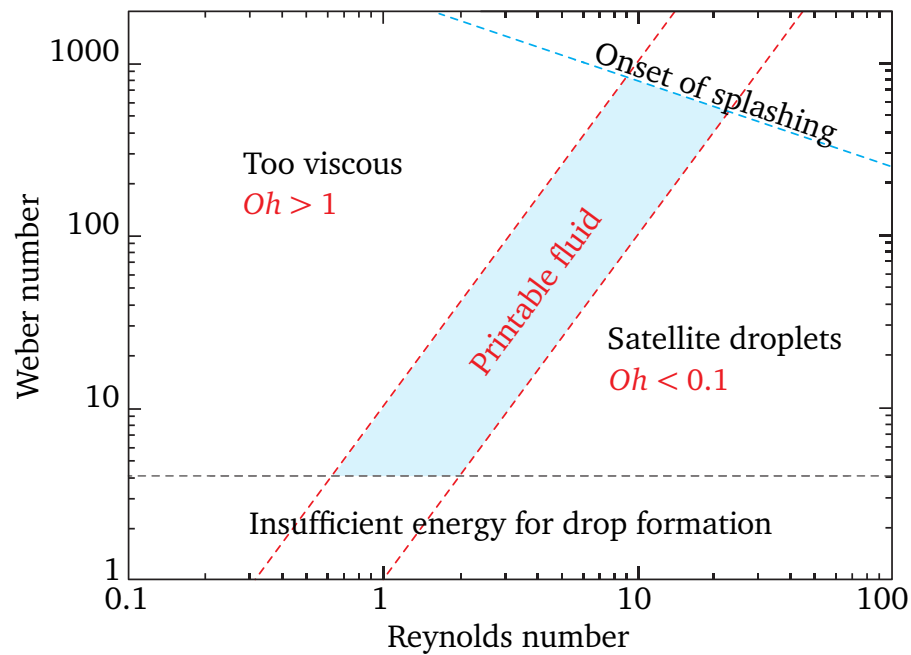


Figure 4.3: Weber number plotted over Re , depicting the printable regime [125].

a cross sectional micrograph of a clogged nozzle. The obtained information was used as boundary conditions for a CFD simulation with the standard ink's rheological properties. Figure 4.4 shows the polished cross sectional view of the printhead nozzle. The nozzle diameter was found to be around $56\ \mu\text{m}$. Diameter and funnel angle were used as geometric boundaries and open ambient pressure at the nozzle orifice and negative backpressure against gravitation as fluid dynamic boundaries. To simulate droplet formation due to a piezo pulse a short pressure increase on the backside of the reservoir was implied.

Figure 4.5 shows the result of a representative CFD simulation as a timed sequence of frames after the jetting pulse. The droplet ejected from the nozzle is formed within $50\ \mu\text{s}$. Additional to the main droplet two satellite drops are formed which quickly fuse to one droplet. However, the resulting satellite does not merge with the main droplet as it travels at a lower velocity. The main droplet has an approximate volume of $360\ \text{pL}$, whereas the satellite droplet has about $120\ \text{pL}$. Such jetting behavior is considered not optimal, since two drops moving at different speed towards the substrate ejected from a moving printhead will not hit the substrate at the same spot, thus reducing the print resolution. Furthermore the droplets in this specific scenario were about one order of magnitude larger in volume than desirable. The jetting behavior can be optimized tuning the Pulse Peak Duration (PPD)

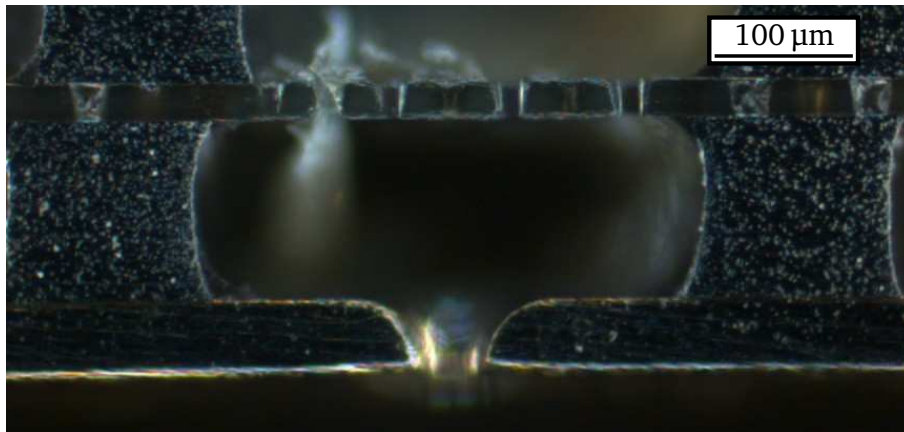


Figure 4.4: Polished cross-sectional view of a spectra S-Class 128-AA printhead nozzle. The nozzle can be seen at the lower end of the structure, above a filter element is visible. Nozzle diameter was measured to be around 56 μm. The nozzle shape was used as boundary condition for the CFD simulation.

as depicted in Figure 4.6. According to the pulse profile the jetting behavior varies. Here the photograph of a single droplet is taken 100 μs after the jetting pulse. The different droplet formations correspond to the respective PPD as given on the axis in the figure.

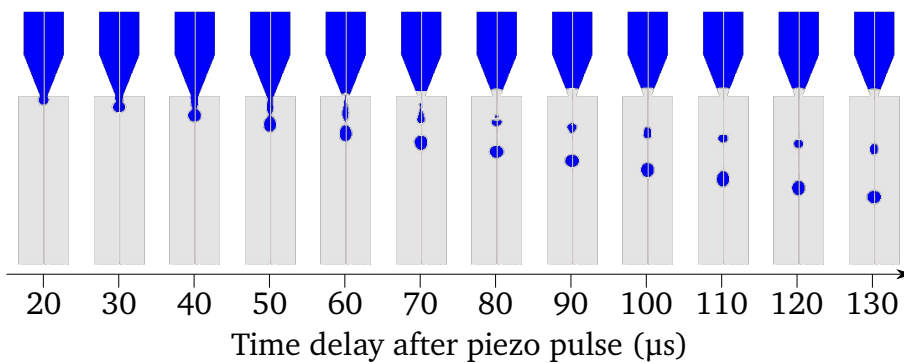


Figure 4.5: CFD simulation of jetting behaviour for a specific ink with the employed print-head. The images show the jet for the same settings after time increments of 10 μs per image after the piezo pulse.

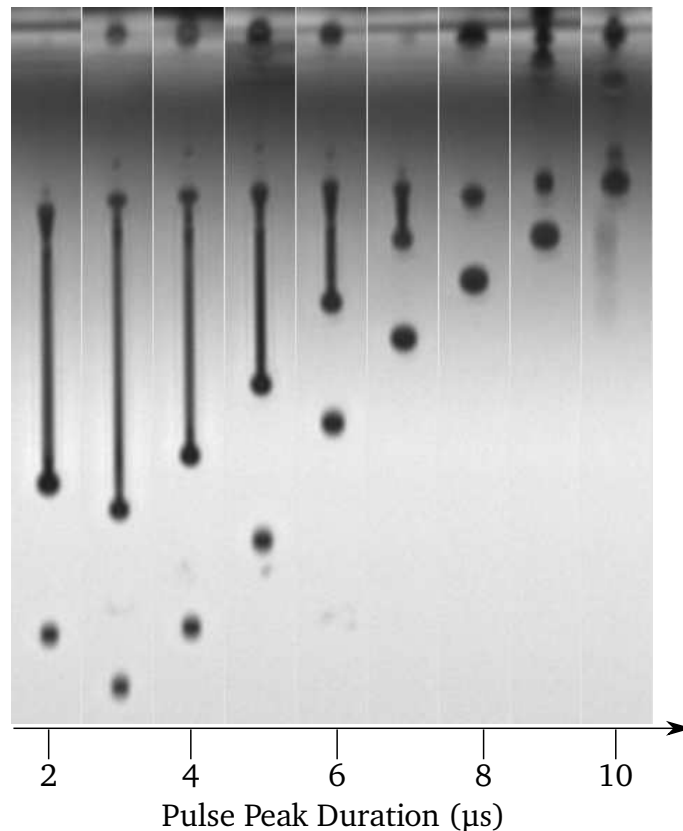


Figure 4.6: Jetting analysis according to time between rising and falling edge of the piezo pulse, called pulse peak duration (PPD). Single images for different PPDs are taken from the same nozzle 100 μs after jetting.

4.2 Aerosol-Jet Printing

Aerosol Jet[®] is a registered product name by Optomec (USA), since it's the only machine using this technique the product name shall be used. Aerosol Jet printing is a comparatively new printing method in which no single droplets are ejected, but an aerosol of the ink is produced using a so called "ultrasonic atomizer", which is subsequently sprayed onto the substrate [133]. Spraying is conducted using very thin nozzles and coaxial gas flows of the aerosol and a guiding gas. Figure 4.7 shows a schematic drawing of the Aerosol Jet printing process. An aerosol of the ink is generated by either ultrasonic or pneumatic atomizers and carried by a flow of N₂-gas towards the nozzle. Coaxially with the aerosol a second stream of N₂-gas is thrust from a ring shaped nozzle, guiding the ink in a very thin stream towards the substrate.

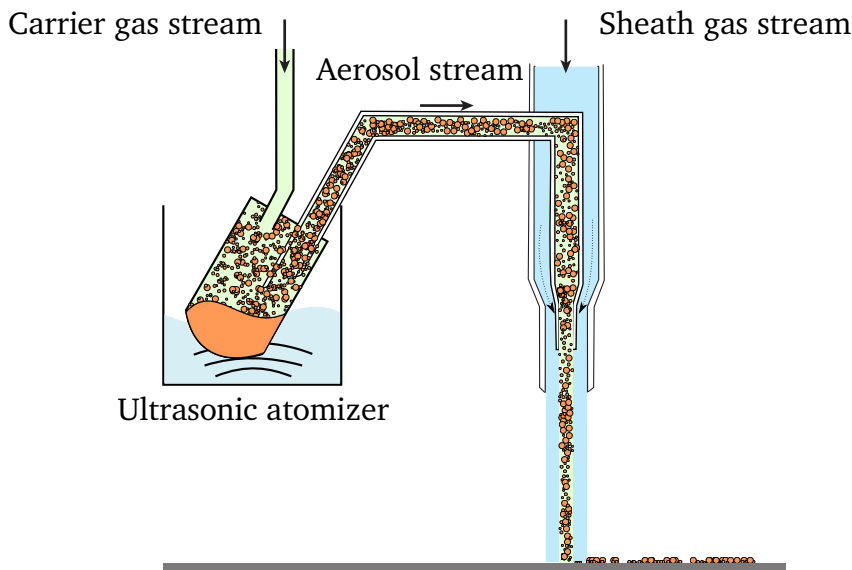


Figure 4.7: Working principle of Aerosoljet printing: an aerosol of the ink is produced with an ultrasonic atomizer. The aerosol stream is coaxially fed through a nozzle with a guiding gas. Adapted from [135].

This enables printing of high resolution patterns with feature sizes down to ten micrometers [134]. In contrast to IJP printheads usually contain only one nozzle, making the process significantly slower. On the other side, the technology features some advantages over IJP, as the ink is not in contact with the nozzle the risk of clogging is greatly reduced, provided the particles aren't too large. The high velocity of the gas stream leads to a trajectory of the jetted spray which is far more stable than that of an inkjet printed droplet. Therefore the distance between substrate and printhead may be much larger (up to 5 mm in comparison to less than 1 mm), thus enabling printing on non-flat substrates [135].

4.3 Screen Printing

Screen printing in opposition to the other introduced printing methods is a mask process, hence not able to dynamically deposit material in any arbitrary pattern. The rheological properties of the printing paste vary strongly from those of inkjet printing inks: Viscosity is generally much higher and in a very broad range of (1000 mPas to 10000 mPas) [47, 136]. A mask ("screen") made from a fine mesh

is covered with a Cu layer and structured via optical lithography. The screen is brought to close proximity of the substrate, which has to be flat. The paste is poured onto the screen and using a scraper transferred through the mesh in the desired regions. The mask on the mesh acts as stencil in this setup. Resolutions achievable with screen printing were reported to lines as narrow as $40\ \mu\text{m}$ [136].

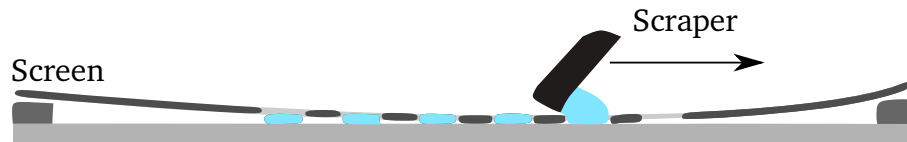


Figure 4.8: Schematic drawing of the screen printing process. The stencil pushes the ink through the flexible screen onto the substrate, adapted from [136]

4.4 Direct writing

Direct writing is the simplest of the introduced deposition methods. The fluid is held in a syringe and pushed through a single nozzle by a piston driven with a pneumatic pressure pulse. The nozzle capillary is often made from glass, steel or plastic and ranges in diameter from $45\ \mu\text{m}$ to $2\ \text{mm}$. The ejected fluid does not form single droplets but is in contact with substrate and nozzle at the same time, thus forming a meniscus between nozzle and the substrate. As the fluid wets the outside surface of the nozzle tip, the outer diameter of the tip is crucial regarding resolution and achievable line width. Additionally, the offset between nozzle tip and substrate is of large importance, as a breakaway of the meniscus must be prevented while laterally moving the syringe. Direct write systems are most often designed as Three Dimensional (3D) gantry machines, allowing the fluid deposition along lateral trajectories within a three dimensional working volume [137]. Figure 4.9 shows a schematic drawing of the working principle of direct write dispensing.

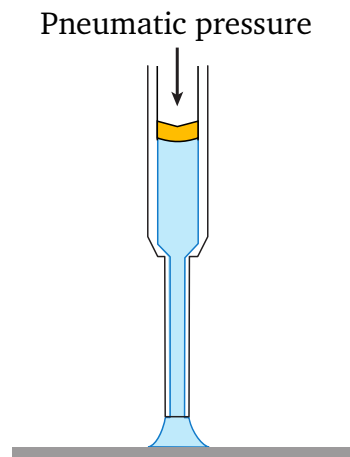


Figure 4.9: Working principle of printing by direct writing. The highly viscous fluid is stored in a syringe with a pneumatically driven piston. The fluid gets ejected through a capillary tip onto the substrate, being in contact with the substrate and the tip at the same time. The meniscus being formed due to surface tension is depending upon the outer diameter of the tip, wettability of substrate and tip and distance between tip and substrate.

4.5 Review

The previously described printing technologies were compared by six key aspects: Initial investment, running costs, printing resolution, flexibility of pattern design, particle size constraints and high volume production capability.

Aerosol jet printers need the highest initial investment, followed closely by IJP. Screen printing tools can be acquired for comparably low amount and direct write machines feature by far the lowest price of these four. Since direct writing can also be done manually it may be started off with almost zero costs, while often used gantry or robot-based systems can be quite expensive.

Running costs of the techniques vary also strongly. Screen printing comes with the need of producing masks for each print job, which naturally produces expenses. Aerosol Jet and Inkjet don't produce high operational costs unless a printhead needs to be replaced due to nozzle clogging. Especially Inkjet printheads are at higher risk for clogging, since their nozzles are typically much smaller. Direct writing is

the most affordable to operate. Consumables needed for this technique are usually disposable items with very low price.

Achievable printing resolution is strongly influenced by employed ink and substrate, but also one characteristic factor for printing technologies. Aerosol Jet printing enables very small feature sizes, which cannot be matched by the other techniques. Inkjet printing follows shortly behind, whereas screen printing and direct writing are more suitable for low resolution applications.

This constrain, on the other hand, enables the use of much larger particle sizes with direct writing and screen printing. IJP with its small nozzles requires the smallest particle size while Aerosol Jet printing lies in the middle of the spectrum.

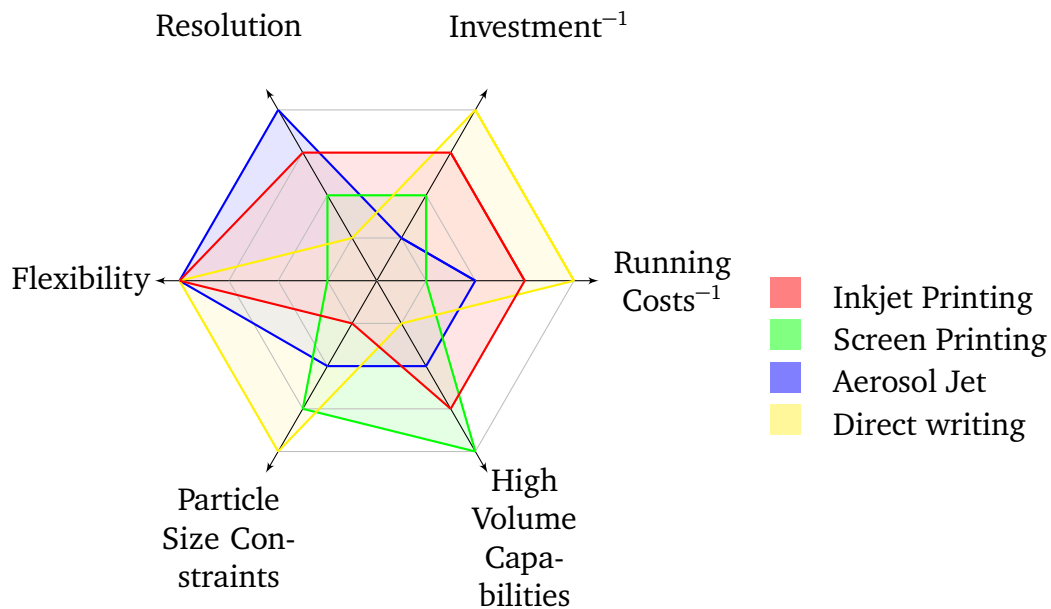


Figure 4.10: Radar plot comparing the introduced printing technologies. All axis from center to outside: poor to good in their categories respective performance or suitability. Scales are normalized to highest value on the outermost ring and lowest value on the inner ring, respectively. Direct writing was chosen for the experimental stage of this project, IJP was selected as the prospective production process.

Capability for high volume production is the greatest for screen printing, since it enables printing of a large number of devices e. g. on a wafer simultaneously. Inkjet printing can also be employed for large number fabrication. Multi-nozzle print-

4 Printing and Fluid Deposition Methods

heads and multiple heads per printer enable throughput slightly lower than screen printing. Aerosol Jet and direct writing are single nozzle techniques, thus feature a limited capability for high volume production.

One aspect which is crucial for this work is the flexibility to adapt to new print patterns. Direct writing, IJP and Aerosol Jet are digital fabrication methods and produce the desired design directly from a CAD file. Hence maximum flexibility is given. In contrast, screen printing needs masks for each application, which makes it highly inflexible.

Figure 4.10 shows a graphical juxtaposition of the introduced printing technologies. Direct writing and IJP feature the best overall performance. The former was employed for the experimental stage of this project, while the latter was chosen as prospective production process.

5 Printed Reactive Nanocomposite Layers – Concept Development

Contents

| | |
|---|-----------|
| 5.1 Materials and Processing | 50 |
| 5.1.1 Thermodynamic Properties | 52 |
| 5.2 Theory of Reaction | 53 |
| 5.2.1 Intermetallic Phase Formation | 54 |

Summing up the advantages and disadvantages of the various established bonding methods (refer to section 2.2) and of reactive bonding with multilayer systems (as described in chapter 3) one quickly comes to the conclusion that there is no bonding technique available falling into the *sweet spot* as described in figure 2.6 and thus fulfilling the following requirements:

- Low bonding temperature
- Capability to bond heterogeneous materials combinations
- Enable gas-tight packaging under inert atmospheres
- Deposition of bonding material in arbitrary patterns

To develop a bonding technique capable of addressing all these requirements is certainly of high interest. The bonding concept developed in this thesis is an approach to tackle this challenge. The novel concept is named Reactive Nanocomposite (RNC)-Bonding. Figure 5.1 shows a drawing of the bonding concept using a RNC with only four process stages using the example of bonding a capping substrate to a micromirror device with a square shaped bond fram. The RNC is an ink

or paste comprising nanoparticles of at least two materials which can undergo an exothermic reaction after initiation by supplying an energy pulse, as described in section 3.2.

Stage one is to deposit the reactive nanocomposite dispersed in a carrier fluid onto the bottom substrate by inkjet printing, direct dispensing or comparable techniques. After the carrier fluid is removed by low pressure assisted evaporation, in stage two, the top substrate is aligned. Stage three is to ignite the RNC layer while applying pressure to the substrates perpendicular to the bonding surface. Following the ignition a self-propagating high temperature reaction will propagate laterally through the bonding layer. At the reaction front, the emitted heat will transfer into the adjacent materials, causing the solder layer to melt. After the reaction front has propagated through the bonding layer, the solder solidifies and the bond is finished (stage four). The amount of reactive material is well chosen to deliver just a sufficient amount of energy enabling the melting of the solder but not damaging the device's active components.

5.1 Materials and Processing

As aforementioned, in chapter 3 various material combinations were introduced which can undergo SHS reactions. A recent review upon various materials systems employed in microscale multilayer applications is given by Adams [138]. As clearly stated the formation of intermetallic nickel and titanium aluminides are two of the most commonly investigated reaction systems. This is due to high reactivity of the systems, availability and low price of the educts and favorable physical properties of the products like very high melting temperature, high ductility and good thermal and electrical conductivity. Ni, Al and Ti were chosen to serve as educts in this work, giving three possible reactive systems: $\text{Ni} + \text{Al} \rightarrow \text{NiAl}$, $\text{Ni} + \text{Ti} \rightarrow \text{NiTi}$ and $\text{Ti} + \text{Al} \rightarrow \text{TiAl}$. Table 5.1 shows the material combinations that were evaluated in this study for the RNC development. Key properties of the material combinations which are compared are the specific reaction enthalpy and the adiabatic reaction temperature. The reaction enthalpy can be used as an indicator for the ignition

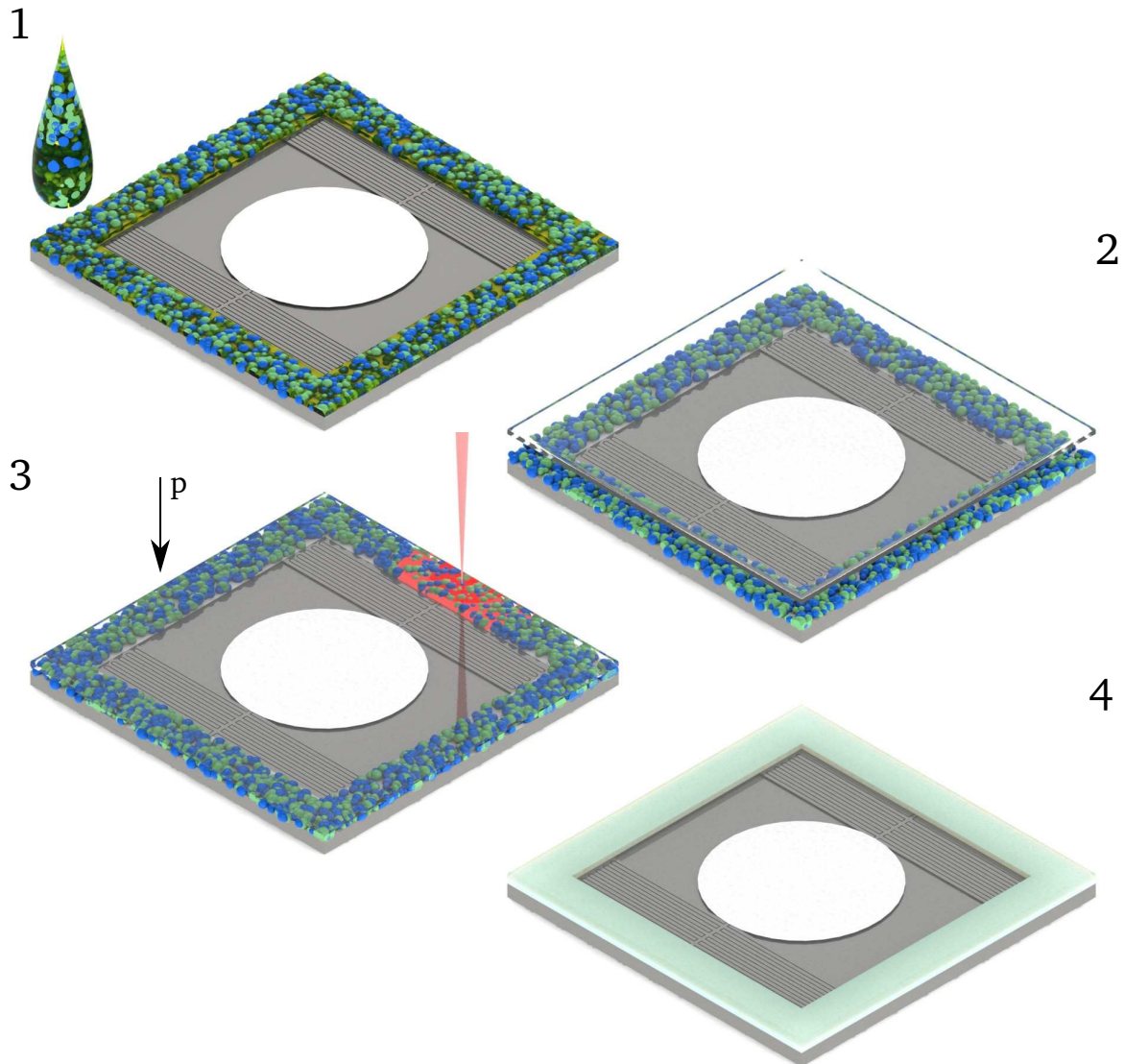


Figure 5.1: Schematic drawing of the concept of reactive nanocomposites based bonding in four stages, using the example of bonding a glass cover onto a micromirror device with a square bond frame:

1. Deposition of the reactive bonding layer in arbitrary pattern onto the bottom substrate.
2. Evaporation of the binding solvent and alignment of the top substrate.
3. Laser ignition of the reactive layer while applying pressure. The resulting reaction leads to a localized heating, enabling a bond at the desired bond frame only.
4. Finished bond.

threshold to start the reaction. Higher enthalpy means lower energy input needed for ignition and is therefore favorable. The adiabatic reaction temperature is the theoretically maximal temperature reached by the reaction. High reaction temperatures are needed to fulfill the bonding requirements, but extremely high temperatures, like emitted by TiC system for example (more than 3000 °C), are in contrast not desirable as they could easily damage the delicate microsystems.

Table 5.1: Materials combinations evaluated in our studies for RNC development.

| Reaction mechanism | ΔH_f (kJ/mol) | T_{Ad} (K) |
|----------------------------|-----------------------|--------------|
| Ni + Al \rightarrow NiAl | -59 [2] | 1911 [2] |
| Ni + Ti \rightarrow NiTi | -34 [139] | ~1400 [140] |
| Ti + Al \rightarrow TiAl | -36 [2] | 1500 [2] |

5.1.1 Thermodynamic Properties

Equation 3.6 from section 3.1 was used to estimate the critical layer thickness Δ_{cr} for the material systems employed in this work. As inert materials, in consistency with the experimental setup, silicon and fused silica substrates were used for the calculation. Three different setups of substrates were evaluated: bottom and top substrate made from Si, both substrates made from fused silica and one substrate made of each material. In combination with the three available reactive systems, Ni–Al, Ni–Ti and Ni–Ti, nine critical layer thicknesses were calculated. Material properties from the literature that were used for calculating Δ_{cr} are listed in the appendix (B.1). The critical layer thickness is strongly dependent on the reaction temperature and velocity. Due this, the reaction in the Ni–Al is the hardest to extinguish, hence very thin layers of reactive material are necessary to maintain a self-propagating reaction. Depending on the thermal conductivity of the inert material the minimum layer thickness for Ni–Al was estimated to be in the range of 0.174 mm to 1.53 mm. For application in microsystems technologies a thin bonding layer is preferable.

Table 5.2: Critical layer thickness Δ_{cr} in mm of the reactive material for self-sustained reactions in respect to the inert material.

| Inert material | Reactive material | | |
|-------------------------------------|-------------------|-------|-------|
| | Ni-Ti | Ni-Al | Ti-Al |
| Si + Si | 6.377 | 1.934 | 1383 |
| Si + SiO ₂ | 4.987 | 1.513 | 1082 |
| SiO ₂ + SiO ₂ | 0.726 | 0.220 | 157.5 |

Based on the calculation results Ni-Al was chosen as main material system of interest for the experimental works, as described in the following chapters.

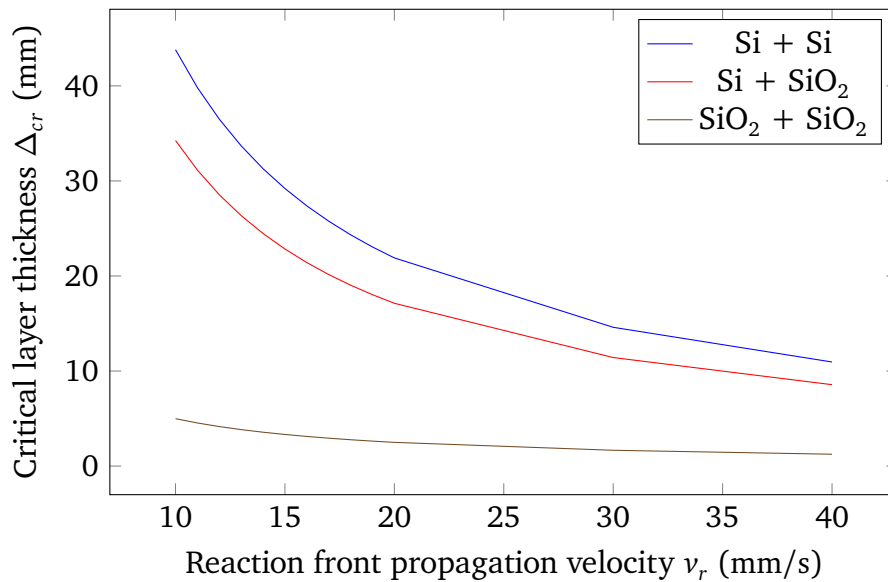


Figure 5.2: Critical layer thickness Δ_{cr} for the reactive layer in a Ni-Al system plotted over reaction front propagation velocity U_a and heat loss parameter γ_{cr} for three different inert material systems: Si + Si, Si + SiO₂, SiO₂ + SiO₂.

5.2 Theory of Reaction

Since the initial description of SHS reactions in 1967 a lot of work was conducted to fundamentally understand the reaction mechanisms (see section 3.1). Additionally, many researchers developed mathematical models of the processes to enable

reliable prediction of reaction parameters and constraining factors. In the following paragraphs the formation of intermetallic NiAl will be described from a materials point of view and subsequently some important modeling approaches will be introduced.

5.2.1 Intermetallic Phase Formation

Intermetallic phases are a special kind of metallic formation, similar to alloys but with stoichiometric ratios of components and ordered crystal structures [141]. Figure 5.3 shows the crystal structures of pure Ni and Al and of the NiAl intermetallic phase, respectively. Ni and Al initially form cubic face centered crystals. During the formation of the intermetallic phase the lattices move into each other, forming a new crystal orientation. The new structure is similar to a mono-elemental cubic volume centered crystal, but with a Ni atom embedded in the Al cubic cell and vice versa [142].

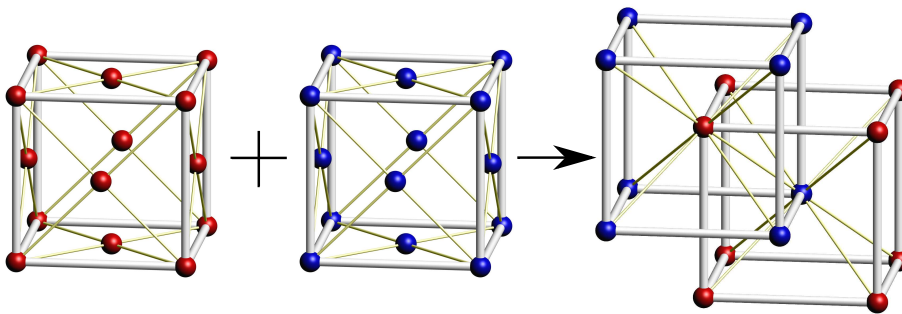


Figure 5.3: Crystal structure of pure Ni and Al and the resulting NiAl intermetallic phase. Al atoms drawn blue, Ni atoms red, respectively. The raw materials are cubic face centered, the intermetallic phase is cubic volume centered [142]. The crystal lattice constants of Al and Ni are 404.95 pm and 352.4 pm, respectively.

Phase formation and sequence of reactions seems to rely on various properties and resulting intermediate phases are not always found the same: Moore *et al.* reported

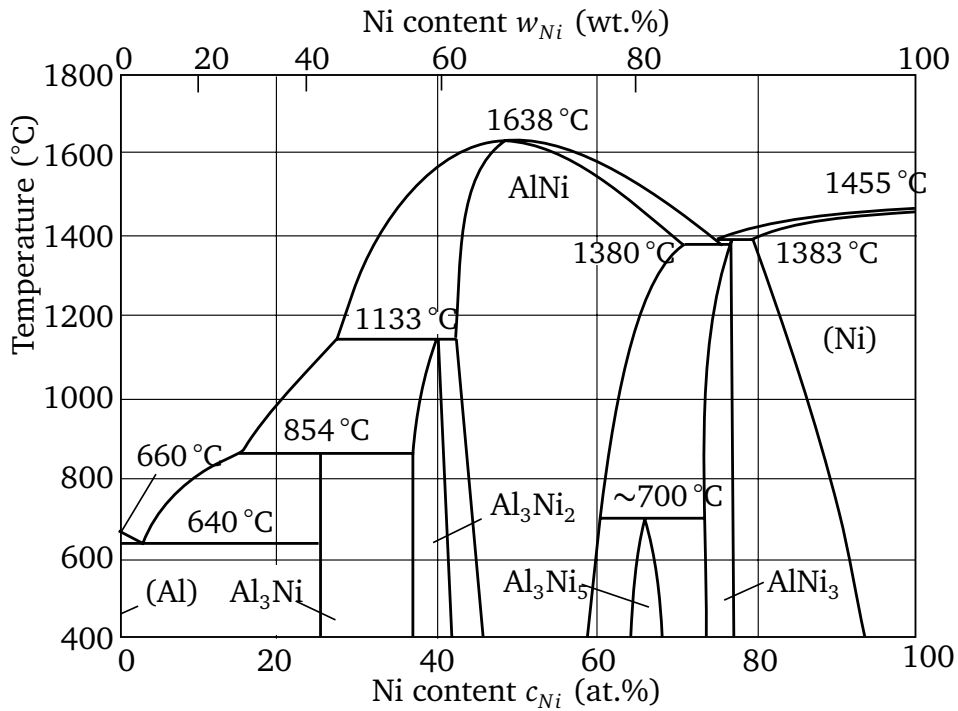


Figure 5.4: Phase diagram of the binary Ni-Al system [79]. Various intermetallic compounds are existing while the most stable one is the stoichiometric AlNi phase. It is noted that the melting temperature of AlNi (1900 K) is well above the melting points of Al and Ni.

the following sequence of reactions [77]:



Shkodich *et al.* studied in a more recent work the formation of phases during SHS reactions of the Ni/Al system *in situ* using dynamic synchrotron radiation diffraction by [143]. The initial Ni and Al phases quickly disappear, forming an intermediate Ni₅Al₃ phase, before eventually resulting in the equiatomic NiAl phase:

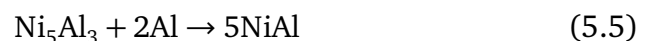


Figure 5.4 shows the phase diagram of the binary Ni-Al system. Equiatomic mix-

5 Printed Reactive Nanocomposite Layers – Concept Development

tures of Nickel and Aluminium form the intermetallic compound AlNi with a melting temperature of 1638 °C which is well above of those of Nickel (1455 °C) and Aluminium (660 °C). In addition to the AlNi phase one commonly sees the aluminium rich Al_3Ni phase and the nickel rich AlNi_3 phase.

6 Experimental Work

Contents

| | |
|--|-----------|
| 6.1 Materials Characterization | 58 |
| 6.1.1 Particle Size, Size Distribution and Morphology | 59 |
| 6.1.2 Chemical Composition and Percentage of Pure Metal | 63 |
| 6.1.3 Nature and Thickness of Passivation Layer and Percentage of Pure Metal | 67 |
| 6.2 Reactive Nanocomposite Fabrication | 69 |
| 6.2.1 Inert Environment – Oxygen contamination | 70 |
| 6.2.2 Grinding | 71 |
| 6.2.3 Ultrasonication | 71 |
| 6.2.4 Particle Dispersion | 72 |
| 6.2.5 Pressing | 74 |
| 6.2.6 Heat chuck | 76 |
| 6.3 Reaction Experiments | 78 |
| 6.3.1 Ignition Mechanisms | 79 |
| 6.3.2 Reaction Front Propagation Velocity | 87 |
| 6.4 Reaction Products Analysis | 89 |
| 6.4.1 XRD | 89 |
| 6.4.2 TEM | 94 |

The experimental work in this thesis were divided into four task-groups, which are described in the respective sections in this chapter. First, the initial materials were characterized to provide sound basis of knowledge about the physical and chemical

properties of the acquired particles and powders.

The second part of the experimental work was to produce the RNC mixtures. A set of 59 samples was produced, varying the composition and processing procedures. Reaction experiments were conducted with the composites fabricated and are described in the third section of this chapter. Ignition threshold and reaction front propagation velocity were measured during the experiments under diverse ambient conditions. Temperature, atmosphere, substrate material, applied pressure and ignition method were modified throughout the experiments.

Finally, in the fourth section of the chapter the characterization of reaction products is depicted. The measures as applied for the initial material analysis were employed again to investigate the reaction products.

6.1 Materials Characterization

The initial nanoparticles to be used as the reaction educts were characterized regarding their key properties, as defined by Rossi [144]:

- Particle size
- Size distribution
- Particle morphology
- Chemical composition
- Nature and thickness of passivation layer
- Percentage of pure metal

Pure Al, Ni and Ti particles were acquired over a wide size range from 18 nm to 250 μm . Nanosized particles were bought from *Iolitec* (Heilbronn, Germany) and micron sized powders from *GoodFellow* (Bad Nauheim, Germany), respectively. The latter ones were acquired for comparative experiments but are not main aspect of this work.

6.1.1 Particle Size, Size Distribution and Morphology

These key parameters of physical properties were measured using Scanning Electron Microscopy (SEM) and Transmission Electron Microscopy (TEM). SEM analysis was done with a *JEOL JSM-6500F* field emission SEM with attached Electron Dispersive X-ray Spectroscopy (EDX) detector *Oxford Instruments INCA X-Sight*. To measure particle sizes, a semi-automatic image processing based approach was chosen. The SEM-micrographs were edited to enhance contrast and find edges between particles. These tasks were conducted using an image manipulation software (*Gimp*). After applying a color threshold, a watershed algorithm was used to differentiate between combined particles and finally an image processing tool (*ImageJ*) was used to automatically find circular shapes and measure their diameter, area and circumference. The resulting data was used to calculate mean particle diameters and plot size distribution.

This approach did not work sufficiently with SEM graphs with a high overlap of particles. For these kind of figures, the particle sizes were manually measured using *ImageJ*: particles were identified and elliptical selections were fitted to their contours. From the measured area of the ovals a diameter was calculated in estimation of a spherical particle with a cross section equivalent to the fitted shape. Morphology of the nanoparticles was found to be spherical and the average diameters were below 100 nm. Figure 6.1 shows the particle size distribution of the Nickel nanoparticles, mean diameter specified by supplier: 20 nm (Ni20) sample. The average diameter was 47 nm, with 50 % of the particles having a diameter below 43 nm. Figure 6.2 shows the SEM micrograph that was used for particle size analysis on the left and the processed image on the right. Size distribution graphs and their according SEM micrographs for the other starting materials and ground mixtures are shown in the appendix (section A).

Table 6.1 gives an overview of the acquired particles, their sizes and the names to which is referred consecutively. Although the measured diameters did not always comply with the specified ones, the samples were called as declared.

6 Experimental Work

Table 6.1: Batch description and particle sizes of the acquired material.

| Nanoparticles | | | |
|---------------|-----------|-------------------------|--------------------------|
| Batch name | Material | Specified diameter (nm) | Measured diameter (nm) |
| Al18 | Aluminium | 18 | 42.9 ($\sigma = 28.8$) |
| Al40 | Aluminium | 40-60 | —* |
| Ni20 | Nickel | 20 | 47.9 ($\sigma = 23.6$) |
| Ni60 | Nickel | 60-80 | —* |
| Ti60 | Titanium | 60-80 | 62.3 ($\sigma = 38.4$) |

| Microparticles** | | |
|------------------|-----------|--------------------------------------|
| Batch name | Material | Specified diameter (μm) |
| Al25p | Aluminium | 25 |
| Al125p | Aluminium | 125 |
| Ni45p | Nickel | 45 |
| Ni250p | Nickel | 250 |
| Ti45p | Titanium | 45 |
| Ti150p | Titanium | 150 |

* Particle size measurement of these batches did not return valid values.

** No particle size measurement conducted for these batches.

Optical Microscopy

Traditional optical microscopy was used to visually check the homogeneity of the samples and is due to the low process costs widely available. The resolution of conventional optical microscopes is fundamentally limited by diffraction and cannot be higher than $\lambda/2$, which equals approximately 250 nm in the visible range. Actual magnification limits are usually much lower due to imperfect optics and other irregularities, resulting in even lower resolution. Thus, the particles employed in this work are not detectable with optical microscopes.

Scanning Electron Microscopy

In contrast to optical microscopy a focused electron beam is used to image the sample in scanning electron microscopy. The beam is electrostatically accelerated

and focused using electromagnetic lenses. The focused beam gets scanned over the sample and secondary electrons are detected. High resolution in the range of few nm can be achieved, offering the capability to characterize the materials employed in this work as well as the produced samples. SEM measurements were conducted in collaboration with Treibacher Industrie AG (Althofen, Austria) and Institut Jožef Stefan (Ljubljana, Slovenia).

Transmission Electron Microscopy

High resolution transmission electron microscopy provides highest resolution measurements of the sample specimen down to atomic level. Samples have to be electron transparent, which applies usually for objects with a thickness of less than 100 nm. Particle diameters can be measured with high accuracy and core-shell structures are visible due to the transmission measurement principle. Fringes on the measurement graphs are due to crystal structure of the sample and give a direct information whether the material is amorphous or crystalline. TEM measurements were conducted in collaboration with USTEM at TU Wien (Vienna, Austria). TEM graphs of unreacted and reacted are presented in section 6.1.3.

White Light Interferometry

To measure the topography of the samples, white light interferometry was used. Using an interferometric measurement principle, the resolution along the Z-axis is well below the diffraction limit in White Light Interferometry (WLI). This method was employed to measure layer thickness and layer densification by reaction. A *Polytec Micro Systems Analyzer 500* was employed, enabling layer thickness measurements at a vertical resolution of 0.35 nm.

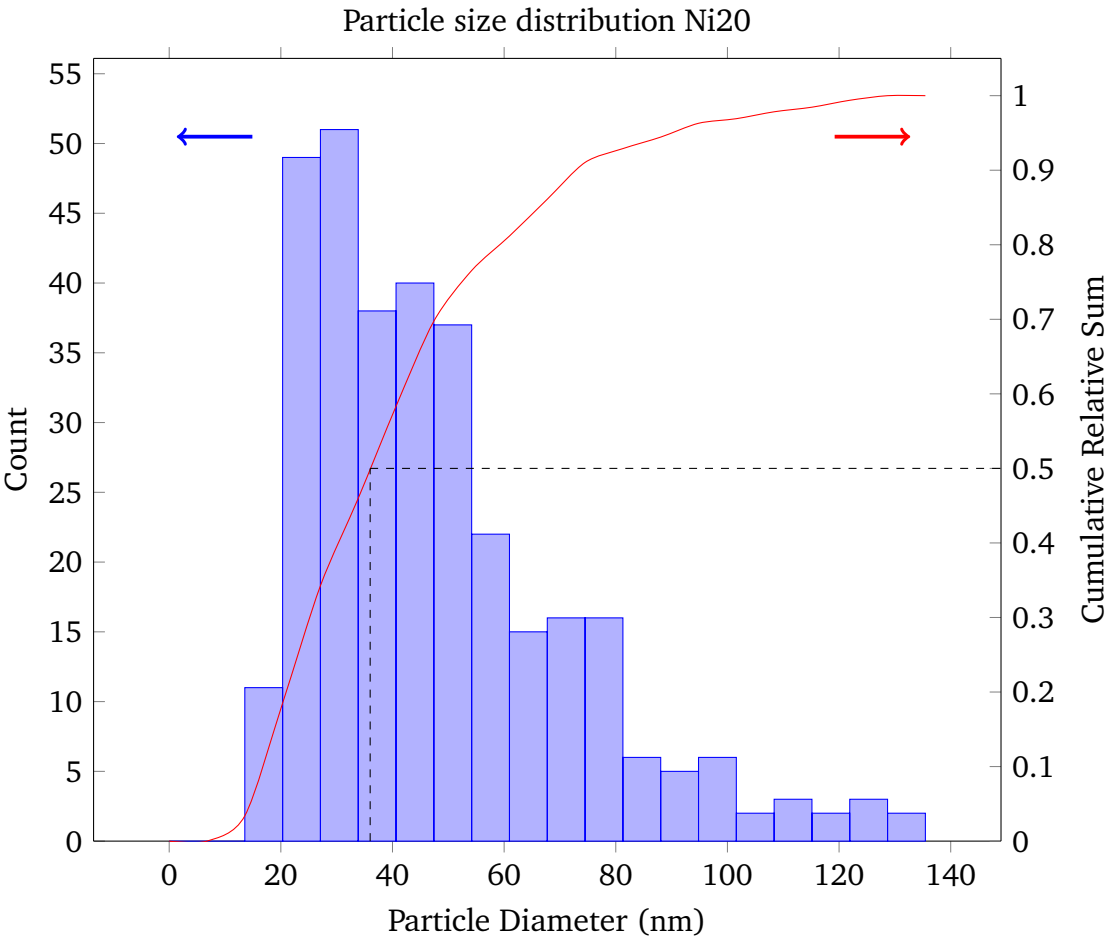


Figure 6.1: Particle size distribution of the Ni20 sample. Average particle diameter is 47 nm, with 50% of the particles having a diameter below 36 nm.

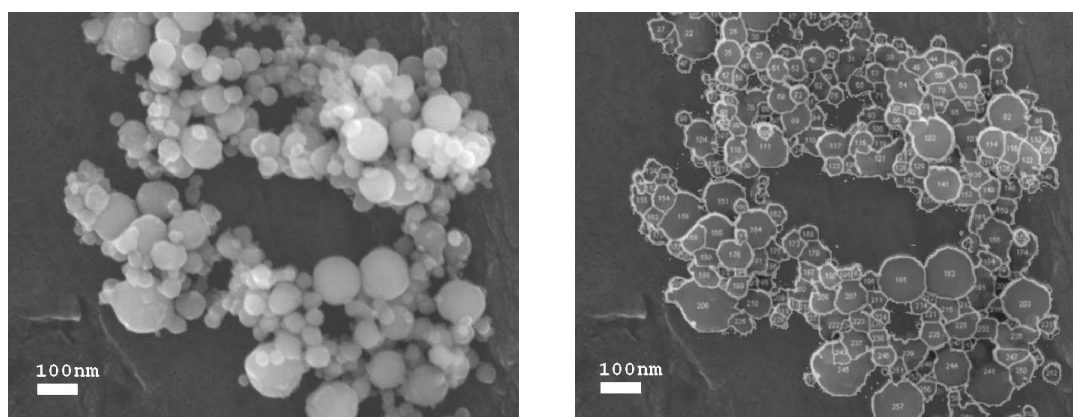


Figure 6.2: SEM graph and particle count overlay of raw Ni20 sample. The error resulting from false recognition of single particles to be a large one is assumed to be canceled out by the opposing error of larger particles to be recognized as multiple smaller ones.

6.1.2 Chemical Composition and Percentage of Pure Metal

Were measured using EDX and X-ray Powder Diffraction Analysis (XRD). While EDX is directly implemented into SEM machines, it offers spectroscopic analysis of the materials in very localized regions. Whereas XRD measurements are applied for bulk powders and give detailed information about the crystal structure of the sample and quantitative data about the composition. An X-ray beam is guided towards the sample and the *Bragg*-reflected radiation is collected by a detector. As reflection angles are depending on crystal structure, the measured spectrum can be fit to reference data from material databases. Matching the reflection angles of the measured material with the literature values provides high accuracy to identify specific materials. Figure 6.3 shows a schematic drawing of the *Bragg*-reflection with a description of the condition which has to be fulfilled for positive interference. A *PANalytical X'pert Pro* XRD machine was employed with a Cu-K_α anode at 8.04 keV to analyze the materials in this work. The first batch of nanoparticles acquired was handled at normal atmosphere and showed significant oxygen contamination in the respective EDX measurements. After reaction experiments with this batch turned out unsuccessful a second batch was acquired and exclusively handled within an inert atmosphere inside a glove box. XRD measurements for the second batch showed high purity of the samples and low grade of oxygen contamination. Figure 6.4 shows the respective XRD graphs of the pristine samples and the

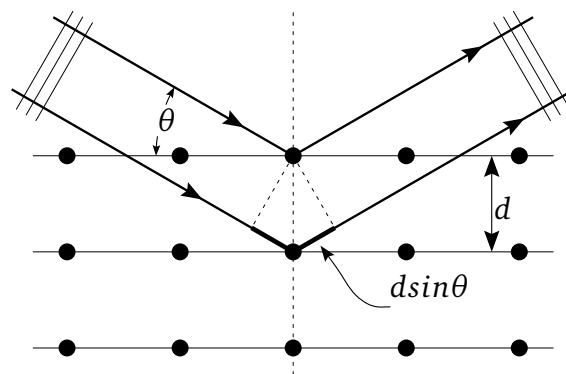


Figure 6.3: Bragg reflection, the effect on which XRD measurements are based. Positive interference only occurs if the condition $2d \sin\theta = n\lambda$ is fulfilled [145].

referred peaks from literature for pure Al and Ni, respectively [146]. The measured graphs show good conformity to the reference values.

Differential Thermal Analysis

To provide detailed information about thermodynamical properties of a sample Differential Thermal Analysis (DTA) was employed. In DTA, the sample is put into a sealed glass crucible and continuously heated. During the heating process an empty reference crucible is heated the same way allowing the differential measurement. While the energy input is kept constant, the temperature of the measurement crucible is tracked and changes relative to the reference crucible are noted. This way one can measure the ignition temperature and the reaction temperature. Phase changes and the corresponding temperatures at which they occur can be measured as well as energy released by exothermic reactions.

One of each Al-Ni and Al-Ti RNC mixtures were characterized using DTA to determine the thermodynamic potential of the mixtures. After the DTA measurement the samples were characterized using XRD again, to analyze the products which originated from the reaction during the DTA measurement.

Figure 6.5 shows the DTA plot for a Ni-Al sample. The crucibles with 25 mg samples were heated from room temperature to 1000 °C (a), cooled to 100 °C (b), heated to 1000 °C again (c) and finally cooled to 100 °C (d). All steps were executed at

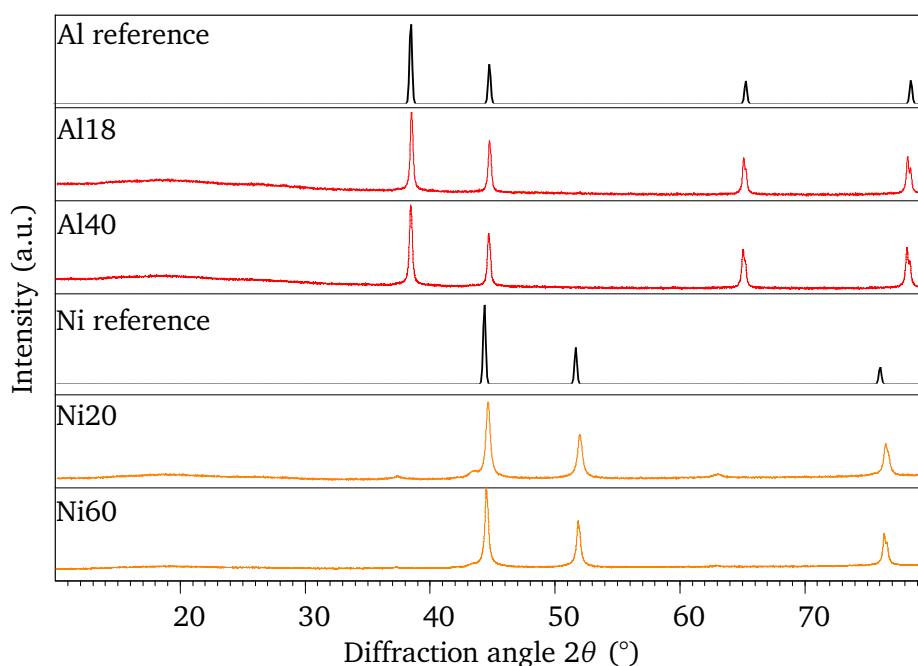


Figure 6.4: XRD measurements of initial raw Al and Ni nanoparticle samples as acquired and the respective reference values. The spectra fit well to reported data from literature, showing low peaks of oxygen contamination [146].

a heating and cooling rate of 10 K/min. The negative peaks on the graph of the first measurement indicate at which temperatures reactions were initiated. Integration of the shaded area above the graph gives quantitative information about the energy dissipated during the reactions. As the cooling graph shows no peaks, it is concluded that no phase change occurred. Solidification of a molten phase would result in a significant peak, just as the exothermic reaction did. The second heating-cooling cycle features no peaks as well, showing that the sample fully reacted during the first heating period. As the XRD measurement of the reacted sample shows (Figure 6.6), exclusively the intermetallic phases NiAl and Ni₃Al were formed during the reactions. Neither of these phases undergoes any phase transformation within the temperature range of 100 °C to 1000 °C. The respective DTA and XRD graphs for the Ti–Al sample are shown in the appendix (Figure B.5 and Figure B.6).

6 Experimental Work

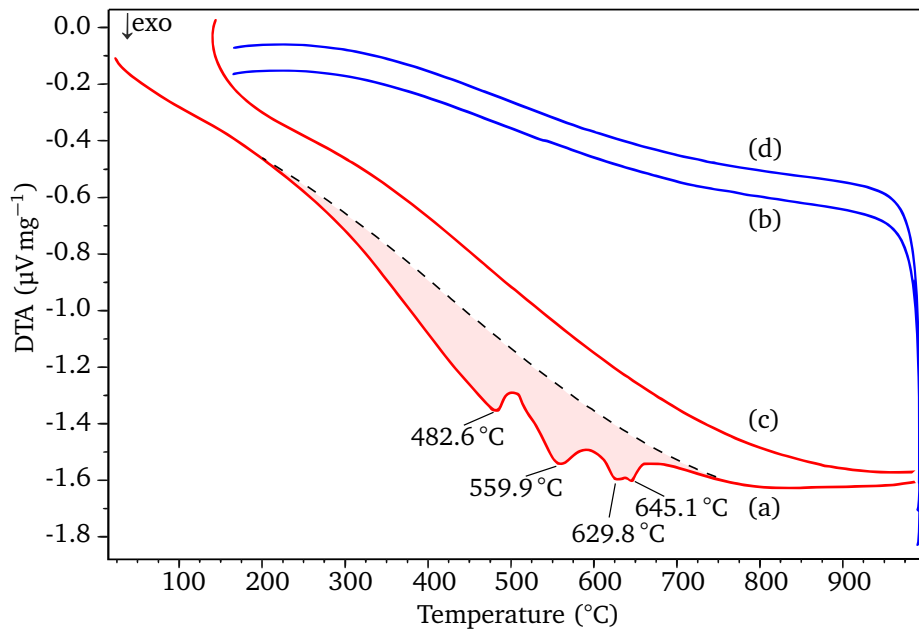


Figure 6.5: Differential thermal analysis graph of Ni–Al sample. Chronological order of measurements: a) heating, b) cooling, c) heating, d) cooling.

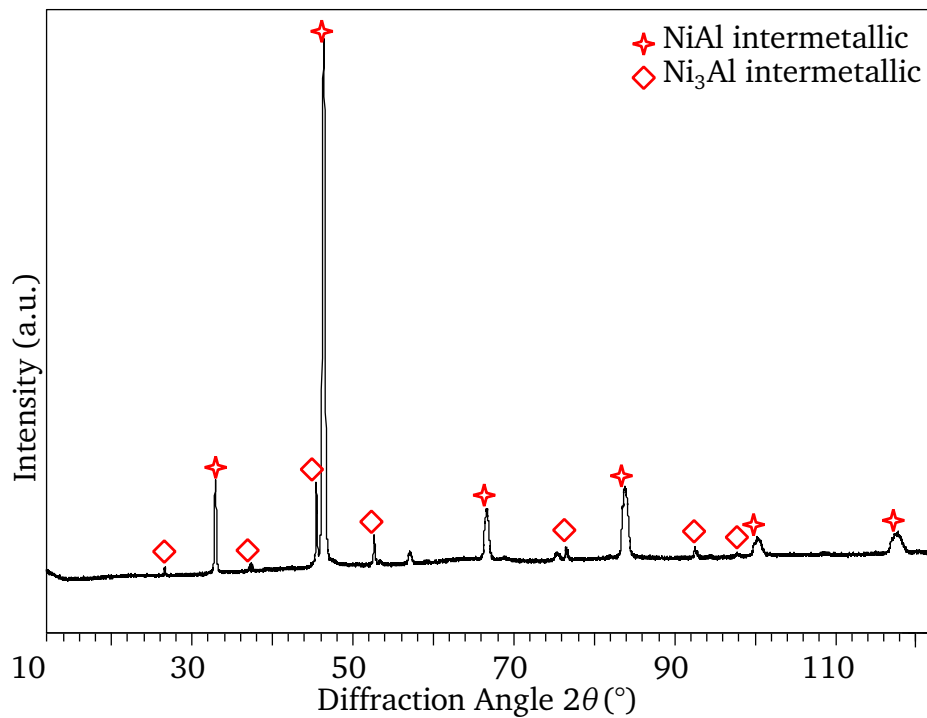


Figure 6.6: XRD Graph of the DTA sample after the DTA measurement. Sample was 100 % reacted during the first heating cycle, as only intermetallic Ni–Al compounds were found.

6.1.3 Nature and Thickness of Passivation Layer and Percentage of Pure Metal

Transmission electron microscopy is well suited to investigate the presence of passivation layers and their respective nature and thickness. The method allows for observing passivation layers with thicknesses down to the sub-nm scale. Metallic nanoparticles show clearly visible crystal lines in TEM measurements. Amorphous materials however, like Al_2O_3 or NiO and other metal-oxides appear blurry in TEM graphs. This enables measurement of passivation layer thickness.

A further indication for the presence of oxides can be given by the electron diffraction graphs, which shows discreet point patterns for crystallite samples and rings for amorphous structures. Additionally, using the TEM in scanning mode (Scanning Transmission Electron Microscopy (STEM)), enables imaging using Z contrast. In these measurements heavy elements appear brighter than lighter ones, enabling a clear distinction between Al and Ni particles. Using *in situ* EDX measurement during the STEM session enabled for precise space-resolved elemental analysis. Figure 6.7 shows an STEM measurement and the respective EDX line scan graph for a ground, unreacted Al18Ni60 sample. Small amounts of O could be detected on both particles, with Ni exhibiting slightly stronger contamination. Figure 6.8

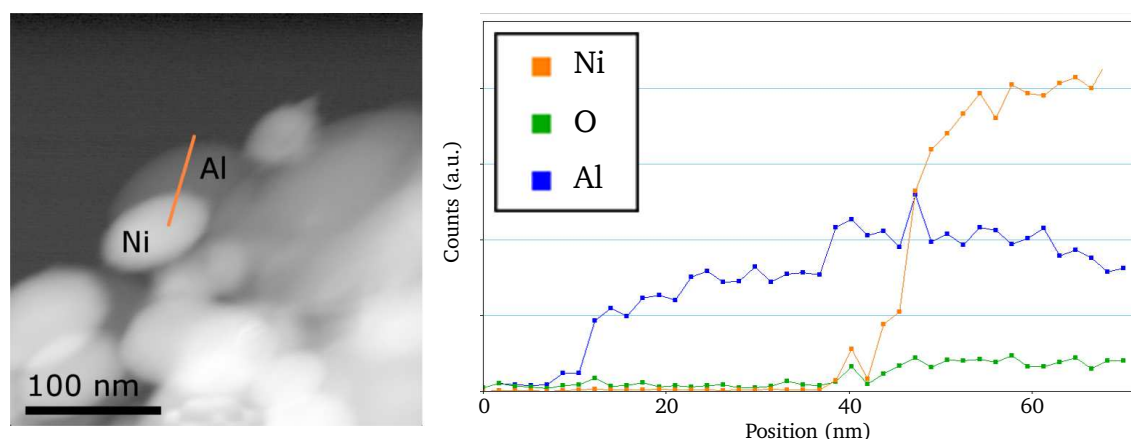


Figure 6.7: STEM and *in situ* EDX measurement of an Al18Ni60 sample. The elliptically distorted STEM graph in Z contrast mode shows heavy elements brighter than lighter elements. Accordingly, the Ni particles appear white, while Al particles are shown grey. The *in situ* EDX line scan along the orange line revealed only very small amounts of oxygen, in both Al and Ni particles.

6 Experimental Work

shows TEM images for the ground and unreacted Al₁₈Ni₆₀ sample. Crystalline lines can be observed in all graphs throughout the particles with only very thin (1.2 nm) amorphous shells on some of the particles. The electron diffraction exhibited a clear crystallite pattern without amorphous rings.

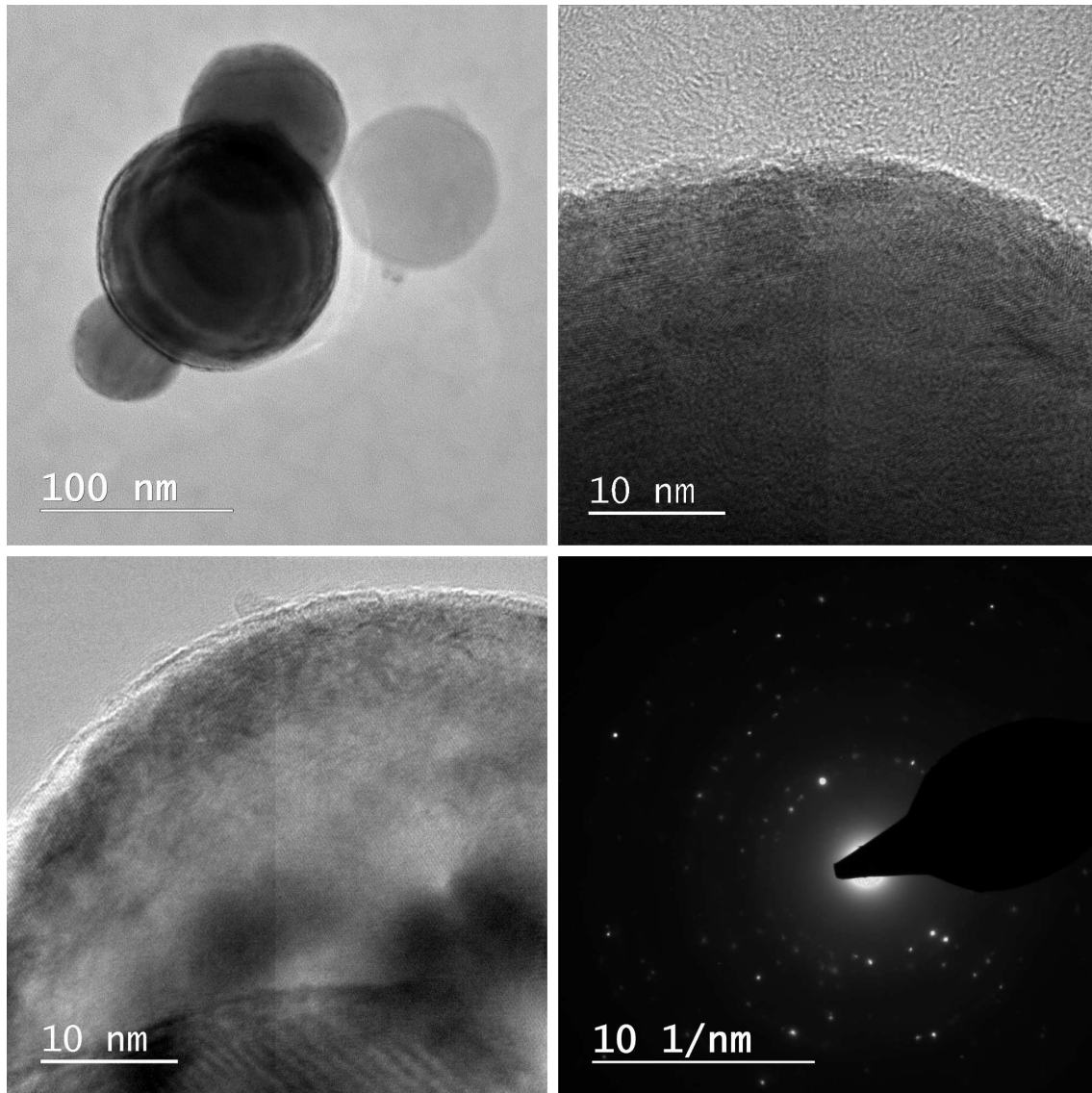


Figure 6.8: TEM images of a ground unreacted Al₁₈Ni₆₀ sample. Scale bars are given in each picture. Crystal structure can be observed throughout the particles, only very thin amorphous layers (presumably oxides) can be seen on the particle surfaces. Electron diffraction graph (centre right) shows no amorphous rings which would indicate the presence of oxides.

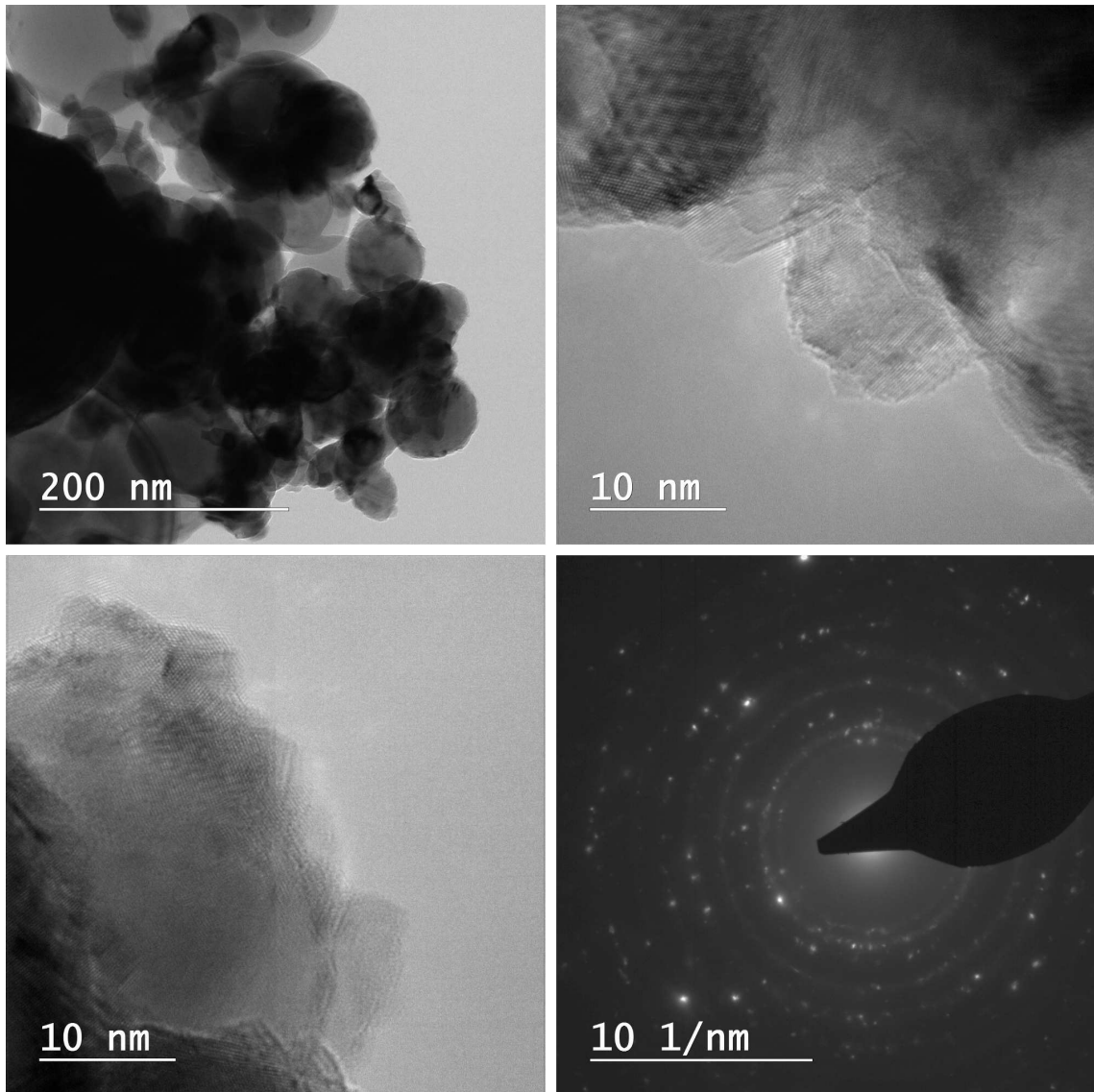


Figure 6.9: TEM images of a ground unreacted Al₄₀Ni₂₀ sample. Scale bars are given in each picture. Crystal structures can be observed throughout the particles, only very thin amorphous layers can be seen on the particle surfaces, which are accounted for as oxides. Electron diffraction graph (bottom right) shows fine crystalline pattern with very thin amorphous rings.

6.2 Reactive Nanocomposite Fabrication

Several different routes for fabrication of the reactive nanocomposites were investigated along with various post processing steps.

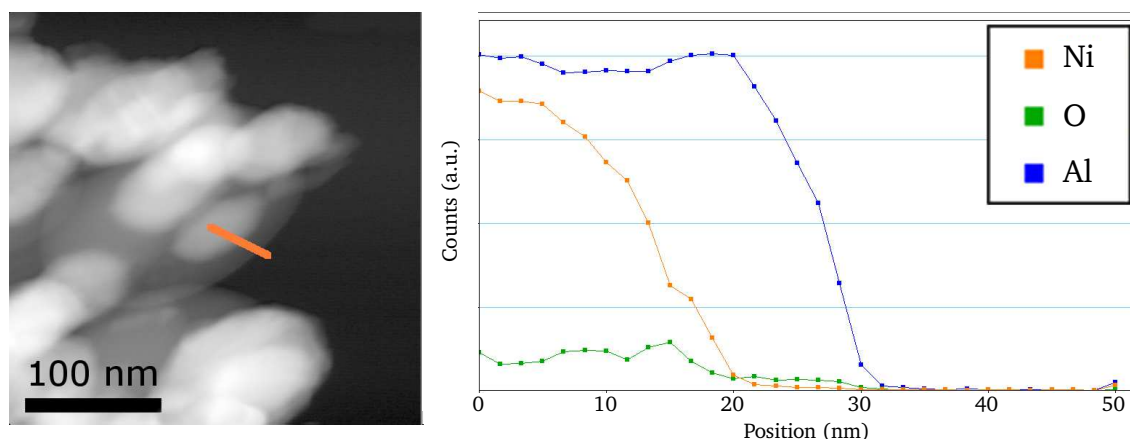


Figure 6.10: Z contrast enabled STEM image shows distinctive Ni and Al particles (Ni white, Al grey). The *in situ* EDX line scan was conducted along the orange line. The Ni particle showed considerable oxygen amounts on the surface, whereas the Al particle seemed almost O free.

6.2.1 Inert Environment – Oxygen contamination

To prevent oxygen contamination of the nanoparticles, experimental work was conducted under inert atmosphere in a glove box whenever feasible. Argon, 99.99990% purity (Ar 5.0) was used as inert medium. The working atmosphere in the glove box was continually circulated and cleaned and the machine was equipped with sensors for O_2 and H_2O concentration measurement. The concentrations of oxygen and water were kept below 0.5 ppm. The atmospheric pressure inside the glovebox was set slightly above ambient pressure, to prevent inbound air stream in case of leakage. The particles were moved as acquired in the sealed containers into the glove box.

Whenever experimental protocols required transferring the samples from the glovebox it was taken care of sealing the respective containers, before exposing them to air. Figure 6.11 shows a photograph of the glovebox type *LabStar* (MBraun, Germany), which was used in this work.



Figure 6.11: Photograph of the glove box in which experiments were conducted.

6.2.2 Grinding

As shown in several works, mechanical activation by milling can have significant influence on reactivity of reactive powders (compare chapter 3). To increase the reactive surface area, the particles were ground using a pestle and a mortar. After several minutes of grinding, the mixture was removed from the mortar using a spatula. The ground mixture was collected and used in all following process steps. Samples were manually ground in a porcellain mortar for several minutes. The powders were weighted into the mortar in stoichiometric amounts, producing sample badges with a weight from 10 mg to 1000 mg. After grinding the particles were removed with a lab spatula and put into a sealed tube. Grinding was performed under Ar 5.0 atmosphere.

6.2.3 Ultrasonication

As stated by Rossi, ultrasonication is the most commonly applied technique to disperse and mix metallic nanoparticles in a solvent [144]. The dry nanoparticles were weighed into test tubes in stoichiometric amounts, at an atomic ratio of 1:1, Ni 69 wt% and Al 31 wt%, respectively, using a *Sartorius Cubis MSE* lab balance with 1 mg accuracy. Subsequently, the solvent and the surfactants were added. Finally the test tubes were sealed and put into an ultrasonic bath. Ultrasonication was

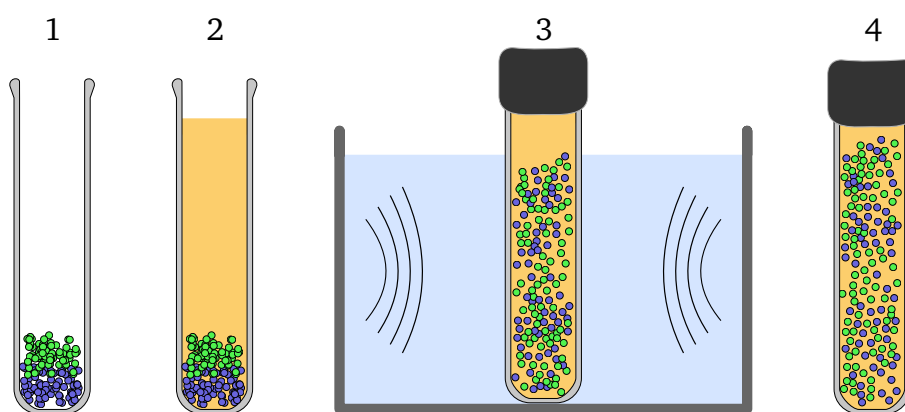


Figure 6.12: Schematic drawing of the sonication process and effect. The reactive components were subsequently weighed into the vial (1). Adding the solvent resulted in sedimentation and segregation of agglomerations of the nanoparticles (2). During sonication (3), the agglomerates break, the particles undergo homogenization and get dispersed evenly. After sonication a temporarily stable and homogenous dispersion is obtained (4).

executed using an ultrasonic bath and applied for varying times from few minutes to 12 h with $f = 48$ kHz, $p = 2$ W, frequency and power of the ultrasonic transducers, respectively.

The sample powder was weighed into sealed glass tubes according to the mass ratio of the reactants and an amount of solvent was added. The glass tubes were filled under Ar 5.0 atmosphere and only after sealing removed from the glove box for sonication. An overview of samples produced within this work and their respective compositions is given in table C.1 in Appendix C, *Sample Database*. Figure 6.12 shows a schematic drawing of the sonication process and effect.

6.2.4 Particle Dispersion

To prevent passivation by oxidation of the reactive particles, a solvent with low oxidizing potential was sought for. Additionally, a high vapor pressure, thus increased evaporation rate at low temperatures was preferred. The solvent to be used as a carrier fluid for the particles was chosen to be cyclohexane (C_6H_{12}), which is an oxygen-free carbohydrate. As cyclohexane is a volatile organic compound (vapor pressure at room temperature of about 10.4 kPa), it evaporates quickly at low tem-

peratures. In addition to ultrasonic agitation, the dispersed solvents were exposed to violently mechanical stirring with a lab stirrer. The frequency was set up to 1000 min^{-1} and stirring was conducted for 5 min.

To enable printing of the materials a colloidal dispersion is necessary. As the non functionalized particles sedimented in cyclohexane quickly, the addition of surfactants was evaluated to enhance stability of the dispersion. Triethylene Glycol Monomethyl Ether (MTG), oleic acid and methanol were evaluated as additives to enhance stability of the dispersion as well as surface tension and viscosity. MTG and oleic acid both offered high viscosity and low vapour pressures. This combination eases the stabilization of the dispersion, while at the same time evaporation takes longer and significant amounts of solvent residues remain on the dried sample.

Methanol on the other side has a low viscosity and a high vapour pressure of 13 kPa, which is even higher than the main solvent's cyclohexane (10.4 kPa), enabling faster drying. However, with water as a common impurity a potential source of passivation was identified and hence the further use of methanol terminated.

Since the main aspect of this work were the development and characterization of the reactive nanocomposite, the stabilization of the samples was not further optimized as few-minutes stable dispersions.

Using non-optimized dispersions, application of IJP for sample preparation was not possible. Instead deposition of the dispersed samples was conducted using manual dispensing methods with a pipette. The samples were collected using a fine-tip *Eppendorf* pipette from the vial, enabling the manual deposition along predefined paths.

To dry the RNC layers, solvent evaporation occurred under ambient conditions due to usage of volatile organic compounds as solvents. To shorten the evaporation time the samples could be put into a heat chuck, providing elevated temperatures or into a vacuum chamber, thus increasing the gas-pressure of the solvent.

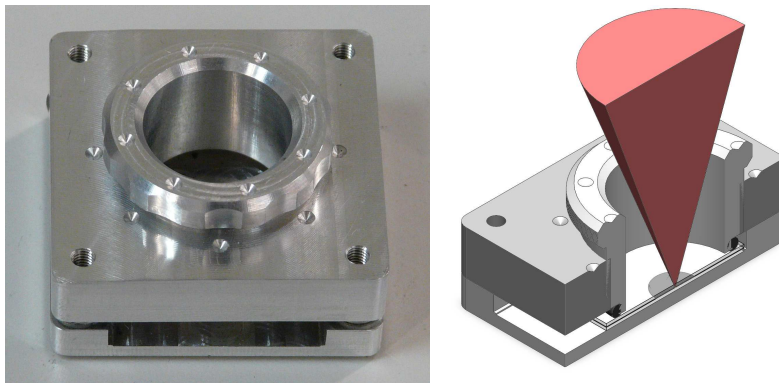


Figure 6.13: Sample holder enabling pressure application while performing laser ignition: Photograph (left) and cross section view with schematic laser application (right). Samples were inserted through the slit visible on the front side. Normal pressure was applied by fastening the hollow screw hand-tight.

6.2.5 Pressing

To apply pressure during the bonding experiments, two sample holders were constructed. The first one uses a screw mechanism to apply pressure, while at the same time enabling optical access towards the sample for laser ignition. Figure 6.13 shows a photograph of the sample holder.

The mount was designed in such way, that pressure was applied homogeneously along a circular profile around the sample to the holding substrates. Samples were put in between two glass slides and inserted into the mount through a slit on the side. Closing the screw mechanism the sample was sandwiched between the slides. By using glass as specimen carrier and pressure transmitter optical access through the top hole of the holder for laser ignition was granted. A major disadvantage of this setup was the uncertainty of the applied pressure, since no measurement principle was enclosed. Furthermore due to closing it by hand and tightening it *hand-tight* no repeatability of the pressure was given.

To facilitate the ignition by laser pulse while applying pressure to the sample a special holder was designed. The device was constructed in a compact form to enable usage inside the glove box. It comprised a case made of aluminium with centering grooves and a circular opening on the top aligned concentrically with the sample groove. Using the thread on the opening, a hollow shaft was screwed

through the top to apply pressure to the sample. An o-ring sitting in a groove on the shaft's lower end acted as the force transmitter while preventing damage to the sample by its ductility. Usage of the device was simple and quite crude: the reactive Nano composite was sandwiched between the bottom substrate and a transparent top substrate. Typical test specimen for the substrates were microscope slides. The slides with the rnc sample in between were inserted into the ignition holder through a slit in the side and centered in the groove. The screw shaft was lowered towards the sample and screwed hand tight to firmly press the substrates together. The device with the sample mounted was placed under the optics setup to commence the ignition experiment.

Figure 6.14 shows a schematic drawing of the application of the ignition holder in 3 steps: insertion of the sample, pressure application and laser ignition.

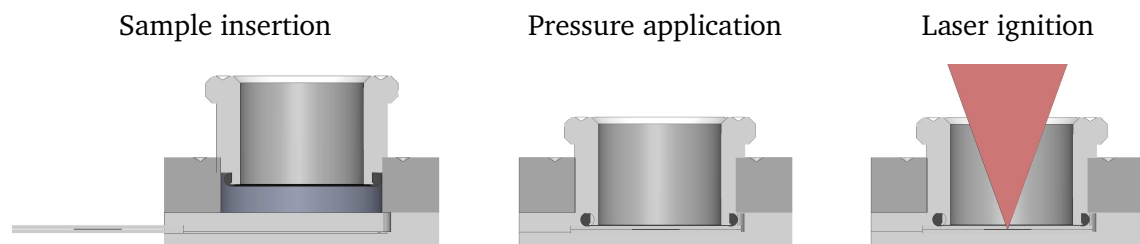


Figure 6.14: Schematic drawing of the using principle of the sample holder. The sample is inserted through the slot on the left side of the figure. While applying pressure using the top screw ignition is performed with focus laser radiation.

The second version of sample holder made use of a quick release clamp, enabling repeatable pressure on the sample. This setup made use of centric pressure application, thus not enabling laser ignition while applying a normal force. It was employed for two procedures. First, pressing samples for some time which were afterwards subject to ignition investigations under no pressure. Second, while applying pressure using this clamp, the whole setup was put into the heat chuck, which is described in the following section.



Figure 6.15: Photograph of the heat chuck. The ceramic heat plate in the middle is thermally isolated from the housing. A glass lid was available, enabling observation of operation with a shut housing.

6.2.6 Heat chuck

To enable reaction experiments at different ambient temperatures and to study ignition by uniform heating of the sample a heat chuck was built. The device contained a ceramic heating plate, which was ohmically heated. Attached to the heater was a PT100 thermocouple, to allow closed loop control of the temperature. The heated platen was suspended by a holder made from an insulating glass ceramic (Macor, thermal conductivity below 1.4 W/mK above $100 \text{ }^\circ\text{C}$ [147]) and housed in an aluminium case. Process temperature was controlled in a range of $25 \text{ }^\circ\text{C}$ to $700 \text{ }^\circ\text{C}$ using a PID controller and a control software with an accuracy of $\pm 2 \text{ }^\circ\text{C}$. Samples could be heated at a rate of up to $1 \text{ }^\circ\text{C/s}$, while cooling had to be done passively by turning off the heating until the required temperature was met. Figure 6.15 shows a photograph of the heat chuck with opened lid. A glass lid was used to enable temperature control and laser ignition simultaneously. Three main differences were distinguished in the heat chuck experiment design: First, heating at a low heating rate ($1 \text{ }^\circ\text{C/s}$) by placing the sample onto the room-temperature heat plate followed by ramping the temperature using the software controller. No SHS-reactions were observed using this protocol. Second, by pre-heating the platen and placing the sample onto it to enable a much higher but uncontrolled heating rate. In this case it was assumed that the sample would reach the aspired temperature after not more than 10 s, leading to a heating rate of at least $67.5 \text{ }^\circ\text{C/s}$. This method ren-



Figure 6.16: Screenshot of the heatchuck driver software developed for controlling the temperature within the heat chuck. In the upper window part the pre-set temperature profile is plotted, in the lower window area the actual temperature graph.

dered varied results depending on the way of sample deposition. Placing droplets of the RNC dispersion onto the heated platen lead to rapid evaporation of small amounts of the solvent which built an insulating vapour layer between the droplet and the hotplate. This phenomenon, called Leidenfrost effect, leads to hovering of the droplet and increased evaporation time [148]. Under these circumstances no self-propagating reactions were noted. If a dry powder sample was placed directly onto the hotplate this effect could naturally not take place. However, SHS-reactions were still not observed. Third, by increasing the sample temperature slowly to certain elevated values and ignition with a laser pulse. This protocol generally lead to positive results, which will be discussed in section 6.3.2. Figure 6.17 shows a photographs of the heat chuck setup with laser focusing, laser trigger and camera.

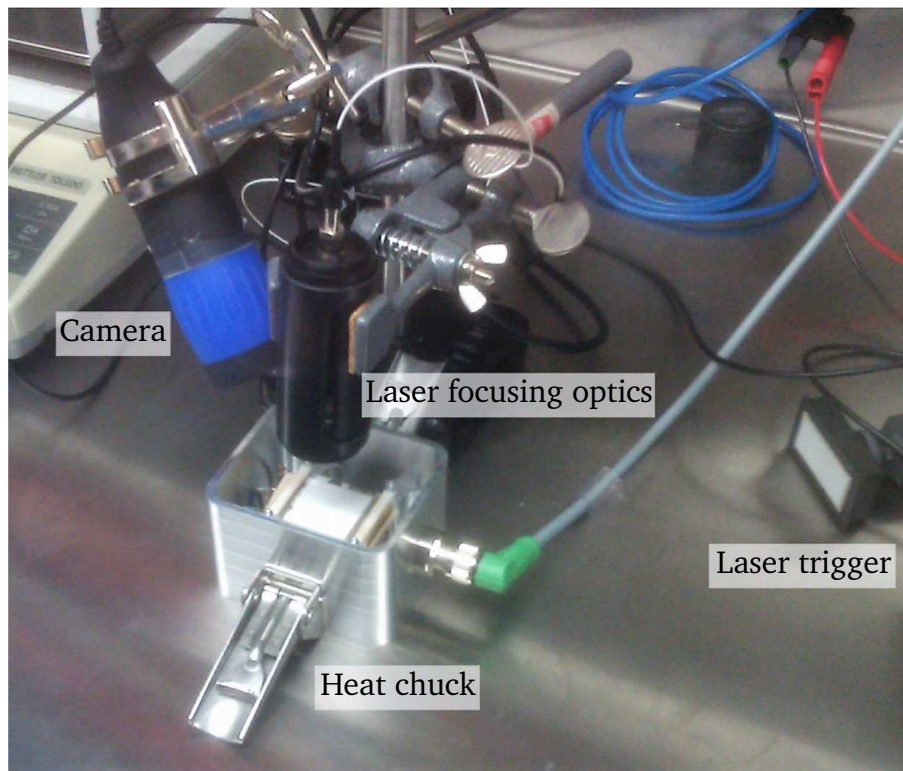


Figure 6.17: Photograph of the heat chuck setup with laser focusing optics, laser trigger and camera.

6.3 Reaction Experiments

The produced RNC mixtures were subject to reaction experiments comprising evaluation of capability to form a SHS reaction, ignition threshold, reaction front propagation velocity, reaction temperature as well as chemical composition and morphology of the products. As was found, most of the samples were not able to form a self-sustaining reaction. Therefore, the analysis of these samples is restricted to documentation of ignition attempts and chemical and morphological characterization of the sample areas which were subject to the energy input.

6.3.1 Ignition Mechanisms

As described in chapter 3, various ways of igniting reactive composites was shown in the literature, i.e. electric current, mechanical heat contact, laser pulse, mechanical shock and microwave radiation. In the scope of this work five different ignition mechanisms were evaluated:

- Contact to a glowing hot wire
- Contact to an ignited NanoFoil®
- Electric spark
- High power 1064 nm laser pulse
- Low power 808 nm laser pulse

The setups for each ignition method were as follows:

Contact to Glowing Hot Wire

Direct physical contact to a glowing hot wire was evaluated as further ignition method. Usage of a glowing coil as ignitor has repeatedly been reported in SHS related literature [98, 100, 117]. A thin tungsten wire ($\varnothing 200 \mu\text{m}$) was brought to a bright yellow glowing only via ohmic heating using an attached 9 V battery. The device was hand held and operated in such way, that the wire would get into direct contact with the sample material while it was glowing hot. Figure 6.18 depicts a schematic drawing of the ignition experiments using a glowing wire as igniter.

Due to its low mass and therefore low heat capacitance the wire immediately lost its temperature upon contact and stopped glowing. Ignition of the RNC samples was unsuccessful using this method.

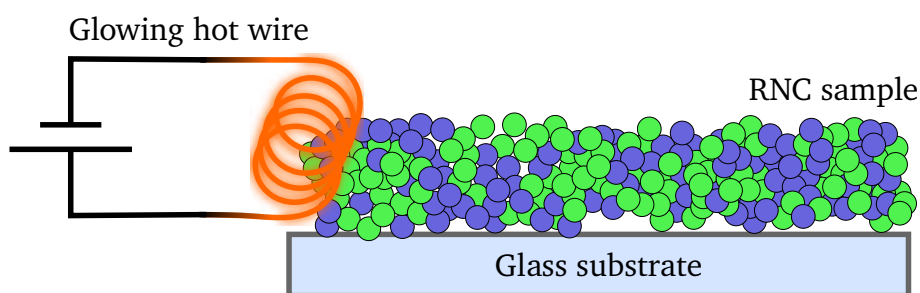


Figure 6.18: Schematic drawing of ignition experiments using a glowing hot wire. The RNC sample was placed onto a glass substrate and brought into direct contact with a glowing hot tungsten wire.

Contact to Ignited NanoFoil

Since NanoFoil reaches very high temperatures during their reaction they were chosen as an alternative heat source for igniting RNC samples. The experimental setup contained the reactive media which was deposited onto a substrate with parts of the substrate covered by a NanoFoil. A glass slide was placed on top to enable pressure application and ensure close contact of the NanoFoil and the reactive sample. The foil was placed in such way that few mm stood out of the assembly for facile ignition of the NanoFoil.

The latter was conducted using an electric current. Two wires were soldered to the contacts of a 9 V battery and placed on either side of the NanoFoil, delivering a current perpendicular through the multilayer system. This approach was proven to be reliable for ignition of the reactive foils. Figure 6.19 shows a schematic drawing of the set-up for the ignition experiments with a Nanofoil as igniter.

However, further ignition of the RNC layer by the reaction of the NanoFoil was not successful. It is assumed that heat transfer from the foil to the porous layer was not sufficient and additionally the heating period is considered too short to reach the ignition threshold within the reactive nanoparticles.

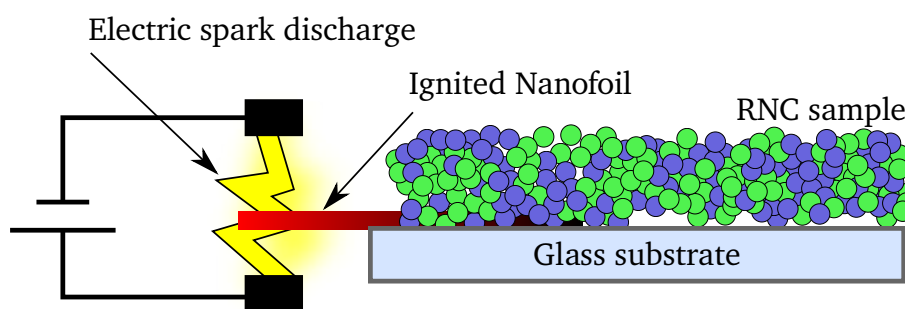


Figure 6.19: Ignition experiment using an ignited Nanofoil as heat source. A Nanofoil was placed onto a glass substrate in a way that it would partly stand over the edge of the substrate. The overhang was used to ignite the Nanofoil by electric discharge perpendicular to the foil's plane. The RNC sample was placed onto the glass substrate covering the Nanofoil.

Electric Spark

For electric spark ignition experiments a piezo-electric ignitor was acquired. Upon button pressing a 15 kV spark was released which would travel up to 2 cm through air. The setup contained a holder for the ignitor electrode which was aligned roughly 0.5 cm above the reactive sample. An insulating substrate (glass slide) was carrying the sample powder. To enable discharge of the voltage through the specimen, a part of the substrate was covered by a piece of Al foil, which was connected to ground.

Ignition of the RNC samples using electric spark discharge was not successful.

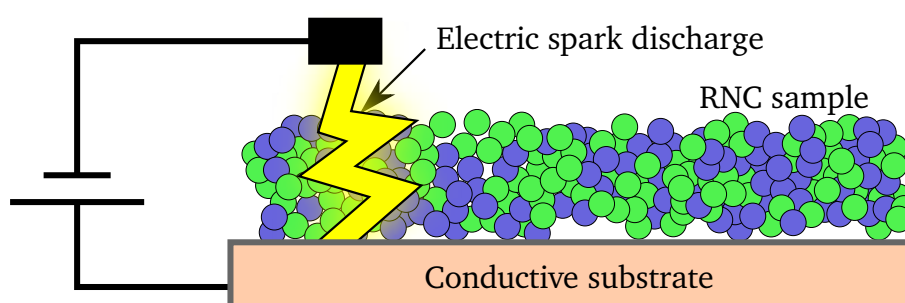


Figure 6.20: Schematic drawing of the ignition experiment using an electric spark discharge. The RNC sample was placed onto a conductive substrate (Cu). Electrodes were aligned above and below the substrate, respectively, allowing the discharge spark to travel vertically through the sample layer. The discharge potential was 15 kV.

High Power Laser Pulse

A laser welding machine (ALP 35S, Alphalaser) with a Nd-YAG laser source ($\lambda = 1064\text{ nm}$) was employed for high power laser ignition tests. Pulse energy could be tuned from 0.15 J to 75 J at pulse durations from 0.5 ms to 20 ms, giving a range of pulse peak power of 7.5 W to 9000 W. The resulting optical power density in the focal spot was around 3.8 kW/cm^2 at the minimum settings for a focal diameter of $500\text{ }\mu\text{m}$. Due to its size, the machine was operated outside the glove box, therefore not offering an inert environment.

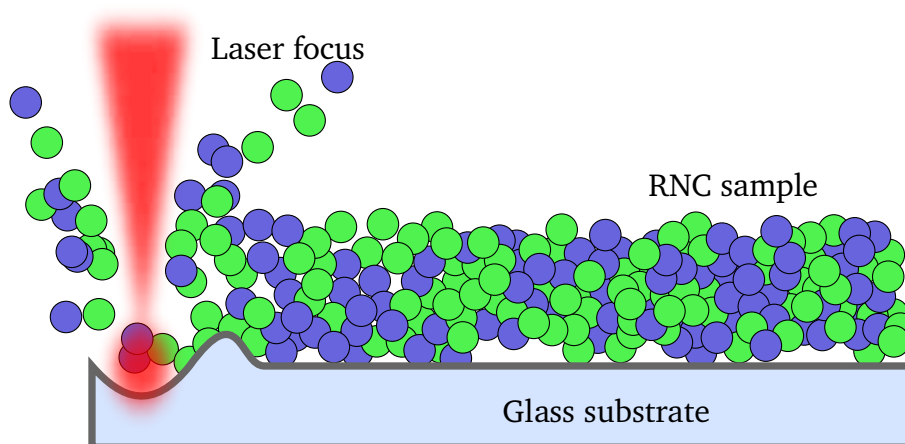


Figure 6.21: Schematic drawing of ignition experiment using the high power laser. The RNC sample was placed onto a glass substrate and exposed to a focused laser pulse. The excessive energy of the laser blast most of the particles away and damaged the substrate.

It was found that even at the lowest power settings the laser pulses were too strong for the tested nanopowder based RNC samples. The pulses cut straight through the reactive material layer into the substrates and blasting the sample away. Figure 6.21 shows a schematic drawing of the ignition experiment with a depiction of the result: the laser damaging the substrate and removing the reactive particles. Figure 6.22 shows a SEM graph of an Al₁₈Ni₆₀ sample which was used in this experiment. One can see that almost all of the reactive layer was removed from the substrate within the focal spot, the substrate itself suffering damage and few large molten particles covering the area around the impact.

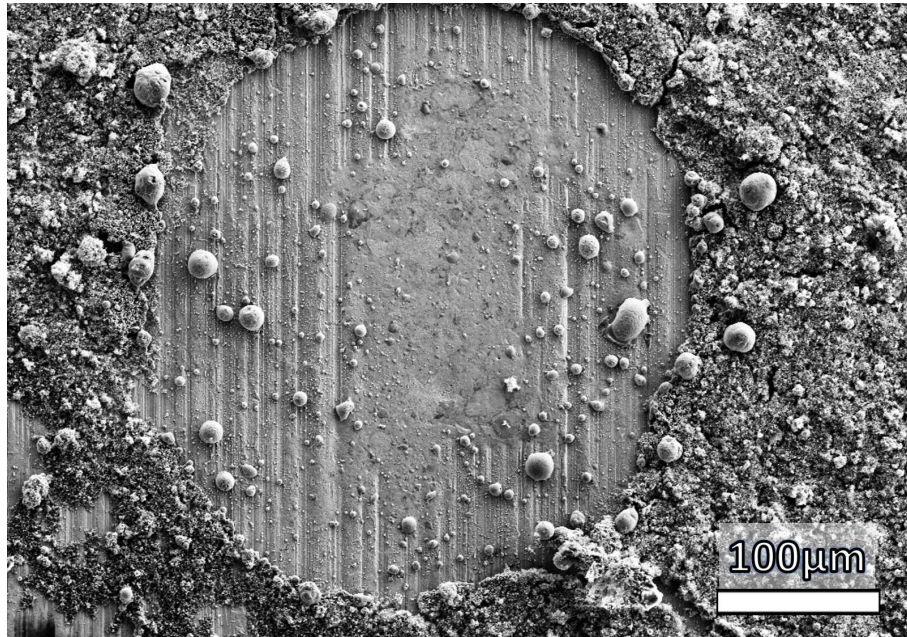


Figure 6.22: SEM graph of an Al18Ni60 sample subject to a high power laser ignition attempt. The laser pulse shot straight through the reactive material, blasting most of the particles away. Few large molten particles can be seen around the impact area.

Low Power Laser Pulse

For the low power laser ignition setup a fibre coupled laser diode was used. The laser's wavelength was 808 nm, emitted in continuous wave mode. Driven at constant DC voltage, a maximum optical output power of 440 mW was available. The trigger was manually operated using a push-button, enabling minimum exposure times of about 0.5 s and unlimited maximum exposure. The fibre was connected to a simple optical set-up comprising a collimator and a focal lens. A focus diameter of approximately 500 µm was set up, resulting in an optical power density of up to 254 W/cm². The focal length was 50 mm and the set-up was fixed in a stand so that the samples could be placed directly in the focus of the laser.

Figure 6.23 shows a schematic drawing of the ignition experiment, comprising the optical set-up and the sample. Ignition of ground Al-Ni samples was successful using this set-up. To determine the ignition threshold of the RNC sample the laser diode was first characterized using a pyrometer. At 166 mW (equivalent to 84.5 W/cm²) the ignition threshold was found for the ground samples. Figure 6.24

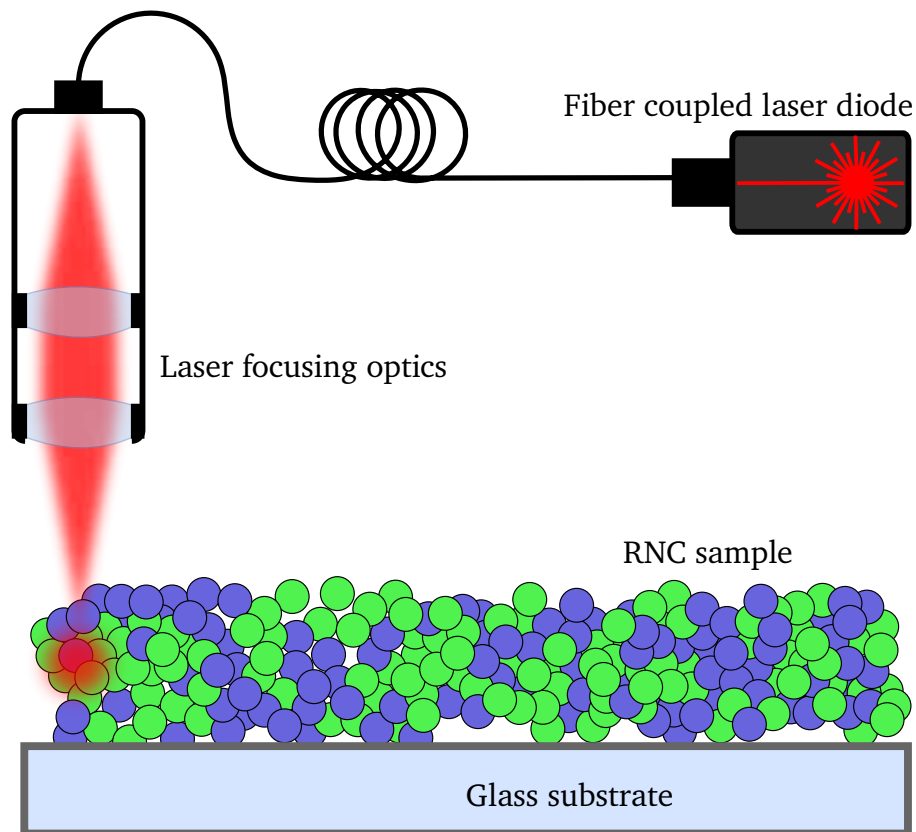


Figure 6.23: Schematic drawing of ignition experiment using a laser. The RNC sample was placed onto a glass substrate and ignited with a focused laser pulse.

shows the respective correlation of optical output power over electrical input power and the region in which ignition occurred.

This process was the only method to be found working for the ground Al-Ni samples within this work. Table 6.2 gives a brief summary of the evaluated ignition modes and the respective outcome.

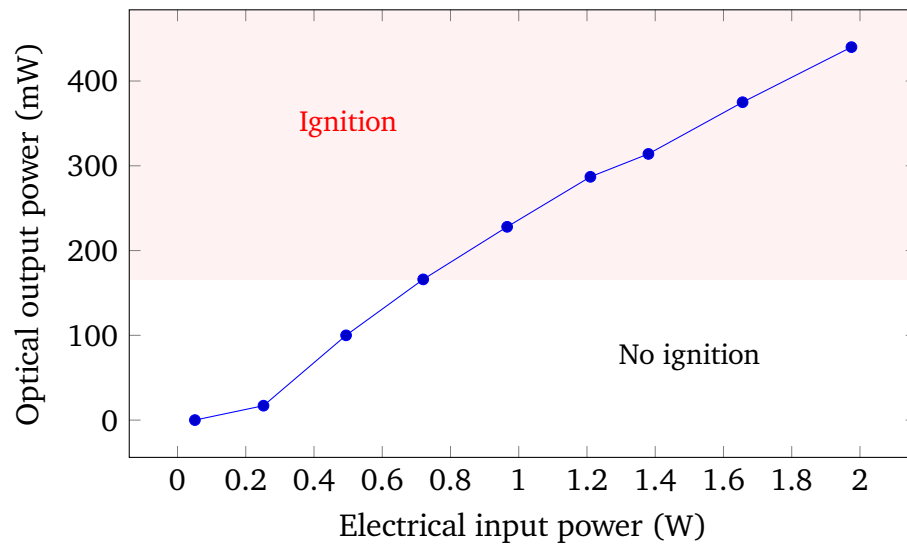
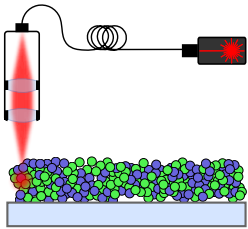
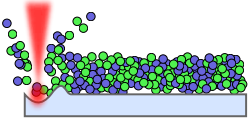
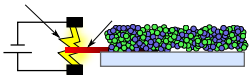
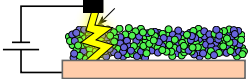


Figure 6.24: Graph depicting the optical output power over the electrical input power of the employed laser diode. Ignition occurred above the threshold of 166 mW.

Table 6.2: Review of experimentally evaluated ignition mechanisms.

| | Lower power laser | High power laser | Glowing wire | Nanofoil | Electric spark |
|----------------------|--|---|--|--|--|
| Mechanism | Light absorption | Light absorption | Direct heat transfer | Direct heat transfer | Spark plasma |
| Reference works | [138, 149] | [138, 149] | [98, 100, 117] | — | [138, 149, 150] |
| Ignition successful? | Yes | No | No | No | No |
| Sketch |  |  |  |  |  |

6.3.2 Reaction Front Propagation Velocity

The reaction front can propagate throughout a sample when the laterally transferred heat is sufficient for ignition of the adjunct material. The intra-layer heat transfer must also be not too high, as this could lead to an extinction of the reaction due to insufficient heat at the reaction front to enable further propagation. When using only a fused silica bottom substrate reaction front propagation veloc-

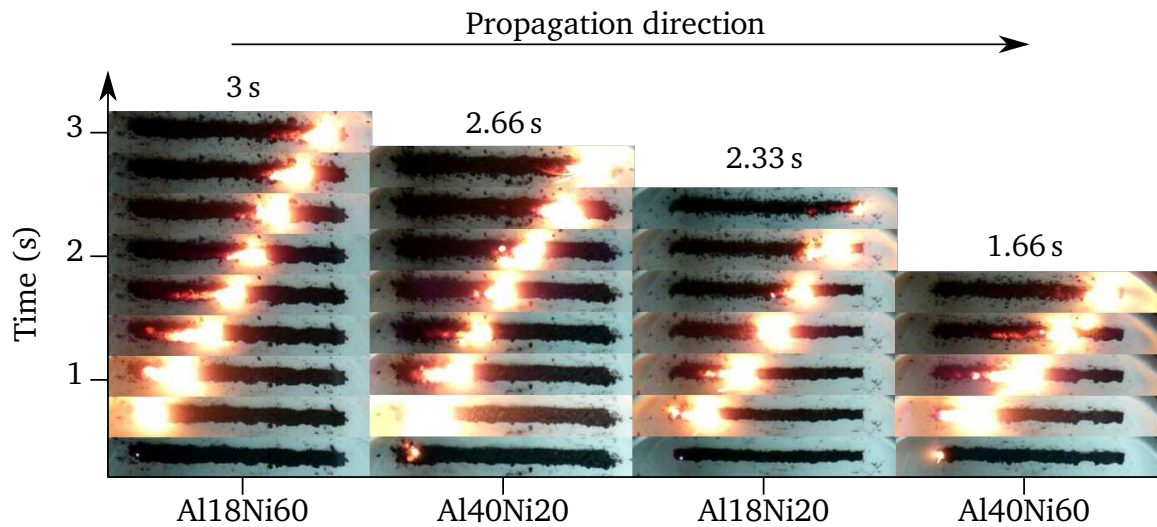


Figure 6.25: Comparison of reaction speed of Al18Ni20, Al18Ni40, Al40Ni20 and Al40Ni60 samples at room temperature. Graph shows time-scaled screen captures of high-speed imaging video footage of the experiments. Time between each shown frame is 333 ms, graphic published previously by M. P. Kremer et al. [151].

ities in the range of 10 mm/s to 22 mm/s were measured at room temperature. These values were observed using high-speed video imaging of the reactions. A line of reactive material with a length of 30 mm was put onto the glass substrate and ignited at one end using the laser as described in chapter 6. Using the video footage of the reactions the reaction front propagation velocity v_R was measured according to the time difference between the frames of the video. Recordings were taken with 2000 Hz [151]. Figure 6.25 shows screen captures of the videos taken of four different reaction experiments at room temperature. The images are aligned on a time scale, giving a comparison of reaction front propagation velocity between the different samples.

6 Experimental Work

Placing the samples into the heat chuck enabled measuring the impact of ambient temperature on reaction front propagation velocity. As activation energy decreases with increasing temperature an increase in reactivity was measured. Figure 6.26

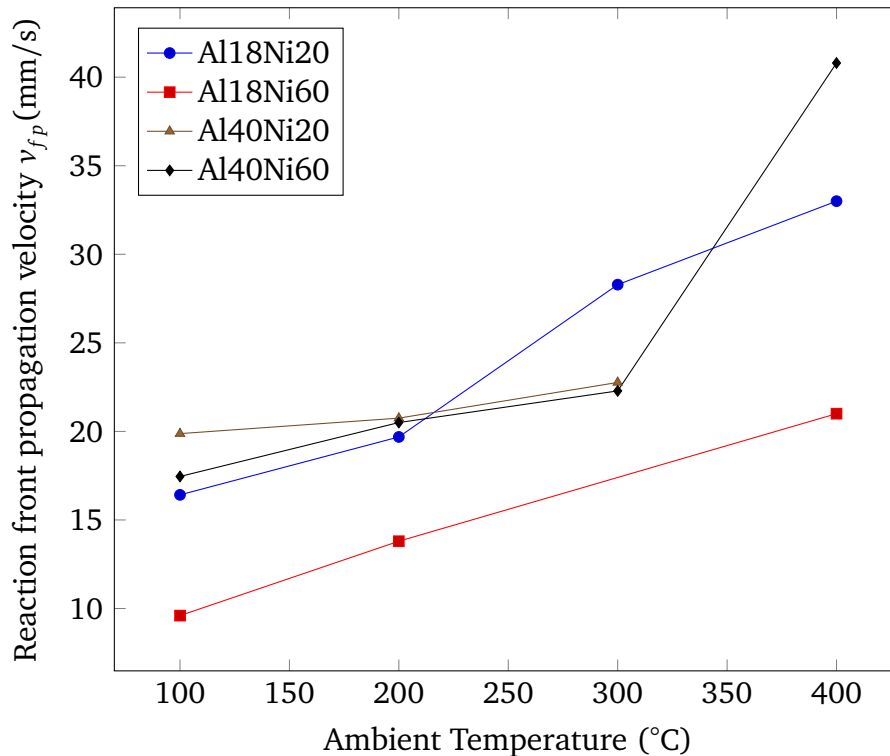


Figure 6.26: Reaction front propagation velocity over ambient temperature and particle size combination. Velocity increases with temperature for all samples.

shows a graph of reaction front propagation velocity over ambient temperature. Four samples with differing particle size combinations were heated in the temperature range of 100 °C to 400 °C and ignited via laser pulse. Reaction speed increased for all samples with increasing temperature, in agreement with literature (see section 3.1). An increase of reaction speed by a factor of approximately two was measured over a temperature rise from 100 °C to 400 °C. Values as high as 40 mm/s were measured for the Al40Ni60 sample at 400 °C. To ensure that the sample reached the wanted temperature throughout, the particles were deposited onto a copper substrate which was placed onto the heat chuck, enabling high thermal conductivity.

6.4 Reaction Products Analysis

The reaction products were subject to further analysis with the goal of determining the reasons for variation in reactivity and propagation velocity. Characterization of the products was conducted using XRD, SEM and TEM.

6.4.1 XRD

X-ray spectroscopy was used as the main tool to analyze the chemical composition of both, the reaction educts and products.

Analysis of the pristine materials showed high purity with no to very little oxygen contamination, as described in subsection 6.1.2. The following figures 6.27, 6.28, 6.29 and 6.30 show the respective measurements for samples according to their particle sizes. Each figure shows a collection of XRD graphs, comprising the spectra of the pristine educts, the mixed samples, the ground samples and finally the reaction products. For all samples it can be observed that during mixing and – more importantly – during grinding no mechanical alloying occurred. Expectedly, the graph of the mixed samples equals the combined spectra of both starting materials. Furthermore the measurement of the ground samples match the respective graphs for mixed samples precisely. Significant differences were observed in the reacted material samples depending on the initial particle sizes.

Additionally, each of the figures 6.27-6.30 contains a bar chart showing the phase composition of the reacted samples. Using relative peak height analysis a quantitative conclusion can be drawn from XRD measurements revealing the material composition of the sample.

6 Experimental Work

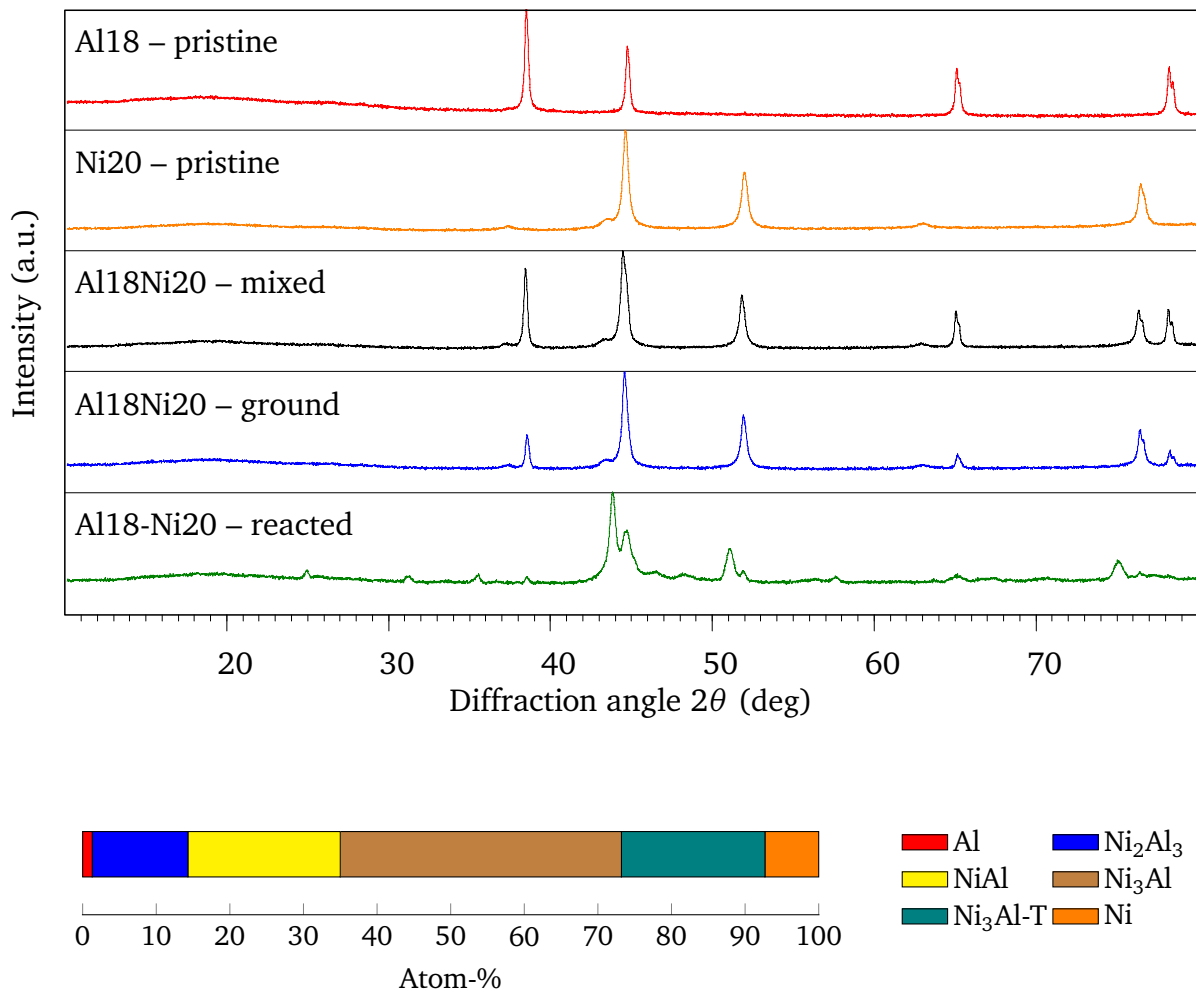


Figure 6.27: XRD Graph of pure Al18 and Ni20 particles as acquired, mixed, ground and reacted nanocomposites (from top to bottom.) One can easily see that no phase transformation takes place during mixing or grinding, hence the process of mechanical activation does not involve mechanical alloying. The reacted sample shows main peaks for the intermetallic Ni_2Al_3 , NiAl , Ni_3Al and $\text{Ni}_3\text{Al-T}$ phases with only little amount of unreacted Ni and Al.

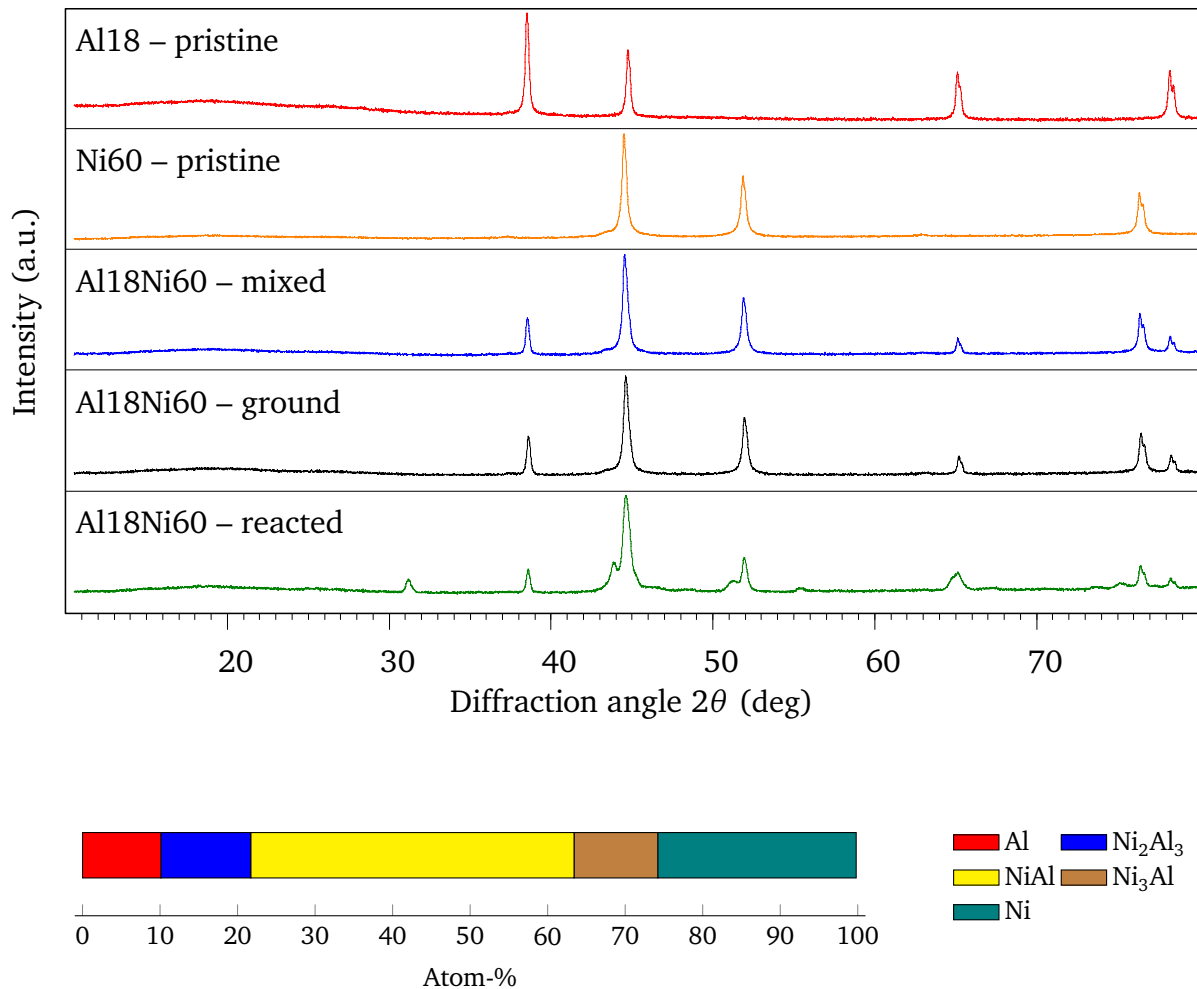


Figure 6.28: XRD Graph of pure Al18 and Ni60 particles as acquired, mixed, ground and reacted nanocomposites (from top to bottom.) The ground sample again shows no phase transformation, indicating no mechanical alloying. The reacted sample shows main peaks for the intermetallic NiAl phase, some secondary intermetallic phases and a large amount of about 26% unreacted Ni.

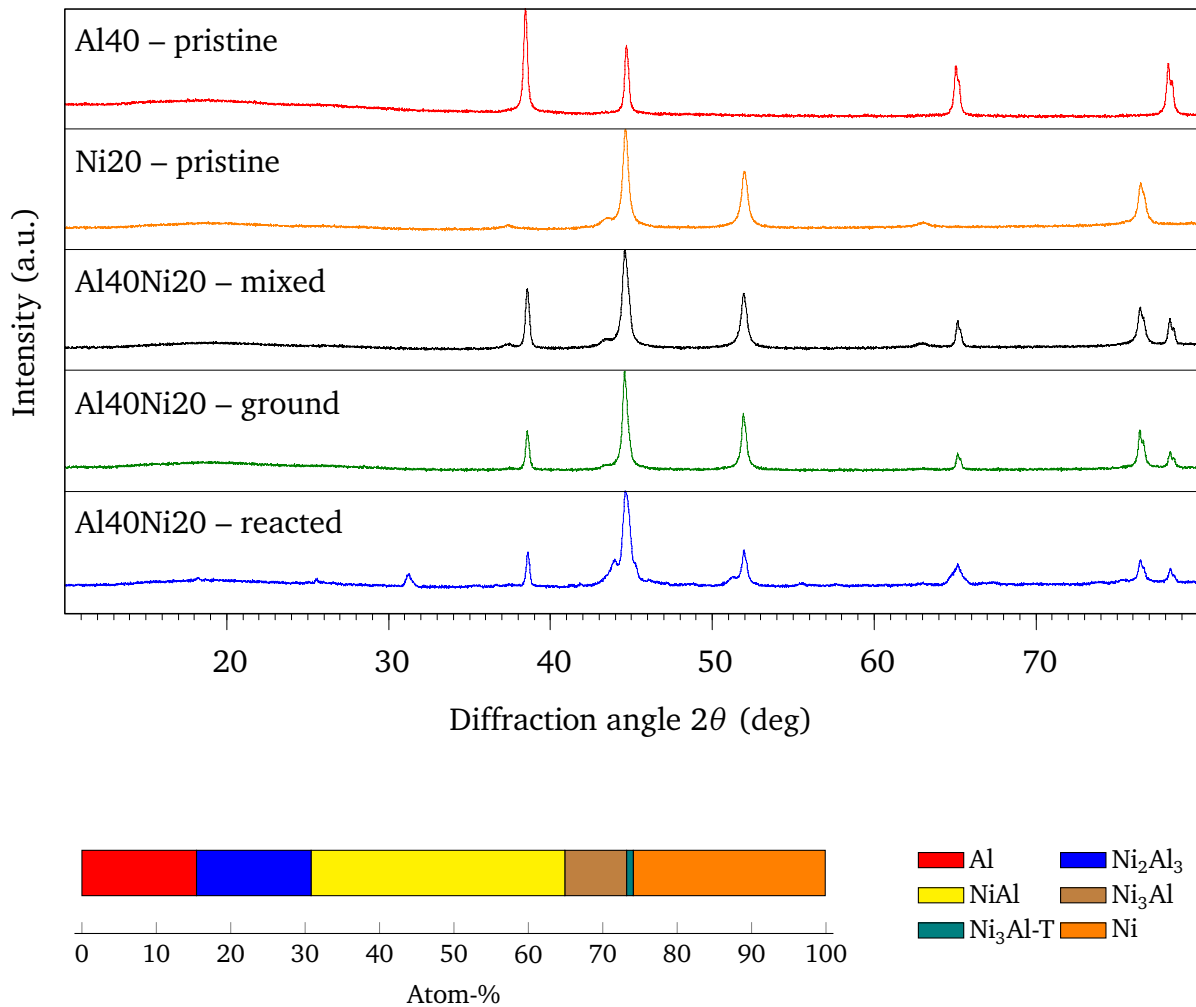


Figure 6.29: XRD Graph of pure Al40 and Ni20 particles as acquired, mixed, ground and reacted nanocomposites (from top to bottom.) As the previous samples, this one does not show any signs of mechanical alloying. The reacted sample shows the largest amounts of unreacted Ni and Al, adding up to about 41%. Reaction products are some secondary intermetallics along with the main phase being the aspired NiAl phase.

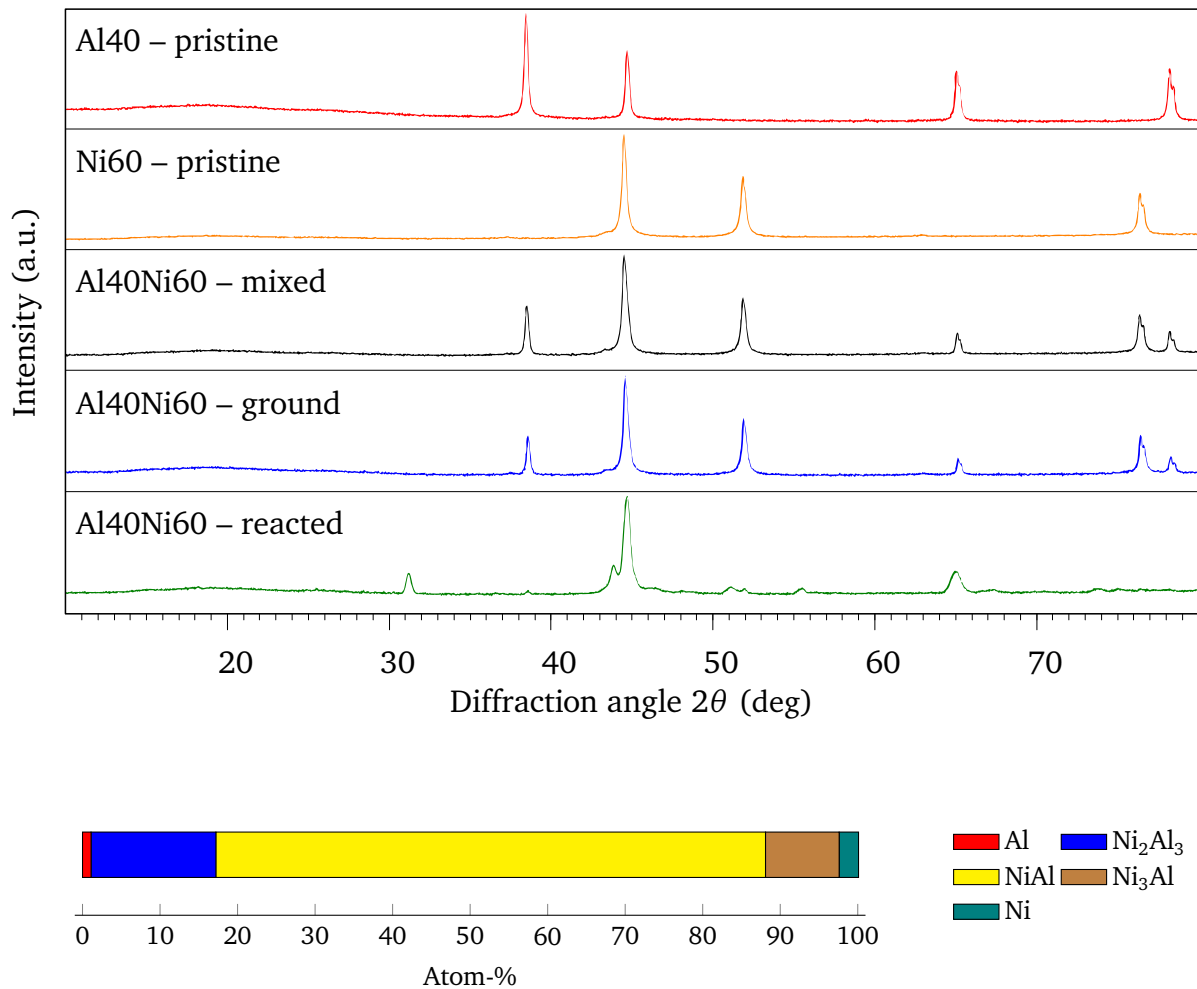


Figure 6.30: XRD Graph of pure Al40 and Ni60 particles as acquired, mixed, ground and reacted nanocomposites (from top to bottom.) Again, one can see that mixed and ground samples show the same peak pattern, indicating no phase transformation during grinding. The reacted sample shows by far the largest amount of reacted material. Out of the reaction products the main peaks for the intermetallic NiAl phase are dominating, representing about 71 % of the final sample.

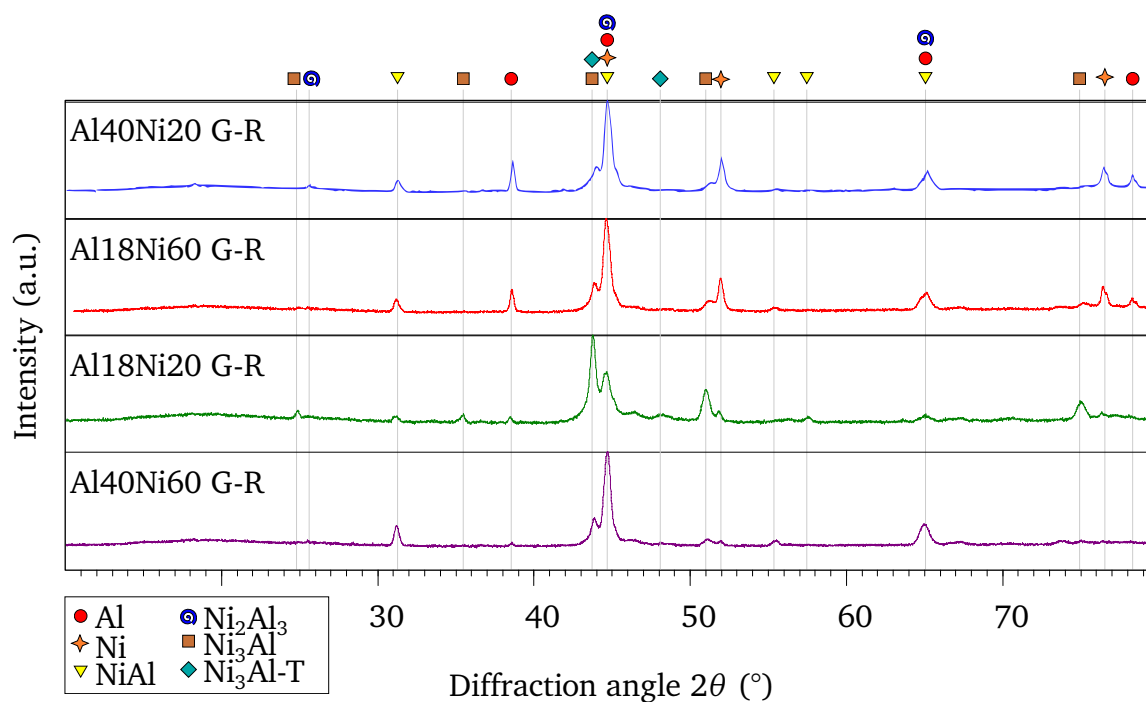


Figure 6.31: Qualitative juxtaposition of XRD graphs of the reaction products. All graphs show peaks assigned to both the pristine material and intermetallic phases.

Figure 6.31 shows a qualitative juxtaposition of the XRD measurements of the reacted samples. All graphs show peaks assigned to both the pristine material and intermetallic phases. As reaction products, Ni_2Al_3 , NiAl , Ni_3Al and $\text{Ni}_3\text{Al-T}$ (tetragonal) were observed. To quantitatively compare the composition of the reaction products figure 6.32 shows a line-up of the respective bar charts. The amount of reacted material varies greatly, as well as the amount per phase within the reaction products. The $\text{Al}_{40}\text{Ni}_{20}$ sample showed the lowest amount of reacted material (58%), whereas more than 96% of the $\text{Al}_{40}\text{Ni}_{60}$ sample reacted into intermetallic phases. The ratio of reacted material was 91.4% for the $\text{Al}_{18}\text{Ni}_{20}$ sample and 64.3% for $\text{Al}_{18}\text{Ni}_{60}$, respectively.

6.4.2 TEM

TEM analysis of reacted $\text{Al}_{18}\text{Ni}_{60}$ and $\text{Al}_{40}\text{Ni}_{20}$ samples was subsequently carried out. It was found that the specimen sustained a particulate structure after reaction.

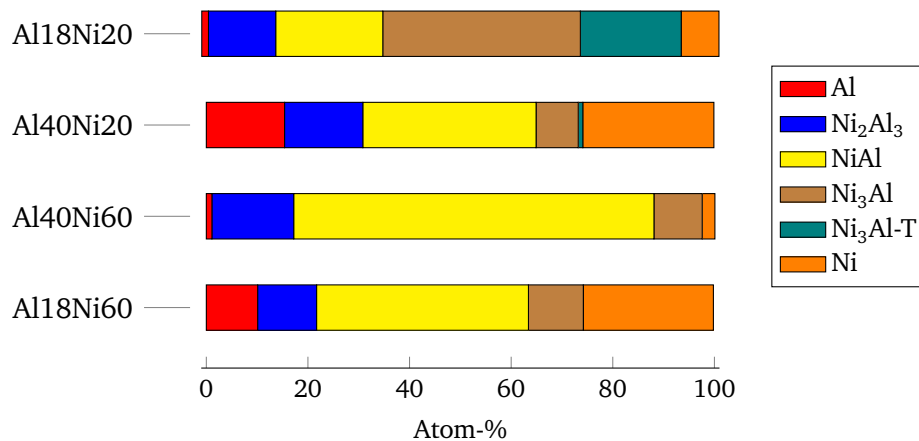


Figure 6.32: Quantitative comparison of chemical composition of reaction products. The Al40Ni60 sample showed the highest relative amount of intermetallic phases, accounting for more than 96%. The other extreme, Al40Ni20 exhibited only around 58% of intermetallic phases.

However, the particles did exhibit a change in morphology. Figure 6.33 show TEM graphs at varying magnifications for the Al18Ni60 sample. It is observed, that the particle surface dramatically increased in roughness.

In the first figure, the lowest magnification image (top left) reveals an increase in particle mean diameter to approximately 108 nm. The higher magnification figures show additional details which are of interest: In the top right figure one can see evidence for sintering of particles as the conjunction of two particles, forming an hourglass like shape, took place. The bottom left figure reveals a thin amorphous layer of about 1.2 nm, while the bottom right figure shows a detailed view of the strongly distorted surface a particle.

The measurements of the Al40Ni20 sample gave slightly different results. Again, TEM graphs at varying magnifications are shown for this sample in figure 6.34. In the low magnification frame (top left) it is observed that the mean particle diameter increased to about 103 nm as well. However, the close-up figures show a much rougher surface of the particles (top right and bottom left) and a thick amorphous layer on the bottom right panel with a thickness of more than 3 nm.

Using STEM and *in situ* EDX the graphs shown in figures 6.35 and 6.36 were measured, giving insight in chemical composition with spacial resolution. An almost constant but marginal oxygen contamination could be shown with slightly stronger

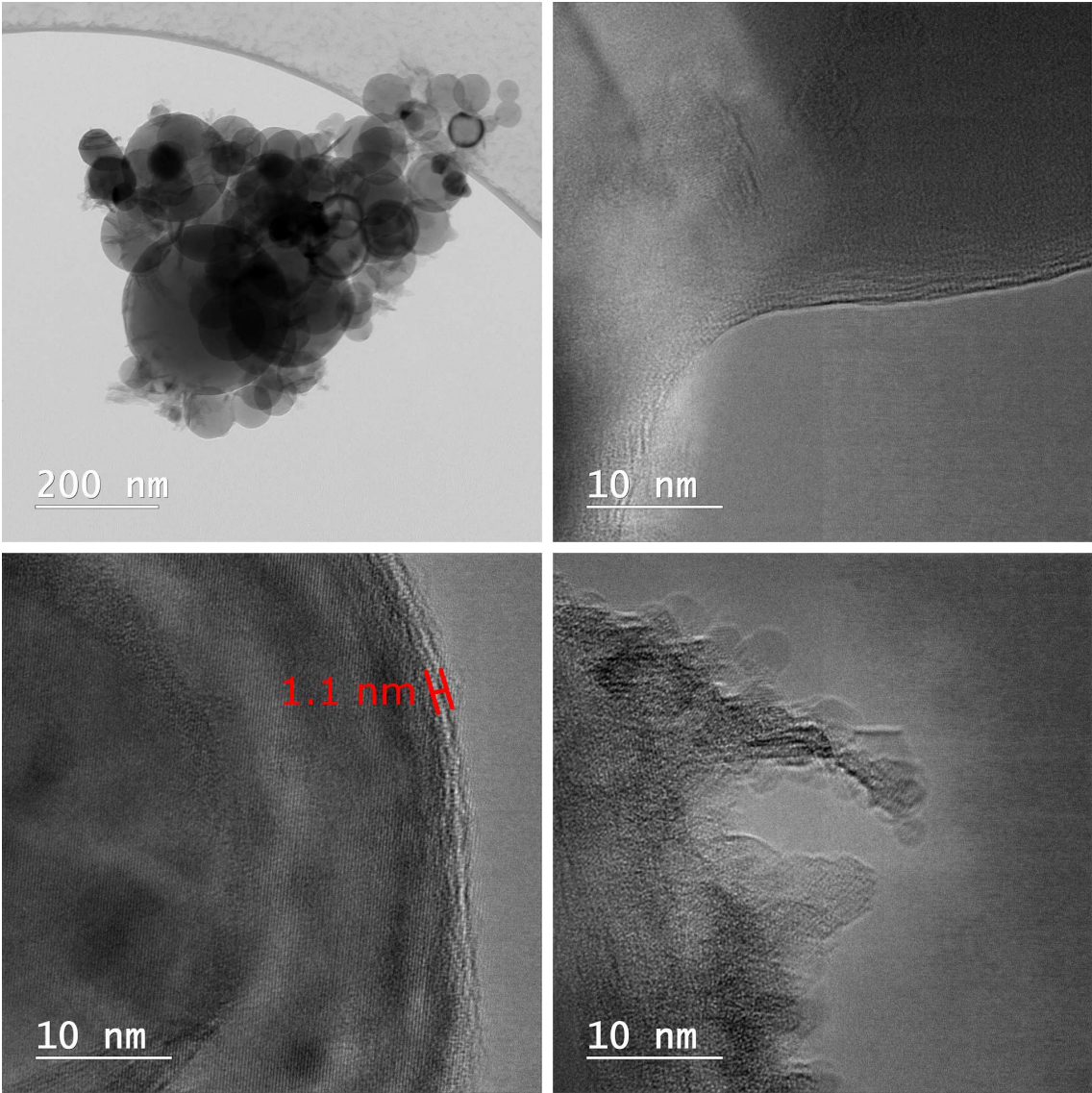


Figure 6.33: TEM images of a ground and reacted Al₁₈Ni₆₀ sample. Note that particles are still separate and in the nanoscale. Crystal structures are measurable throughout the particles with very thin amorphous layers at the particle surfaces.

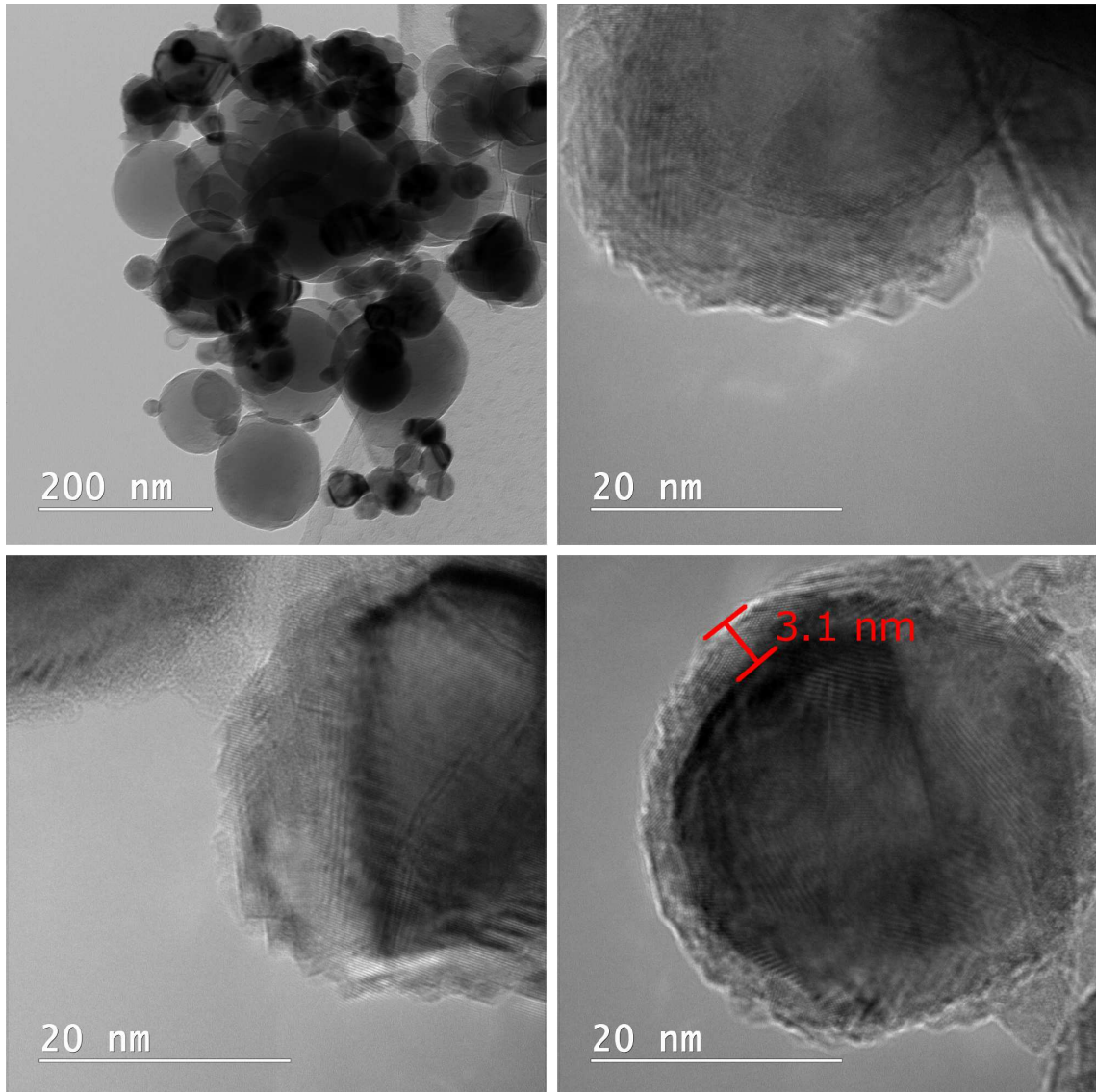


Figure 6.34: TEM images of a ground and reacted Al₄₀Ni₂₀ sample. Note that particles are still separate and in the nanoscale. Crystal structures are measurable throughout the particles with very thin amorphous layers at the particle surfaces.

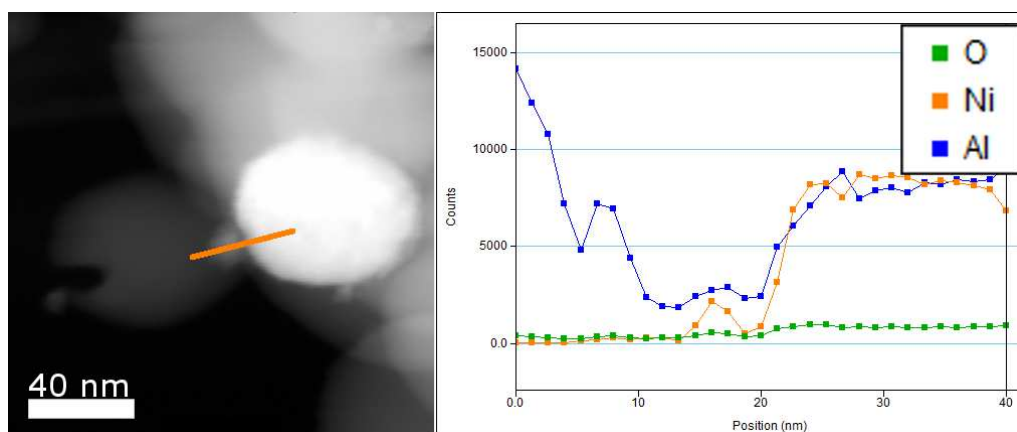


Figure 6.35: Z contrast enabled STEM graph and *in situ* EDX measurement of the reacted Al₁₈Ni₆₀ sample. Nickel particles appear white, aluminium particles grey, respectively. The EDX linescan was performed along the orange line, crossing Al and Ni rich regions and revealing very little amounts of O.

signals on Ni than on Al at the Al₁₈Ni₆₀ sample. Likewise, STEM and *in situ* EDX measurements of the Al₄₀Ni₂₀ sample revealed generally low amounts of O with a higher ratio of oxide at the Ni particle than the Al particle.

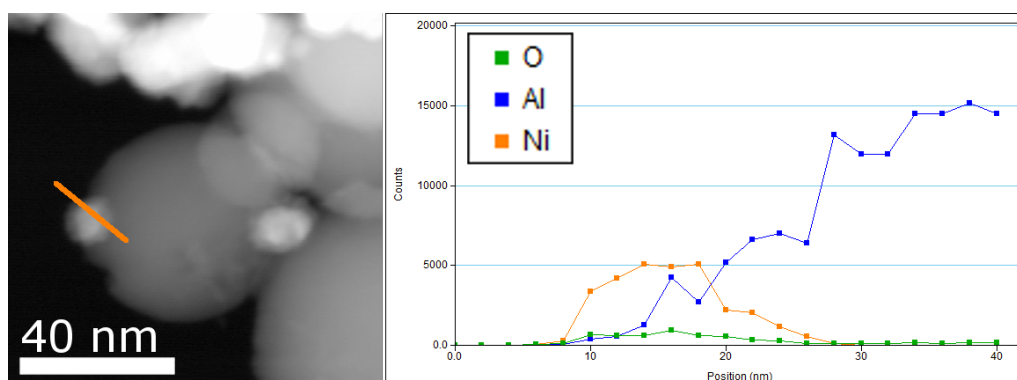


Figure 6.36: STEM and *in situ* EDX measurement of the reacted Al₄₀Ni₂₀ sample. The Z contrast in the STEM measurement renders Ni particles white and Al particles grey. The EDX linescan along the orange line in the STEM graph covered a small Ni and a larger Al particle and exhibited very small amounts of oxygen.

7 Discussion

Contents

| | |
|---|-----|
| 7.1 Initial Experiments | 99 |
| 7.2 Mechanically Activated Samples | 100 |
| 7.3 Oxygen Contamination | 105 |
| 7.4 Reactive Nanocomposite Bonding – Initial Trials | 108 |

Experimental results are discussed in the following chapter. Initial experiments with pure ultrasonic-mixed samples and different material systems will be addressed first, followed by the latest experiments with mechanically activated Ni–Al samples. Finally, the outcome of the printing investigations will be covered.

7.1 Initial Experiments

The first large set of experiments was conducted using only ultrasonic-agitated samples with all three different materials systems: Ni–Al, Ti–Al and Ni–Ti. Pure metal nanoparticles were dispersed in a solvent and mixed using ultrasound agitation in an ultrasonic bath. The mixtures were subsequently dispensed onto sample substrates and ignition experiments were performed using a high power welding laser. Impact of the laser pulse resulted in severe damage to the substrate and big parts of the sample’s materials were blown off the substrate due to the shock wave. These experiments were conducted under regular atmosphere, leading to combustion reactions in the samples where all the components were oxidized. EDX measurements confirmed the assumption of oxidation during combustion. SEM analysis revealed

7 Discussion

the micro structure of the samples after laser impact, showing large pieces of debris of the substrate material and the sample all over the place. Performing comparative experiments under inert atmosphere showed no self-propagating reactions. Sintering of the particles was observed in the laser exposed regions for the low power laser experiments. Figure 7.1 shows SEM graphs of an Al40Ni60 sample which was subject to low power laser treatment under inert atmosphere. Figure 7.2 shows the respective interferometric topography measurement of this sample. Along the trajectory of the laser spot densification can be measured, providing further evidence for sintering in the laser focus.

It was concluded that the reactivity of the materials mixture had to be significantly increased to enable self-propagating reactions under inert atmosphere.

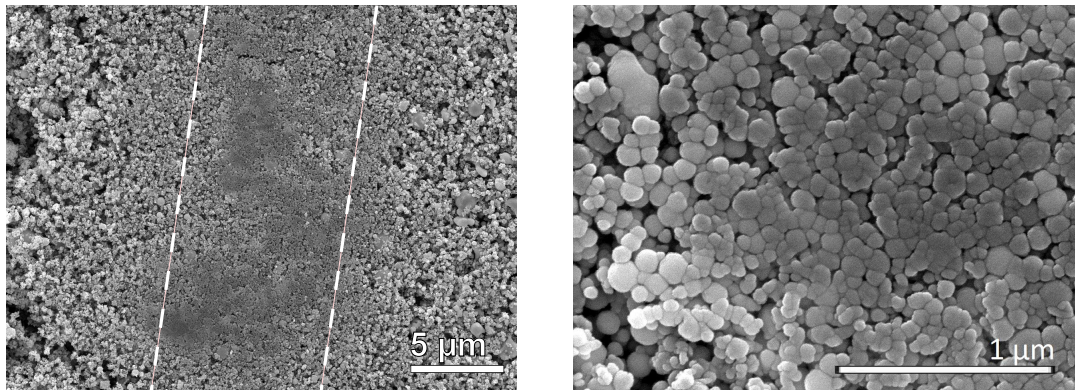


Figure 7.1: SEM graphs of an Al40Ni60 sample, showing sintered regions in the laser treated areas. Left figure: The dashed lines indicate the path the laser focal spot was moved. In between the lines one can observe sintered particles, whereas the surrounding material remained unaffected. Right figure: higher magnification of the same sample in the laser treated region.

7.2 Mechanically Activated Samples

Using a porcelain mortar, the Ni and Al nanoparticles were mechanically activated. As discussed in the literature (refer to chapter 3) mechanical activation has a number of effects on the sample:

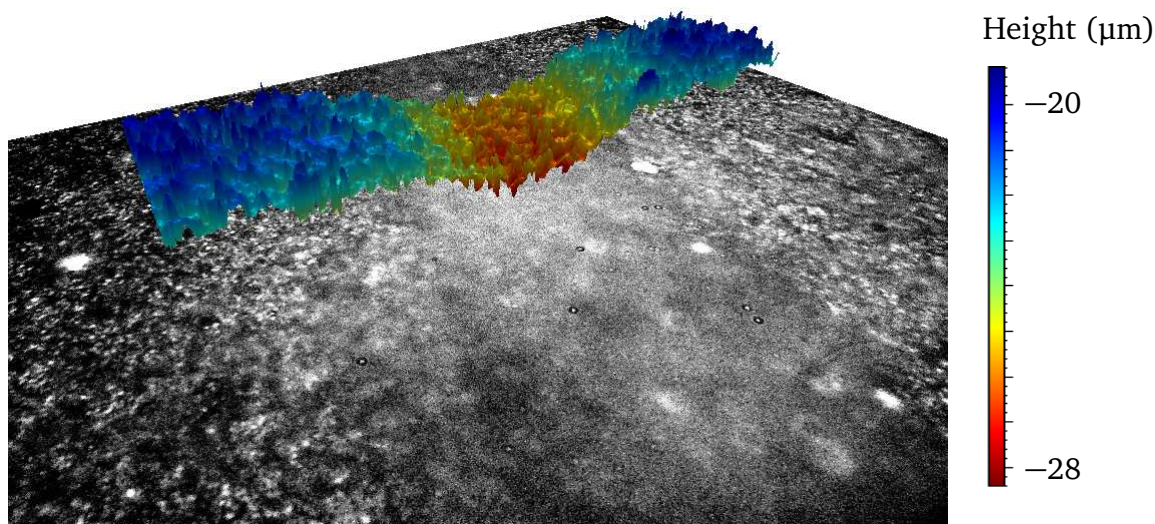


Figure 7.2: White light interferometric measurement of laser sintered trench. The trajectory of the scanned laser produced a trench in the sample due to densification during sintering with a difference in thickness of about 6 μm .

1. Enhanced active surface area: During grinding the particle mixture gets homogenized, increasing the ratio of particles which are in contact with particles of the reaction partners instead of the same material. This effect is fortified by the breaking up of particle agglomerates that were formed prior to mixing. Furthermore, the overall porosity gets reduced, bringing the particles in closer contact to each other.
2. Increased defect density and number of grain boundaries: Pressure and shear forces applied during grinding raise the number of defects in the crystal structure of the particles and thus increases the amount of grain boundaries. Any kind of reaction is more likely to start from a crystal lattice defect.
3. Destabilization of oxide layers: Potentially present oxide layers which would hinder the reactivity of the sample can be compromised by grinding. Since the oxides of Al and Ni feature high brittleness cracks occur during grinding, enabling the diffusion of elemental Al and Ni atoms to the reaction surface.

It is not determinable which of these effects has the highest influence on the reactivity of the sample. The mechanically activated nanoparticle mixtures showed dramatically increased reactivity. Self-propagating reactions could be ignited under inert atmosphere using low-energy laser pulses. Four different sample batches

7 Discussion

of Ni–Al nanoparticle mixtures were produced by manual grinding based on the particle sizes that were acquired. Stoichiometry of all samples was 1:1, equaling Ni 69 wt% and Al 31 wt%. Resulting in the different particle sizes a ratio of number of particles was assessed in the range $10^{-1} n_{\text{Al}}/n_{\text{Ni}}$ to $10^2 n_{\text{Al}}/n_{\text{Ni}}$. Reaction speeds were measured using high-speed imaging of the reaction front passing a predefined track length. Reaction front propagation velocities ranged from 10.5 mm/s to 24 mm/s at room temperature. A correlation was found between number of parti-

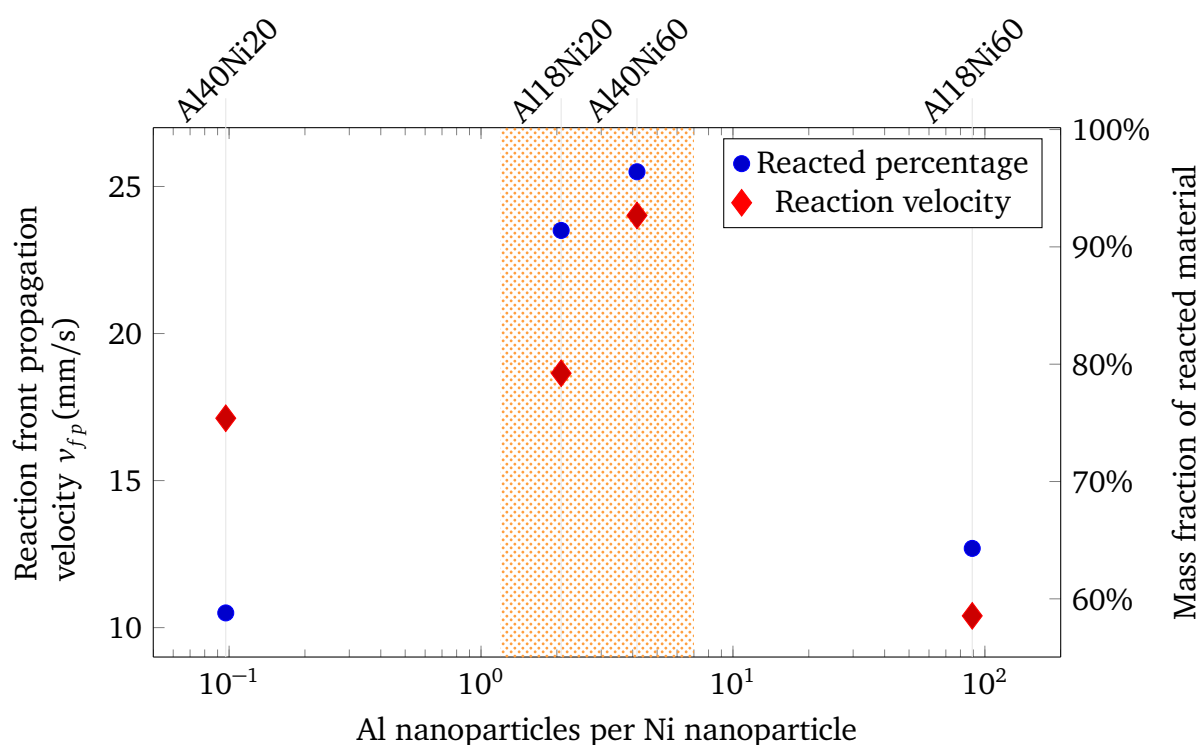


Figure 7.3: The graph shows the reaction front propagation velocity as a function of the number of particles ratio of aluminium and nickel in an equiatomic mixture on the left axis, marked with diamonds. The right axis shows the mass fraction of reacted material of the sample, marked with circles. Experiments conducted at room temperature.

cles ratio and reaction front propagation velocity. Highest velocities were measured for the two sample batches which have a number of particle ratio in the range 1 to 10. In good agreement with the high reactivity of these two samples, XRD analysis of the reaction products also showed a very low amount of unreacted material (<10%), while the fraction of unreacted material of the two samples with a particle ratio of $10^{-1} n_{\text{Al}}/n_{\text{Ni}}$ and $10^2 n_{\text{Al}}/n_{\text{Ni}}$ was well above 40%. Figure 7.3 shows the

correlation of fraction of reacted material and reaction front propagation velocity over number of particles ratio.

Applying the theoretical approach from section 3.1 [110, 111], one can derive the reaction temperature from the measured reaction front propagation velocity in respect to the theoretical reaction temperature without heat loss:

$$T_R = \frac{E_a T_C}{E_a - 2RT_C \ln\left(\frac{v_R}{v_C}\right)} \quad (7.1)$$

Where T_R is the reaction temperature, E_a activation energy, T_C the adiabatic combustion temperature, v_R the reaction velocity and R the universal gas constant. Figure 7.4 shows a plot of the respective reaction temperatures for the four measured reaction velocities. This derivation is based on the assumption that a reaction propagating at the theoretical speed of 0.2 m/s would reach the adiabatic reaction temperature of 1911 K.

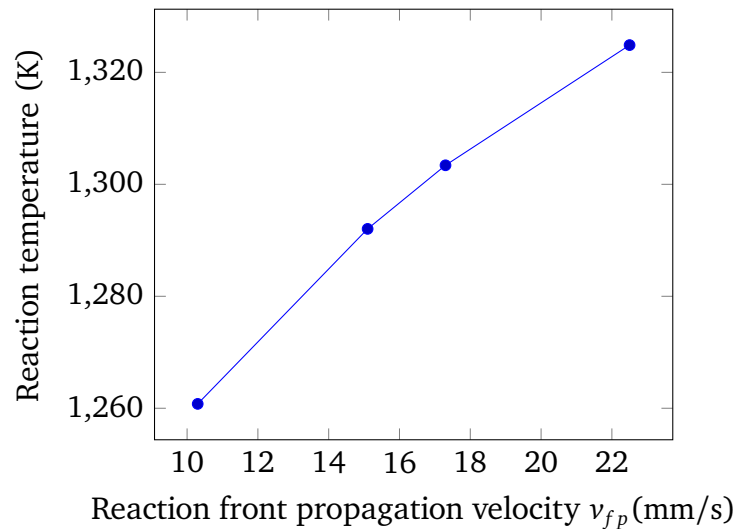


Figure 7.4: Reaction temperature as derived from the measured reaction front propagation velocity.

SEM analysis of reacted samples revealed differing morphologies, depending on the sample configuration. Figure 7.5 shows a series of SEM graphs of an Al18Ni60 sample. The two top figures show the unreacted state, while the two on the figures depict the reacted sample. In the unreacted state the single particles are clearly

distinguishable. The reacted sample shows an almost homogeneous surface with low roughness and only very few single particles on top of this surface.

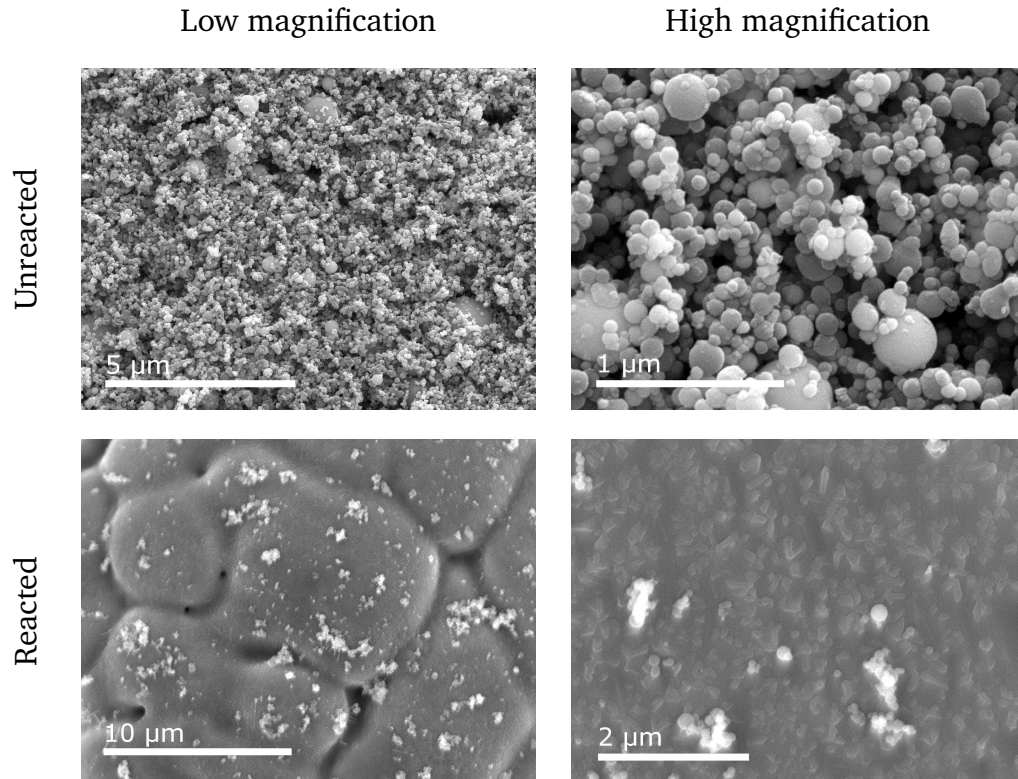


Figure 7.5: SEM graphs of unreacted and fully reacted Al18Ni60 samples. Top images show the ground, yet unreacted sample at different magnifications. Bottom figures show the reaction product at low and high magnification.

Figure 7.6 shows SEM graphs of an Al40Ni20 sample, again the two top images show the unreacted state, whereas the two bottom figures show the reaction product. For this sample the reacted state also shows very low roughness in high magnification but at lower magnification (figure at the bottom left) one can see that the morphology is very inhomogeneous. This was attributed to the incomplete combustion of the sample as indicated by XRD measurement. The smooth reaction product as depicted in this figure presumably relates to an area within the sample where the intended NiAl phase was established.

At other areas, as shown in figure 7.7 one can observe nanoworms that formed on the surface. It is assumed that these structures are the result of secondary reactions forming the compound Ni_2Al_3 , which could take place in an anisotropic way, simi-

lar to the oxidation of Al nanoparticles as described by Koga and Hirasawa [152].

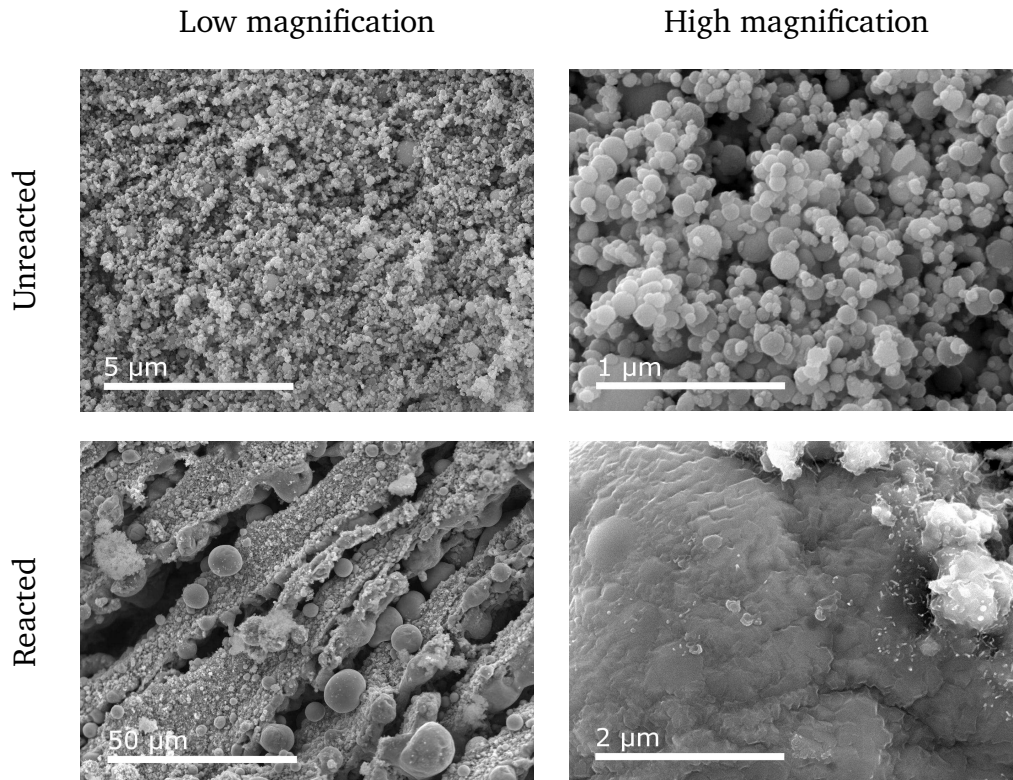


Figure 7.6: SEM graphs of unreacted and fully reacted Al₄₀Ni₂₀ samples. Top images show the ground, yet unreacted sample at different magnifications. The bottom line figures show the reaction product at low and high magnification.

7.3 Oxygen Contamination

The reactive nature of the employed metallic nanoparticles is not exclusively directed towards each other, but all used materials have a high oxygen affinity. A typical Al particle that was not stored in oxygen free environment has a passivation layer in the order of 4 nm [153]. For a nanoparticle with a diameter of only 18 nm that would make a mass percentage of 53 % passivated, thus non reactive, material. It is apparent that such a high amount of passivated material reduces the reactiv-

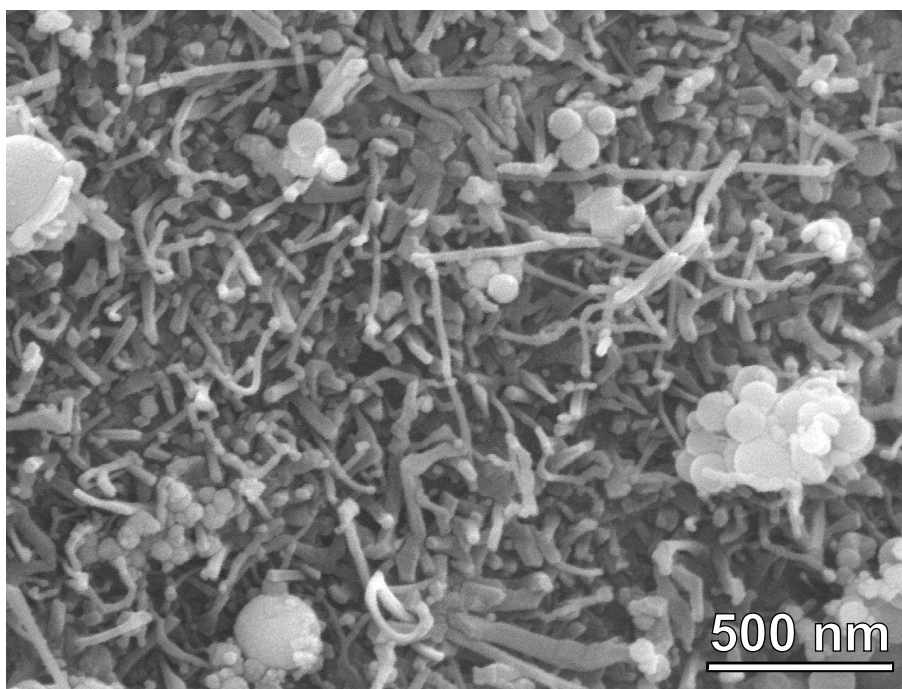


Figure 7.7: SEM graph of an anisotropically reacted Al₄₀Ni₂₀ sample. The nanoworms with thicknesses well below 100 nm are suspected to have grown from single Ni particles at the interface with molten Al. Scale bar is 500 nm.

ity of the RNC mixture and constrains a self-propagating reaction. Therefore, the materials were stored and handled in an inert atmosphere (Ar 5.0) inside a glove box. It was found that during sonication of the samples oxygen contamination occurred, despite the use of vials which were filled within the glove box. It is assumed that some oxygen was dissolved in the solvent. Additionally the vials might have not been properly sealed, allowing oxygen to diffuse into the sample during ultrasonication. Figure 7.8 shows comparative XRD measurements of a sonicated and a ground Al₁₈Ni₂₀ sample. The sonicated sample shows significant amounts of oxides, while the ground sample remained purely Al and Ni.

In addition, some experiments were conducted under regular atmosphere, resulting in heavily oxidized samples as well. Figure 7.9 shows a representative SEM graph and the respective EDX mappings for Ni, Al and O of an Al₁₈Ni₆₀ sample, which was treated with the high power laser under regular atmosphere. It is apparent that the intensities for Al and O correlate, indicating a high amount of Al has oxidized. The Ni particles remained mainly elemental in these experiments.

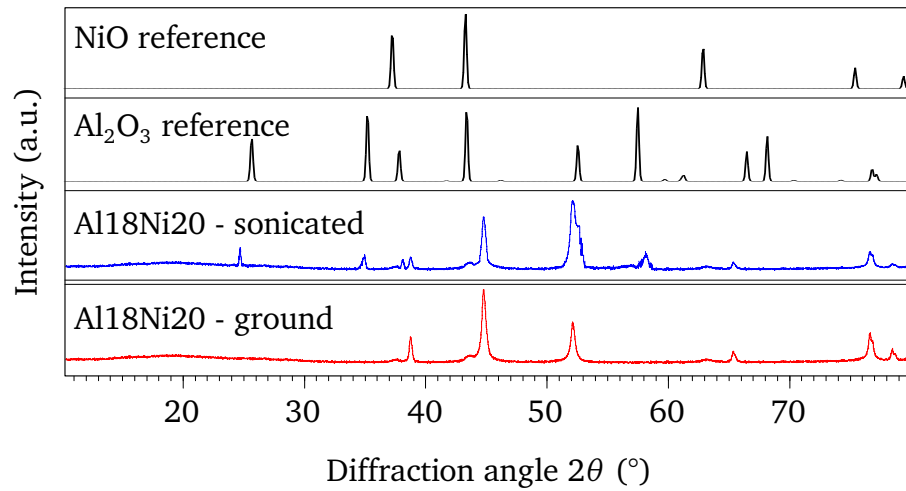


Figure 7.8: Comparative XRD measurement of sonicated vs. ground Al18Ni20 sample. The sonicated sample shows significant oxygen contamination, while the ground sample remained purely Al and Ni. Reference data for Al₂O₃ from [154], for NiO from [155].

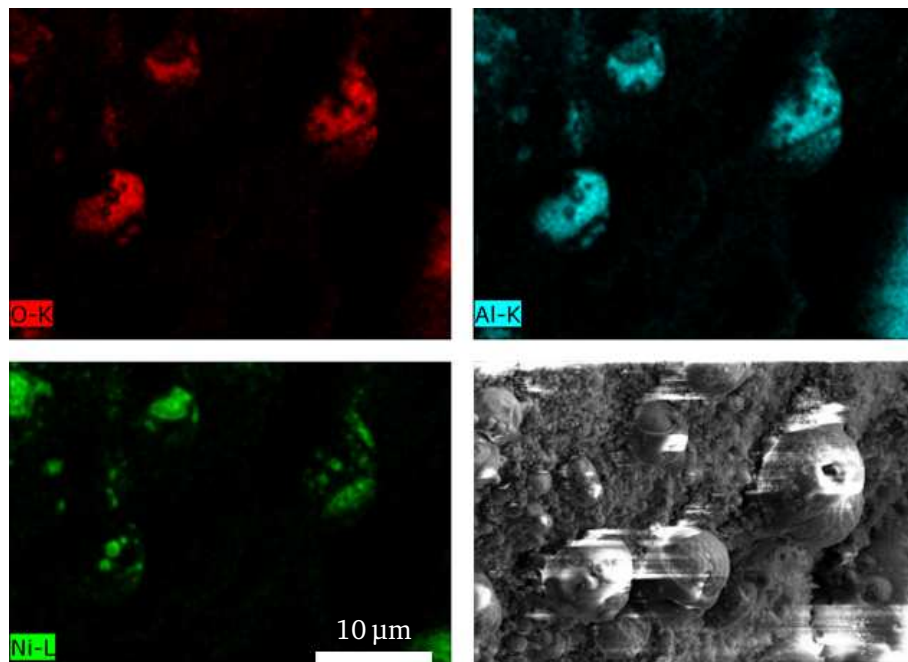


Figure 7.9: SEM graph (bottom right) of an Al18Ni60 sample with respective EDX mappings for Oxygen (top left), Aluminium (top right) and Nickel (bottom left). The appearance of O and Al at the same locations indicates oxidation of Al, whereas Ni remained predominantly elemental.

7.4 Reactive Nanocomposite Bonding – Initial Trials

As for the non-mechanically activated samples no self-sustaining reactions were observed, it is concluded that the reaction enthalpy was below the expected level according to the theoretical considerations, as described in chapter 5, although the estimated critical layer thickness was exceeded in all experiments. Preliminary bonding experiments were therefore conducted only with the manually ground samples. Standard microscope slides, made of fused silica with a thickness of about 1 mm were used as both, top and bottom substrates. It was found that bonding could not be achieved with the produced RNC mixtures, moreover, application of a second substrate quenched any SHS reaction. Despite the significant rise in reactivity of the ground samples over the non-ground mixtures, it was not sufficient for the proposed use.

This lack of reactivity is assumed to be caused by impurity of the samples, heat transfer into the substrates, high porosity of the reactive layer, inhomogeneous material distribution within the sample and non controlled wetting of the surfaces at the substrate-RNC-interface:

1. Low heat transfer within the reactive material layer compared to the heat transfer in the surrounding substrates. Loose nanoparticles feature a very low specific density, only using high compression forces a dense package can be achieved. Within a porous structure as the reactive layers (as can be seen from the SEM measurements), the heat transfer is slowed down, since only a fraction can be transferred via direct thermal conductivity. The amount which could be conducted via radiation gets more likely transferred into the fully dense substrates. Figure 7.10 illustrates the problem occurring if the RNC

layer's density is too low.

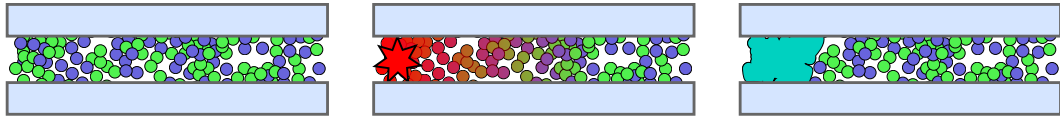


Figure 7.10: High RNC layer porosity can constrain self-propagating reactions due to poor heat transfer within the reactive layer. The schematic illustration shows a sequence from left to right of a porous RNC layer between two glass slides. Left: initial state, centre: ignition on one side, right: only small areas adjacent to the ignition spot reacted.

2. Distribution of materials within the RNC layer partly inhomogeneous leading to localized non-optimal stoichiometry. Mixing of the nanoparticles was conducted using a mortar and ultrasonic agitation. As EDX measurements have shown, an inhomogeneous distribution of the materials across the samples could still be observed to some extent. In these regions with non-optimal ratio of reactants two types of reactions can occur:

- a) A secondary reaction takes place, consuming all present reactive material but leading to less heat dissipated by the reaction.
- b) The primary reaction takes place, consuming only the stoichiometric amount of material, leading to unreacted particles within the reaction zone. These passive particles get heated by the reaction, only lowering the available reaction energy instead of contributing to the available heat of reaction.

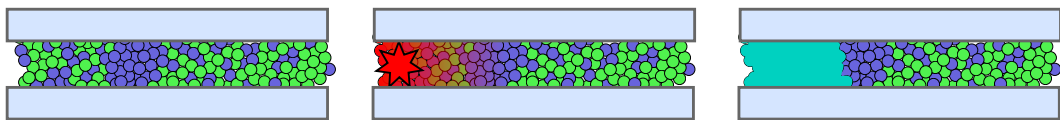


Figure 7.11: Inhomogeneous RNC layers cause regions of non stoichiometric materials ratio. In these regions loss of energy can lead to extinction of the reaction. The schematic illustration shows a sequence from left to right of an inhomogeneous RNC layer between two glass slides. Left: initial state, centre: ignition on one side, right: only small areas adjacent to the ignition spot reacted.

A schematic drawing of the problem is depicted in figure 7.11. The inhomogeneity of the RNC layer leads to an excess of one material (blue coloured) in the centre of the workpiece, making it impossible for the reaction front to

pass that area.

3. High impact of potential passivation layers on the reactivity of the particles due their nanoscale size. As aforementioned (section 7.3), even slight contamination of oxygen has significant impact on the reactivity of the material and can constrain a self-sustaining reaction. Though the particles were stored in an inert atmosphere and experiments were conducted within the same, XRD and EDX measurements have showed occasional oxygen contamination. Figure 7.12 shows a schematic drawing of an RNC layer containing a large amount of passivated particles (yellow circumference).

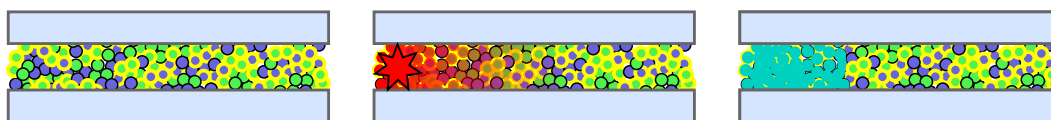


Figure 7.12: Thick passivation layers on the reactive particles reduce the reactivity significantly, causing poor performance of the reaction.

Based on findings of the literature review and the experiments conducted in this work it is concluded that the proposed bonding concept should be realizable with the employed material systems under modified conditions, however, this would have been beyond the scope of the present thesis.

An outlook on how to implement RNC bonding is given in the following chapter.

8 Summary and Outlook

Contents

| | |
|---|------------|
| 8.1 Summary | 111 |
| 8.2 Outlook | 115 |
| 8.2.1 Closing Remarks and Recommended Actions | 118 |

The work conducted within this project is summarized in the following, pointing out where the executed tasks diverted from the planned and what results were achieved. In the following outlook, recommended actions to improve performance of the introduced systems and realize the proposed concept are given. A brief look at most recent results by other groups in the scientific community emphasizes the timeliness of this work and which concepts have proven most promising so far.

8.1 Summary

The concept development for a novel bonding process based on printable reactive nanocomposites was described. An extensive literature review covering current state of the art bonding technologies has shown the potential for such process, the feasibility of the concept and the demand. Furthermore, an FEM simulation was conducted to affirm the problem of high temperature bonding processes when dealing with heterogeneous material systems. The main points evaluated in the literature studies are:

- Usage of MOEMS devices is steadily increasing.

- Many MOEMS devices perform better under low pressure (i.e. vacuum) conditions
- Low in-package pressures require hermetic sealing.
- Optical access is essential, inducing the need for transparent top substrates.
- Borosilicate glasses which performs well as cap material can be bonded to silicon, which in turn is the most common base substrate for micro devices, with conventional bonding processes. These techniques, however, involve high process temperatures.
- Combining materials with large differences in their coefficients of thermal expansion, such as Si and glass, results in large intrinsic stress after bonding at high temperatures, as confirmed in the FEM analysis.

To solve this problem, a novel concept for bonding of heterogeneous material systems applied in MOEMS devices was developed in this work. The concept comprises the usage of a reactive nanocomposite based on Ni and Al nanoparticles. This composite can undergo a self-sustaining high temperature synthesis (SHS) reaction, forming intermetallic NiAl and reaching high temperatures of up to 1500 K within short time frames of only a few ms.

The usage of a deposition technology like inkjet printing for application of the reactive nanocomposite at the desired location, i.e. the bonding frame on the bottom substrate, is stipulated. To enable printing, the RNC particles have to be present as colloidal dispersion in a solvent. Subsequently to printing, the solvent should be removed by evaporation and the second bonding partner applied. Using pulsed laser irradiation the SHS reaction can be initiated, starting the high temperature reaction front moving along the bond frame. Heat dissipated by the reaction should suffice to join the bonding partners while not imposing significant rise of temperature in the surrounding regions of the device.

Following the design of that concept, further literature studies were put into execution, investigating the state of the art in SHS reactions and printing technologies. A brief overview of history of SHS research and applications was given and reactive material systems were introduced. Promising combinations for this project were identified, namely Ni-Al, Ti-Al and Ni-Ti. Theory of reaction was studied and models of reaction kinetics of comparable systems were investigated.

Four printing techniques were described in detail and evaluated towards their feasibility for usage in this project. Inkjet printing was identified as the prospective method for deposition of the RNC layer in a production process, whereas direct writing was chosen as deposition method for the first experimental stage of the project.

Based on the findings of this second literature review phase the reactive nanocomposite bonding concept was further detailed and a plan for experimental validation of the concept was set up.

- The reactive material system to be used was Ni and Al nanoparticles with diameters below 100 nm.
- Non-oxidizing solvents like hexane were to be used as dispersion medium.
- Initial trials should incorporate material deposition by manual pipetting, eventually followed by inkjet printing at a later stage of the project.
- A reactivity study of different composites of the reactive components should be carried out, investigating the influence of particle size, chemical composition, sample preparation techniques, ignition methods, ignition threshold, substrate material and ambient conditions.
- Using a heat dissipation model, a minimum thickness of the reactive material was calculated.
- A prototype bond should be realised by the end of the project to demonstrate the feasibility of the concept.

Target of this project was, to realize a functioning prototype for the reactive nanocomposite bonding process. Some progress was made on the path towards the goal, but ultimately, it proved elusive. The experimental progress over the project was more gradual than initially anticipated, resulting in severe falling behind the schedule and in the end failure to realize a prototype.

Experimental tasks concluded within this work incorporate:

- All materials employed in the project were subject to XRD and SEM analysis, pre- and post-reaction.
- Select samples were further more subject to HR-TEM analysis.

- Select samples were additionally characterized via differential thermal analysis.
- Five different means of ignition were evaluated (high power welding laser, low power diode laser, Nanofoil, glowing hot wire and electric spark), out of which the low power laser setup was most successful.
- A respective experimental set-up was designed, comprising the optical set-up for the laser diode and trigger as well as the sample holders, which allowed positioning and pressure application.
- Additionally, a heat chuck setup was designed to facilitate study of ambient temperature over reactivity of samples. The heat chuck was built in house and operated using a PID controller and respective software via PC.
- In good agreement with theory and literature, the reactivity of the samples increased with increasing ambient temperature.
- Size proportions of the reactant particles were found to have a major impact on reactivity, reaction propagation velocity, reaction temperature and reaction product purity.
- Reaction experiments were recorded to obtain reaction propagation velocity using a regular camera and a high speed camera in some experiments.

The results drawn from these experiments clearly point into the direction of further investigating the RNC bonding concept. It was shown how the reactivity depends greatly on the size relationship between the reactants. It was also found, that any oxygen contamination significantly reduces the reactivity and thus the overall performance of the system.

In contrast to reactivity experiments without a top substrate, all bonding trials with a top substrate failed. Possible explanations for the failure of these experiments are:

- Excessive heat dissipation into top substrate. Since no change was made towards the material system between reactivity studies and bonding experiments, this seems the most likely reason. Both substrates act as heat sinks and additionally, due to compression of the powder an increased thermal conductivity within the RNC layer has to be assumed. As shown in the modelling

section of chapter 3.1, heat transfer from the reaction zone into the substrates and the reactive layer can both lead to reaction quenching.

- General issues with the RNC layer like oxygen contamination, inhomogeneous reactant distribution and high porosity. All of these aspects do have negative impact on the reactivity and can cause the extinction of a self-propagating reaction. However, since no change to the material system was made between successful reactivity trials and the failing bonding experiments it is less likely that these points were the actual reasons for constraining the reaction.

8.2 Outlook

Experiments have validated the promising approach, as high reactivity of the mixtures was obtained using only very cheap and simple processing methods and maintaining the reactivity after suspension and dispersion of the mixtures. Steps required to further develop this concept are:

- Development of heterogeneous composite reactive nanoparticles to enhance reactivity
- Stabilization of dispersions and enabling of deposition via printing technologies
- Establishment of a full bonding process

The reactivity of the RNC layer is a key property, as described. Very recent studies by Shuck and co-workers have shown, that High Energy Ball Milling (HEBM) of nanoparticles under controlled atmosphere can be used to produce heterogeneous composite particles with lamellar phases [156]. Composite reactive nanoparticles feature much higher reactivity than mixtures of monophase reactive nanoparticles due to increased reactive surface area, reduced influence of contaminations like oxides and higher volatility of atoms due to high density of defects and large amount of grain boundaries. A linear regression of activation energy over surface area to volume ratio of composite nanoparticles was newly reported [157]. Figure 8.1

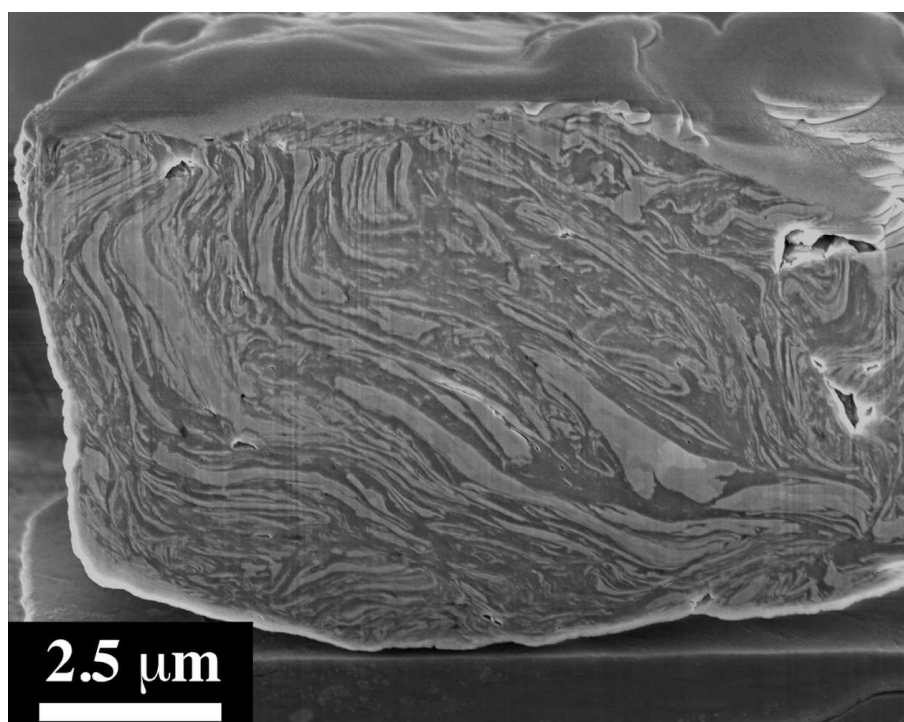


Figure 8.1: FIB cut cross sectional SEM graph of a ball milled Ni-Al binary microparticle. The bright phase is Ni, the dark phase represents Al [157].

shows a FIB cut cross sectional view of a ball milled binary phase micro particle. Activation energy is a linear factor of the critical layer thickness, thus a reduced amount of reactive material should be sufficient to maintain a reaction. Figure 8.2 shows a schematic comparison of reactive nanocomposite and reactive nanocomposite nanoparticles (RNCNP) as proposed in this work for future RNC bonding applications. The composite particles are in the same order of magnitude in size as the single-phase particles but comprise multiple phases of each reactant. Note that contrarily the size of the single phases of Ni and Al in figure 8.1 are on the nano-scale, while the full particle is tens of microns in size. Furthermore, HEBM is a feasible method for dispersing particles in solvents, when combined with such. It is proposed that employing of a high energy ball mill would significantly increase the probability of success of the novel bonding concept.

Another approach worth investigating is the production of RNCNP by ball milling or grinding of reactive multilayer foils. This will be challenging, as initiation of reaction has to be prevented during milling (e.g. by cooling and usage of inert

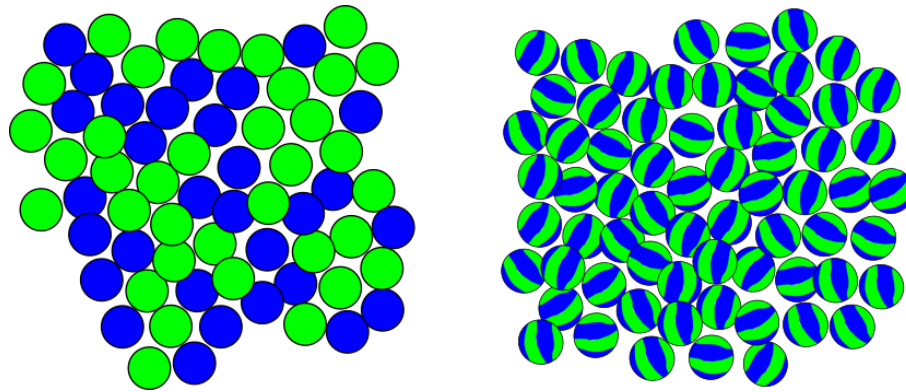


Figure 8.2: Schematic comparison of RNC (left) and the envisioned RNCNP (right). The particles in either drawing are the same size, whereas the RNC particles are uniphase and each RNCNP contains alternating phases of the reactants.

atmosphere). The prospective results however, seem compelling as powders for deposition via printing could be achieved with well defined binary phases within each particle.

A study by Gunduz *et al.* shows that other research groups have shown interest in this topic and evaluated bonding with reactive Ni-Al micropowders [158]. Coarse powders of the reactants were ball milled at low intensity to form a loose mixture of the materials. Bonding of two surfaces of bulk Al parts was shown but not quantitatively characterized. Furthermore, the bonding of Si wafers was tested with promising yet not convincing results, as temporarily achieved bonds failed upon detailed examination. No follow up studies further investigating this approach are known.

Recent studies on iRMS have shifted their focus from the Ni-Al system towards other material systems like Pd-Al, Pd-Sn, Pd-Zn and Ti-Si [59, 65, 67]. Despite the high price of palladium, further exploration of the RNC concept using these material systems might in analogy be beneficial as well.

8.2.1 Closing Remarks and Recommended Actions

It is apparent that the concept of reactive bonding with high energy ball milled powders has great potential and application by means of printing would render a very attractive technology. This way produced composite reactive nanoparticles should be subject to thorough investigations upon dispersion stabilization while maintaining the particles' high reactivity. This way a highly reactive *ink* should be prepared, enabling printing of the reactive bonding material in any arbitrary pattern. While it is quite challenging to tune the rheological properties of an ink for a specific printing method like ink-jet printing, requirements for dispensing are not very high and should be matched easily once a stabilized dispersion is created. Furthermore, potential impact on adhesion of the surface roughness of bonding partners should be studied.

The production of large quantities of reactive bonding ink could finally lead to a commercialization of the process. After a reliable bonding process based on printed reactive nanocomposite bonding layers was shown, the number of advantages over conventional bonding techniques should speak for it self:

- Deposition of bonding layer in arbitrary patterns by printing – no mask based processes necessary.
- Low thermal impact on the system allows usage for temperature sensitive parts.
- Heterogeneous material combinations with large differences in their CTE can be bonded as the whole system is not heated when the bond is established.
- Digital printing processes allow fast change in patterns to adopt for design changes or prototyping.
- Independence from oxygen enables bonding under arbitrary atmospheres, even under vacuum conditions, greatly improving the performance of many MOEMS devices.
- Contact-less ignition via laser pulse enables bonding under transparent parts without mechanical contact.

Appendix A: Reactants Size Distributions

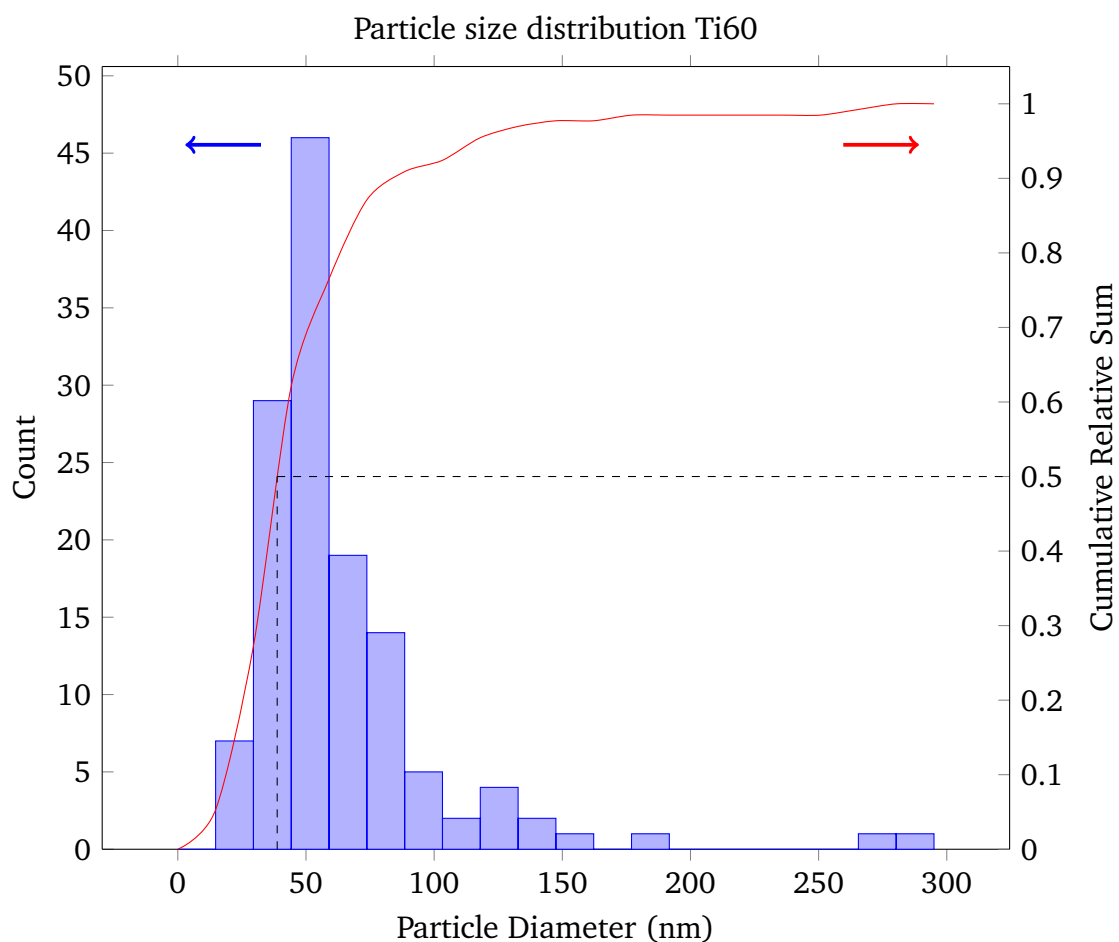


Figure A.1: Particle size distribution of the Ti60 sample. Average particle diameter is 67 nm, with 50% of the particles having a diameter below 62 nm.

A Reactants Size Distributions

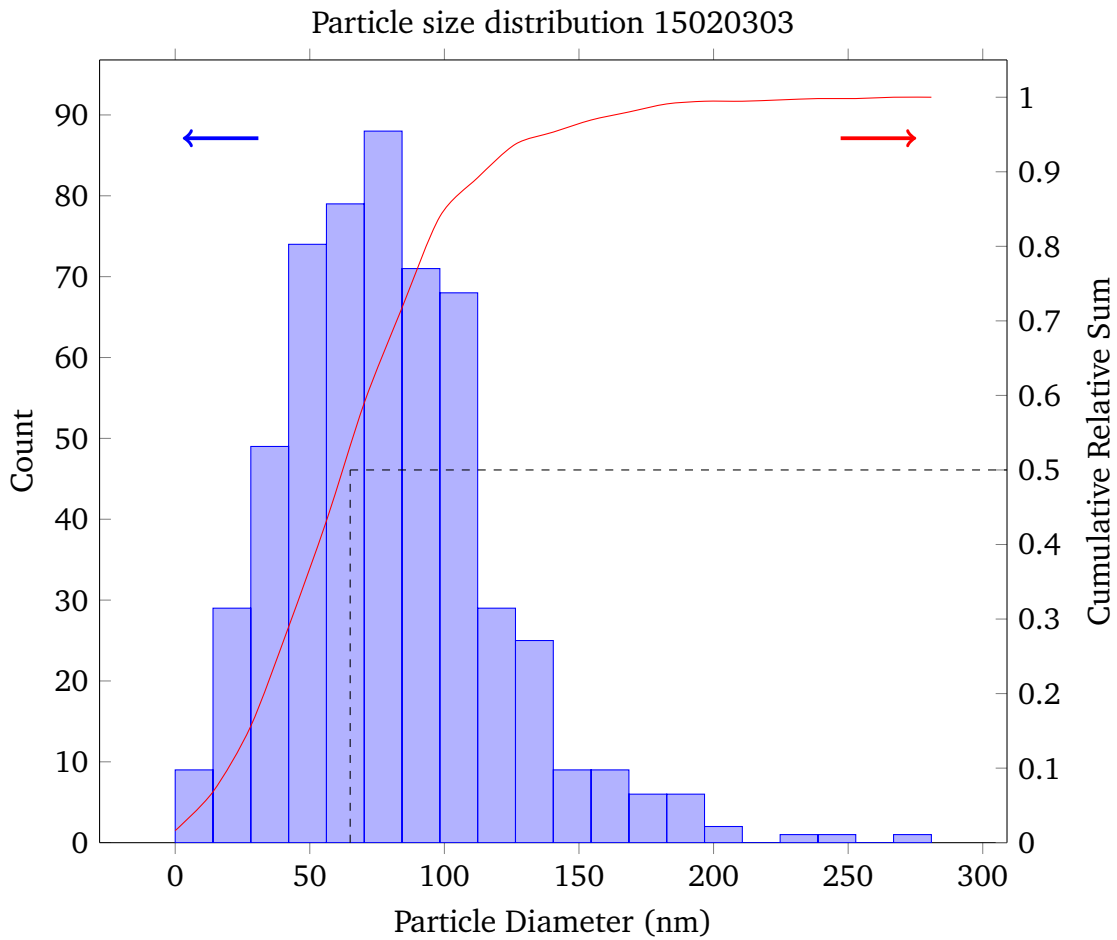


Figure A.2: Particle size distribution of sample no. 27, Al₄₀Ni₆₀. Average particle diameter is 80 nm, with 50% of the particles having a diameter below 65 nm.

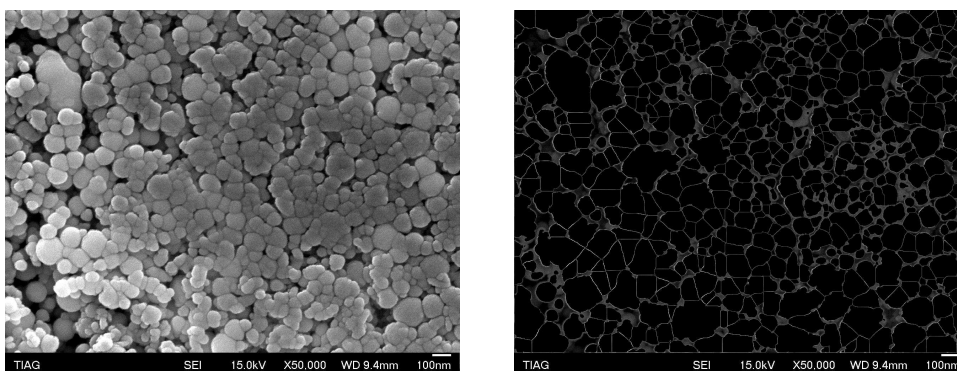


Figure A.3: SEM graph and particle count overlay of sample no. 27.

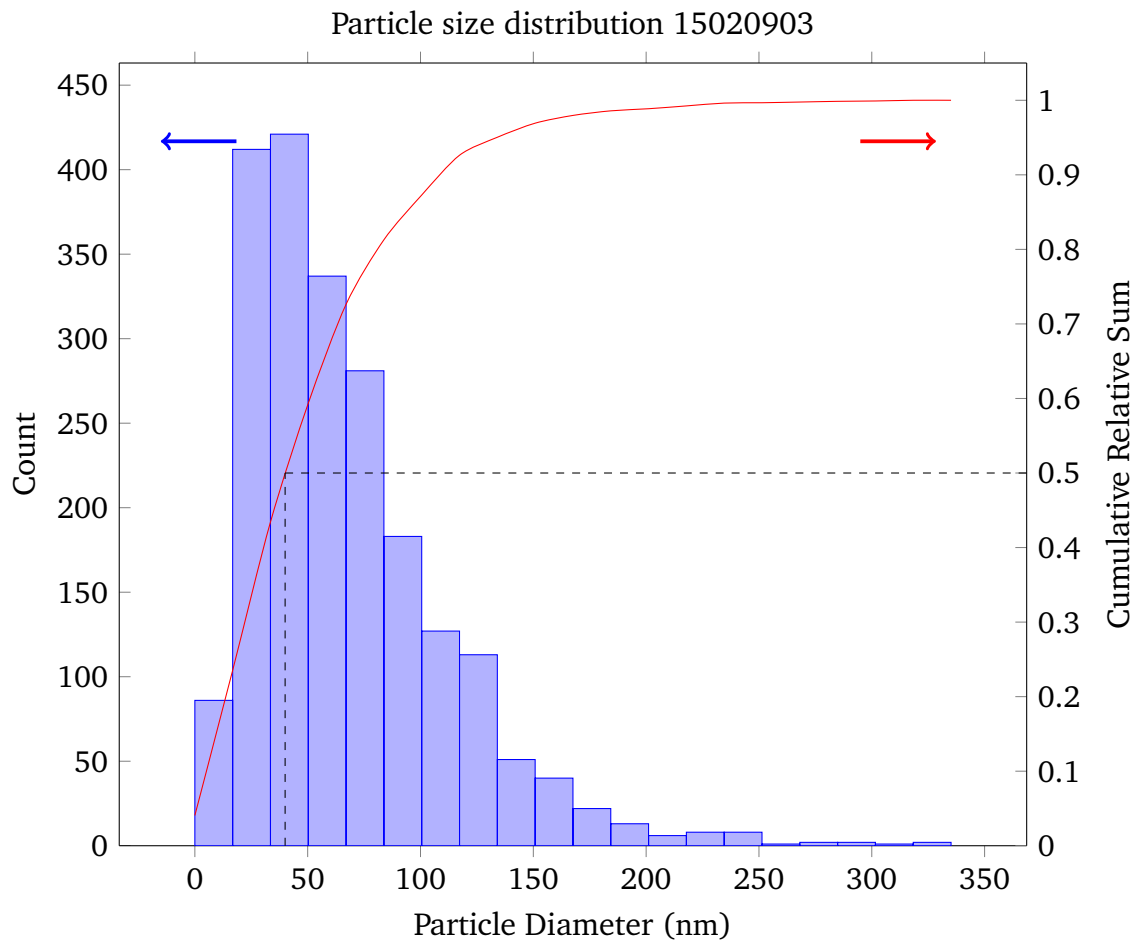


Figure A.4: Particle size distribution of sample no. 33, Al₄₀Ti₆₀. Average particle diameter is 67 nm, with 50 % of the particles having a diameter below 40 nm.

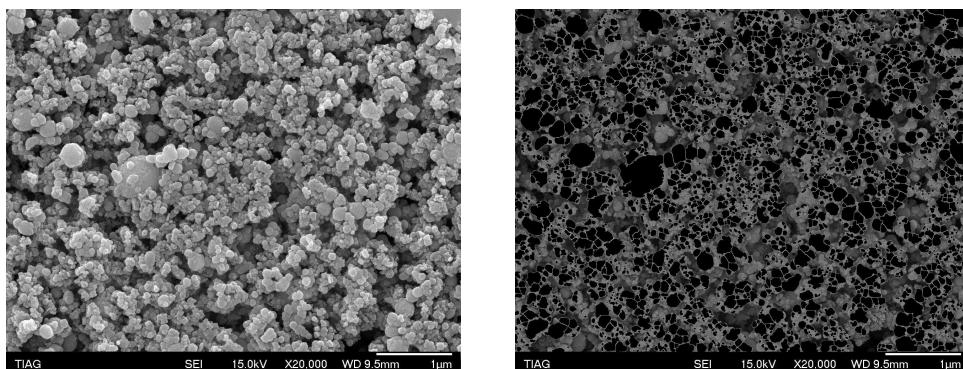


Figure A.5: SEM graph and particle count overlay of sample no. 33.

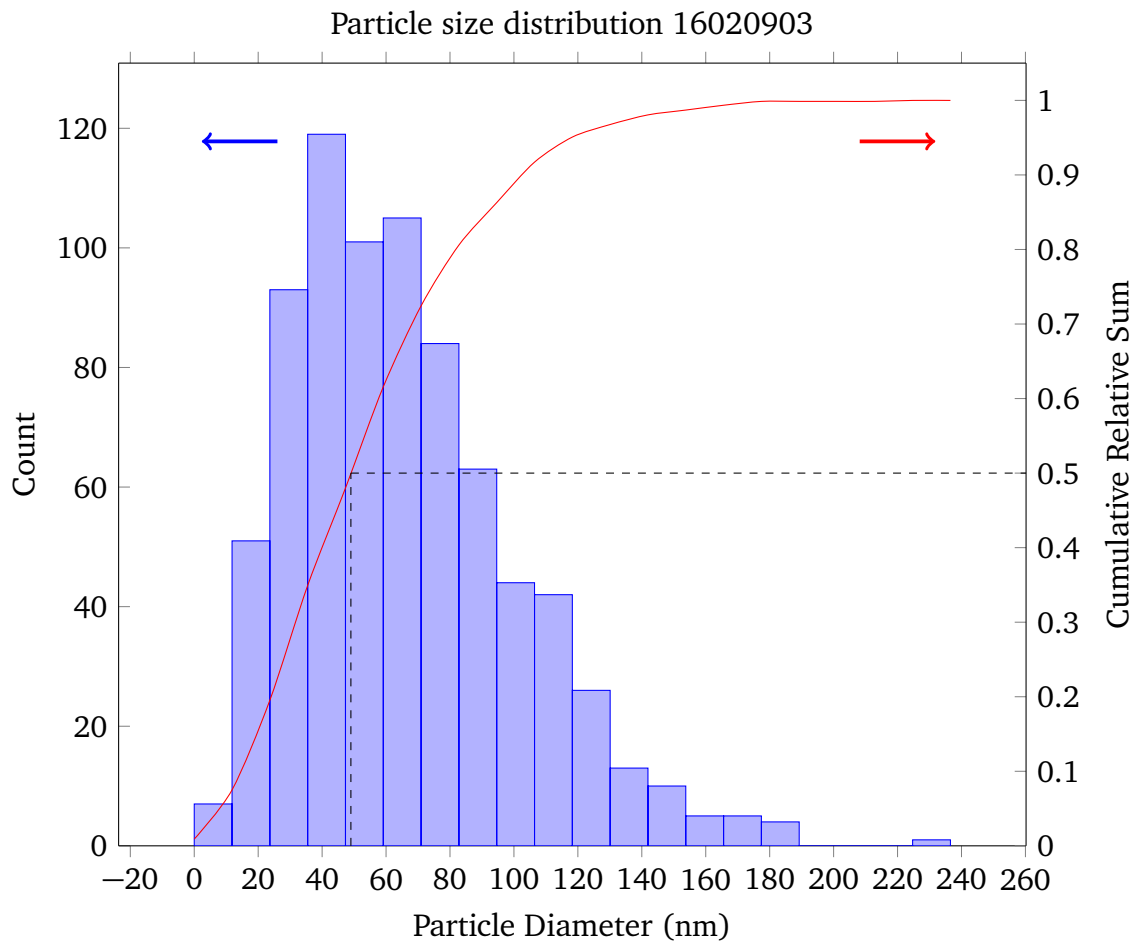


Figure A.6: Particle size distribution of the no. 40, Al40Ni20. Average particle diameter is 67 nm, with 50% of the particles having a diameter below 49 nm.

Appendix B: Material Data

Table B.1: Thermodynamic properties of selected Boride-, Carbide-, Silicide- and Aluminide-SHS reactions [109]

| Reaction mechanism | ΔH_f (kJ/mol) | T_{Ad} (K) | State of reaction products at temperature |
|---|-----------------------|--------------|---|
| Hf+C → HfC | -105 | 4102 | Solid and liquid |
| Zr+C → ZrC | -104 | 3689 | Solid and liquid |
| Hf+2B → HfB ₂ | -110 | 3642 | Solid and liquid |
| Ti+C → TiC | -93 | 3339 | Solid and liquid |
| Zr+2B → ZrB ₂ | -108 | 3272 | Solid and liquid |
| Ti+2B → TiB ₂ | -108 | 3192 | Solid and liquid |
| Ta+C → TaC | -72 | 3103 | Solid |
| Pt+Al → PtAl | -100 | 3072 | Liquid |
| Nb+C → NbC | -69 | 2970 | Solid |
| Ta+2B → TaB ₂ | -63 | 2672 | Solid |
| Pd+Al → PdAl | -92 | 2652 | Liquid |
| V+2B → VB ₂ | -68 | 2569 | Solid |
| Nb+2B → NbB ₂ | -72 | 2554 | Solid |
| 5Zr+3Si → Zr ₅ Si ₃ | -72 | 2522 | Solid and liquid |
| 5Hf+3Si → Hf ₅ Si ₃ | -70 | 2472 | Solid and liquid |
| 5Ti+3Si → Ti ₅ Si ₃ | -72 | 2392 | Solid and liquid |
| 5Nb+3Si → Nb ₅ Si ₃ | -57 | 2332 | Solid |
| V+C → VC | -50 | 2229 | Solid |
| Co+Al → CoAl | -60 | 1911 | Solid and liquid |
| Ni+Al → NiAl | -59 | 1911 | Solid and liquid |
| 5Ta+3Si → Ta ₅ Si ₃ | -42 | 1819 | Solid |
| 5V+3Si → V ₅ Si ₃ | -58 | 1791 | Solid |
| Zr+Al → ZrAl | -45 | 1752 | Solid and liquid |
| 2Ni+Si → Ni ₂ Si | -48 | 1578 | Solid and liquid |
| Ti+Al → TiAl | -36 | 1499 | Solid |

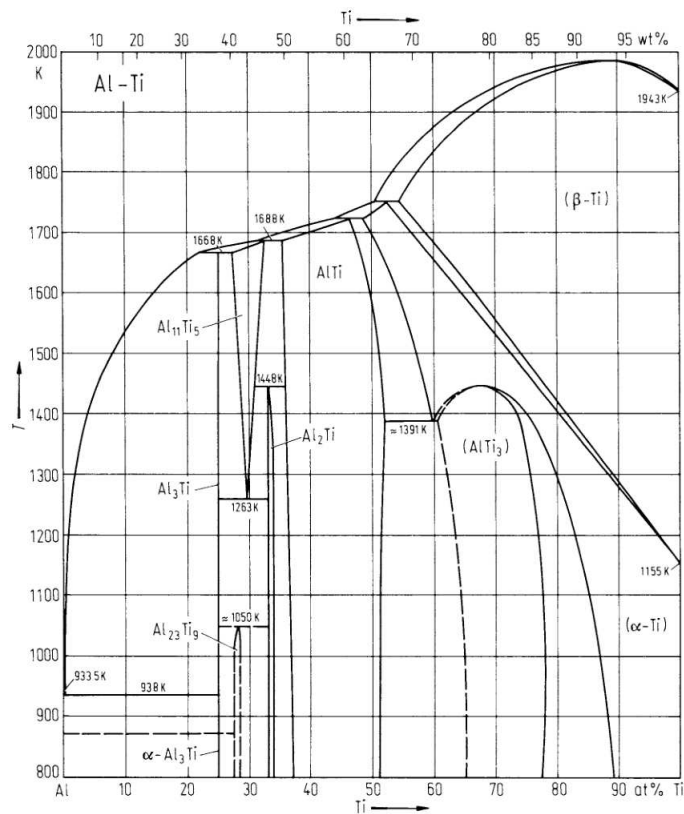


Figure B.1: Phase diagram of the binary Al-Ti system [159]. The melting point of the primary AlTi phase is around 1700 K.

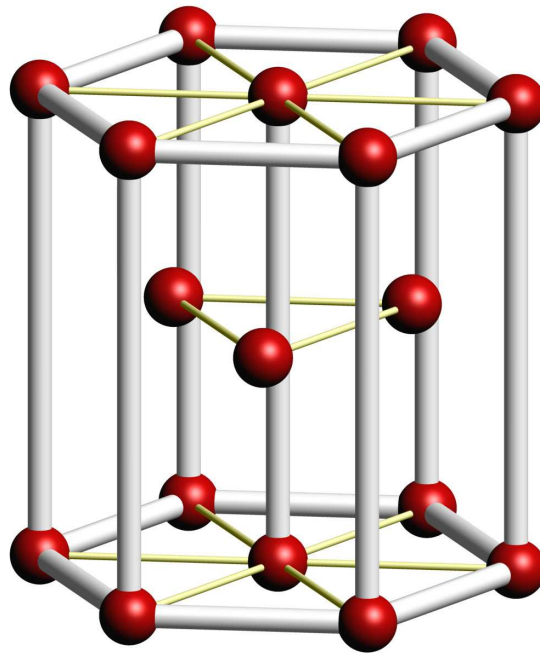


Figure B.2: Crystal structure of elemental Titanium, hexagonal close packed (HCP).

Crystal structure of elemental Titanium is hexagonal close packed (HCP).

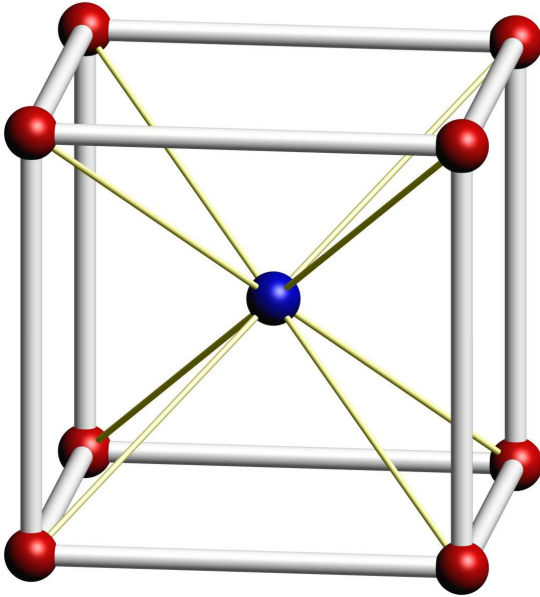


Figure B.3: Crystal structure of intermetallic NiTi

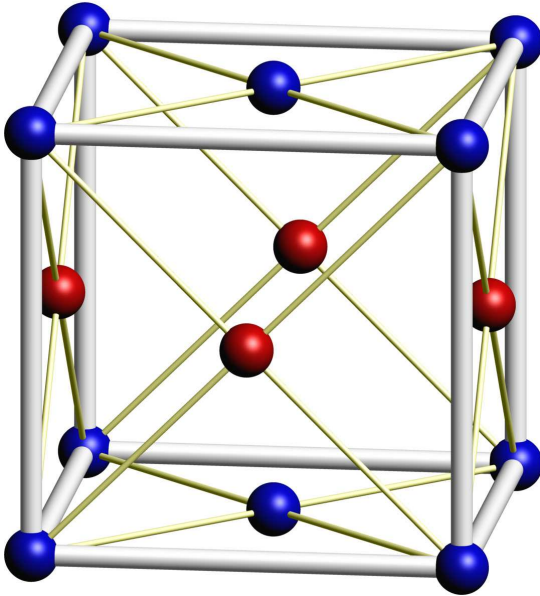


Figure B.4: Crystal structure of intermetallic TiAl

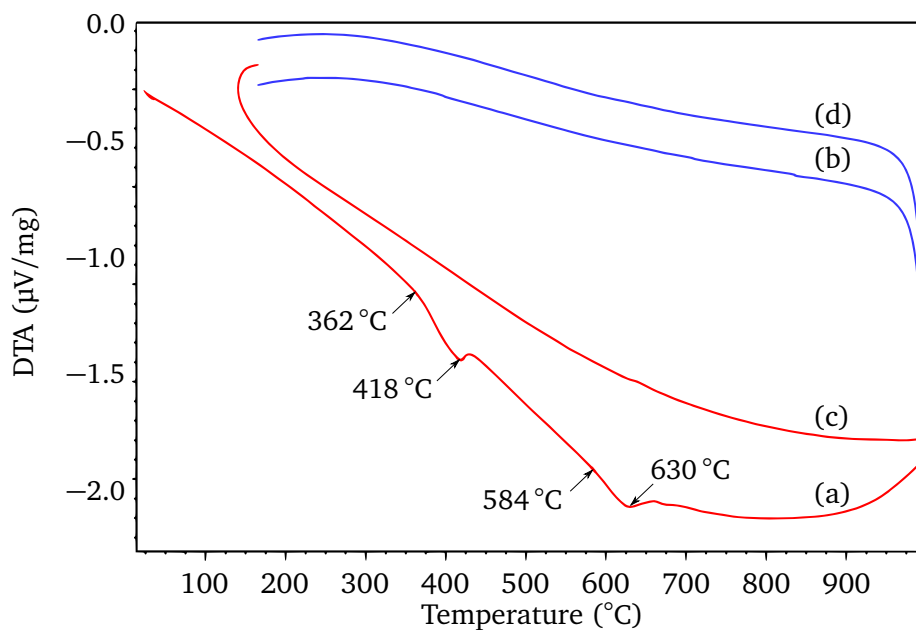


Figure B.5: Differential thermal analysis graph of Ti–Al sample. Chronological order of measurements: a) heating, b) cooling, c) heating, d) cooling. Temperature range 100 °C to 1000 °C, heating and cooling rate 10 K/min.

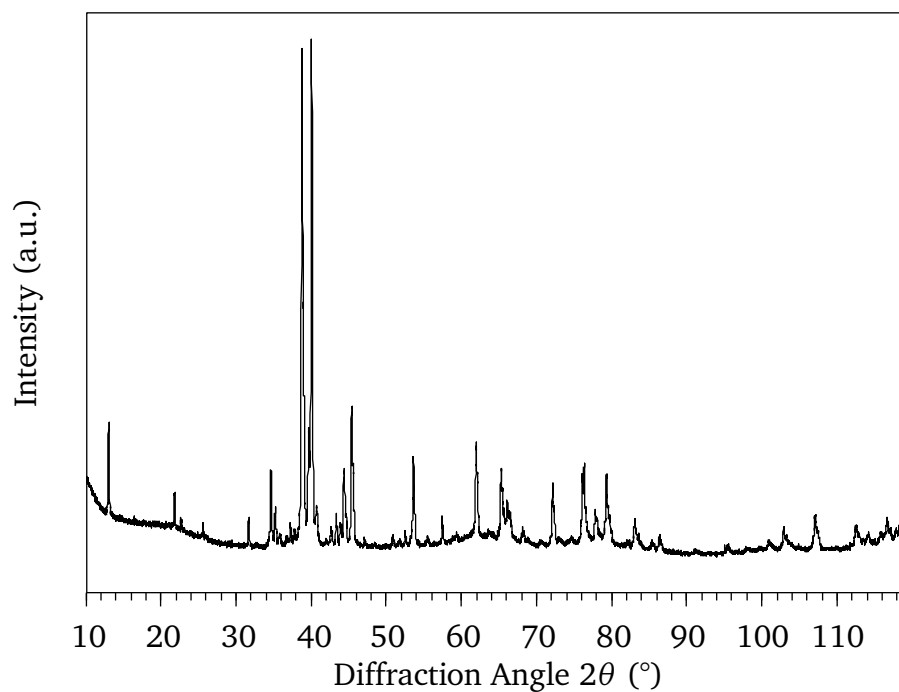


Figure B.6: XRD graph of the Ti–Al sample post DTA measurement.

B.1 Material Data Used for Critical Layer Thickness Calculation

Table B.2: Material properties used to calculate the critical layer thickness

| | Thermal conductivity λ (W/mK) | Density ρ (kg/m ³) | Heat capacity c (J/kgK) | Atomic weight (g/mol) |
|-----------------------|--|--|------------------------------|--------------------------|
| Nickel | 90.9 | 8900 | 444 | 58.69 |
| Titan | 21.9 | 4506 | 523 | 47.867 |
| Aluminium | 237 | 2700 | 897 | 26.98 |
| Si | 150 | 2336 | 703 | 28.085 |
| SiO ₂ | 1.38 | 2201 | 1052 | 60.085 |
| Si + SiO ₂ | 75.69 | 2268.5 | 877.5 | 44.085 |

Table B.3: Material systems properties used to calculate the critical layer thickness [77, 160–163]

| | | Material system | | |
|---------------|---|-----------------------|-----------------------|-----------------------|
| | | Ni–Ti | Ni–Al | Ti–Al |
| T_c | Combustion temp (K) | 1400 | 1911 | 1500 |
| E_a | Act. Energy (J/mol) | 12 040 | 17 000 | 298 700 |
| U | Combustion rate without heat loss (m/s) | 5.00×10^{-3} | 2.00×10^{-2} | 1.00×10^{-3} |
| γ_{cr} | Dimensionless parameter characterizing the quantity of heat losses from the reaction zone in the inert. | 0.54 | 0.54 | 0.54 |
| λ_r | Thermal conductivity (W/mK) | 59.90 | 136.91 | 99.44 |
| ρ_r | Density (kg/m ³) | 6926.15 | 6947.44 | 3854.99 |
| c_r | Heat capacity (J/kgK) | 479.49 | 586.66 | 657.82 |
| T_0 | Initial Temperature (K) | 293 | 293 | 293 |
| a_r | Temperature conductivity $\frac{\lambda}{\rho c}$ | 1.80×10^{-5} | 3.36×10^{-5} | 3.92×10^{-5} |
| R | Universal gas constant (J/molK) | 8.3144598 | 8.3144598 | 8.3144598 |

Appendix C: Sample Database

Table C.1: Sample Database

| Sample Number | 1 | 2 | 3 | 4 |
|----------------------|-----------------------|-----------------------|-----------------------|-----------------------|
| Date | 14090401 | 14090402 | 14090403 | 14090404 |
| Material A | Al | Al | Al | Al |
| Particle Diameter A | 40 | 40 | 40 | 40 |
| Particles per gram A | 5.66×10^{15} | 5.66×10^{15} | 5.66×10^{15} | 5.66×10^{15} |
| Molar Mass A | 2.70×10^1 | 2.70×10^1 | 2.70×10^1 | 2.70×10^1 |
| Material B | Ti | Ti | Ni | Ni |
| Particle Diameter B | 60 | 60 | 60 | 60 |
| Particles per Gram B | 1.24×10^{15} | 1.24×10^{15} | 6.26×10^{14} | 6.26×10^{14} |
| Molar Mass B | 4.79×10^1 | 4.79×10^1 | 5.87×10^1 | 5.87×10^1 |
| Stoichiometry | 1:1 | 1:1 | 1:1 | 1:1 |
| Mass particles (mg) | 5.00×10^1 | 5.00×10^1 | 5.00×10^1 | 5.00×10^1 |
| Mass A (mg) | 3.20×10^1 | 3.20×10^1 | 3.43×10^1 | 3.43×10^1 |
| Mass B (mg) | 1.80×10^1 | 1.80×10^1 | 1.57×10^1 | 1.57×10^1 |
| Solvent | Cyclohexane | Cyclohexane | Cyclohexane | Cyclohexane |
| Mass Solvent (mg) | 5.00×10^2 | 1.00×10^3 | 1.00×10^3 | 5.00×10^2 |
| Volume Solvent (ml) | 6.41×10^{-1} | 1.28 | 1.28 | 6.41×10^{-1} |
| Additive | n/a | n/a | n/a | n/a |
| Mass Additive | 0.00 | 0.00 | 0.00 | 0.00 |
| Density Additive | 0.00 | 0.00 | 0.00 | 0.00 |
| Volume Additive (ml) | 0.00 | 0.00 | 0.00 | 0.00 |
| wt-% Dispersion | 10 % | 5.00 % | 5.00 % | 10 % |
| # Particles per ml | 3.17×10^{14} | 1.59×10^{14} | 1.59×10^{14} | 3.18×10^{14} |
| Process steps* | US, D | US, D | US, D | US, D |

* US = Ultrasonic Agitation, D = Dispersed, S = Shaked, G = Ground

Sample Database (page 2 of 15)

| Sample Number | 5 | 6 | 7 | 8 |
|----------------------|-----------------------|-----------------------|-----------------------|-----------------------|
| Date | 14090405 | 14090406 | 14090407 | 14090408 |
| Material A | Al | Al | Al | Al |
| Particle Diameter A | 18 | 18 | 18 | 18 |
| Particles per gram A | 1.21×10^{17} | 1.21×10^{17} | 1.21×10^{17} | 1.21×10^{17} |
| Molar Mass A | 2.70×10^1 | 2.70×10^1 | 2.70×10^1 | 2.70×10^1 |
| Material B | Ti | Ti | Ni | Ni |
| Particle Diameter B | 60 | 60 | 20 | 20 |
| Particles per Gram B | 1.24×10^{15} | 1.24×10^{15} | 2.68×10^{16} | 2.68×10^{16} |
| Molar Mass B | 4.79×10^1 | 4.79×10^1 | 5.87×10^1 | 5.87×10^1 |
| Stoichiometry | 1:1 | 1:1 | 1:1 | 1:1 |
| Mass particles (mg) | 5.00×10^1 | 5.00×10^1 | 5.00×10^1 | 5.00×10^1 |
| Mass A (mg) | 3.20×10^1 | 3.20×10^1 | 3.43×10^1 | 3.43×10^1 |
| Mass B (mg) | 1.80×10^1 | 1.80×10^1 | 1.57×10^1 | 1.57×10^1 |
| Solvent | Cyclohexane | Cyclohexane | Cyclohexane | Cyclohexane |
| Mass Solvent (mg) | 5.00×10^2 | 1.00×10^3 | 5.00×10^2 | 1.00×10^3 |
| Volume Solvent (ml) | 6.41×10^{-1} | 1.28 | 6.41×10^{-1} | 1.28 |
| Additive | n/a | n/a | n/a | n/a |
| Mass Additive | 0.00 | 0.00 | 0.00 | 0.00 |
| Density Additive | 0.00 | 0.00 | 0.00 | 0.00 |
| Volume Additive (ml) | 0.00 | 0.00 | 0.00 | 0.00 |
| wt-% Dispersion | 10 % | 5.00 % | 10 % | 5.00 % |
| # Particles per ml | 6.07×10^{15} | 3.04×10^{15} | 7.12×10^{15} | 3.56×10^{15} |
| Process steps* | US, D | US, D | US, D | US, D |

* US = Ultrasonic Agitation, D = Dispersed, S = Shaked, G = Ground

C Sample Database

Sample Database (page 3 of 15)

| Sample Number | 9 | 10 | 11 | 12 |
|----------------------|-----------------------|-----------------------|-----------------------|-----------------------|
| Date | 14090801 | 14090801 | 14090803 | 14090804 |
| Material A | Al | Al | 0 | 0 |
| Particle Diameter A | 40 | 40 | 0 | 0 |
| Particles per gram A | 5.66×10^{15} | 5.66×10^{15} | 0.00 | 0.00 |
| Molar Mass A | 2.70×10^1 | 2.70×10^1 | 0.00 | 0.00 |
| Material B | Ti | Ni | 0 | 0 |
| Particle Diameter B | 60 | 60 | 0 | 0 |
| Particles per Gram B | 1.24×10^{15} | 6.26×10^{14} | 0.00 | 0.00 |
| Molar Mass B | 4.79×10^1 | 5.87×10^1 | 0.00 | 0.00 |
| Stoichiometry | 1:1 | 1:1 | 0 | 0 |
| Mass particles (mg) | 2.50×10^1 | 2.50×10^1 | 0.00 | 0.00 |
| Mass A (mg) | 1.60×10^1 | 1.71×10^1 | 0.00 | 0.00 |
| Mass B (mg) | 9.01 | 7.87 | 0.00 | 0.00 |
| Solvent | Oleic Acid | Oleic Acid | Oleic Acid | Oleic Acid |
| Mass Solvent (mg) | 5.00×10^2 | 5.00×10^2 | 5.00×10^2 | 5.00×10^2 |
| Volume Solvent (ml) | 5.62×10^{-1} | 5.62×10^{-1} | 5.62×10^{-1} | 5.62×10^{-1} |
| Additive | n/a | n/a | Methanol | Methanol |
| Mass Additive | 0.00 | 0.00 | 7.90 | 1.58×10^1 |
| Density Additive | 0.00 | 0.00 | 7.90×10^{-1} | 7.90×10^{-1} |
| Volume Additive (ml) | 0.00 | 0.00 | 1.00×10^{-2} | 2.00×10^{-2} |
| wt-% Dispersion | 5.00 % | 5.00 % | 0.00 % | 0.00 % |
| # Particles per ml | 1.81×10^{14} | 1.81×10^{14} | 0.00 | 0.00 |
| Process steps* | US, D | US, D | US, D | US, D |

* US = Ultrasonic Agitation, D = Dispersed, S = Shaked, G = Ground

Sample Database (page 4 of 15)

| Sample Number | 13 | 14 | 15 | 16 |
|----------------------|-----------------------|-----------------------|-----------------------|-----------------------|
| Date | 14090805 | 14091901 | 14111101 | 14111102 |
| Material A | 0 | 0 | Al | Al |
| Particle Diameter A | 0 | 0 | 40 | 40 |
| Particles per gram A | 0.00 | 0.00 | 5.66×10^{15} | 5.66×10^{15} |
| Molar Mass A | 0.00 | 0.00 | 2.70×10^1 | 2.70×10^1 |
| Material B | 0 | 0 | Ti | Ti |
| Particle Diameter B | 0 | 0 | 60 | 60 |
| Particles per Gram B | 0.00 | 0.00 | 1.24×10^{15} | 1.24×10^{15} |
| Molar Mass B | 0.00 | 0.00 | 4.79×10^1 | 4.79×10^1 |
| Stoichiometry | 0 | 0 | 1:1 | 1:1 |
| Mass particles (mg) | 0.00 | 0.00 | 5.90×10^1 | 5.00×10^1 |
| Mass A (mg) | 0.00 | 0.00 | 3.77×10^1 | 3.20×10^1 |
| Mass B (mg) | 0.00 | 0.00 | 2.13×10^1 | 1.80×10^1 |
| Solvent | Oleic Acid | Methanol | MTG | MTG |
| Mass Solvent (mg) | 5.00×10^2 | 7.92×10^2 | 5.00×10^2 | 5.50×10^2 |
| Volume Solvent (ml) | 5.62×10^{-1} | 1.00 | 4.87×10^{-1} | 5.36×10^{-1} |
| Additive | n/a | Oleic Acid | n/a | Methanol |
| Mass Additive | 0.00 | 8.95 | 0.00 | 5.00 |
| Density Additive | 0.00 | 8.90×10^{-1} | 0.00 | 7.90×10^{-1} |
| Volume Additive (ml) | 0.00 | 1.01×10^{-2} | 0.00 | 6.33×10^{-3} |
| wt-% Dispersion | 0.00 % | 0.00 % | 11.80 % | 9.01 % |
| # Particles per ml | 0.00 | 0.00 | 4.92×10^{14} | 3.75×10^{14} |
| Process steps* | US, D | US, D | US, D | US, D |

* US = Ultrasonic Agitation, D = Dispersed, S = Shaked, G = Ground

C Sample Database

Sample Database (page 5 of 15)

| Sample Number | 17 | 18 | 19 | 20 |
|----------------------|-----------------------|-----------------------|-----------------------|-----------------------|
| Date | 14111103 | 14111104 | 14111105 | 14111106 |
| Material A | Al | Al | Al | Al |
| Particle Diameter A | 40 | 40 | 40 | 40 |
| Particles per gram A | 5.66×10^{15} | 5.66×10^{15} | 5.66×10^{15} | 5.66×10^{15} |
| Molar Mass A | 2.70×10^1 | 2.70×10^1 | 2.70×10^1 | 2.70×10^1 |
| Material B | Ni | Ni | Ti | Ti |
| Particle Diameter B | 60 | 60 | 60 | 60 |
| Particles per Gram B | 6.26×10^{14} | 6.26×10^{14} | 1.24×10^{15} | 1.24×10^{15} |
| Molar Mass B | 5.87×10^1 | 5.87×10^1 | 4.79×10^1 | 4.79×10^1 |
| Stoichiometry | 1:1 | 1:1 | 1:1 | 1:1 |
| Mass particles (mg) | 5.00×10^1 | 5.00×10^1 | 5.00×10^1 | 5.00×10^1 |
| Mass A (mg) | 3.43×10^1 | 3.43×10^1 | 3.20×10^1 | 3.20×10^1 |
| Mass B (mg) | 1.57×10^1 | 1.57×10^1 | 1.80×10^1 | 1.80×10^1 |
| Solvent | MTG | MTG | Cyclohexane | Cyclohexane |
| Mass Solvent (mg) | 5.00×10^2 | 5.00×10^2 | 5.00×10^2 | 5.00×10^2 |
| Volume Solvent (ml) | 4.87×10^{-1} | 4.87×10^{-1} | 6.41×10^{-1} | 6.41×10^{-1} |
| Additive | n/a | Methanol | MTG | MTG |
| Mass Additive | 0.00 | 5.00 | 2.00×10^1 | 5.70×10^1 |
| Density Additive | 0.00 | 7.90×10^{-1} | 1.03 | 1.03 |
| Volume Additive (ml) | 0.00 | 6.33×10^{-3} | 1.95×10^{-2} | 5.56×10^{-2} |
| wt-% Dispersion | 10% | 9.90% | 9.62% | 8.98% |
| # Particles per ml | 4.18×10^{14} | 4.13×10^{14} | 3.08×10^{14} | 2.92×10^{14} |
| Process steps* | US, D | US, D | US, D | US, D |

* US = Ultrasonic Agitation, D = Dispersed, S = Shaked, G = Ground

Sample Database (page 6 of 15)

| Sample Number | 21 | 22 | 23 | 24 |
|----------------------|-----------------------|-----------------------|-----------------------|-----------------------|
| Date | 14111107 | 14111108 | 14111109 | 14111110 |
| Material A | Al | Al | Al | Al |
| Particle Diameter A | 40 | 40 | 40 | 40 |
| Particles per gram A | 5.66×10^{15} | 5.66×10^{15} | 5.66×10^{15} | 5.66×10^{15} |
| Molar Mass A | 2.70×10^1 | 2.70×10^1 | 2.70×10^1 | 2.70×10^1 |
| Material B | Ni | Ni | Ti | Ni |
| Particle Diameter B | 60 | 60 | 60 | 60 |
| Particles per Gram B | 6.26×10^{14} | 6.26×10^{14} | 1.24×10^{15} | 6.26×10^{14} |
| Molar Mass B | 5.87×10^1 | 5.87×10^1 | 4.79×10^1 | 5.87×10^1 |
| Stoichiometry | 1:1 | 1:1 | 1:1 | 1:1 |
| Mass particles (mg) | 5.00×10^1 | 5.00×10^1 | 5.00×10^1 | 5.00×10^1 |
| Mass A (mg) | 3.43×10^1 | 3.43×10^1 | 3.20×10^1 | 3.43×10^1 |
| Mass B (mg) | 1.57×10^1 | 1.57×10^1 | 1.80×10^1 | 1.57×10^1 |
| Solvent | Cyclohexane | Cyclohexane | Cyclohexane | Cyclohexane |
| Mass Solvent (mg) | 5.00×10^2 | 5.00×10^2 | 5.00×10^2 | 5.00×10^2 |
| Volume Solvent (ml) | 6.41×10^{-1} | 6.41×10^{-1} | 6.41×10^{-1} | 6.41×10^{-1} |
| Additive | MTG | MTG | n/a | n/a |
| Mass Additive | 2.00×10^1 | 4.50×10^1 | 0.00 | 0.00 |
| Density Additive | 1.03 | 1.03 | 0.00 | 0.00 |
| Volume Additive (ml) | 1.95×10^{-2} | 4.39×10^{-2} | 0.00 | 0.00 |
| wt-% Dispersion | 9.62 % | 9.17 % | 10 % | 10 % |
| # Particles per ml | 3.08×10^{14} | 2.97×10^{14} | 3.17×10^{14} | 3.18×10^{14} |
| Process steps* | US, D | US, D | US, D | US, D |

* US = Ultrasonic Agitation, D = Dispersed, S = Shaked, G = Ground

C Sample Database

Sample Database (page 7 of 15)

| Sample Number | 25 | 26 | 27 | 28 |
|----------------------|-----------------------|-----------------------|-----------------------|-----------------------|
| Date | 15020301 | 15020302 | 15020303 | 15020304 |
| Material A | Al | Al | Al | Al |
| Particle Diameter A | 18 | 18 | 40 | 40 |
| Particles per gram A | 1.21×10^{17} | 1.21×10^{17} | 5.66×10^{15} | 5.66×10^{15} |
| Molar Mass A | 2.70×10^1 | 2.70×10^1 | 2.70×10^1 | 2.70×10^1 |
| Material B | 0 | 0 | Ni | Ni |
| Particle Diameter B | 0 | 0 | 60 | 60 |
| Particles per Gram B | 0.00 | 0.00 | 6.26×10^{14} | 6.26×10^{14} |
| Molar Mass B | 0.00 | 0.00 | 5.87×10^1 | 5.87×10^1 |
| Stoichiometry | 0 | 0 | 1:1 | 1:1 |
| Mass particles (mg) | 2.50×10^1 | 1.00×10^1 | 3.70×10^1 | 3.70×10^1 |
| Mass A (mg) | 2.50×10^1 | 1.00×10^1 | 2.53×10^1 | 2.53×10^1 |
| Mass B (mg) | 0.00 | 0.00 | 1.17×10^1 | 1.17×10^1 |
| Solvent | Cyclohexane | Cyclohexane | Cyclohexane | Cyclohexane |
| Mass Solvent (mg) | 4.00×10^3 | 4.00×10^3 | 4.00×10^3 | 4.00×10^3 |
| Volume Solvent (ml) | 5.13 | 5.13 | 5.13 | 5.13 |
| Additive | MTG | MTG | n/a | MTG |
| Mass Additive | 5.00×10^1 | 4.00×10^1 | 0.00 | 1.50×10^1 |
| Density Additive | 1.03 | 1.03 | 0.00 | 1.03 |
| Volume Additive (ml) | 4.87×10^{-2} | 3.90×10^{-2} | 0.00 | 1.46×10^{-2} |
| wt-% Dispersion | 0.62 % | 0.25 % | 0.93 % | 0.92 % |
| # Particles per ml | 5.84×10^{14} | 2.34×10^{14} | 2.94×10^{13} | 2.93×10^{13} |
| Process steps* | US, S, D | US, S, D | US, S, D | US, S, D |

* US = Ultrasonic Agitation, D = Dispersed, S = Shaked, G = Ground

Sample Database (page 8 of 15)

| Sample Number | 29 | 30 | 31 | 32 |
|-----------------------------|-----------------------|-----------------------|-----------------------|-----------------------|
| Date | 15020305 | 15020306 | 15020901 | 15020902 |
| Material A | Al | Al | Ni | Ti |
| Particle Diameter A | 40 | 40 | 60 | 60 |
| Particles per gram A | 5.66×10^{15} | 5.66×10^{15} | 6.26×10^{14} | 1.24×10^{15} |
| Molar Mass A | 2.70×10^1 | 2.70×10^1 | 5.87×10^1 | 4.79×10^1 |
| Material B | Ni | Ni | 0 | 0 |
| Particle Diameter B | 60 | 60 | 0 | 0 |
| Particles per Gram B | 6.26×10^{14} | 6.26×10^{14} | 0.00 | 0.00 |
| Molar Mass B | 5.87×10^1 | 5.87×10^1 | 0.00 | 0.00 |
| Stoichiometry | 1:1 | 1:1 | 0 | 0 |
| Mass particles (mg) | 3.70×10^1 | 3.70×10^1 | 1.20×10^1 | 1.00×10^1 |
| Mass A (mg) | 2.53×10^1 | 2.53×10^1 | 1.20×10^1 | 1.00×10^1 |
| Mass B (mg) | 1.17×10^1 | 1.17×10^1 | 0.00 | 0.00 |
| Solvent | Cyclohexane | Cyclohexane | Cyclohexane | Cyclohexane |
| Mass Solvent (mg) | 4.00×10^3 | 4.00×10^3 | 4.00×10^3 | 4.00×10^3 |
| Volume Solvent (ml) | 5.13 | 5.13 | 5.13 | 5.13 |
| Additive | MTG | MTG | MTG | MTG |
| Mass Additive | 5.00×10^1 | 1.00×10^2 | 4.00×10^1 | 4.00×10^1 |
| Density Additive | 1.03 | 1.03 | 1.03 | 1.03 |
| Volume Additive (ml) | 4.87×10^{-2} | 9.75×10^{-2} | 3.90×10^{-2} | 3.90×10^{-2} |
| wt-% Dispersion | 0.91 % | 0.90 % | 0.30 % | 0.25 % |
| # Particles per ml | 2.91×10^{13} | 2.89×10^{13} | 1.45×10^{12} | 2.40×10^{12} |
| Process steps* | US, S, D | US, S, D | US, S, D | US, S, D |

* US = Ultrasonic Agitation, D = Dispersed, S = Shaked, G = Ground

C Sample Database

Sample Database (page 9 of 15)

| Sample Number | 33 | 34 | 35 | 36 |
|----------------------|-----------------------|-----------------------|-----------------------|-----------------------|
| Date | 15020903 | 15020904 | 15020905 | 15020906 |
| Material A | Al | Al | Al | Ni |
| Particle Diameter A | 40 | 40 | 40 | 60 |
| Particles per gram A | 5.66×10^{15} | 5.66×10^{15} | 5.66×10^{15} | 6.26×10^{14} |
| Molar Mass A | 2.70×10^1 | 2.70×10^1 | 2.70×10^1 | 5.87×10^1 |
| Material B | Ti | Ti | Ti | Ti |
| Particle Diameter B | 60 | 60 | 60 | 60 |
| Particles per Gram B | 1.24×10^{15} | 1.24×10^{15} | 1.24×10^{15} | 1.24×10^{15} |
| Molar Mass B | 4.79×10^1 | 4.79×10^1 | 4.79×10^1 | 4.79×10^1 |
| Stoichiometry | n/a | n/a | 1:1 | n/a |
| Mass particles (mg) | n/a | n/a | 1.90×10^1 | n/a |
| Mass A (mg) | n/a | n/a | 1.22×10^1 | n/a |
| Mass B (mg) | n/a | 1.20×10^1 | 6.85 | n/a |
| Solvent | Cyclohexane | Cyclohexane | Cyclohexane | Cyclohexane |
| Mass Solvent (mg) | 4.00×10^3 | 4.00×10^3 | 4.00×10^3 | 4.00×10^3 |
| Volume Solvent (ml) | 5.13 | 5.13 | 5.13 | 5.13 |
| Additive | n/a | MTG | MTG | MTG |
| Mass Additive | 0.00 | 4.00×10^1 | 2.00×10^1 | n/a |
| Density Additive | 0.00 | 1.03 | 1.03 | 1.03 |
| Volume Additive (ml) | 0.00 | 3.90×10^{-2} | 1.95×10^{-2} | n/a |
| wt-% Dispersion | n/a | n/a | 0.47% | n/a |
| # Particles per ml | n/a | n/a | 1.50×10^{13} | n/a |
| Process steps* | US, S, D | US, S, D | US, S, D | US, S, D |

* US = Ultrasonic Agitation, D = Dispersed, S = Shaked, G = Ground

Sample Database (page 10 of 15)

| Sample Number | 37 | 38 | 39 | 40 |
|-----------------------------|-----------------------|-----------------------|-----------------------|-----------------------|
| Date | 15041401 | 15041402 | 15091412 | 15091413 |
| Material A | Al | Al | Al | Al |
| Particle Diameter A | 18 | 18 | 18 | 40 |
| Particles per gram A | 1.21×10^{17} | 1.21×10^{17} | 1.21×10^{17} | 5.66×10^{15} |
| Molar Mass A | 2.70×10^1 | 2.70×10^1 | 2.70×10^1 | 2.70×10^1 |
| Material B | Ti | Ni | 0 | 0 |
| Particle Diameter B | 60 | 60 | 0 | 0 |
| Particles per Gram B | 1.24×10^{15} | 6.26×10^{14} | 0 | 0 |
| Molar Mass B | 4.79×10^1 | 5.87×10^1 | 0.00 | 0.00 |
| Stoichiometry | 1:1 | 1:1 | 0 | 0 |
| Mass particles (mg) | 3.30×10^1 | 3.40×10^1 | 20 | 22 |
| Mass A (mg) | 2.11×10^1 | 2.33×10^1 | 2.00×10^1 | 2.20×10^1 |
| Mass B (mg) | 1.19×10^1 | 1.07×10^1 | 0.00 | 0.00 |
| Solvent | Cyclohexane | Cyclohexane | Cyclohexan | Cyclohexan |
| Mass Solvent (mg) | 4.00×10^3 | 4.00×10^3 | 156 | 156 |
| Volume Solvent (ml) | 5.13 | 5.13 | 0.20 | 0.20 |
| Additive | n/a | n/a | n/a | n/a |
| Mass Additive | 0.00 | 0.00 | 0 | 0 |
| Density Additive | 0.00 | 0.00 | 0 | 0 |
| Volume Additive (ml) | 0.00 | 0.00 | 0 | 0 |
| wt-% Dispersion | 0.83 % | 0.85 % | 12.80 % | 14.10 % |
| # Particles per ml | 5.01×10^{14} | 5.51×10^{14} | 1.21×10^{16} | 6.23×10^{14} |
| Process steps* | US, S, D | US, S, D | S, D | S, D |

* US = Ultrasonic Agitation, D = Dispersed, S = Shaked, G = Ground

C Sample Database

Sample Database (page 11 of 15)

| Sample Number | 41 | 42 | 43 | 44 |
|----------------------|--------------------|--------------------|-----------------------|--------------------|
| Date | 15091414 | 15091415 | 15091416 | 15091417 |
| Material A | Al | Al | Ti | Ti |
| Particle Diameter A | 25 000 | 125 000 | 60 | 45 000 |
| Particles per gram A | 4.53×10^7 | 3.62×10^5 | 1.24×10^{15} | 4.66×10^6 |
| Molar Mass A | 2.70×10^1 | 2.70×10^1 | 4.79×10^1 | 4.79×10^1 |
| Material B | 0 | 0 | 0 | 0 |
| Particle Diameter B | 0 | 0 | 0 | 0 |
| Particles per Gram B | 0 | 0 | 0 | 0 |
| Molar Mass B | 0.00 | 0.00 | 0.00 | 0.00 |
| Stoichiometry | 0 | 0 | 0 | 0 |
| Mass particles (mg) | 23 | 23 | 22 | 55 |
| Mass A (mg) | 2.30×10^1 | 2.30×10^1 | 2.20×10^1 | 5.50×10^1 |
| Mass B (mg) | 0.00 | 0.00 | 0.00 | 0.00 |
| Solvent | Cyclohexan | Cyclohexan | Cyclohexan | Cyclohexan |
| Mass Solvent (mg) | 156 | 156 | 156 | 156 |
| Volume Solvent (ml) | 0.20 | 0.20 | 0.20 | 0.20 |
| Additive | n/a | n/a | n/a | n/a |
| Mass Additive | 0 | 0 | 0 | 0 |
| Density Additive | 0 | 0 | 0 | 0 |
| Volume Additive (ml) | 0 | 0 | 0 | 0 |
| wt-% Dispersion | 14.70 % | 14.70 % | 14.10 % | 35.30 % |
| # Particles per ml | 5 209 500 | 41 630 | 1.36×10^{14} | 1 281 500 |
| Process steps* | S, D | S, D | S, D | S, D |

* US = Ultrasonic Agitation, D = Dispersed, S = Shaked, G = Ground

Sample Database (page 12 of 15)

| Sample Number | 45 | 46 | 47 | 48 |
|----------------------|--------------------|-----------------------|-----------------------|--------------------|
| Date | 15091418 | 15091419 | 15091420 | 15091421 |
| Material A | Ti | Ni | Ni | Ni |
| Particle Diameter A | 150 000 | 20 | 60 | 45 000 |
| Particles per gram A | 1.26×10^5 | 2.68×10^{16} | 6.26×10^{14} | 2.35×10^6 |
| Molar Mass A | 4.79×10^1 | 5.87×10^1 | 5.87×10^1 | 5.87×10^1 |
| Material B | 0 | 0 | 0 | 0 |
| Particle Diameter B | 0 | 0 | 0 | 0 |
| Particles per Gram B | 0 | 0 | 0 | 0 |
| Molar Mass B | 0.00 | 0.00 | 0.00 | 0.00 |
| Stoichiometry | 0 | 0 | 0 | 0 |
| Mass particles (mg) | 20 | 20 | 20 | 35 |
| Mass A (mg) | 2.00×10^1 | 2.00×10^1 | 2.00×10^1 | 3.50×10^1 |
| Mass B (mg) | 0.00 | 0.00 | 0.00 | 0.00 |
| Solvent | Cyclohexan | Cyclohexan | Cyclohexan | Cyclohexan |
| Mass Solvent (mg) | 156 | 156 | 156 | 156 |
| Volume Solvent (ml) | 0.20 | 0.20 | 0.20 | 0.20 |
| Additive | n/a | n/a | n/a | n/a |
| Mass Additive | 0 | 0 | 0 | 0 |
| Density Additive | 0 | 0 | 0 | 0 |
| Volume Additive (ml) | 0 | 0 | 0 | 0 |
| wt-% Dispersion | 12.80 % | 12.80 % | 12.80 % | 22.40 % |
| # Particles per ml | 12 600 | 2.68×10^{15} | 6.26×10^{13} | 411 250 |
| Process steps* | S, D | S, D | S, D | S, D |

* US = Ultrasonic Agitation, D = Dispersed, S = Shaked, G = Ground

C Sample Database

Sample Database (page 13 of 15)

| Sample Number | 49 | 50 | 51 | 52 |
|----------------------|--------------------|--------------------|--------------------|-----------------------|
| Date | 15091422 | 15091801 | 15091802 | 15091803 |
| Material A | Ni | Al | Al | Al |
| Particle Diameter A | 250 000 | 25 000 | 125 000 | 18 |
| Particles per gram A | 1.37×10^4 | 45 300 000 | 3.62×10^5 | 1.21×10^{17} |
| Molar Mass A | 5.87×10^1 | 2.70×10^1 | 2.70×10^1 | 2.70×10^1 |
| Material B | 0 | Ni | Ni | Ni |
| Particle Diameter B | 0 | 45 000 | 250 000 | 20 |
| Particles per Gram B | 0 | 2.35×10^6 | 1.37×10^4 | 2.68×10^{16} |
| Molar Mass B | 0.00 | 5.87×10^1 | 5.87×10^1 | 5.87×10^1 |
| Stoichiometry | 0 | 1:1 | 1:1 | 1:1 |
| Mass particles (mg) | 20 | 146 | 100 | 50 |
| Mass A (mg) | 2.00×10^1 | 1.00×10^2 | 6.85×10^1 | 3.43×10^1 |
| Mass B (mg) | 0.00 | 4.60×10^1 | 3.15×10^1 | 1.57×10^1 |
| Solvent | Cyclohexan | Cyclohexan | Cyclohexan | Cyclohexan |
| Mass Solvent (mg) | 156 | 4000 | 4000 | 4000 |
| Volume Solvent (ml) | 0.20 | 5.13 | 5.13 | 5.13 |
| Additive | n/a | n/a | n/a | n/a |
| Mass Additive | 0 | 0 | 0 | 0 |
| Density Additive | 0 | 0 | 0 | 0 |
| Volume Additive (ml) | 0 | 0 | 0 | 0 |
| wt-% Dispersion | 12.80 % | 3.70 % | 2.50 % | 1.30 % |
| # Particles per ml | 1370 | 904 599.61 | 4920.05 | 8.91×10^{14} |
| Process steps* | S, D | S, D | S, D | S, D |

* US = Ultrasonic Agitation, D = Dispersed, S = Shaked, G = Ground

Sample Database (page 14 of 15)

| Sample Number | 53 | 54 | 55 | 56 |
|-----------------------------|-----------------------|-----------------------|-----------------------|-----------------------|
| Date | 15091804 | 15091805 | 16020901 | 16020902 |
| Material A | Al | Al | Al | Al |
| Particle Diameter A | 18 | 40 | 18 | 18 |
| Particles per gram A | 1.21×10^{17} | 5.66×10^{15} | 1.21×10^{17} | 1.21×10^{17} |
| Molar Mass A | 2.70×10^1 | 2.70×10^1 | 2.70×10^1 | 2.70×10^1 |
| Material B | Ni | Ni | Ni | Ti |
| Particle Diameter B | 60 | 60 | 60 | 60 |
| Particles per Gram B | 6.26×10^{14} | 6.26×10^{14} | 6.26×10^{14} | 1.24×10^{15} |
| Molar Mass B | 5.87×10^1 | 5.87×10^1 | 5.87×10^1 | 4.79×10^1 |
| Stoichiometry | 1:1 | 1:1 | 1:1 | 1:1 |
| Mass particles (mg) | 50 | 50 | 2000 | 3000 |
| Mass A (mg) | 3.43×10^1 | 3.43×10^1 | 1.37×10^3 | 1.92×10^3 |
| Mass B (mg) | 1.57×10^1 | 1.57×10^1 | 6.30×10^2 | 1.08×10^3 |
| Solvent | Cyclohexan | Cyclohexan | n/a | n/a |
| Mass Solvent (mg) | 4000 | 4000 | 0 | 0 |
| Volume Solvent (ml) | 5.13 | 5.13 | 0 | 0 |
| Additive | n/a | n/a | n/a | n/a |
| Mass Additive | 0 | 0 | 0 | 0 |
| Density Additive | 0 | 0 | 0 | 0 |
| Volume Additive (ml) | 0 | 0 | 0 | 0 |
| wt-% Dispersion | 1.30 % | 1.30 % | n/a | n/a |
| # Particles per ml | 8.10×10^{14} | 3.97×10^{13} | n/a | n/a |
| Process steps* | S, D | S, D | G | G |

* US = Ultrasonic Agitation, D = Dispersed, S = Shaked, G = Ground

Sample Database (page 15 of 15)

| Sample Number | 57 | 58 | 59 |
|----------------------|--------------------|--------------------|-----------------------|
| Date | 16021001 | 16021002 | 16021003 |
| Material A | Al | Al | Al |
| Particle Diameter A | 25 000 | 125 000 | 40 |
| Particles per gram A | 4.53×10^7 | 3.62×10^5 | 5.66×10^{15} |
| Molar Mass A | 2.70×10^1 | 2.70×10^1 | 2.70×10^1 |
| Material B | Ni | Ni | Ni |
| Particle Diameter B | 45 000 | 250 000 | 20 |
| Particles per Gram B | 2.35×10^6 | 1.37×10^4 | 2.68×10^{16} |
| Molar Mass B | 5.87×10^1 | 5.87×10^1 | 5.87×10^1 |
| Stoichiometry | 1:1 | 1:1 | 1:1 |
| Mass particles (mg) | 9000 | 10 000 | 1000 |
| Mass A (mg) | 6.17×10^3 | 6.85×10^3 | 6.85×10^2 |
| Mass B (mg) | 2.83×10^3 | 3.15×10^3 | 3.15×10^2 |
| Solvent | n/a | n/a | n/a |
| Mass Solvent (mg) | 0 | 0 | 0 |
| Volume Solvent (ml) | 0 | 0 | 0 |
| Additive | n/a | n/a | n/a |
| Mass Additive | 0 | 0 | 0 |
| Density Additive | 0 | 0 | 0 |
| Volume Additive (ml) | 0 | 0 | 0 |
| wt-% Dispersion | n/a | n/a | n/a |
| # Particles per ml | n/a | n/a | n/a |
| Process steps* | G | G | G |

* US = Ultrasonic Agitation, D = Dispersed, S = Shaked, G = Ground

Appendix D: Datasheets

Datasheets of the acquired nanoparticles and photographs of the respective sample containers are shown on the following pages.

Technical Data Sheet

Aluminium Nanopowder, 18 nm

Revision Date: 12/12/2009

Date Issued: 03/02/2007

1 IDENTIFICATION OF THE SUBSTANCE/PREPARATION AND THE COMPANY / UNDERTAKING

| | |
|----------------------------|---|
| Product name | Aluminium nanopowder, 18 nm |
| Product code | NM-0015-HP |
| Supplier | IoLiTec Ionic Liquids Technologies GmbH Salzstrasse 184 D-74076 Heilbronn Germany |
| Telephone | +49 (0)7131 - 898390 |
| Fax | +49 (0)7131 - 89839109 |
| Emergency telephone | +49 (0)179 - 5322578 |

2 COMPOSITION / INFORMATION ON INGREDIENTS

| | |
|------------------------------|--|
| Ingredient name | Aluminium powder (partially passivated with approximately 15% O) |
| Empirical Formula | Al |
| CAS No. | 7429-90-5 |
| Molecular weight | 26.98 amu |
| Purity | 99.9 % (metal basis) |
| Average Particle Size | 18 nm (TEM) |
| Particle size range | 0-50 nm (TEM) |
| Specific Surface Area | 40-60 m ² /g (BET) |
| Morphology | Spherical |
| Colour | Black |
| Bulk Density | 0.08-0.20 g/cm ³ |

Technical Data Sheet

Aluminium powder, 40-60 nm

Revision Date: 02/12/2014

Date Issued: 03/02/2007

1 IDENTIFICATION OF THE SUBSTANCE/PREPARATION AND THE COMPANY / UNDERTAKING

| | |
|----------------------------|---|
| Product name | Aluminium powder, 60-80 nm |
| Product code | NM-0039-HP |
| Supplier | IoLiTec Ionic Liquids Technologies GmbH Salzstrasse 184 D-74076 Heilbronn Germany |
| Telephone | +49 (0)7131 - 898390 |
| Fax | +49 (0)7131 - 89839109 |
| Emergency telephone | +49 (0)179 - 5322578 |
| Email | msds@iolitec.de |

2 COMPOSITION / INFORMATION ON INGREDIENTS

| | |
|------------------------------|----------------------------|
| Ingredient name | Aluminium |
| Empirical Formula | Al |
| CAS No. | 7429-90-5 |
| Molecular weight | 26.98 amu |
| Purity | 99.9 % (metal basis) |
| Particle size range | 40-60 nm |
| Specific surface area | 20-48 m ² /g |
| Colour | grey |
| Morphology | spherical |
| Bulk density | 0.08-0.2 g/cm ³ |
| True density | 2.7 g/cm ³ |
| Melting point | 660.3°C |
| Production method | N/A |

Technical Data Sheet

Nickel nanopowder, 20 nm

Revision Date: 03/06/2009

Date Issued: 03/02/2007

1 IDENTIFICATION OF THE SUBSTANCE/PREPARATION AND THE COMPANY / UNDERTAKING

| | |
|----------------------------|---|
| Product name | Nickel nanopowder, 20 nm |
| Product code | NM-0028-HP |
| Supplier | IoLiTec Ionic Liquids Technologies GmbH Salzstrasse 184 D-74076 Heilbronn Germany |
| Telephone | +49 (0)7131 - 898390 |
| Fax | +49 (0)7131 - 89839109 |
| Emergency telephone | +49 (0)179 - 5322578 |

2 COMPOSITION / INFORMATION ON INGREDIENTS

| | |
|------------------------------|-------------------------------|
| Ingredient name | Nickel powder |
| Empirical Formula | Ni |
| CAS No. | 7440-02-0 |
| Molecular weight | 58.69 amu |
| Purity | 99.9% |
| Average particle size | 20 nm |
| Particle size range | 0 – 50 nm |
| Specific Surface Area | 40 - 60 m ² /g |
| Colour | black |
| Morphology | spherical |
| Bulk Density | 0.08 – 0.20 g/cm ³ |
| True Density | - |

Technical Data Sheet

Nickel nanopowder, 60 – 80 nm

Revision Date: 03/06/2009

Date Issued: 03/02/2007

1 IDENTIFICATION OF THE SUBSTANCE/PREPARATION AND THE COMPANY / UNDERTAKING

| | |
|----------------------------|---|
| Product name | Nickel nanopowder, 60 - 80 nm |
| Product code | NM-0028-HP |
| Supplier | IoLiTec Ionic Liquids Technologies GmbH Salzstrasse 184 D-74076 Heilbronn Germany |
| Telephone | +49 (0)7131 - 898390 |
| Fax | +49 (0)7131 - 89839109 |
| Emergency telephone | +49 (0)179 - 5322578 |

2 COMPOSITION / INFORMATION ON INGREDIENTS

| | |
|------------------------------|--------------------------|
| Ingredient name | Nickel powder |
| Empirical Formula | Ni |
| CAS No. | 7440-02-0 |
| Molecular weight | 58.71 amu |
| Purity | 99.9% |
| Average particle size | 60-80 nm |
| Specific Surface Area | 8 - 10 m ² /g |
| Colour | black |
| Morphology | spherical |
| Bulk Density | - |
| True Density | 8.9 g/cm ³ |
| Melting point | - |

Technical Data Sheet

Titanium Nanopowder, 60 - 80 nm

Revision Date: 03/06/2009

Date Issued: 03/02/2007

1 IDENTIFICATION OF THE SUBSTANCE/PREPARATION AND THE COMPANY / UNDERTAKING

| | |
|----------------------------|---|
| Product name | Titanium nanopowder, 60 - 80 nm |
| Product code | NM-0031-HP |
| Supplier | IoLiTec Ionic Liquids Technologies GmbH Salzstrasse 184 D-74076 Heilbronn Germany |
| Telephone | +49 (0)7131 - 898390 |
| Fax | +49 (0)7131 - 89839109 |
| Emergency telephone | +49 (0)179 - 5322578 |

2 COMPOSITION / INFORMATION ON INGREDIENTS

| | |
|------------------------------|------------------------------|
| Ingredient name | Titanium powder |
| Empirical formula | Ti |
| CAS No. | 7440-32-6 |
| Molecular weight | 47.87 amu |
| Purity | 99% |
| Average Particle Size | 60 - 80 nm (TEM) |
| Specific Surface Area | 13.8 m ² /g (BET) |
| Colour | Black |
| Morphology | Spherical |
| Bulk Density | N/A |
| True Density | 2.86 g/cm ³ |
| Melting point | N/A |



Figure D.1: Nanoparticles acquired from Iolitec.

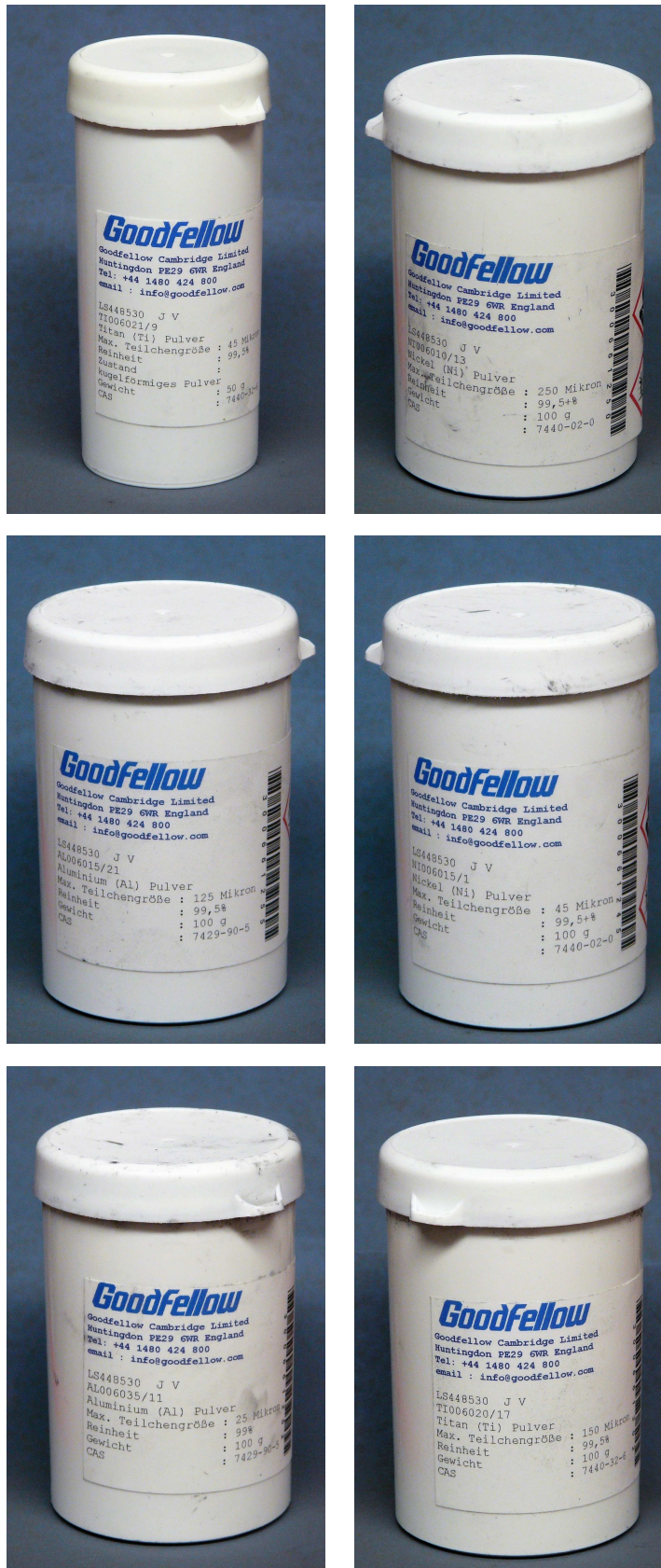


Figure D.2: Micropowders acquired from GoodFellow.

Bibliography

- [1] J. Braeuer, J. Besser, M. Wiemer, and T. Gessner, “A novel technique for MEMS packaging: Reactive bonding with integrated material systems”, in *Sensors and Actuators, A: Physical*, vol. 188, Elsevier B.V., 2012, pp. 212–219. doi: 10.1016/j.sna.2012.01.015 (cit. on pp. ix, xi, 22, 26, 33).
- [2] T. P. Weihs, O. M. Knio, M. Reiss, and K. J. Blobaum, “Reactive Multi-layer Structures for ease of processing and enhanced ductility”, US Patent 2013033834, 2001 (cit. on pp. ix, xi, 52).
- [3] A. B. Mann, A. J. Gavens, M. E. Reiss, D. Van Heerden, G. Bao, and T. P. Weihs, “Modeling and characterizing the propagation velocity of exothermic reactions in multilayer foils”, *Journal of Applied Physics*, vol. 82, no. 3, p. 1178, 1997, issn: 00218979. doi: 10.1063/1.365886 (cit. on pp. ix, xi, 29).
- [4] Infineon Technologies Austria and CTR Carinthian Tech Research AG. (2016). EPPL - Enhanced Power Pilot Line, [Online]. Available: <http://www.eppl-project.eu/> (visited on 06/26/2017) (cit. on p. 1).
- [5] J. Baron, E. Mounier, and L. Robin, “MEMS Packaging Market & Technology Trends”, Tech. Rep., 2012, p. 310 (cit. on pp. 1, 9, 10).
- [6] G. Zhang, M. Graef, and F. van Roosmalen, “The paradigm of “more than moore””, in *56th Electronic Components and Technology Conference 2006*, IEEE, 2006, pp. 151–157, isbn: 1-4244-0152-6. doi: 10.1109/ECTC.2006.1645639 (cit. on p. 1).
- [7] B. Rader-Brunner, “Boosting Energy Efficiency with New Electronics”, *CTR times special issue EPPL project*, 2016 (cit. on p. 2).
- [8] J. Shang, “A novel wafer level hermetic packaging for MEMS devices using micro glass cavities fabricated by a hot forming process”, *2010 11th International Conference on Electronic Packaging Technology & High Density Packaging*, pp. 921–924, 2010. doi: 10.1109/ICEPT.2010.5582657 (cit. on p. 2).

- [9] M. Lenzhofer. (2014). MOEMS-Modul-Martin-Lenzhofer, [Online]. Available: <http://www.ctr.at/newspressevideos/presseaussendungen/presseaussendung-von-ctr/martin-lenzhofer-gewinnt-pcb-design-award/70cd53a10aa04310c1ae06f86a1c8734.html> (visited on 09/23/2016) (cit. on p. 3).
- [10] K. Najafi, “Micropackaging technologies for integrated microsystems: Applications to MEMS and MOEMS”, *Micromachining and Microfabrication*, vol. 4979, J. A. Yasaitis, M. A. Perez-Maher, and J. M. Karam, Eds., pp. 1–19, 2003. doi: 10.1117/12.484953 (cit. on pp. 3, 9, 10).
- [11] M. E. Motamedi, “Micro-opto-electro-mechanical systems”, *Optical Engineering*, vol. 33, no. 11, p. 3505, 1994, issn: 0091-3286. doi: 10.1117/12.181572 (cit. on p. 4).
- [12] H. Goldschmidt and C. Vautin, “Aluminium as a heating and reducing agent”, *Journal of the Society of Chemical Industry*, vol. 17, no. 6, pp. 543–545, 1898, issn: 03684075. doi: 10.1002/jctb.5000170601 (cit. on pp. 3, 27).
- [13] T. P. Weihs and M. Reiss, “Method of making reactive multilayer foil and resulting product”, US Patent 6534194, 2001 (cit. on pp. 3, 33).
- [14] M. D. Wiemer, J. Braeuer, D. Wünsch, and T. Gessner, “Reactive Bonding and Low Temperature Bonding of Heterogeneous Materials”, *ECS Transactions*, vol. 33, no. 4, pp. 307–318, 2010 (cit. on pp. 5, 33, 35).
- [15] M. Wiemer and K. Vogel. (2014). Reaktives bonden mit multi-nanoschichtsystemen, [Online]. Available: https://www.enas.fraunhofer.de/content/dam/enas/de/documents/Downloads/datenblaetter/ReaktivesBonden_DE_web.pdf (visited on 06/26/2017) (cit. on p. 5).
- [16] C. O’Neal, A. Malshe, S. Singh, W. Brown, and W. Eaton, “Challenges in the packaging of MEMS”, in *Proceedings International Symposium on Advanced Packaging Materials. Processes, Properties and Interfaces (IEEE Cat. No.99TH8405)*, vol. 22, IMAPS - Int. Microelectron. & Packaging Soc, 1999, pp. 41–47, isbn: 0-930815-56-4. doi: 10.1109/ISAPM.1999.757284 (cit. on p. 9).
- [17] H. Henmi, S. Shoji, Y. Shoji, K. Yoshimi, and M. Esashi, “Vacuum packaging for microsensors by glass-silicon anodic bonding”, *Sensors and Actuators A: Physical*, vol. 43, no. 1-3, pp. 243–248, 1994, issn: 09244247. doi: 10.1016/0924-4247(94)80003-0 (cit. on pp. 9, 14, 26).
- [18] B. Shivkumar and C. J. Kim, “Microrivets for MEMS packaging: Concept, fabrication, and strength testing”, *Journal of Microelectromechanical Systems*, vol. 6, no. 3, pp. 217–225, 1997, issn: 10577157. doi: 10.1109/84.623110 (cit. on p. 9).

- [19] J. T. Butler, V. M. Bright, P. B. Chu, and R. J. Saia, "Adapting multi-chip module foundries for MEMS packaging", *Proceedings. 1998 International Conference on Multichip Modules and High Density Packaging (Cat. No.98EX154)*, pp. 106–111, 1998. doi: 10.1109/ICMCM.1998.670763 (cit. on p. 9).
- [20] M. M. Torunbalci, S. E. Alper, and T. Akin, "Advanced MEMS Process for Wafer Level Hermetic Encapsulation of MEMS Devices Using SOI Cap Wafers With Vertical Feedthroughs", *Journal of Microelectromechanical Systems*, no. c, pp. 2–3, 2015, issn: 10577157. doi: 10.1109/JMEMS.2015.2406341 (cit. on p. 9).
- [21] F. Niklaus and M. Lapisa, "Wafer-level heterogeneous 3D integration for MEMS and NEMS", *2012 3rd IEEE International Workshop on Low Temperature Bonding for 3D Integration (LTB-3D)*, no. 288670, pp. 247–252, 2012. doi: 10.1109/LTB-3D.2012.6238096 (cit. on p. 10).
- [22] R. Pelzer, "Wafer-to-wafer bonding techniques: From MEMS packaging to IC integration applications", *Electronic Packaging Technology, 2005 6th International Conference on*, 2005. doi: 10.1109/ICEPT.2005.1564704 (cit. on p. 14).
- [23] T. Suga, "Low temperature bonding for 3D integration – A review of the surface activated bonding (SAB)", in *2012 3rd IEEE International Workshop on Low Temperature Bonding for 3D Integration*, IEEE, May 2012, pp. 7–10, isbn: 978-1-4673-0742-0. doi: 10.1109/LTB-3D.2012.6238040 (cit. on p. 14).
- [24] J. W. J. W. Gardner and V. K. Varadan, *Microsensors, MEMS and smart devices*. Wiley, 2001, isbn: 047186109X. doi: 10.1002/9780470846087 (cit. on p. 14).
- [25] J. G. Korvink and O. Paul, *MEMS: A Practical Guide to Design, Analysis, and Applications*. Berlin, Heidelberg: Springer Berlin Heidelberg, 2006, p. 979, isbn: 978-3-540-21117-4. doi: 10.1007/978-3-540-33655-6 (cit. on pp. 14, 26).
- [26] K. Schjølberg-Henriksen, E. Poppe, S. Moe, P. Storås, M. M. V. Taklo, D. T. Wang, and H. Jakobsen, "Anodic bonding of glass to aluminium", *Microsystem Technologies*, vol. 12, no. 5, pp. 441–449, 2005, issn: 0946-7076. doi: 10.1007/s00542-005-0040-8 (cit. on pp. 14, 26).
- [27] G. Wallis and D. I. Pomerantz, "Field assisted glass-metal sealing", *Journal of Applied Physics*, vol. 40, no. 10, pp. 3946–3949, 1969, issn: 00218979. doi: 10.1063/1.1657121 (cit. on pp. 14, 26).
- [28] Z. Cui, "Anodic Bonding", in *Encyclopedia of Microfluidics and Nanofluidics*, New York, NY: Springer New York, 2015, pp. 68–73. doi: 10.1007/978-1-4614-5491-5_41 (cit. on pp. 14, 26).

- [29] S. Mack, “Eine vergleichende Untersuchung der physikalisch-chemischen Prozesse an der Grenzschicht direkt und anodisch verbundener Festkörper”, German, Zugl.: Halle, Saale, Univ., Diss., PhD thesis, Düsseldorf, 1997, isbn: 3-18-343602-7 (cit. on pp. 15, 26).
- [30] J. Wei, Z. Wang, H. Xie, and Ng Fern Lan, “Role of bonding temperature and voltage in silicon-to-glass anodic bonding”, in *4th Electronics Packaging Technology Conference, 2002.*, IEEE, 2002, pp. 85–90, isbn: 0-7803-7435-5. doi: 10.1109/EPTC.2002.1185603 (cit. on pp. 15, 26).
- [31] S. Langa, C. Drabe, C. Kunath, A. Dreyhaupt, and H. Schenk, “Wafer level vacuum packaging of scanning micro-mirrors using glass-frit and anodic bonding methods”, R. Ramesham and H. R. Shea, Eds., vol. 8614, 2013, 86140F. doi: 10.1117/12.2003525 (cit. on pp. 15, 26).
- [32] Z. Cui, “Wafer Bonding”, in *Encyclopedia of Microfluidics and Nanofluidics*, 2, vol. 1, New York, NY: Springer New York, 2015, pp. 3473–3478, isbn: 978-0-387-32468-5. doi: 10.1007/978-1-4614-5491-5_1682 (cit. on pp. 15, 18, 26).
- [33] U. Gösele, Q. Y. Tong, A. Schumacher, G. Kräuter, M. Reiche, A. Plößl, P. Kopperschmidt, T. H. Lee, and W. J. Kim, “Wafer bonding for microsystems technologies”, *Sensors and Actuators, A: Physical*, vol. 74, no. 1, pp. 161–168, 1999, issn: 09244247. doi: 10.1016/S0924-4247(98)00310-0 (cit. on pp. 15, 26).
- [34] J. B. Lasky, “Wafer bonding for silicon-on-insulator technologies”, *Applied Physics Letters*, vol. 48, no. 1, pp. 78–80, Jan. 1986, issn: 0003-6951. doi: 10.1063/1.96768 (cit. on pp. 15, 26).
- [35] U. Gösele and Q.-Y. Tong, “Semiconductor Wafer Bonding”, *Annual Review of Materials Science*, vol. 28, no. 1, pp. 215–241, 1998, issn: 0084-6600. doi: 10.1146/annurev.matsci.28.1.215 (cit. on p. 15).
- [36] V. Dragoi, G. Mittendorfer, C. Thanner, and P. Lindner, “Wafer-level plasma activated bonding: New technology for MEMS fabrication”, *Microsystem Technologies*, vol. 14, no. 4-5, pp. 509–515, 2008, issn: 0946-7076. doi: 10.1007/s00542-007-0437-7 (cit. on pp. 16, 26).
- [37] T. Plach, V. Dragoi, G. Mittendorfer, M. Wimplinger, and K. Hingerl, “Wafer Bonding of Plasma Activated Surfaces”, in *ECS Transactions*, vol. 13, ECS, 2008, pp. 39–45, isbn: 9781605606637. doi: 10.1149/1.3007997 (cit. on pp. 16, 26).
- [38] R. Pelzer, P. Kettner, and D. Lee, “Wafer-level packaging of ic devices”, in *Proceedings of the 6th International Conference on Electronic Materials and Packaging (EMAP) 2004*, 2004, pp. 18–21 (cit. on pp. 16, 26).

- [39] K. Schjøberg-Henriksen, S. Moe, M. M. V. Taklo, P. Storås, and J. H. Ulvensøen, “Low-temperature plasma activated bonding for a variable optical attenuator”, *Sensors and Actuators A: Physical*, vol. 142, no. 1, pp. 413–420, 2008, issn: 09244247. doi: 10.1016/j.sna.2007.02.020 (cit. on pp. 16, 26).
- [40] V. Dragoi and S. Farrens, “Low temperature mems manufacturing processes: Plasma activated wafer bonding”, in *MRS Proceedings*, Cambridge Univ Press, vol. 872, 2005, J7–1 (cit. on pp. 16, 26).
- [41] G. Harman, *Wire Bonding in Microelectronics*, 3rd ed. McGraw-Hill, 2010, p. 446, isbn: 978-0-07-164265-1 (cit. on pp. 17, 26).
- [42] J. Kim, M. Chiao, and L. Lin, “Ultrasonic bonding of In/Au and Al/Al for hermetic sealing of MEMS packaging”, in *Technical Digest. MEMS 2002 IEEE International Conference. Fifteenth IEEE International Conference on Micro Electro Mechanical Systems (Cat. No.02CH37266)*, IEEE, 2002, pp. 415–418, isbn: 0-7803-7185-2. doi: 10.1109/MEMSYS.2002.984291 (cit. on pp. 17, 26).
- [43] J. Kim, B. Jeong, M. Chiao, and L. Lin, “Ultrasonic Bonding for MEMS Sealing and Packaging”, *IEEE Transactions on Advanced Packaging*, vol. 32, no. 2, pp. 461–467, 2009, issn: 1521-3323. doi: 10.1109/TADVP.2008.2009927 (cit. on pp. 17, 26).
- [44] R. Knechtel, “Glass frit bonding: an universal technology for wafer level encapsulation and packaging”, *Microsystem Technologies*, vol. 12, no. 1-2, pp. 63–68, 2005, issn: 0946-7076. doi: 10.1007/s00542-005-0022-x (cit. on pp. 18, 26).
- [45] G. Wu, D. Xu, X. Sun, B. Xiong, and Y. Wang, “Wafer-level vacuum packaging for microsystems using glass frit bonding”, *IEEE Transactions on Components, Packaging and Manufacturing Technology*, vol. 3, no. 10, pp. 1640–1646, Oct. 2013, issn: 2156-3950. doi: 10.1109/TCPMT.2013.2279135 (cit. on pp. 18, 26).
- [46] S. Langa, C. Drabe, A. Herrmann, T. Ludewig, A. Rieck, A. Flemming, and C. Kaden, “Wafer level vacuum packaging of micro-mirrors with buried signal lines”, *Microsystem Technologies*, vol. 21, no. 5, pp. 1021–1028, 2015, issn: 1432-1858. doi: 10.1007/s00542-015-2433-7 (cit. on pp. 18, 26).
- [47] J.-S. Chang, J.-Y. Lin, S.-C. Ho, and Y.-J. Lee, “Wafer level glass frit bonding for MEMS hermetic packaging”, in *2010 5th International Microsystems Packaging Assembly and Circuits Technology Conference*, IEEE, Oct. 2010, pp. 1–4, isbn: 978-1-4244-9783-6. doi: 10.1109/IMPACT.2010.5699614 (cit. on pp. 18, 26, 44).

- [48] V. Stenchly, H.-J. J. Quenzer, U. Hofmann, C. Eisermann, and W. Benecke, “Viscous hot glass forming for optical wafer level packaging of micro mirrors”, *Procedia Engineering*, vol. 47, pp. 64–67, 2012, issn: 18777058. doi: 10.1016/j.proeng.2012.09.085 (cit. on pp. 18, 26).
- [49] G. Hu, “Mechanism of glass-frit fracture in MEMS packaging”, in *2012 13th International Conference on Electronic Packaging Technology & High Density Packaging*, IEEE, Aug. 2012, pp. 1564–1568, isbn: 978-1-4673-1681-1. doi: 10.1109/ICEPT-HDP.2012.6474905 (cit. on pp. 18, 26).
- [50] M. M. V. Taklo, P. Storås, K. Schjølberg-Henriksen, H. K. Hasting, and H. Jakobsen, “Strong, high-yield and low-temperature thermocompression silicon wafer-level bonding with gold”, *Journal of Micromechanics and Microengineering*, vol. 14, no. 7, pp. 884–890, 2004, issn: 0960-1317. doi: 10.1088/0960-1317/14/7/007 (cit. on pp. 18, 26).
- [51] C. S. Tan, J. Fan, D. F. Lim, G. Y. Chong, and K. H. Li, “Low temperature wafer-level bonding for hermetic packaging of 3D microsystems”, *Journal of Micromechanics and Microengineering*, vol. 21, no. 7, p. 175 006, 2011, issn: 0960-1317. doi: 10.1088/0960-1317/21/7/075006 (cit. on pp. 18, 26).
- [52] J. Froemel, M. Baum, M. Wiemer, F. Roscher, M. Haubold, C. Jia, and T. Gessner, “Investigations of thermocompression bonding with thin metal layers”, in *2011 16th International Solid-State Sensors, Actuators and Microsystems Conference*, IEEE, Jun. 2011, pp. 990–993, isbn: 978-1-4577-0157-3. doi: 10.1109/TRANSDUCERS.2011.5969495 (cit. on pp. 18, 19, 26).
- [53] M. Baum, Chenping Jia, M. Haubold, M. Wiemer, A. Schneider, H. Rank, A. Trautmann, and T. Gessner, “Eutectic wafer bonding for 3-D integration”, in *3rd Electronics System Integration Technology Conference ESTC*, IEEE, Sep. 2010, pp. 1–6, isbn: 978-1-4244-8553-6. doi: 10.1109/ESTC.2010.5642870 (cit. on pp. 19, 26).
- [54] R. F. Wolffenbuttel and K. D. Wise, “Low-temperature silicon wafer-to-wafer bonding using gold at eutectic temperature”, *Sensors and Actuators: A. Physical*, vol. 43, no. 1-3, pp. 223–229, 1994, issn: 09244247. doi: 10.1016/0924-4247(93)00653-L (cit. on pp. 19, 26).
- [55] S. Cvetkovic, R. Kruppe, and L. Rissing, “Technology development for packaging of the gmr-sensor via eutectic bonding”, *Proceedings Smart System Integration*, no. March, p. 17, 2013 (cit. on pp. 19, 26).
- [56] V. Dragoi, T. Glinsner, G. Mittendorfer, B. Wieder, and P. Lindner, “Adhesive wafer bonding for MEMS applications”, in *Proceedings of SPIE*, J.-C. Chiao, V. K. Varadan, and C. Can, Eds., vol. 5116, Apr. 2003, p. 160. doi: 10.1117/12.499077 (cit. on pp. 20, 26).

- [57] S. Satyanarayana, R. N. Karnik, and A. Majumdar, “Stamp-and-stick room-temperature bonding technique for microdevices”, *Journal of Microelectromechanical Systems*, vol. 14, no. 2, pp. 392–399, 2005, issn: 1057-7157. doi: 10.1109/JMEMS.2004.839334 (cit. on pp. 20, 26).
- [58] M. Schmidt, “Wafer-to-wafer bonding for microstructure formation”, *Proceedings of the IEEE*, vol. 86, no. 8, pp. 1575–1585, 1998, issn: 00189219. doi: 10.1109/5.704262 (cit. on pp. 20, 26).
- [59] B. Boettge, J. Braeuer, M. Wiemer, M. Petzold, J. Bagdahn, and T. Gessner, “Fabrication and characterization of reactive nanoscale multilayer systems for low-temperature bonding in microsystem technology”, *Journal of Micromechanics and Microengineering*, vol. 20, no. 6, p. 164 018, 2010, issn: 0960-1317. doi: 10.1088/0960-1317/20/6/064018 (cit. on pp. 20, 26, 33, 34, 117).
- [60] Indium Corporation. (2016). NanoFoil Properties, [Online]. Available: <http://www.indium.com/nanofoil/properties/> (visited on 11/27/2016) (cit. on pp. 20, 26).
- [61] X. Qiu, D. Welch, J. B. Christen, J. Zhu, J. Oiler, C. Yu, Z. Wang, and H. Yu, “Reactive nanolayers for physiologically compatible microsystem packaging”, *Journal of Materials Science: Materials in Electronics*, vol. 21, no. 6, pp. 562–566, 2009, issn: 0957-4522. doi: 10.1007/s10854-009-9957-5 (cit. on pp. 20, 26).
- [62] A. Rogachev, S. Vadchenko, F. Baras, O. Politano, S. Rouvimov, N. Sachkova, and A. Mukasyan, “Structure evolution and reaction mechanism in the Ni/Al reactive multilayer nanofoils”, *Acta Materialia*, vol. 66, pp. 86–96, Mar. 2014, issn: 13596454. doi: 10.1016/j.actamat.2013.11.045 (cit. on pp. 20, 26).
- [63] J. Braeuer and T. Gessner, “A hermetic and room-temperature wafer bonding technique based on integrated reactive multilayer systems”, *Journal of Micromechanics and Microengineering*, vol. 24, no. 11, p. 115 002, 2014, issn: 0960-1317. doi: 10.1088/0960-1317/24/11/115002 (cit. on pp. 22, 26, 33).
- [64] J. Braeuer, J. Besser, M. Wiemer, and T. Gessner, “Room-temperature reactive bonding by using nano scale multilayer systems”, in *2011 16th International Solid-State Sensors, Actuators and Microsystems Conference*, IEEE, Jun. 2011, pp. 1332–1335, isbn: 978-1-4577-0157-3. doi: 10.1109/TRANSDUCERS.2011.5969498 (cit. on pp. 22, 26, 33).
- [65] J. Braeuer, J. Besser, S. Hertel, R. Masser, W. Schneider, M. Wiemer, and T. Gessner, “(invited) Reactive bonding with integrated reactive and nano scale energetic material systems (iRMS): State-of-the-art and future development trends”, *ECS Transactions*, vol. 64, no. 5, pp. 329–337, Oct. 2014,

- issn: 1938-6737. doi: 10.1149/06405.0329ecst (cit. on pp. 22, 26, 35, 117).
- [66] K. Vogel and M. Wiemer, “Reaktives Bonden mit Multi-Nanoschicht-Systemen”, Fraunhofer ENAS, Tech. Rep., 2014, p. 2 (cit. on pp. 22, 26).
- [67] J. Braeuer, J. Besser, E. Tomoscheit, D. Klimm, S. Anbumani, M. Wiemer, and T. Gessner, “Investigation of Different Nano Scale Energetic Material Systems for Reactive Wafer Bonding”, *ECS Transactions*, vol. 50, no. 7, pp. 241–251, Mar. 2013, issn: 1938-6737. doi: 10.1149/05007.0241ecst (cit. on pp. 22, 26, 117).
- [68] W. C. Welch III, J. C. J. Chae, S.-H. L. S.-H. Lee, N. Yazdi, and K. Najafi, “Transient liquid phase (TLP) bonding for microsystem packaging applications”, *Proc. 13th International Conference on Solid-State Sensors, Actuators and Microsystems*, pp. 1350–1353, 2005. doi: 10.1109/SENSOR.2005.1497331 (cit. on pp. 23, 26).
- [69] N. Budhiman, B. Jensen, S. Chemnitz, and B. Wagner, “High temperature investigation on a nickel–tin transient liquid-phase wafer bonding up to 600°”, *Microsystem Technologies*, 2015, issn: 0946-7076. doi: 10.1007/s00542-015-2738-6 (cit. on pp. 23, 26).
- [70] W. C. Welch III, “Vacuum and Hermetic Packaging of MEMS Using Solder”, PhD thesis, University of Michigan, 2008, p. 219 (cit. on pp. 23, 26).
- [71] S. Marauska, M. Claus, T. Lisec, and B. Wagner, “Low temperature transient liquid phase bonding of Au/Sn and Cu/Sn electroplated material systems for MEMS wafer-level packaging”, *Microsystem Technologies*, vol. 19, no. 8, pp. 1119–1130, 2013, issn: 09467076. doi: 10.1007/s00542-012-1708-5 (cit. on pp. 23, 26).
- [72] Y. Tao, A. P. Malshe, and W. D. Brown, “Laser Bonding and Modeling for Wafer-Level and Chip-Scale Packaging of Micro-Electro-Mechanical Systems”, in *Electronic and Photonic Packaging, Electrical Systems Design and Photonics, and Nanotechnology*, vol. 2002, ASME, 2002, pp. 55–60, isbn: 0-7918-3648-7. doi: 10.1115/IMECE2002-39271 (cit. on pp. 23, 26).
- [73] Y. Tao, A. P. Malshe, W. D. Brown, D. R. DeReus, and S. Cunningham, “Laser-assisted sealing and testing for ceramic packaging of MEMS devices”, *IEEE Transactions on Advanced Packaging*, vol. 26, no. 3, pp. 283–288, 2003, issn: 15213323. doi: 10.1109/TADVP.2003.817969 (cit. on pp. 23, 26).
- [74] Y. Tao, A. P. Malshe, and W. D. Brown, “Selective bonding and encapsulation for wafer-level vacuum packaging of MEMS and related micro systems”, *Microelectronics Reliability*, vol. 44, no. 2, pp. 251–258, 2004, issn: 00262714. doi: 10.1016/S0026-2714(03)00192-6 (cit. on pp. 24, 26).

- [75] H. Kirchberger, P. Lindler, and M. Wimpliger, “Novel bonding technologies for wafer-level transparent packaging of MOEMS”, *ArXiv preprint arXiv:0802.3103*, no. April 2007, pp. 25–27, 2008 (cit. on p. 26).
- [76] H. Goldschmidt, *Reactions: A Quarterly Publication Devoted to the Science of Aluminothermics*, 1. New York: Goldschmidt Thermit Company, 1908, vol. 1 (cit. on p. 27).
- [77] J. J. Moore and H. J. Feng, “Combustion synthesis of advanced materials: Part II. Classification, applications and modelling”, *Progress in Materials Science*, vol. 39, no. 4-5, pp. 275–316, 1995, issn: 00796425. doi: 10.1016/0079-6425(94)00012-3 (cit. on pp. 27, 29, 55, 130).
- [78] A. G. Merzhanov, “History and recent developments in SHS”, *Ceramics International*, vol. 21, no. 5, pp. 371–379, 1995, issn: 02728842. doi: 10.1016/0272-8842(95)96211-7 (cit. on p. 28).
- [79] G. Sauthoff, *Intermetallics*. Weinheim, New York: Wiley VCH, 1995, isbn: 9783527615407 (cit. on pp. 28, 55).
- [80] V. I. Itin, A. D. Bratchikov, V. N. Doronin, and G. A. Pribytkov, “Formation of self-propagating high-temperature synthesis products in Ti-Ni and Ti-Co systems”, *Soviet Physics Journal*, vol. 24, no. 12, pp. 1134–1139, 1981, issn: 0038-5697. doi: 10.1007/BF00893742 (cit. on p. 29).
- [81] K. Morsi, “The diversity of combustion synthesis processing: A review”, *Journal of Materials Science*, vol. 47, pp. 68–92, 2012, issn: 00222461. doi: 10.1007/s10853-011-5926-5 (cit. on p. 29).
- [82] J. Subrahmanyam and M. Vijayakumar, “Self-propagating high-temperature synthesis”, *Journal of Materials Science*, vol. 27, no. 23, pp. 6249–6273, 1992, issn: 0022-2461. doi: 10.1007/BF00576271 (cit. on p. 29).
- [83] J. J. Moore and H. J. Feng, “Combustion synthesis of advanced materials: Part I. Reaction parameters”, *Progress in Materials Science*, vol. 39, no. 4-5, pp. 243–273, 1995, issn: 00796425. doi: 10.1016/0079-6425(94)00011-5 (cit. on p. 29).
- [84] H. C. Yi and J. J. Moore, “Self-propagating high-temperature (combustion) synthesis (SHS) of powder-compacted materials”, *Journal of Materials Science*, vol. 25, pp. 1159–1168, 1990, issn: 00222461. doi: 10.1007/BF00585421 (cit. on p. 29).
- [85] I. E. Gunduz, K. Fadenberger, M. Kokonou, C. Rebholz, C. C. Doumanidis, and T. Ando, “Modeling of the self-propagating reactions of nickel and aluminum multilayered foils”, *Journal of Applied Physics*, vol. 105, no. 7, pp. 1–9, 2009, issn: 00218979. doi: 10.1063/1.3091284 (cit. on p. 29).

- [86] P. M. Krishenik, S. A. Rogachev, and K. G. Shkadinsky, "Combustion of multilayer systems with random layer thickness distribution: Mathematical modeling", *International Journal of Self-Propagating High-Temperature Synthesis*, vol. 21, no. 2, pp. 83–88, 2012, issn: 1061-3862. doi: 10.3103/S1061386212020057 (cit. on p. 29).
- [87] L. Wang, B. He, and X. H. Jiang, "Modeling the velocity of self-propagating exothermic reactions in multilayer foils", *Combustion Science and Technology*, vol. 182, no. 8, pp. 1000–1008, 2010, issn: 0010-2202. doi: 10.1080/00102200903489311 (cit. on p. 29).
- [88] M. J. Cherukara, T. P. Weihs, and A. Strachan, "Molecular dynamics simulations of the reaction mechanism in Ni/Al reactive intermetallics", *Acta Materialia*, vol. 96, pp. 1–9, 2015, issn: 13596454. doi: 10.1016/j.actamat.2015.06.008 (cit. on p. 29).
- [89] B. J. Henz, T. Hawa, and M. Zachariah, "Molecular dynamics simulation of the kinetic sintering of Ni and Al nanoparticles", *Molecular Simulation*, vol. 35, no. 10-11, pp. 804–811, 2009, issn: 0892-7022. doi: 10.1080/08927020902818021 (cit. on pp. 29, 32, 33).
- [90] M. Salloum and O. M. Knio, "Simulation of reactive nanolaminates using reduced models: I. Basic formulation", *Combustion and Flame*, vol. 157, no. 2, pp. 288–295, 2010, issn: 0010-2180. doi: 10.1016/j.combustflame.2009.06.019 (cit. on p. 29).
- [91] M. Salloum and O. M. Knio, "Simulation of reactive nanolaminates using reduced models: II. Normal propagation", *Combustion and Flame*, vol. 157, no. 3, pp. 436–445, 2010, issn: 0010-2180. doi: 10.1016/j.combustflame.2009.08.010 (cit. on p. 29).
- [92] M. Salloum and O. M. Knio, "Simulation of reactive nanolaminates using reduced models: III. Ingredients for a general multidimensional formulation", *Combustion and Flame*, vol. 157, no. 6, pp. 1154–1166, 2010, issn: 0010-2180. doi: 10.1016/j.combustflame.2009.10.005 (cit. on p. 29).
- [93] E. V. Levchenko, A. V. Evteev, D. P. Riley, I. V. Belova, and G. E. Murch, "Molecular dynamics simulation of the alloying reaction in Al-coated Ni nanoparticle", *Computational Materials Science*, vol. 47, no. 3, pp. 712–720, 2010, issn: 09270256. doi: 10.1016/j.commatsci.2009.10.014 (cit. on p. 29).
- [94] S. P. Kiselev and E. V. Zhurov, "Molecular-dynamics simulation of the synthesis of intermetallic Ti–Al", *Intermetallics*, vol. 49, pp. 106–114, 2014, issn: 09669795. doi: 10.1016/j.intermet.2014.01.008 (cit. on p. 29).
- [95] B. J. Henz, T. Hawa, and M. Zachariah, "Molecular Dynamics Simulation of the Kinetic Reaction of Nickel and Aluminum Nanoparticles", no. March, 2010 (cit. on p. 29).

- [96] V. I. Yukhvid, “Modifications of SHS processes”, *Pure and Applied Chemistry*, vol. 64, no. 7, Jan. 1992, issn: 1365-3075. doi: 10.1351/pac199264070977 (cit. on p. 29).
- [97] Y. N. Picard, D. P. Adams, J. a. Palmer, and S. M. Yalisove, “Pulsed laser ignition of reactive multilayer films”, *Applied Physics Letters*, vol. 88, no. 14, p. 144 102, 2006, issn: 00036951. doi: 10.1063/1.2191952 (cit. on p. 29).
- [98] E. L. Dreizin, “Metal-based reactive nanomaterials”, *Progress in Energy and Combustion Science*, vol. 35, no. 2, pp. 141–167, Apr. 2009, issn: 03601285. doi: 10.1016/j.pecs.2008.09.001 (cit. on pp. 29, 79, 86).
- [99] D. M. Makowiecki and R. M. Bionta, “Low temperature reactive bonding”, US Patent 5381944, 1995 (cit. on p. 29).
- [100] X. Zhou, M. Torabi, J. Lu, R. Shen, and K. Zhang, “Nanostructured energetic composites: synthesis, ignition/combustion modeling, and applications.”, *ACS applied materials & interfaces*, vol. 6, no. 5, pp. 3058–74, 2014, issn: 1944-8252. doi: 10.1021/am4058138 (cit. on pp. 29, 79, 86).
- [101] S. Dong, P. Hou, H. Yang, and G. Zou, “Synthesis of intermetallic NiAl by SHS reaction using coarse-grained nickel and ultrafine-grained aluminum produced by wire electrical explosion”, *Intermetallics*, vol. 10, no. 3, pp. 217–223, 2002, issn: 09669795. doi: 10.1016/S0966-9795(01)00109-1 (cit. on p. 29).
- [102] A. Swiston, T. Hufnagel, and T. Weihs, “Joining bulk metallic glass using reactive multilayer foils”, *Scripta Materialia*, vol. 48, no. 12, pp. 1575–1580, Jun. 2003, issn: 13596462. doi: 10.1016/S1359-6462(03)00164-7 (cit. on pp. 29, 33).
- [103] G. Dietrich, S. Braun, P. Gawlitza, and A. Leson, “Reaktive Nanometer-Multischichten als maßgeschneiderte Wärmequellen beim Fügen”, German, *Vakuum in Forschung und Praxis*, vol. 21, no. 1, pp. 15–21, 2009, issn: 0947076X. doi: 10.1002/vipr.200900375 (cit. on p. 29).
- [104] S. Apperson, R. V. Shende, S. Subramanian, D. Tappmeyer, S. Gangopadhyay, Z. Chen, K. Gangopadhyay, P. Redner, S. Nicholich, and D. Kapoor, “Generation of fast propagating combustion and shock waves with copper oxide/aluminum nanothermite composites”, *Applied Physics Letters*, vol. 91, no. 24, pp. 4–7, 2007, issn: 00036951. doi: 10.1063/1.2787972 (cit. on p. 29).
- [105] K. S. Martirosyan, L. Wang, A. Vicent, and D. Luss, “Nanoenergetic gas-generators: design and performance”, *Propellants, Explosives, Pyrotechnics*, vol. 34, no. 6, pp. 532–538, 2009, issn: 07213115. doi: 10.1002/prop.200800059 (cit. on p. 29).

Bibliography

- [106] K. T. Higa, “Energetic Nanocomposite Lead-Free Electric Primers”, *Journal of Propulsion and Power*, vol. 23, no. 4, pp. 722–727, 2007, issn: 0748-4658. doi: 10.2514/1.25354 (cit. on p. 29).
- [107] S. J. Apperson, A. V. Bezmelnitsyn, R. Thiruvengadathan, K. Gangopadhyay, S. Gangopadhyay, W. A. Balas, P. E. Anderson, and S. M. Nicolich, “Characterization of nanothermite material for solid-fuel microthruster applications”, *Journal of Propulsion and Power*, vol. 25, no. 5, pp. 1086–1091, 2009, issn: 0748-4658. doi: 10.2514/1.43206 (cit. on p. 29).
- [108] J. Wang, E. Besnoin, O. M. Knio, and T. P. Weihs, “Effects of physical properties of components on reactive nanolayer joining”, *Journal of Applied Physics*, vol. 97, no. 11, p. 114307, 2005, issn: 00218979. doi: 10.1063/1.1915540 (cit. on pp. 29, 33).
- [109] T. Weihs, “Fabrication and characterization of reactive multilayer films and foils”, in *Metallic Films for Electronic, Optical and Magnetic Applications*, Elsevier, 2014, pp. 160–243, isbn: 9780857090577. doi: 10.1533/9780857096296.1.160 (cit. on pp. 29, 34, 125).
- [110] S. S. Rybanin and S. L. Sobolev, “Velocity and combustion limits in a thermally thin condensed substance layer undergoing heat exchange with an inert medium”, *Combustion, Explosion, and Shock Waves*, vol. 25, no. 5, pp. 524–531, 1989, issn: 0010-5082. doi: 10.1007/BF00772962 (cit. on pp. 30, 32, 103).
- [111] S. S. Rybanin and S. L. Sobolev, “Velocity and limits of combustion of a thermally thick condensed substance layer exchanging heat with an inert medium”, *Combustion, Explosion, and Shock Waves*, vol. 25, no. 5, pp. 531–540, 1989, issn: 0010-5082. doi: 10.1007/BF00772963 (cit. on pp. 30, 103).
- [112] Рыбанин, С. С. and Соболев, С. Л., “Скорость и пределы горения термически толстого слоя конденсированного вещества при теплообмене с инертной средой”, *Russian, Физика горения и взрыва*, vol. 25, no. 5, pp. 16–25, 1989 (cit. on pp. 30, 31).
- [113] Рыбанин, С. С. and Соболев, С. Л., “Скорость и пределы горения термически тонкого слоя конденсированного вещества при теплообмене с инертной средой”, *Russian, Физика горения и взрыва*, vol. 25, no. 5, pp. 8–15, 1989 (cit. on pp. 30, 31).
- [114] J. Wang, E. Besnoin, O. M. Knio, and T. P. Weihs, “Investigating the effect of applied pressure on reactive multilayer foil joining”, *Acta Materialia*, vol. 52, no. 18, pp. 5265–5274, 2004, issn: 13596454. doi: 10.1016/j.actamat.2004.07.012 (cit. on p. 33).
- [115] X. Qiu, “Reactive Multilayer Foils and their Applications in Joining”, PhD thesis, Louisiana State University, 2007 (cit. on p. 33).

- [116] C. Pascal and R. M. Marin-Ayral, “Simultaneous synthesis and joining of a nicrally layer to a superalloy substrate by self-propagating high-temperature synthesis”, *Journal of Materials Synthesis and Processing*, vol. 9, no. 6, pp. 375–381, 2001, issn: 10647562. doi: 10.1023/A:1016364825219 (cit. on p. 33).
- [117] A. S. Mukasyan and J. D. E. White, “Combustion joining of refractory materials”, *International Journal of Self-Propagating High-Temperature Synthesis*, vol. 16, no. 3, pp. 154–168, 2007, issn: 1061-3862. doi: 10.3103/S1061386207030089 (cit. on pp. 33, 79, 86).
- [118] A. Duckham, J. E. Newson, M. V. Brown, T. R. Rude, O. Knio, E. M. Heian, and J. S. Subramanian, “Method for fabricating large dimension bonds using reactive multilayer joining”, US Patent 7354659, 2008 (cit. on p. 33).
- [119] A. Duckham, S. J. Spey, J. Wang, M. E. Reiss, T. P. Weihs, E. Besnoin, and O. M. Knio, “Reactive nanostructured foil used as a heat source for joining titanium”, *Journal of Applied Physics*, vol. 96, no. 4, p. 2336, 2004, issn: 00218979. doi: 10.1063/1.1769097 (cit. on p. 33).
- [120] J. Wang, “Joining of stainless-steel specimens with nanostructured Al/Ni foils”, *Journal of Applied Physics*, vol. 95, no. 1, p. 248, 2004, issn: 00218979. doi: 10.1063/1.1629390 (cit. on p. 33).
- [121] A. E. Sytschev, D. Vrel, O. D. Boyarchenko, S. G. Vadchenko, and N. V. Sachkova, “Load-assisted SHS joining of NiAl to Ni”, *International Journal of Self-Propagating High-Temperature Synthesis*, vol. 22, no. 1, pp. 52–55, 2013, issn: 1061-3862. doi: 10.3103/S1061386213010111 (cit. on p. 33).
- [122] X. Qiu and J. Wang, “Bonding silicon wafers with reactive multilayer foils”, *Sensors and Actuators A: Physical*, vol. 141, no. 2, pp. 476–481, 2008, issn: 09244247. doi: 10.1016/j.sna.2007.10.039 (cit. on p. 33).
- [123] J. G. Korvink, P. J. Smith, D. Y. Shin, O. Brand, G. K. Fedder, C. Hierold, and O. Tabata, *Inkjet-Based Micromanufacturing*, J. G. Korvink, P. J. Smith, and D.-Y. Shin, Eds., ser. Advanced Micro and Nanosystems. Weinheim, Germany: Wiley-VCH Verlag GmbH & Co. KGaA, 2012, isbn: 9783527647101. doi: 10.1002/9783527647101 (cit. on p. 38).
- [124] I. M. Hutchings and G. D. Martin, *Inkjet Technology for Digital Fabrication*. Wiley, 2012, isbn: 9781118452929 (cit. on p. 38).
- [125] B. Derby, “Inkjet Printing of Functional and Structural Materials: Fluid Property Requirements, Feature Stability, and Resolution”, *Annual Review of Materials Research*, vol. 40, no. 1, pp. 395–414, 2010, issn: 1531-7331. doi: 10.1146/annurev-matsci-070909-104502 (cit. on pp. 39–41).
- [126] “Weber Number”, in *Encyclopedia of Microfluidics and Nanofluidics*, D. Li, Ed., Boston, MA: Springer US, 2008, pp. 2185–2185. doi: 10.1007/978-0-387-48998-8_1689 (cit. on p. 40).

Bibliography

- [127] “Reynolds Number”, in *Encyclopedia of Microfluidics and Nanofluidics*, D. Li, Ed., Boston, MA: Springer US, 2008, pp. 1790–1790. doi: 10.1007/978-0-387-48998-8_1358 (cit. on p. 40).
- [128] “Ohnesorge Number”, in *Encyclopedia of Microfluidics and Nanofluidics*, Dongqing Li, Ed., Boston, MA: Springer US, 2008, pp. 1513–1513. doi: 10.1007/978-0-387-48998-8_1141 (cit. on p. 40).
- [129] G. H. McKinley and M. Renardy, “Wolfgang von Ohnesorge”, *Physics of Fluids*, vol. 23, no. 12, p. 127 101, Dec. 2011, issn: 1070-6631. doi: 10.1063/1.3663616 (cit. on p. 40).
- [130] Magdassi, “Ink requirements and formulations guidelines”, in *The Chemistry of Inkjet Inks*, S. Magdassi, Ed., World Scientific Publishing Co. Pte. Ltd., 2010, ch. 2, pp. 19–42, isbn: 9789812818218 (cit. on p. 40).
- [131] C. Yaws, *Chemical properties handbook: Physical, thermodynamics, environmental transport, safety & health related properties for organic &*, ser. Chemical engineering books. McGraw-Hill Education, 1999, isbn: 9780070734012 (cit. on p. 40).
- [132] G. Vazquez, E. Alvarez, and J. M. Navaza, “Surface Tension of Alcohol Water + Water from 20 to 50°C”, *Journal of Chemical & Engineering Data*, vol. 40, no. 3, pp. 611–614, May 1995, issn: 0021-9568. doi: 10.1021/je00019a016 (cit. on p. 40).
- [133] B. H. King, M. J. Renn, M. Essien, G. J. Marquez, M. G. Giridharan, and J.-C. Sheu, “Annular aerosol jet deposition using an extended nozzle”, US Patent 7938079B2, May 2011 (cit. on p. 43).
- [134] J. H. Cho, J. Lee, Y. Xia, B. Kim, Y. He, M. J. Renn, T. P. Lodge, and C. Daniel Frisbie, “Printable ion-gel gate dielectrics for low-voltage polymer thin-film transistors on plastic”, *Nature Materials*, vol. 7, no. 11, pp. 900–906, Nov. 2008, issn: 1476-1122. doi: 10.1038/nmat2291 (cit. on p. 44).
- [135] C. Goth, S. Putzo, and J. Franke, “Aerosol Jet printing on rapid prototyping materials for fine pitch electronic applications”, in *2011 IEEE 61st Electronic Components and Technology Conference (ECTC)*, IEEE, May 2011, pp. 1211–1216, isbn: 978-1-61284-497-8. doi: 10.1109/ECTC.2011.5898664 (cit. on p. 44).
- [136] W. J. Hyun, E. B. Secor, M. C. Hersam, C. D. Frisbie, and L. F. Francis, “High-resolution patterning of graphene by screen printing with a silicon stencil for highly flexible printed electronics”, *Advanced Materials*, vol. 27, no. 1, pp. 109–115, Jan. 2015, issn: 15214095. doi: 10.1002/adma.201404133 (cit. on pp. 44, 45).

- [137] T. Gaugel, S. Bechtel, and J. Neumann-Rodekirch, “Advanced micro-dispensing system for conductive adhesives”, in *First International IEEE Conference on Polymers and Adhesives in Microelectronics and Photonics. Incorporating POLY, PEP & Adhesives in Electronics. Proceedings (Cat. No.01TH8592)*, IEEE, 2001, pp. 40–45, isbn: 0-7803-7220-4. doi: 10.1109/POLYTR.2001.973253 (cit. on p. 45).
- [138] D. P. Adams, “Reactive multilayers fabricated by vapor deposition: A critical review”, *Thin Solid Films*, vol. 576, pp. 98–128, 2015, issn: 00406090. doi: 10.1016/j.tsf.2014.09.042 (cit. on pp. 50, 86).
- [139] F. De Boer, R. Boom, W. Mattens, A. Miedema, and A. Niessen, *Cohesion in Metals Transition Metal Alloys*. Amsterdam: North-Holland, 1988, isbn: 0-444-87098-9 (cit. on p. 52).
- [140] B. Li, L. J. Rong, Y. Y. Li, and V. E. Gjunter, “Synthesis of porous Ni-Ti shape-memory alloys by self-propagating high-temperature synthesis: reaction mechanism and anisotropy in pore structure”, *Acta Materialia*, vol. 48, no. 15, pp. 3895–3904, 2000, issn: 13596454. doi: 10.1016/S1359-6454(00)00184-1 (cit. on p. 52).
- [141] G. Sauthoff, “Intermetallic materials”, in *Powder Metallurgy Data. Refractory, Hard and Intermetallic Materials*, R. Beiss, P. Ruthardt and H. Warlimont, Eds., vol. 2A2, 2002, pp. 14–38, isbn: 3-540-42961-1. doi: 10.1007/10858641_18 (cit. on p. 54).
- [142] G. K. Dey, “Physical metallurgy of nickel aluminides”, *Sadhana*, vol. 28, no. 1-2, pp. 247–262, Feb. 2003, issn: 0256-2499. doi: 10.1007/BF02717135 (cit. on p. 54).
- [143] N. F. Shkodich, N. A. Kochetov, A. S. Rogachev, A. E. Grigoryan, M. R. Sharafutdinov, and B. P. Tolochko, “Formation of the crystal structure of intermetallic compounds in mechanically activated Ni-Al and Ti-Al systems during self-propagating high-temperature synthesis”, *Bulletin of the Russian Academy of Sciences: Physics*, vol. 71, no. 5, pp. 650–652, 2007, issn: 1062-8738. doi: 10.3103/S1062873807050152 (cit. on p. 55).
- [144] C. Rossi, *Al-Based Energetic Nanomaterials*. Hoboken, NJ, USA: John Wiley & Sons, Inc., 2015, isbn: 9781119007456. doi: 10.1002/9781119007456 (cit. on pp. 58, 71).
- [145] Hydrargyrum. (2011). File:Bragg diffraction 2.svg - Wikimedia Commons, [Online]. Available: https://commons.wikimedia.org/wiki/File:Bragg_diffraction_2.svg (visited on 08/01/2017) (cit. on p. 64).
- [146] A. W. Hull, “X-ray crystal analysis of thirteen common metals”, *Physical Review*, vol. 17, no. 5, p. 571, 1921 (cit. on pp. 64, 65).

- [147] Corning SAS. (2012). Macor® machinable glass ceramic for industrial applications, [Online]. Available: <https://www.corning.com/media/worldwide/csm/documents/71759a443535431395eb34ebad091cb.pdf> (visited on 12/06/2017) (cit. on p. 76).
- [148] B. Gottfried, C. Lee, and K. Bell, “The leidenfrost phenomenon: film boiling of liquid droplets on a flat plate”, *International Journal of Heat and Mass Transfer*, vol. 9, no. 11, pp. 1167–1188, Nov. 1966, issn: 00179310. doi: 10.1016/0017-9310(66)90112-8 (cit. on p. 77).
- [149] R. Masser, J. Braeuer, and T. Gessner, “Modelling the reaction behavior in reactive multilayer systems on substrates used for wafer bonding”, *Journal of Applied Physics*, vol. 115, no. 24, p. 244311, 2014, issn: 0021-8979. doi: 10.1063/1.4885457 (cit. on p. 86).
- [150] V. V. Barzykin, “Initiation of SHS processes”, *Pure and Applied Chemistry*, vol. 64, no. 7, pp. 909–918, 1992, issn: 0033-4545. doi: 10.1351/pac199264070909 (cit. on p. 86).
- [151] M. P. Kremer, A. Roshanghias, and A. Tortschanoff, “Self-propagating reactive Al/Ni nanocomposites for bonding applications”, *Micro and Nano Systems Letters*, vol. 5, no. 1, p. 12, 2017, issn: 2213-9621. doi: 10.1186/s40486-017-0046-x (cit. on p. 87).
- [152] K. Koga and M. Hirasawa, “Evidence for the anisotropic oxidation of gas-phase Al nanoparticles”, *Journal of Nanoparticle Research*, vol. 17, no. 7, p. 290, 2015, issn: 1388-0764. doi: 10.1007/s11051-015-3095-1 (cit. on p. 105).
- [153] L. Wang, D. Luss, and K. S. Martirosyan, “The behavior of nanothermite reaction based on Bi₂O₃/Al”, *Journal of Applied Physics*, vol. 110, no. 7, p. 174311, 2011, issn: 00218979. doi: 10.1063/1.3650262 (cit. on p. 105).
- [154] L. W. Finger and R. M. Hazen, “Crystal structure and compression of ruby to 46 kbar”, *Journal of Applied Physics*, vol. 49, no. 12, pp. 5823–5826, Dec. 1978, issn: 0021-8979. doi: 10.1063/1.324598 (cit. on p. 107).
- [155] S. SASAKI, K. FUJINO, and Y. TAKEUCHI, “X-Ray Determination of Electron-Density Distributions in Oxides, MgO, MnO, CoO, and NiO, and Atomic Scattering Factors of their Constituent Atoms”, *Proceedings of the Japan Academy. Ser. B: Physical and Biological Sciences*, vol. 55, no. 2, pp. 43–48, 1979, issn: 0386-2208. doi: 10.2183/pjab.55.43 (cit. on p. 107).
- [156] C. E. Shuck, M. Frazee, A. Gillman, M. T. Beason, I. E. Gunduz, K. Matouš, R. Winarski, and A. S. Mukasyan, “X-ray nanotomography and focused-ion-beam sectioning for quantitative three-dimensional analysis of nanocomposites”, *Journal of Synchrotron Radiation*, vol. 23, no. 4, pp. 990–996, 2016, issn: 1600-5775. doi: 10.1107/S1600577516007992 (cit. on p. 115).

- [157] C. E. Shuck and A. S. Mukasyan, "Reactive Ni/Al Nanocomposites: Structural Characteristics and Activation Energy", *The Journal of Physical Chemistry A*, vol. 121, no. 6, pp. 1175–1181, Feb. 2017, issn: 1089-5639. doi: 10.1021/acs.jpca.6b12314 (cit. on pp. 115, 116).
- [158] I. E. Gunduz, A. Kyriakou, N. Vlachos, T. Kyratsi, C. C. Doumanidis, S. Son, and C. Rebholz, "Spark ignitable Ni–Al ball-milled powders for bonding applications", 2014. doi: 10.1016/j.surfcoat.2014.06.068 (cit. on p. 117).
- [159] B. Predel, "Al-Ti (Aluminum-Titanium)", in *Landolt-Börnstein - Group IV Physical Chemistry 5A (Ac-Au – Au-Zr)*, O. Madelung, Ed., Berlin/Heidelberg: Springer-Verlag, 1991, pp. 1–8. doi: 10.1007/10000866_151 (cit. on p. 126).
- [160] L. Zhang and Z. Wang, "Thermal investigation of fabricating porous NiTi SMA by SHS", *Experimental Thermal and Fluid Science*, vol. 32, no. 6, pp. 1255–1263, May 2008, issn: 08941777. doi: 10.1016/j.expthermflusci.2008.02.006 (cit. on p. 130).
- [161] E. M. Hunt and M. L. Pantoya, "Ignition dynamics and activation energies of metallic thermites: From nano- to micron-scale particulate composites", *Journal of Applied Physics*, vol. 98, no. 3, p. 034 909, Aug. 2005, issn: 0021-8979. doi: 10.1063/1.1990265 (cit. on p. 130).
- [162] C. Yeh and W. Sung, "Synthesis of NiTi intermetallics by self-propagating combustion", *Journal of Alloys and Compounds*, vol. 376, no. 1-2, pp. 79–88, Aug. 2004, issn: 09258388. doi: 10.1016/j.jallcom.2003.12.016 (cit. on p. 130).
- [163] M. Adeli, S. Seyedein, M. Aboutalebi, M. Kobashi, and N. Kanetake, "A study on the combustion synthesis of titanium aluminide in the self-propagating mode", *Journal of Alloys and Compounds*, vol. 497, no. 1-2, pp. 100–104, May 2010, issn: 09258388. doi: 10.1016/j.jallcom.2010.03.050 (cit. on p. 130).

List of Figures

| | | |
|------|---|----|
| 1.1 | EPPL Project Outline | 2 |
| 1.2 | Photograph of a MOEMS device | 3 |
| 1.3 | Structurization of MOEMS concept | 4 |
| 1.4 | Schematic drawing of the RNC bonding concept | 6 |
| 2.1 | Drawing depicting the warpage of a package due to CTE mismatch and thermal loading during the bonding process | 11 |
| 2.2 | Technical drawing of the model employed in the simulation in cross section view | 12 |
| 2.3 | FEM simulation of heatstress induced warpage in a package | 13 |
| 2.4 | Systemization of bonding technologies, inspired by [23]. | 14 |
| 2.5 | NanoFoil combustion image series | 21 |
| 2.6 | Plot of bonding technologies: MOEMS packaging feasibility over deposition and patterning complexity | 25 |
| 3.1 | Schematic drawing of the concept of thermite railroad welding | 28 |
| 3.2 | Axis description for modeling of the reaction front | 31 |
| 3.3 | Molecular dynamics simulation of Ni and Al nanoparticle fusion | 33 |
| 3.4 | Schematic drawing of the iRMS bonding concept | 34 |
| 4.1 | Systemization of some relevant fluid deposition technologies. Emphasized printing technologies are discussed in more detail in this work. | 38 |
| 4.2 | Working principles of DOD and CIJ printhead technology | 39 |
| 4.3 | Weber number plotted over Reynold's number, depicting the printable regime | 41 |
| 4.4 | Cross-sectional view of a spectra S-Class 128-AA printhead nozzle. | 42 |
| 4.5 | CFD simulation of nozzle jetting | 42 |
| 4.6 | Piezo Printhead Driving Pulse and Jetting Behaviour | 43 |
| 4.7 | Working principle of Aerosoljet printing | 44 |
| 4.8 | Schematic drawing of the screen printing process | 45 |
| 4.9 | Working principle of direct writing | 46 |
| 4.10 | Radar plot comparing the introduced printing technologies | 47 |

List of Figures

| | | |
|------|--|----|
| 5.1 | Schematic drawing of the concept of reactive nanocomposites based bonding | 51 |
| 5.2 | Critical layer thickness for SHS reactions | 53 |
| 5.3 | Crystal structure of pure Ni and Al and the resulting NiAl intermetallic phase | 54 |
| 5.4 | Phase diagram of the binary Ni-Al system | 55 |
| 6.1 | Ni ₂₀ particle size distribution | 62 |
| 6.2 | SEM graph and particle count overlay of raw Ni ₂₀ sample. The error resulting from false recognition of single particles to be a large one is assumed to be canceled out by the opposing error of larger particles to be recognized as multiple smaller ones. | 63 |
| 6.3 | Measurement principle of XRD: Bragg reflection | 64 |
| 6.4 | XRD measurements of initial raw Al and Ni nanoparticle samples. . . | 65 |
| 6.5 | DTA graph of Ni–Al sample | 66 |
| 6.6 | XRD Graph of DTA sample | 66 |
| 6.7 | STEM and in situ EDX measurement of an Al ₁₈ Ni ₆₀ sample. | 67 |
| 6.8 | TEM images of an Al ₁₈ Ni ₆₀ sample | 68 |
| 6.9 | TEM images of an Al ₄₀ Ni ₂₀ sample | 69 |
| 6.10 | STEM and in situ EDX measurement of an unreacted Al ₄₀ Ni ₂₀ sample. | 70 |
| 6.11 | Photograph of the glove box in which experiments were conducted. . | 71 |
| 6.12 | Schematic drawing of the sonication process and effect. | 72 |
| 6.13 | Pressure applicator for laser ignition | 74 |
| 6.14 | Schematic drawing of the using principle of the sample holder | 75 |
| 6.15 | Photograph of the heat chuck | 76 |
| 6.16 | Screenshot of the heatchuck driver software | 77 |
| 6.17 | Photograph of the heat chuck setup with laser focusing optics, laser trigger and camera. | 78 |
| 6.18 | Schematic drawing of ignition experiments using a glowing hot wire. | 80 |
| 6.19 | Ignition experiment using an ignited Nanofoil as heat source. | 81 |
| 6.20 | Schematic drawing of the ignition experiment using an electric spark discharge. | 81 |
| 6.21 | Schematic drawing of ignition experiment using a laser | 82 |
| 6.22 | SEM graph of an Al ₁₈ Ni ₆₀ sample subject to a high power laser ignition attempt. | 83 |
| 6.23 | Schematic drawing of ignition experiment using a laser | 84 |
| 6.24 | Laser power graph showing ignition threshold | 85 |
| 6.25 | Comparison of reaction speed of different samples | 87 |
| 6.26 | Reaction front propagation velocity over ambient temperature | 88 |
| 6.27 | XRD Graph of the Al ₁₈ Ni ₂₀ samples | 90 |
| 6.28 | XRD Graph of the Al ₁₈ Ni ₆₀ samples | 91 |
| 6.29 | XRD Graph of the Al ₄₀ Ni ₂₀ samples | 92 |
| 6.30 | XRD Graph of the Al ₄₀ Ni ₆₀ samples | 93 |

| | | |
|------|--|-----|
| 6.31 | Qualitative juxtaposition of XRD graphs of the reaction products . . . | 94 |
| 6.32 | Quantitative comparison of chemical composition of reaction products. | 95 |
| 6.33 | TEM images of a reacted Al18Ni60 sample. | 96 |
| 6.34 | TEM images of a reacted Al40Ni20 sample | 97 |
| 6.35 | STEM and <i>in situ</i> EDX measurement of the reacted Al18Ni60 sample. | 98 |
| 6.36 | STEM and <i>in situ</i> EDX measurement of the reacted Al40Ni20 sample. | 98 |
| 7.1 | SEM graphs of an Al40Ni60 sample, showing sintered regions in the laser treated areas. | 100 |
| 7.2 | White light interferometric measurement of laser sintered trench. . . | 101 |
| 7.3 | Reaction front propagation velocity and reacted material ratio over number of particles ratio | 102 |
| 7.4 | Reaction temperature as derived from the measured reaction front propagation velocity. | 103 |
| 7.5 | SEM graphs of unreacted and fully reacted Al18Ni60 samples. . . . | 104 |
| 7.6 | SEM graphs of unreacted and fully reacted Al40Ni20 samples. . . . | 105 |
| 7.7 | SEM graph of an anisotropically reacted Al40Ni20 sample | 106 |
| 7.8 | Comparative XRD measurement of sonicated vs. ground Al18Ni20 sample | 107 |
| 7.9 | SEM graph with respective EDX mappings for Nickel, Aluminium and Oxygen | 107 |
| 7.10 | High RNC layer porosity can constrain self-propagating reactions due to poor heat transfer within the reactive layer. The schematic illustration shows a sequence from left to right of a porous RNC layer between two glass slides. Left: initial state, centre: ignition on one side, right: only small areas adjacent to the ignition spot reacted. . . | 109 |
| 7.11 | Inhomogeneous RNC layers cause regions of non stoichiometric materials ratio. In these regions loss of energy can lead to extinction of the reaction. The schematic illustration shows a sequence from left to right of an inhomogeneous RNC layer between two glass slides. Left: initial state, centre: ignition on one side, right: only small areas adjacent to the ignition spot reacted. | 109 |
| 7.12 | Thick passivation layers on the reactive particles reduce the reactivity significantly, causing poor performance of the reaction. | 110 |
| 8.1 | FIB cut cross sectional SEM graph of a ball milled RNC microparticle | 116 |
| 8.2 | Schematic comparison of RNC and RNCNP | 117 |
| A.1 | Ti60 particle size distribution | 121 |
| A.2 | Sample no. 27 particle size distribution | 122 |
| A.3 | SEM graph and particle count overlay of sample no. 27. | 122 |
| A.4 | Sample no. 33 particle size distribution | 123 |
| A.5 | SEM graph and particle count overlay of sample no. 33. | 123 |
| A.6 | Sample no. 40 particle size distribution | 124 |

List of Figures

| | | |
|-----|---|-----|
| B.1 | Phase diagram of the binary Al-Ti system | 126 |
| B.2 | Crystal structure of elemental Titanium | 127 |
| B.3 | Crystal structure of intermetallic NiTi | 128 |
| B.4 | Crystal structure of intermetallic TiAl | 128 |
| B.5 | DTA graph for the Ti–Al sample | 129 |
| B.6 | XRD graph of the Ti–Al sample post DTA measurement. | 129 |
| D.1 | Nanoparticles acquired from Iolitec. | 153 |
| D.2 | Micropowders acquired from GoodFellow. | 154 |

List of Tables

| | | |
|------|--|-----|
| 2.1 | Anodic bonding: Advantages and disadvantages | 15 |
| 2.2 | Direct bonding: Advantages and disadvantages | 16 |
| 2.3 | Plasma-activated bonding: Advantages and disadvantages | 17 |
| 2.4 | Ultrasonic bonding: Advantages and disadvantages | 17 |
| 2.5 | Glass frit bonding: Advantages and disadvantages | 18 |
| 2.6 | Thermocompression bonding: Advantages and disadvantages | 19 |
| 2.7 | Eutectic bonding: Advantages and disadvantages | 19 |
| 2.8 | Adhesive bonding: Advantages and disadvantages | 20 |
| 2.9 | Reactive NanoFoil bonding: Advantages and disadvantages | 21 |
| 2.10 | iRMS bonding: Advantages and disadvantages | 22 |
| 2.11 | Transient liquid phase diffusion bonding: Advantages and disadvantages | 23 |
| 2.12 | Selective laser bonding: Advantages and disadvantages | 24 |
| 2.13 | Comparison of bonding techniques employed in microsystems technologies | 26 |
| 3.1 | Thermodynamic properties of selected Aluminide-SHS reactions [109]. A comprehensive list of Boride-, Carbide-, Silicide- and Aluminide-SHS reactions is shown in Appendix B. The two highlighted reactions were subject to further investigation in this work. | 29 |
| 5.1 | Materials combinations evaluated in our studies for RNC development. | 52 |
| 5.2 | Critical layer thickness Δ_{cr} in mm of the reactive material for self-sustained reactions in respect to the inert material. | 53 |
| 6.1 | Batch description and particle sizes of the acquired material. | 60 |
| 6.2 | Review of experimentally evaluated ignition mechanisms. | 86 |
| B.1 | Thermodynamic properties of selected Boride-, Carbide-, Silicide- and Aluminide-SHS reactions [109] | 125 |
| B.2 | Material properties used to calculate the critical layer thickness | 130 |
| B.3 | Material systems properties used to calculate the critical layer thickness [77, 160–163] | 130 |

List of Tables

C.1 Sample Database 132

Abbreviations, Nomenclature and Symbols

Abbreviations

| | |
|--------|--|
| 2D | Two Dimensional |
| 3D | Three Dimensional |
| C2C | Chip to Chip Bonding |
| C2W | Chip to Wafer Bonding |
| CFD | Continuous Fluid Dynamics |
| CIJ | Continuous Inkjet |
| CTE | Coefficient of Thermal Expansion |
| DOD | Drop on Demand Inkjet |
| DSC | Differential Scanning Calorimetry |
| DTA | Differential Thermal Analysis |
| EDX | Electron Dispersive X-ray Spectroscopy |
| EPPL | Enhanced Power Pilot Line |
| FEM | Finite Element Modelling |
| HEBM | High Energy Ball Milling |
| HR-TEM | High Resolution Transmission Electron Microscopy |
| IC | Integrated Circuits |
| IJP | Inkjet Printing |
| IoT | Internet of Things |
| iRMS | Integrated Reactive Material Systems |
| MA | Mechanical Activation |
| MEMS | Micro-Electro-Mechanical Systems |
| MOEMS | Micro-Opto-Electro-Mechanical Systems |
| MST | Microsystem Technologies |
| NEMS | Nano-Electro-Mechanical Systems |
| NP | Nanoparticles |

| | |
|------|---|
| PPD | Pulse Peak Duration |
| RNC | Reactive Nanocomposite |
| SEM | Scanning Electron Microscopy |
| SF | Solid Flame |
| SHS | Self-Propagating High Temperature Synthesis |
| STEM | Scanning Transmission Electron Microscopy |
| TEM | Transmission Electron Microscopy |
| W2W | Wafer to Wafer Bonding |
| WLI | White Light Interferometry |
| WLP | Wafer Level Packaging |
| XRD | X-ray Powder Diffraction Analysis |

Materials Nomenclature

| | |
|--------|---|
| Al125p | Aluminium powder, maximum particle size specified by supplier: 125 μm |
| Al18 | Aluminium nanoparticles, mean diameter specified by supplier: 18 nm |
| Al25p | Aluminium powder, maximum particle size specified by supplier: 25 μm |
| Al40 | Aluminium nanoparticles, mean diameter specified by supplier: 40 nm to 60 nm |
| Ar 5.0 | Argon, 99.99990 % purity |
| Ni20 | Nickel nanoparticles, mean diameter specified by supplier: 20 nm |
| Ni250p | Nickel powder, maximum particle size specified by supplier: 250 μm |
| Ni45p | Nickel powder, maximum particle size specified by supplier: 45 μm |
| Ni60 | Nickel nanoparticles, mean diameter specified by supplier: 60 nm to 80 nm |
| Ti150p | Titanium powder, maximum particle size specified by supplier: 150 μm |
| Ti45p | Titanium powder, maximum particle size specified by supplier: 45 μm |
| Ti60 | Titanium nanoparticles, mean diameter specified by supplier: 60 nm to 80 nm |

Mathematical Symbols

| | |
|-----------------|--|
| E_a | Activation Energy (J) |
| Oh | Ohnesorge number (dimensionless) |
| R | Universal Gas Constant (J/molK) |
| Re | Reynold's number (dimensionless) |
| T_0 | Initial Temperature (K) |
| U_0 | Combustion Rate without heat losses (m/s) |
| We | Weber number (dimensionless) |
| γ_{cr} | Heat loss parameter (dimensionless) |
| $\rho_{i/r}$ | Density of the inert (_i) and reactive (_r) material, respectively (kg/m ³) |
| a_f | Temperature conductivity, $a_f = \frac{\lambda}{\rho c}$ () |
| $c_{i/r}$ | Specific heat of thermal conductivity of the inert (_i) and reactive (_r) material, respectively (J/mol) |
| d_l | RNC layer thickness (μm) |
| v_R | Reaction front propagation velocity (mm/s) |
| M | Molar mass (g) |
| T_a | Adiabatic reaction temperature (K) |
| Δ_{cr} | Critical RNC layer thickness (μm) |
| γ | Viscosity (mN/m) |
| $\lambda_{i/r}$ | Thermal conductivity of the inert (_i) and reactive (_r) material, respectively (W/mK) |

Curriculum Vitae

Personal Data

| | |
|----------------|--|
| Name | Matthias Peter Kremer |
| Adress | 9 Hawthorn Mews Hawthorn Ave Dublin 3 Ireland |
| Born | August 18. 1987 in Mainz, Germany |
| Marital status | Married |
| Nationality | German |

Education

| | |
|-----------------|--|
| 10/2007–08/2013 | Mechanical Engineering at Karlsruhe Institute of Technology (KIT) Major: Mechatronics and Microsystem Technology |
| 02/2011–08/2011 | Mid-study Thesis, topic: <i>An Approach for experimental Validation of microscale Shaft-Hub-Connections</i> , Grade: 1.0 |
| 02/2013–08/2013 | Diploma Thesis, topic: <i>MOEMS Based Variable-Focus Laser Scanning and Application in Light-Driven Microfluidics</i> , Grade: 1.0 |
| 30.08.2013 | Diplom-Ingenieur, Grade: 1.5 |
| 09/2013–09/2016 | PhD Student in Microsystem Technologies, topic: <i>Printed Bonding Layers for MEMS Package Sealing</i> |

Employment History

- 05/2006–01/2007 Werkstätten für behinderte Menschen, Mainz
- 08/2007–09/2007 Schott AG, Mainz
Basic internship for mechanical engineering
- 05/2008–05/2012 PTV AG, Karlsruhe
Student assistant in software testing
- 07/2012–12/2012 TRUMPF Laser- und Systemtechnik GmbH, Ditzingen
Advanced internship in the research and development of laser machines and optical components department
- 02/2013–08/2013 CTR Carinthian Tech Research AG, Villach
Diploma Thesis
- 09/2013–09/2016 CTR Carinthian Tech Research AG, Villach
PhD Student
- From 11/2016 Trinity College Dublin, The University of Dublin
Research Assistant

Own Publications

Related Journal Article

- [1] **M. P. Kremer**, A. Roshanghias, and A. Tortschanoff, “Self-propagating reactive Al/Ni nanocomposites for bonding applications”, *Micro and Nano Systems Letters*, vol. 5, no. 1, p. 12, 2017, issn: 2213-9621. doi: 10.1186/s40486-017-0046-x.

Related Conference Presentations

- [1] **M. P. Kremer**, A. Roshanghias, and A. Tortschanoff, “Mechanical Activation of Reactive Nanocomposites for Bonding Applications”, in *NanoFIS 2016 Functional Integrated nanoSystems*, Graz, 2016.
- [2] **M. P. Kremer**, A. Tortschanoff, and A. E. Guber, “SHS-Enabled Reactive Bonding for Application in Microsystems Technologies”, in *International Symposium on Self-Propagating High Temperature Synthesis*, Antalya, 2015.
- [3] **M. P. Kremer**, A. Tortschanoff, and A. E. Guber, “Mikrofügen mit reaktiven Nanokompositen”, in *Mikrosystemtechnik Kongress 2015*, Karlsruhe, 2015.
- [4] **M. P. Kremer**, A. Tortschanoff, and A. E. Guber, “Reactive nanocomposites for heterogeneous integration”, in *Smart Systems Integration 2015*, T. Gessner, Ed., Copenhagen: Apprimus Verlag, Aachen, 2015, pp. 418–421, isbn: 9783863592967. doi: 978-3-86359-296-7.
- [5] **M. P. Kremer**, A. Tortschanoff, and A. E. Guber, “Reactive nanocomposites for joining materials”, in *NanoFIS 2014 - Functional Integrated nanoSystems*, Graz, 2014.

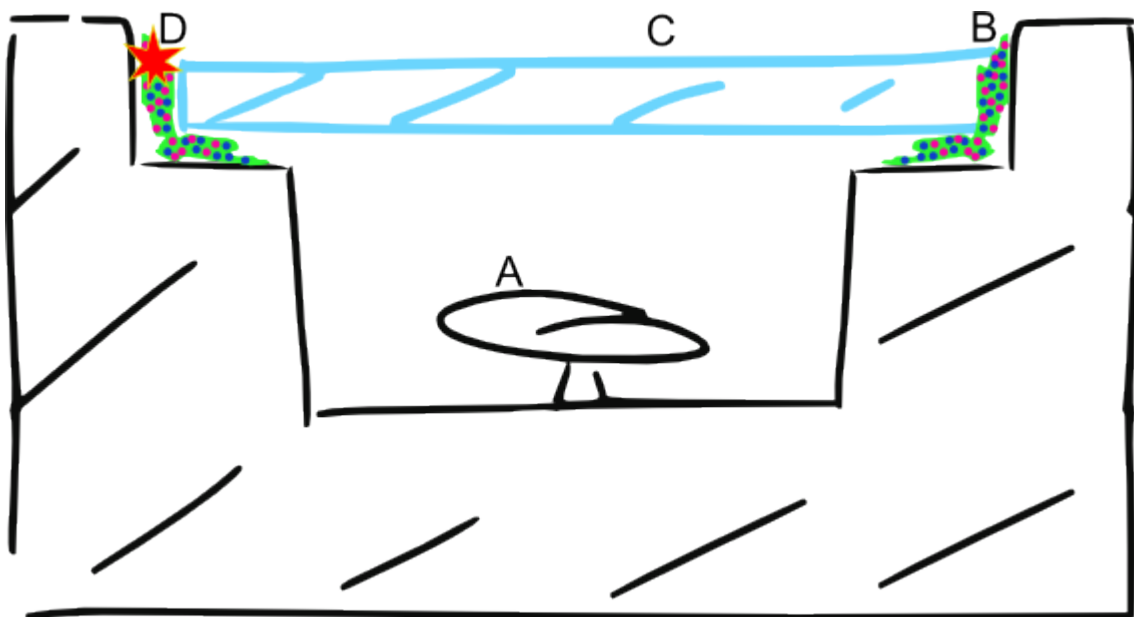
Unrelated Journal Articles

- [1] **M. P. Kremer**, C. J. Zhang, A. Seral-Ascaso, S.-H. Park, N. McEvoy, B. Anasori, Y. Gogotsi, and V. Nicolosi, “Stamping of Flexible, Coplanar Micro-Supercapacitors Using MXene Inks”, *Advanced Functional Materials*, vol. 28, no. 9, p. 1705–1706, Feb. 2018, issn: 1616301X. doi: 10.1002/adfm.201705506.
- [2] A. Tortschanoff, D. Damian, and **M. P. Kremer**, “MOEMS based Laser Scanning Device for Light-Driven Microfluidics”, *International Journal of Science and Engineering Investigations*, vol. 4, no. 46, pp. 65–70, 2015.
- [3] A. Tortschanoff, D. Damian, and **M. P. Kremer**, “MOEMS based laser scanner for light-driven microfluidics”, *Procedia Engineering*, vol. 120, pp. 1063–1066, 2015, issn: 18777058. doi: 10.1016/j.proeng.2015.08.757.

Unrelated Conference Presentations

- [1] **M. P. Kremer**, C. Zhang, and V. Nicolosi, “3D Printing-Enabled Rapid Reproduction of Mxene Based Supercapacitors”, *Meeting Abstracts*, vol. MA2017-01, no. 23, pp. 1175–1175, Apr. 2017, issn: 2151-2041.
- [2] **M. P. Kremer**, C. Zhang, and V. Nicolosi, “Scalability of Low Cost Production Methods for MXene Based Supercapacitors”, in *Flatlands – Beyond Graphene*, Lausanne, 2017.
- [3] C. Zhang, **M. P. Kremer**, Y. Gogotsi, J. N. Coleman, and V. Nicolosi, “Two-Dimensional Titanium Carbide (MXene): Oxidation Stability and Energy Storage Applications”, in *Advanced Automotive Batteries Conference*, Mainz, 2018.
- [4] M. Baumgart, A. Tortschanoff, D. Damian, and **M. P. Kremer**, “Light-driven microfluidics with a MOEMS based laser scanner”, in *EOSOF 2015*, Munich, 2015.
- [5] A. Tortschanoff, D. Damian, and **M. P. Kremer**, “MOEMS based laser scanner for light-driven microfluidics”, in *Euroensors 2015*, Freiburg, 2015.
- [6] M. Baumgart, M. Lenzhofer, **M. P. Kremer**, and A. Tortschanoff, “Integrated packaging of 2D MOEMS mirrors with optical position feedback”, in *Proc. SPIE*, vol. 9375, San Francisco, 2015, 93750R–93750R–7, isbn: 9781628414653. doi: 10.1117/12.2079219.

- [7] D. Damian, **M. P. Kremer**, and A. Tortschanoff, “MOEMS Based Laser Scanning for Light-Driven Microfluidics and Microbiological Analytics”, in *4th International Conference on Materials and Applications for Sensors and Transducers*, Bilbao, 2014.
- [8] **M. P. Kremer** and A. Tortschanoff, “Thermally Induced Light-Driven Microfluidics using a MOEMS-Based Laser Scanner for Particle Manipulation”, in *Proc. SPIE 8976, Microfluidics, BioMEMS, and Medical Microsystems XII, 89761F (March 6, 2014)*, San Francisco, 2014.
- [9] A. Tortschanoff, **M. P. Kremer**, T. Sandner, and A. Kenda, “Optical design of MOEMS-based micro-mechatronic modules for applications in spectroscopy”, in *Proc. SPIE 9101, Next-Generation Spectroscopic Technologies VII, 910109 (May 21, 2014)*, Baltimore, 2014, isbn: 9781628410389. doi: 10.1117/12.2053001.
- [10] A. Tortschanoff, A. Kenda, T. Sandner, **M. P. Kremer**, and A. Frank, “Compact driver module for closed-loop control of resonant 2D-MOEMS scanners”, in *Smart systems integration 2014*, Vienna, 2014.
- [11] **M. P. Kremer** and A. Tortschanoff, “Integration of a MOEMS-Based Variable-Focus Laser Scanner for Application in Light-Driven Microfluidics”, in *Smart Systems Integration 2014*, Vienna, 2014.
- [12] **M. P. Kremer** and A. Tortschanoff, “Development of a compact MOEMS-based focus-variable laser scanner”, in *7th International Conference on Quantum, Nano and Micro Technologies (ICQNM 2013)*, Barcelona, 2013.
- [13] M. Baumgart, A. Tortschanoff, and **M. P. Kremer**, “Influence of Radial Light Source Distribution on Optical Angular Position Sensing for Tilttable Mirrors”, in *7th International Conference on Quantum, Nano and Micro Technologies (ICQNM 2013)*, Barcelona, 2013.



First schematic sketch of the RNC-bonding concept – 25.11.2013
A) MOEMS mirror, B) reactive nanocomposite, C) top substrate, D) ignition.